THE UNIVERSITY *of* EDINBURGH

The physics of the flow of concentrated suspensions

Ben Michael Guy

Doctor of Philosophy
The University of Edinburgh
September 2016

Abstract

A particulate suspension under shear is a classic example of a system driven out of equilibrium. While it is possible to predict the equilibrium phase behaviour of a quiescent suspension, linking microscopic details to bulk properties under flow remains an open challenge. Our current understanding of sheared suspensions is restricted to two disparate regimes, the colloidal regime, for particle sizes $d < 1$ μm and the granular regime, for $d > 50$ μm. The physics of the industrially-relevant intermediate size regime, 1 $\mu\text{m} \lesssim d \lesssim 50$ μm, is unclear and has not been explored previously.

In this thesis, we use conventional rheometry on a range of model spheres to develop the foundations of a predictive understanding of suspension flow across the entire size spectrum. In the first part of the thesis, we show that in repulsive particulate systems the rheology is characterised by two viscosity "branches" diverging at different volume fractions ϕ_{RCP} and ϕ_m, which represent states of flow with lubricated (frictionless) and frictional interactions between particles. In the intermediate size regime, there is a transition between these two branches above a critical onset stress σ^* which manifests as shear thickening. This σ^* is related to a barrier (invariably due to the charge or steric stabilisation) keeping particle surfaces apart. Our data are quantitatively fit by the Wyart and Cates theory for frictional thickening [1] if we assume that probability distribution of forces in the system is similar to in dry granular media.

The onset stress for shear thickening is found to decrease with the inverse square of the particle size $\sigma^* \propto d^{-2}$ for diverse systems. We show that it is the competition between the scaling of $\sigma^*(d)$ and the size dependence of the entropic stress scale ($\sim d^{-3}$) that controls the crossover from colloidal to granular rheology with increasing size. Granular systems are "always shear thickened" under typical experimental conditions, while colloidal systems are always in a frictionless state.

In the second part of the thesis, we explore the validity of the frictional framework for shear thickening. Although it quantitatively predicts our steady-state rheology, the frictional framework contradicts traditional fluid-mechanical thinking and has yet to be rigorously tested experimentally. In fact, there is a large body of literature that attributes thickening to purely hydrodynamic effects. Using dimensional analysis and simple physical arguments we examine possible physical origins for thickening and show that previously-proposed mechanisms can be subdivided into three types: two-particle hydrodynamic thickening, many-particle hydrodynamic thickening ("hydroclusters") and frictional-contact driven thickening. Many of these mechanisms can are inconsistent with the experimental two-branch phenomenology and can be disregarded. We further narrow down possible causes of thickening using the technique of flow reversal, which disentangles the relative contributions of contact and hydrodynamic forces to the viscosity. Consistent with recent simulations [2] and theory [1], we find that in each case thickening is dominated by the formation of frictional contacts and that hydrodynamic thickening, if present, is subdominant.

Lay summary

This thesis studies the flow of concentrated suspensions, densely-packed assemblies of solid particles invisible to the naked eye immersed in a fluid. Suspension flow plays a central role in many industrial processes important to everyday life, from the mixing of sugar and cocoa butter to make chocolate, to the flow of cement down a conduit. Despite their ubiquity, the physics of suspensions under flow is still poorly understood in particular, a predictive understanding of flow properties (e.g., viscosity) based on microscopic details of the particles is lacking.

In this thesis, we study the response to deformation (a discipline known as *rheology*) of a range of model suspensions and in doing so lay the foundations for such a fundamental understanding. In the first part of the thesis, we show that in every stable suspension, there is a barrier that keeps the surfaces of the particles apart; this leads to two possible states of flow: one, at low rates of shear, in which the surfaces of particles are separated by a thin fluid film and another, at high shear rates, in which they are pressed into direct mechanical contact. When in contact, the particles experience static friction: they can no longer slide over each other, and have to roll around one another in a cooperative manner, leading to an increase in the viscosity with shear rate, known as shear thickening. At the highest concentrations of solid particles, the suspension is liquid at rest, but jammed into a solid by modest shear.

The notion that shear thickening is caused by the formation of frictional contacts is a relatively new and controversial one. Traditional fluid mechanics tells us that an infinite force is required to push particles into contact, so they should always remain separated by a fluid film. In fact, a large body of literature exists that explains shear thickening entirely in terms of fluid-mediated, or hydrodynamic, forces. We settle this controversy in the second part of the thesis by using a rheological technique called flow reversal, which allows us to disentangle the contributions to shear thickening from hydrodynamic and contact

forces. In the basic experiment, we shear samples in one direction for some time, then rapidly reverse the direction of shear. Immediately after reversal, the contribution from contacts vanishes as particles are pulled apart, but the hydrodynamic contribution remains the same due to the symmetry of the fluid-mechanical equations governing viscous flow. We find that shear thickening is driven primarily by contact formation, in alignment with the frictional paradigm; however, we also find evidence of a small amount of hydrodynamic thickening, indicating that both kinds of thickening can take place simultaneously.

The understanding we have developed of the role of contact interactions in suspension flow has profound implications for the formulation and processing of real industrial systems. It tells us that modifying and properly characterising the properties of the particles, e.g., surface roughness, is crucial to developing a predictive understanding.

Declaration

I declare that this thesis was composed by myself, that the work contained herein is my own except where explicitly stated otherwise in the text, and that this work has not been submitted for any other degree or professional qualification except as specified.

Parts of this work have been published in [3–5].

(*Ben Michael Guy, September 2016*)

Acknowledgements

This thesis would not have seen the light of day without the help and support of a number of people over the past four years.

A big thanks goes to Wilson, whose enthusiasm and unwavering passion for science has been a constant source of inspiration for me. Thank you for your encouragement, for providing me with some fantastic opportunities and educating me in the ways of correctly eating seafood.

Much of the work I have done would not have been possible without the help of Michiel, who I thank for his day-to-day guidance and friendship. I also owe thanks to everyone in the Soft Matter group at Edinburgh for creating such a pleasant and stimulating working environment. One man, Andy Schofield, has had to contend with my propensity for wreaking havoc in the lab more than anyone else: thank you for your tolerance, for introducing me to the wonders of real ale and being with me through many a Premier League relegation battle.

I would also like to thank Mike Cates for his invaluable input and my collaborators, Chris Ness, Jin Sun, Neil Lin and Itai Cohen, for many fruitful discussions. Thanks to everyone I worked with at Johnson Matthey for their continued interest in my project.

To all the people that had the misfortune of doing battle with me on a squash or badminton court: thank you for tolerating my hyper-competitiveness, mood swings and occasional racquet-smashing. A special thanks goes to the members of the KB squash club (Iris, J-Dawg, Andrew Shaw, Niek, Henry and Roger), the evening badminton crew (Li, Iris and Andy) and the physics badminton club – we had some entertaining games!

Thank you to all my friends in Edinburgh for so many unforgettable memories (there is not enough space to list everyone). I owe an enormous debt of gratitude to everyone who supported me during my final year: you gave me the strength and means to get to the finishing line and I would not have made it without you.

Finally, thanks to Becca for her unconditional support and encouragement, and to my family, for all their love and support from the very beginning.

Contents

Chapter 1

Introduction

The fundamental premise of condensed matter physics is to link the macroscopic properties of a system to the properties of its microscopic constituents. For systems in thermal equilibrium, this has long been possible: the temperature T of a fluid is related to the average kinetic energy of its constituent molecules; the magnetisation of a solid is determined by the directions of the magnetic moments of individual atoms; and the elastic properties of a crystal are determined, in part, by the symmetry of the lattice [6]. In each of these systems, microscopic and macroscopic variables are related by so-called bridge equations linking the free energy to the partition function, which encodes the statistical weight of the possible microstates [7].

In soft matter physics, the systems one encounters are rarely in thermal equilibrium; in that case, there is no generic scheme for predicting macroscopic variables from microscopic information. Some systems are out of equilibrium in a quiescent state, e.g., polymer and colloidal glasses, which are trapped in a dynamically arrested state and cannot explore all of phase space on an experimental time scale [8–10]. Others are driven out of equilibrium by mechanical deformation. This second type is perhaps the most important, as characteristic stress scales in soft matter $\sim 1 - 10^4$ Pa, are such that materials are deformed by stresses readily encountered in every-day life. The study of the response of systems to deformation is known as *rheology*.

The canonical driven soft matter system is a sheared assembly of hard, spheroidal particles suspended in a fluid. At rest, the phase behaviour of this system is well understood [11] – it transitions from a fluid, to a crystal, to a glassy phase

with increasing concentration ϕ. In real suspensions of nearly-hard spheres, this picture is relatively insensitive to the details of the particles in question [12]. Under shear, however, they display a rich phenomenology that is exquisitely sensitive not only to ϕ, but to details such as particle size, interaction potential and surface properties (e.g., roughness and surface chemistry). While there is some predictive understanding for the smallest, colloidal, particles with $d \lesssim 1$ μm and the largest, granular, particles with $d \gtrsim 50$ μm, there is almost none for the regime of intermediate size, $1 \lesssim d \lesssim 50$ μm, although such systems are ubiquitous in industry. Even in the regimes which are purportedly well understood, the literature is pervaded by controversy over which particle-level interactions are important and how these interactions are linked to a macroscopic stress [13]. For example, for the stress-induced solidification of suspensions – familiar to anyone that has mixed cornstarch and water in the kitchen – there are at least three opposing schools of thought [5, 14, 15].

The purpose of this thesis is to lay the foundations for a predictive understanding of suspension flow by establishing experimentally the relevant microscopic physics in a diverse range of systems. Our primary goal is to understand the role of particle-level interactions, in particular identifying when these become important as a function of shear rate, d and ϕ.

It may seem perverse that, in a thesis primarily about particle-level interactions, we do not explicitly characterise particle surface properties – that is the realm of *nano-tribology*, a separate, active research field and is outside the scope of the present work.

1.1 Thesis outline

We begin the thesis by introducing the basic principles of rheology in Ch. 2, before reviewing previous experimental work on colloidal and granular systems in Ch. 3.

The first two results chapters concern the steady-state rheology of nominally repulsive particles. In Ch. 5, we establish the basic phenomenology of intermediate-sized particle rheology, in which shear thickening plays a central role. Specifically, we demonstrate that there is a stress-dependent transition between lubricated and frictional viscosity "branches" and fit our data to the Wyart and Cates theory of

shear thickening. In Ch. 6, we show that the two-branch phenomenology can be extended to the colloidal and granular size regimes by probing the size dependence of the onset of thickening.

The final two results chapters focus on the mechanism of shear thickening. In Ch. 7, we adopt a dimensional approach to determine the particle-level ingredients that can lead shear thickening; using previous work and our own steady-state results, we can rule out many of these mechanisms. In Ch. 8, we use a rheological technique called *flow reversal* to further narrow down the likely cause of shear thickening in real systems.

We summarise the main results of the thesis in Ch. 9 and conclude by outlining a scheme for future research into the flow of concentrated suspensions, incorporating preliminary data not presented elsewhere in the thesis.

Chapter 2

Rheology

In this chapter, we give an introduction to the field of *rheology*, the study of the mechanical response of a material to deformation. We focus on issues relevant to the flow of suspensions; however, we point out that most of the standard practices and theoretical developments in rheology were borne out of work on polymeric systems (for which see [16] and [17] for a comprehensive overview). To illustrate the basic premise of rheology, imagine a 1 cm cube of suspension containing particles 1 μm in diameter being squeezed between thumb and finger. Ideally we would have access to the positions $\{\underline{x}^{(\alpha)}\}$ and velocities $\{\underline{v}^{(\alpha)}\}$ of the $N \sim 10^{11}$ particles and the velocity of the suspending fluid at every point. If we also knew the interactions between particles, then in principle we could solve Newton's equations of motion for the $3N$ forces and torques on the particles, subject to constraints imposed by the rigidity of the particles. In practice, we do not know the positions and momenta of all the particles and solving the resulting equations would be an almost impossible, and not very useful, task. What we can probe, however, are macroscopic observables such as the stress exerted by the suspension on the thumb and finger. In much the same way as in equilibrium thermodynamics macroscopic variables such as temperature and pressure are related to the microstates explored by the system, so the stress is related to the local configurations of particles in the suspension. The fundamental premise of rheology is to characterise the *macroscopic* response of the system to deformation without explicitly worrying about microscopic details. Exactly how to relate microscopic details to macroscopic observables in sheared suspensions is the realm of *rheophysics* [18].

In rheology, it is assumed that we can treat the suspension as a continuum made up of *material elements* with volume V that enclose many particles, Fig. 2.1, but each of which is small relative to the volume of the suspension. Instead of considering the velocity components of each particle, we consider a velocity vector field $\underline{v}(\underline{x})$ whose value at position $\underline{x}$ is determined by the average velocity of the particles and fluid in the material element located at $\underline{x}$. Similarly, the forces on the particles and fluid are related to a stress tensor field $\underline{\underline{\sigma}}(\underline{x})$; the positions of the particles to a strain tensor $\underline{\underline{\epsilon}}(\underline{x})$ and the number of particles in the element to the (mass) density field $\rho(\underline{x})$.

In this chapter, we introduce the basic concepts of the rheology of continua followed by a discussion of experimental techniques for measuring the constitutive properties of a suspension.

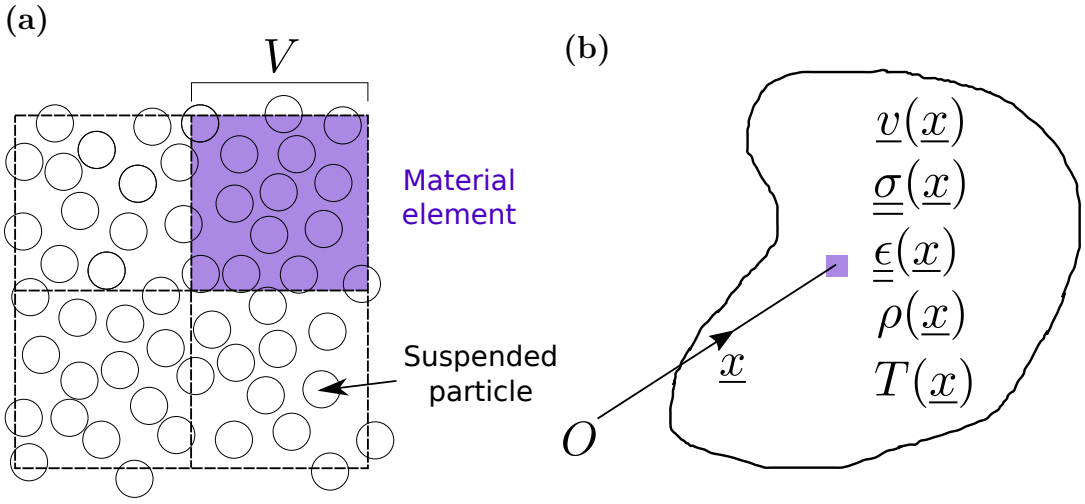

Figure 2.1: Continuum hypothesis for suspensions. (a) Schematic of a suspension of spheres. The shaded purple region represents a continuum material element with volume V that typically contains many particles. (b) Schematic of a general continuum showing an elemental volume (shaded purple region) at position vector $\underline{x}$. The positions, velocities and forces acting upon the particles and fluid are averaged over V [19] to give the strain tensor $\underline{\underline{\epsilon}}$, velocity $\underline{v}$ and stress tensor $\underline{\underline{\sigma}}$ fields, respectively.

2.1 The rheology of continua

2.1.1 The stress tensor

We begin by considering the stress in a continuous medium. The force per unit volume on a material element $\underline{f}^*$ can be written as the sum of two contributions,

$$f_i^* = f_i + \frac{\partial \sigma_{ij}}{\partial x_j}, \tag{2.1}$$

where the repeated index implies summation. Here, the indices refer to the three orthogonal directions $1-$, $2-$ and $3-$, in a Cartesian coordinate system, Fig. 2.2. The first term in Eq. 2.1 represents *body forces* f_i, those which act per unit volume on all elements in a continuum [20]. For example, for a homogeneous continuum in a uniform gravitational field with acceleration $\underline{g}$, $\underline{f} = \rho \underline{g}$. The second term represents the *surface traction* on the i^{th} surface of a material element, where the stress tensor, σ_{ij}, is the force per unit area in the j^{th} direction exerted *on* the plane with normal vector in the i^{th} direction. The stress tensor, depicted schematically in Fig. 2.2, can be written in matrix form as

$$\underline{\underline{\sigma}} = \begin{pmatrix} \sigma_{11} & \sigma_{12} & \sigma_{13} \\ \sigma_{21} & \sigma_{22} & \sigma_{23} \\ \sigma_{31} & \sigma_{32} & \sigma_{33} \end{pmatrix}. \tag{2.2}$$

The diagonal components σ_{11}, σ_{22} and σ_{33} represent normal stresses, while the off-diagonal components, e.g., σ_{12}, represent shear stresses. It is convention to decompose σ_{ij} into an isotropic and a deviatoric part,

$$\sigma_{ij} = -p\delta_{ij} + \tau_{ij}. \tag{2.3}$$

where δ_{ij} is the Kronecker delta,

$$p = -\frac{1}{3}\sigma_{ii} = -\frac{1}{3}\left(\sigma_{11} + \sigma_{22} + \sigma_{33}\right) \tag{2.4}$$

is the *mechanical pressure* and τ_{ij} is the *deviatoric stress tensor*, which is traceless

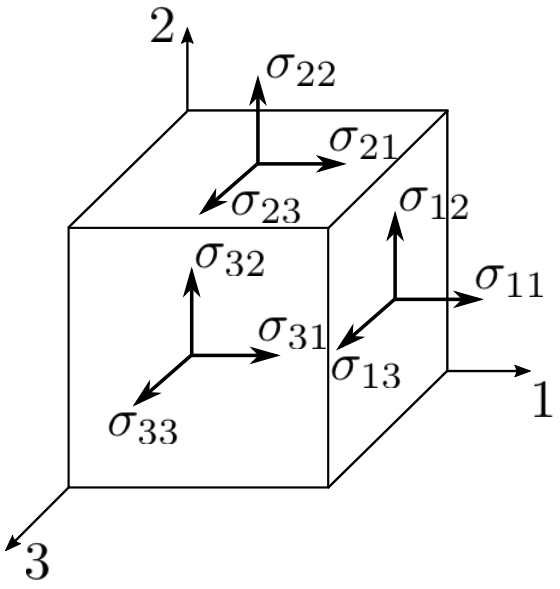

Figure 2.2: Schematic showing the components of the stress tensor σ_{ij} for a material element.

($\tau_{ii} = 0$).

In mechanical equilibrium, the force on each material element vanishes, $\underline{f}^* = 0$, yielding, from Eq. (2.1):

$$f_i + \frac{\partial \sigma_{ij}}{\partial x_j} = 0 \qquad \text{or} \qquad \underline{f} + \underline{\nabla} \cdot \underline{\underline{\sigma}} = 0, \tag{2.5}$$

which is known as Cauchy's equation [21]. For a Newtonian fluid, this implies steady flow; for an elastic solid, it implies that the deformation of the body is not changing in time.

Symmetry of the stress tensor

For the majority of soft matter systems, including suspensions, it is assumed that σ_{ij} is symmetric, i.e., $\sigma_{ij} = \sigma_{ji}$, so that there are only six independent stress components: σ_{11}, σ_{22}, σ_{33}, $\sigma_{12} = \sigma_{21}$, $\sigma_{13} = \sigma_{31}$ and $\sigma_{23} = \sigma_{32}$. This assumption is equivalent to requiring that the net torque on each material element is zero, even when the body is not in mechanical equilibrium. See the book by Aris [22] (chapter 5, therein) for a derivation of this result.

As discussed in [23], σ_{ij} is not *a priori* symmetric for suspensions – this is understandable, as two particles in contact with static friction exert a torque

on one another. It has been shown [23], however, that σ_{ij} is symmetric if the averaging volume V (the volume of the material element) is made sufficiently large.

Stress at boundaries

In most practical situations in complex fluids, the continuum will be in contact with other continua. For example, in suspension rheology, the suspension is in contact with the plates of the rheometer. Then, mechanical equilibrium, Eq. (2.5), places constraints on the stress tensor at the boundary between two media. Specifically, the component of the stress tensors normal to an interface with normal vector $\underline{n}$ separating two continua, I and II, must be equal [21]:

$$\sigma_{ij}^{\mathrm{I}} n_j = \sigma_{ij}^{\mathrm{II}} n_j \qquad \text{or} \qquad \underline{\underline{\sigma}}^{\mathrm{I}} \cdot \underline{n} = \underline{\underline{\sigma}}^{\mathrm{II}} \cdot \underline{n}. \tag{2.6}$$

If the continua are made from different materials, e.g., for an air-fluid interface, then the hydrodynamic stress jump normal to the interface must balance the stress due to interfacial tension Σ_s [24]:

$$(\sigma_{ij}^{I} - \sigma_{ij}^{II}) n_j = \Sigma_s \kappa n_i \qquad \text{or} \qquad (\underline{\underline{\sigma}}^{I} - \underline{\underline{\sigma}}^{II}) \cdot \underline{n} = \Sigma_s \kappa \underline{n}. \tag{2.7}$$

The constant $\kappa = \underline{\nabla} \cdot \underline{n} \sim 1/R$ where R is the radius of curvature of the interface; so, the magnitude of the stress jump is $\sim \Sigma_s / R$.

2.1.2 The strain and strain-rate tensors

The state of deformation at a point is characterised by the strain tensor ϵ_{ij}, defined as [23]:

$$\epsilon_{ij} = \frac{1}{2} \left(\frac{\partial X_i}{\partial x_j} + \frac{\partial X_j}{\partial x_i} \right), \tag{2.8}$$

where $\underline{X}(\underline{x}, t)$ is the displacement of the material element at position $\underline{x}$ relative to a reference state. The strain tensor measures deformation of the material element and therefore vanishes for translation and rotation, Fig. 2.3(a). The i^{th}

diagonal element corresponds to the fractional change in length of the material element in the i^{th} direction, $\delta L_i/L$, Fig. 2.3(b). The trace of ϵ_{ij}, ϵ_{kk}, relates to the fractional change in volume, $\delta V/V$. The off-diagonal elements correspond to *shear* deformations and are equal to half the angle of distortion, Fig. 2.3(c).

Analogously, one can define the *strain rate tensor* e_{ij} as

$$e_{ij} = \frac{1}{2}\left(\frac{\partial v_i}{\partial x_j} + \frac{\partial v_j}{\partial x_i}\right), \tag{2.9}$$

where $\underline{v}(\underline{x}, t)$ is the local velocity field. For simple shear flow in the 1-2 plane,

$$\underline{\underline{e}} = \begin{pmatrix} 0 & \dot{\gamma}/2 & 0 \\ \dot{\gamma}/2 & 0 & 0 \\ 0 & 0 & 0 \end{pmatrix}, \tag{2.10}$$

where $\dot{\gamma}$ is the *shear rate*. Note that both ϵ_{ij} and e_{ij} are symmetric by construction.

In this thesis we will consider only *incompressible* materials, that is, ones for which the volume of a material element [and hence the local density $\rho(\underline{x})$] is unchanged by the deformation. Physically, this is because the bulk moduli of most liquids are $\sim 10^9$ Pa, orders of magnitude greater than the shear stresses typically encountered in soft matter, $\sigma_{12} \sim 1 - 10^4$ Pa. In practice, therefore, both $\underline{\underline{\epsilon}}$ and $\underline{\underline{e}}$ are traceless; for fluids, this corresponds to the condition that the divergence of the velocity field vanishes,

$$\underline{\nabla} \cdot \underline{v} = 0. \tag{2.11}$$

The mechanical pressure in such materials takes on any value necessary to satisfy Eq. (2.11) and prevent changes in density.

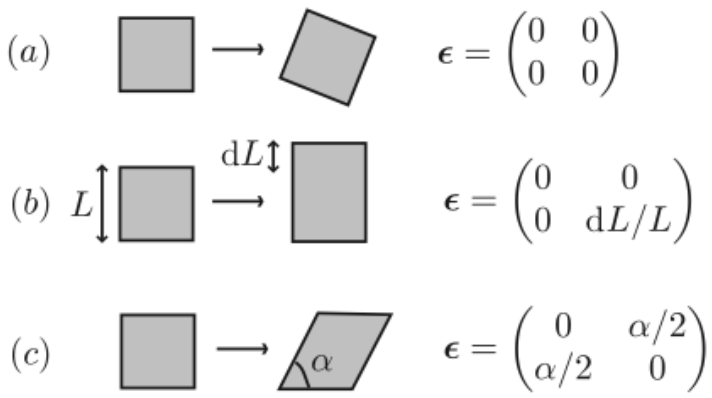

Figure 2.3: Examples of the strain tensor $\underline{\underline{\epsilon}}$ in 2-d for (a) rotation, (b) uni-axial extension and (c) simple shear. Taken from [23].

2.1.3 Constitutive relations

The stress and strain-rate tensors in a fluid flowing *at steady state* are related by a function,

$$\underline{\underline{\sigma}} = \underline{\underline{\mathcal{F}}}(\underline{\underline{e}}), \tag{2.12}$$

known as a *constitutive equation* [1]. For an elastic solid, the constitutive equation is written in terms of the strain tensor $\underline{\underline{\epsilon}}$. The simplest constitutive relation is for a Newtonian fluid,

$$\sigma_{ij} = -p\delta_{ij} + 2\eta e_{ij}, \tag{2.13}$$

in which $\underline{\underline{\sigma}}$ and $\underline{\underline{e}}$ are linearly related. The coefficient η is the shear viscosity of the fluid [2]. In this thesis, we will mainly consider the case of simple shear flow with a velocity gradient in the 1-2 plane, Eq. (2.10). Then, Eq. (2.13) reduces

[1] In a full treatment of continuum mechanics, the mechanical variables σ_{ij} and e_{ij} are coupled to thermodynamic variables such as temperature $T(\underline{x})$. In all that follows, we assume *isothermal* conditions, i.e., uniform temperature, so that the mechanical properties can be treated separately [20].

[2] In general, the constitutive equation for a Newtonian fluid has the form $\sigma_{ij} = \eta_{ijkl}e_{kl}$, where η_{ijkl} is a fourth-rank tensor of viscosity coefficients. For a homogeneous, isotropic fluid there are only two independent components of η_{ijkl}: the bulk viscosity κ, which governs the resistance to volumetric changes, and the shear viscosity η. For incompressible fluids, $e_{kk} = 0$ and κ is irrelevant (its contribution to the stress is $\kappa\delta_{ij}e_{kk}$). In this limit, we recover Eq. (2.13).

to the well-known relation between shear stress σ_{12} and shear rate $\dot{\gamma}$,

$$\sigma_{12} = \eta\dot{\gamma}. \tag{2.14}$$

Examples of Newtonian fluids are water and honey, for which $\eta = 1$ mPa.s and 10 Pa.s at room temperature, respectively.

Non-Newtonian fluids

In a Newtonian fluid, the normal stresses are equal, $\sigma_{11} = \sigma_{22} = \sigma_{33} = -(1/3)p$, so the diagonal elements of the deviatoric stress $\tau_{ij} = 2\eta e_{ij}$ are zero. This is not the case in most complex fluids, however, and the stress tensor can no longer be written in the form of Eq. (2.13) [25]; such a fluid is known as *non Newtonian*. For general non-Newtonian fluids, the stress tensor for simple shear has the form [16] (Ch. 3, pg. 64):

$$\sigma_{ij} = \begin{pmatrix} \sigma_{11} & \sigma_{12} & 0 \\ \sigma_{21} & \sigma_{22} & 0 \\ 0 & 0 & \sigma_{33}, \end{pmatrix},$$

so that shear stresses not in the flow-gradient plane are equal to zero, $\sigma_{13} = \sigma_{31} = \sigma_{23} = \sigma_{32} = 0$. If the material is incompressible, then σ_{ij} is only defined up to an additive (isotropic) pressure and it follows that there are only three independent stresses of rheological significance: the shear stress σ_{12} and the first N_1 and second N_2 normal stress differences,

$$N_1 = \sigma_{11} - \sigma_{22} \qquad \text{and} \qquad N_2 = \sigma_{22} - \sigma_{33}. \tag{2.15}$$

It is usually assumed that these stresses depend only on the local value of the shear rate $\dot{\gamma}$: $\sigma_{12} = \sigma_{12}(\dot{\gamma})$, $N_1 = N_1(\dot{\gamma})$ and $N_2 = N_2(\dot{\gamma})$ [16].

Although suspension flow is typically non-Newtonian at high concentrations, special cases exist (and are in fact common in wet granular flow) in which all the components of σ_{ij} scale linearly with $\dot{\gamma}$. In that case, the rheology is said to

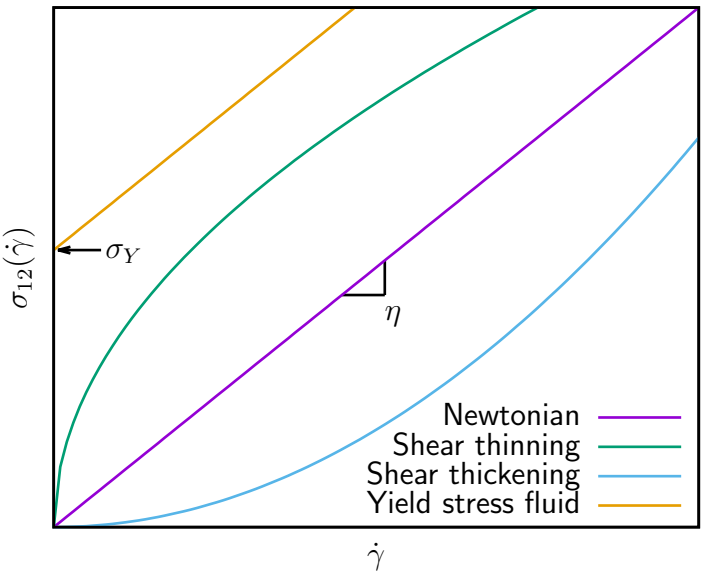

Figure 2.4: Schematics of flow curves $\sigma_{12}(\dot{\gamma})$ for different types of fluid, as labelled.

be *quasi-Newtonian* and the stress can be written as

$$\sigma_{ij} = H_{ij}\dot{\gamma} = \begin{pmatrix} H_{11} & \eta & 0 \\ \eta & H_{22} & 0 \\ 0 & 0 & H_{33} \end{pmatrix} \dot{\gamma}, \tag{2.16}$$

where $\underline{\underline{H}}$ is a constant tensor. Such fluids have a $\dot{\gamma}$-independent shear viscosity $\eta = \sigma_{12}/\dot{\gamma}$ and $\dot{\gamma}$-independent but non-zero N_1 and/or N_2 [3].

Types of non-Newtonian fluid

In the general case, $N_1(\dot{\gamma})$, $N_2(\dot{\gamma})$ and $\eta(\dot{\gamma})$ all depend differently on $\dot{\gamma}$. In practical rheometry, measuring $N_1(\dot{\gamma})$ and $N_2(\dot{\gamma})$ reliably is difficult and it is more common to categorise rheological behaviour according to the shear viscosity $\eta(\dot{\gamma})$. Fig. 2.4 plots σ_{12} versus $\dot{\gamma}$ for four common types of fluid; the gradient of the line in each case corresponds to the shear viscosity. If η decreases with $\dot{\gamma}$ (σ_{12} increases sublinearly with $\dot{\gamma}$) then the fluid is said to be *shear thinning*. If η increases with $\dot{\gamma}$ (σ_{12} increases superlinearly with $\dot{\gamma}$) then the fluid is *shear thickening*. In *yield stress fluids*, a critical stress σ_Y, known as the *yield stress*, must be exceeded before the fluid flows.

[3] Some authors [25] use the term "quasi-Newtonian" to refer to the case where $N_1 = N_2 = 0$, but the shear viscosity η depends on $\dot{\gamma}$. We do not use their convention.

2.1.4 Transient and steady-state rheology

For time-dependent flows, the stress tensor at time t, $\underline{\underline{\sigma}}(t)$, is a functional of the strain rate tensor at all previous times t' [26]:

$$\underline{\underline{\sigma}}(t) = \underline{\underline{\mathcal{F}}}[\underline{\underline{e}}(t' \leq t)] \tag{2.17}$$

– the mechanical response of the system is determined by its entire deformation history. In most complex fluids, applying a fixed $\dot{\gamma}$ (or σ) for a long time results in the system "forgetting" its deformation history, so σ (or $\dot{\gamma}$) does not evolve in time. Such a system is said to be in *steady state* – this was the tacit assumption made in the last section.

A striking example of flow history dependence in suspension flow is demonstrated in experiments by Gadala-Maria and Acrivos [27] on non-Brownian hard spheres in simple shear, Fig. 2.5. They initially shear the system at a rate $\dot{\gamma}_a$ in the positive direction until σ_{12} reaches steady state, then impose $\dot{\gamma} = 0$ for a fixed rest period. In the first experiment, they subsequently continue shearing at $\dot{\gamma}_a$ in the positive direction, point A in Fig. 2.5. The stress σ_{12} immediately resumes the value it had before cessation, σ_∞. In the second experiment, they apply the same shear rate but in the opposing direction, $-\dot{\gamma}_a$, point B. In that case σ_{12} reverses sign immediately after reversal, but is smaller in magnitude than the steady state value; $\sigma_{12}(t)$ then undergoes a transient and reaches σ_∞ after a strain of $\mathcal{O}(1)$. Thus, the rheological behaviour depends on the previous direction of shear. In Ch. 8, we use a similar shear protocol to separate contributions to the stress from hydrodynamics and particle contacts.

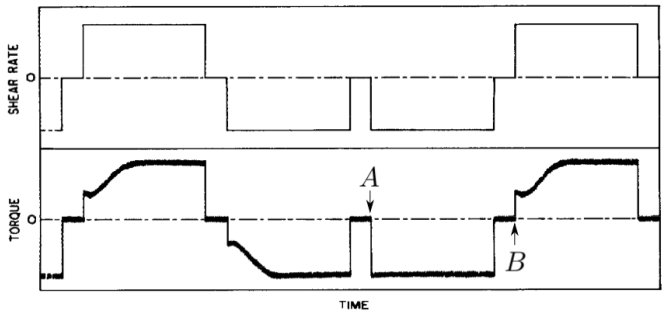

Figure 2.5: Flow reversal rheology from Gadala-Maria and Acrivos [27] illustrating the influence of shear history on the shear stress. The system is subjected to simple shear at shear rate $\dot{\gamma}_a$ before a pause at $\dot{\gamma} = 0$, followed by either (A) shear in the same direction at $\dot{\gamma}_a$, or (B) shear in the opposite direction at $-\dot{\gamma}$.

2.2 Experimental rheometry of continua

The primary goal of experimental rheometry is to measure the functions $\sigma_{12}(\dot{\gamma})$, $N_1(\dot{\gamma})$ and $N_2(\dot{\gamma})$. In this section, we describe the principles of cone-plate and parallel-plate rheometery, the two techniques used in this thesis following the treatment of Lodge [16] (chapters 9 and 12, therein) and Macosko [28] (chapter 5, therein).

2.2.1 Cone-plate rheometry

In cone-plate rheometry, Fig. 2.6, the sample is confined by surface tension between a cone of radius R and angle β and a base plate, also with radius R. Typically, $R \sim 20$ mm and $\beta \sim 1°$. In the standard geometry, the tip of the cone is in contact with the centre of the base plate; however, it is more common to truncate the bottom of the cone, so that there is an ~ 100 μm clearance near the centre. The device is connected to a rheometer which rotates the cone (or plate) with angular speed Ω_0 and measures a torque Γ and the total normal force exerted on the cone (or plate) F_N.

We work in spherical polar coordinates, taking the origin as the tip of the cone (we ignore the truncation for now) and $\underline{\hat{r}}$, $\underline{\hat{\theta}}$ and $\underline{\hat{\phi}}$ as unit vectors in the radial, polar and azimuthal directions, respectively. Flow in the cone-plate geometry is *rheometric*, i.e., the primary velocity field is in one direction only, $\underline{v} = v\underline{\hat{\phi}}$. For small β, the local flow field at position r can be approximated by simple shear between two flat plates, so that the local shear rate is

$$\dot{\gamma}(r) \approx \frac{r\Omega_0}{r\beta} = \frac{\Omega_0}{\beta}, \tag{2.18}$$

independent of r. We identify $\underline{\hat{\phi}}$ as the flow (1) direction, $\underline{\hat{\theta}}$ as the gradient (2) direction and $\underline{\hat{r}}$ as the vorticity (3) direction.

Shear stress

We now seek relationships between the rheometric functions $\sigma_{12}(\dot{\gamma})$, $N_1(\dot{\gamma})$ and $N_2(\dot{\gamma})$ and the measured quantities Γ and F_N. We begin by assuming that

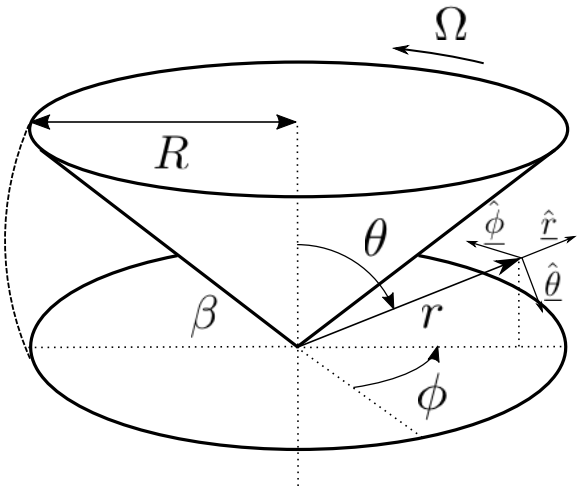

Figure 2.6: Schematic of a cone-plate geometry.

body forces, such as gravity, are absent, and that the flow is inertialess, i.e., the Reynolds number corresponding to the gap height at the edge of the cone is small. In that case, mechanical equilibrium requires, from Eq. (2.5),

$$\underline{\nabla} \cdot \underline{\underline{\sigma}} = 0. \tag{2.19}$$

The $\underline{\hat{\phi}}$ component of this equation in spherical polar coordinates reads [16],

$$\frac{\partial \sigma_{r\phi}}{\partial r} + \frac{1}{r}\frac{\partial \sigma_{\phi\theta}}{\partial \theta} + \frac{1}{r\sin\theta}\frac{\partial \sigma_{\phi\phi}}{\partial \phi} + \frac{1}{r}[3\sigma_{r\phi} + 2\sigma_{\theta\phi}\cot\theta] = 0.$$

The terms involving derivates with respect to ϕ vanish, as the problem is axially symmetric. Also, since locally the material is subjected to simple shear, all shear stresses other than $\sigma_{12} = \sigma_{\phi\theta}$ are zero, and hence

$$\frac{1}{r}\frac{\partial \sigma_{12}}{\partial \theta} + \frac{2}{r}\sigma_{12}\cot\theta = 0,$$

which is solved by the function

$$\sigma_{12}(\theta) = \frac{C}{\sin^2\theta}.$$

The constant C is independent of ϕ due to azimuthal symmetry, and of r because σ_{12} is a function of $\dot{\gamma}$ only and $\dot{\gamma}$ is independent of r. The total torque exerted by the material on the plate at $\theta = \pi/2$ is given by the equation [16]

$$\Gamma = \int_0^R 2\pi r \cdot r \cdot \sigma_{12}(\theta = \pi/2)dr = \frac{2\pi R^3}{3}\sigma_{12}(\pi/2).$$

Using $\sigma_{12}(\pi/2) = C/\sin^2(\pi/2) = C$, we infer $C = 3\Gamma/(2\pi R)$ and hence

$$\sigma_{12}(\theta) = \frac{3\Gamma}{2\pi R^3 \sin^2(\theta)} \approx \frac{3\Gamma}{2\pi R^3}. \tag{2.20}$$

Typically, the cone angle $\beta \lesssim 4^\circ$ so that the stress varies between the cone and plate by $< 0.1\%$. Thus, $\sin^2(\theta) \approx 1$ and the torque on the cone is the same as the torque on the plate in practice.

First normal stress difference

One can also derive a relationship between F_N and N_1 by considering the $\hat{\underline{r}}$-component of Eq. (2.19),

$$\frac{\partial \sigma_{rr}}{\partial r} + \frac{1}{r}\frac{\partial \sigma_{r\theta}}{\partial \theta} + \frac{1}{r\sin\theta}\frac{\partial \sigma_{r\phi}}{\partial \phi} + \frac{1}{r}(2\sigma_{rr} - \sigma_{\theta\theta} - \sigma_{\phi\phi} + \sigma_{r\phi}\cot\theta) = 0. \tag{2.21}$$

Neglecting shear stresses other than $\sigma_{\theta\phi}$ and terms involving $\partial/\partial\phi$ leads to the following equation,

$$\frac{\partial \sigma_{33}}{\partial r} + \frac{1}{r}(2\sigma_{33} - \sigma_{22} - \sigma_{11}) = \frac{\partial \sigma_{33}}{\partial r} - \frac{2N_2 + N_1}{r} = 0. \tag{2.22}$$

where we have used the definitions of the first and second normal stress differences in Eq. (2.15). Recalling that N_1 and N_2 are functions of $\dot{\gamma}$ only and hence independent of r, and neglecting variations of σ_{ij} in the $\hat{\underline{\theta}}$ direction, we can integrate the above equation to yield

$$\sigma_{rr}(r) = \sigma_{rr}(R) + (2N_2 + N_1)\ln\left(\frac{r}{R}\right). \tag{2.23}$$

Thus, if the fluid is non-Newtonian ($N_1 \neq 0$ and/or $N_2 \neq 0$) then the radial normal stress varies logarithmically with r; whether $\sigma_{rr}(r)$ increases or decreases with r depends on the sign of the pre-factor $(2N_2+N_1)$. To maintain normal stress differences that are independent of r requires that this variation is supported by the isotropic part of the stress $-p(R)$, so that $\tau_{rr}(r)$ is constant. Then,

$$-p(r) = -p(R) + (2N_2 + N_1)\ln\left(\frac{r}{R}\right). \tag{2.24}$$

The integration constant $-p(R)$ is set by the value of the radial component of

the stress at the free surface. To make progress, it is assumed that the meniscus is axially symmetric and forms part of a sphere with radius R centred at the apex of the cone, Fig. 2.6; in that case, the stress due to surface tension, $2\Sigma_s/R$, acts radially inwards along the $-\underline{\hat{r}}$ direction. Usually, the interface is in contact with air, which imparts a pressure p_{atm} on the free surface. The meniscus is in mechanical equilibrium, so that the difference between atmospheric pressure and $\sigma_{rr}(R) = -p(R) + \tau_{rr}(R)$ is balanced by surface tension. Applying Eq. (2.7) to the interface yields the relation

$$\sigma_{rr}(R) + \frac{2\Sigma_s}{R} = -p(R) + \tau_{rr} + \frac{2\Sigma_s}{R} = -p_{\text{atm}}. \tag{2.25}$$

The total normal force exerted on the plate by the fluid, F_N, has two contributions (chapter 1 in [29]):

$$F_N = \int_0^R 2\pi r[-p(r) + \tau_{\theta\theta}]dr - 2\pi\Sigma_s R. \tag{2.26}$$

The first term on the right hand side is the integral of the normal force at the fluid-plate boundary. The second term is the surface tension force due to the meniscus, which acts tangentially along the free surface away from the plate, leading to the minus sign. Recalling that $\underline{\underline{\tau}}$ is independent of r and using Eq. (2.24) and (2.25), integrating the above equation leads to a relation between the force exerted on the plate due to the fluid F_N and the first normal stress difference

$$F_N = \pi R^2 p_{\text{atm}} - \frac{\pi R^2}{2} N_1.$$

Note that the surface tension terms have vanished: the spherical free surface ensures that the Laplace pressure acting normally to the interface is cancelled by the contribution to the force per unit area on the plate due to the tangential surface tension force. In most rheometers, the other side of the plate is also open to the atmosphere, so that the total (excess) force experienced experienced by the plate is [29]

$$\Delta F = -\frac{\pi R^2}{2} N_1. \tag{2.27}$$

Thus, measuring F_N in a cone-plate instrument provides access to N_1. We note

that, in our sign convention, $\Delta F > 0$ corresponds to a tensile force on the plate. In most force transducers, $\Delta F > 0$ corresponds to a compressive load and $N_1 > 0$ implies that the plates are pushed apart.

The validity of Eq. (2.27) relies on the free surface forming part of a sphere with radius R. This is usually not achievable in practice, however, as the shape of the meniscus is both distorted by the effects of gravity and governed by the contact angle with the cone and plate. For example, if we consider an aqueous dispersion loaded in a geometry with $R = 25$ mm and $\beta = 1°$, the gravitational stress at the bottom of the meniscus $\rho g R \tan(\beta) \sim 10^3 \cdot 10 \cdot 25 \times 10^{-3} \tan(1°) \approx 4$ Pa is comparable to the Laplace stress of a spherical interface $2\Sigma_s/R = 2 \cdot 0.07/(25 \times 10^{-3}) \approx 6$ Pa. If the radius of curvature of the interface is set by the gap height at the edge of the cone, $R \tan \beta$, then there is an additional apparent normal stress of $\sim 2\Sigma_s/(R \tan \beta) \sim 300$ Pa. Even if the desired meniscus shape was achievable when the system was static, under low non-zero normal stress differences can lead to instabilities at the free surface, ultimately resulting in fracture (see [30] and [31]). Of greater relevance to this thesis is that the form of the meniscus is known to be less important for the shear stress [16]. Indeed, the rheology we measured is insensitive to whether we use an equal-sized cone and plate or a plate that is much larger than the cone; in the latter case, the free surface is only pinned at the cone and cannot be made to form part of a sphere with radius R. We report data with unequal-sized geometries, as it is easier to load samples.

2.2.2 Parallel-plate rheometry

In parallel-plate rheometry, Fig. 2.7, the sample is placed between two parallel discs with radius R and separation H. We direct the interested reader to chapter 5 in [28] for a full derivation of the relationship between Ω and Γ and present only the salient results here.

In contrast to cone-and-plate flow, the flow field between parallel plates is not homogeneous and the shear rate increases linearly from zero at the centre of the plates, $r = 0$, to a maximum value, $\dot{\gamma}_R$, at the rim:

$$\dot{\gamma}(r) = \frac{\Omega r}{H} = \dot{\gamma}_R \frac{r}{R}. \tag{2.28}$$

Thus, one expects radial gradient in the shear stress σ_{12}, even for a Newtonian

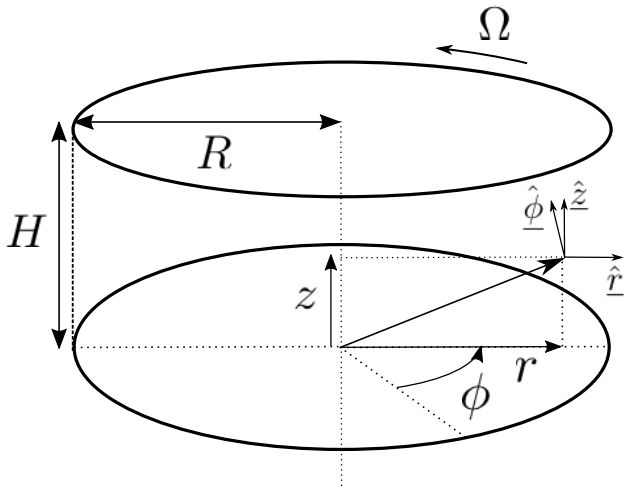

Figure 2.7: Schematic of the parallel-plate geometry.

system. The existence of this gradient in $\dot{\gamma}$ means that there is no simple, exact relationship between a single applied Ω and the measured Γ. Instead, it is possible to derive a relationship between the shear stress at the rim of the plates, $\sigma_{12}(R)$, and the derivative of Γ with respect to $\dot{\gamma}_R$,

$$\sigma_{12}(R) = \frac{\Gamma}{2\pi R^3}\left[3 + \frac{\mathrm{d}\ln\Gamma}{\mathrm{d}\ln\dot{\gamma}_R}\right]. \tag{2.29}$$

In practice, $\Gamma(\dot{\gamma}_R)$ is measured with a Ω sweep and the derivative evaluated numerically. In this thesis, we report the apparent shear stress that would be measured if the liquid was Newtonian,

$$\sigma_{12}^{\mathrm{eff}} = \frac{2\Gamma}{\pi R^3}; \tag{2.30}$$

Eq. (2.30) is a measure of the average stress measured by the plates.

It is also possible to measure $N_1 - N_2$ with parallel plates, which, when combined with cone-plate measurements, allows N_2 to be calculated. Details of how this is done can be found in chapter 5 of [28]. The assumptions used to derive equations (2.28-2.30) are similar to the cone and plate; although, for parallel plates, the free surface is assumed to form a cylinder with radius R and height H.

Chapter 3

Colloids and grains

Our current understanding of suspension rheophysics is confined to two disparate regimes that are well separated in particle size: colloids, with diameter $d \lesssim 1$ μm; and grains, with $d \gtrsim 50$ μm. Since this thesis is primarily concerned with the shear-thickening phenomenology of suspension rheology and not with colloid science *per se*, we introduce only the necessary physics to understand our discussion of the results presented in later chapters. The interested reader is directed to the textbook by Russel, Saville and Schowalter [32] for a general introduction and chapters 10-18 in Israelachvili [33] for a comprehensive treatment of colloid surface science. See the textbook by Jones ([34], chapter 4 therein) for a more elementary treatment. The physics of granular media *in situ* and under flow is discussed in depth in the excellent textbook by Andreotti, Forterre and Pouliquen [23]. For an account of the theoretical approach to colloidal-suspension mechanics, we recommend the text by Guazzelli and Morris [25]; for an accompanying survey of experimental results, see the book by Wagner and Mewis [35].

In the first part of the chapter, we discuss different mechanisms of stabilising colloidal particles, which, as we show in later chapters, is relevant to the onset of shear thickening. We then briefly review experimental rheology results for repulsive colloidal spheres. In the second part, we introduce wet granular suspensions and highlight the salient differences with colloidal particles.

3.1 Colloids

Historically, an assembly of particles with diameter $d \lesssim 1\ \mu$m suspended in a fluid is referred to as a *colloidal dispersion*. The defining characteristic of a colloidal particle is that it is much larger than the molecules of the suspending fluid, so it can be considered as being immersed in a continuum. This constraint sets a lower bound on the size of a colloid at $d > \mathcal{O}(10\text{ nm})$ [36]. The molecular properties of the fluid enter only through continuum variables like temperature T, density ρ_f, relative permittivity ϵ_r and viscosity η_f.

3.1.1 van der Waals attraction

The word colloid is derived from the Greek $\kappa o\lambda\lambda\alpha$, which translates as "glue", reflecting the tendency for colloidal particles to irreversibly aggregate. Aggregation typically results from van der Waals attraction, a purely quantum-mechanical interaction that arises from the interaction between fluctuating atomic dipoles in the particles [34]. The van der Waals potential between two spheres of radius R is given, in the limit of small separations $r \ll R$, by [34]

$$U_{\text{vdW}}(r) = -\frac{AR}{12\pi(r-2R),} \tag{3.1}$$

where A is the Hamaker constant, which has units of energy and depends on the dielectric properties of the particles and fluid. The Hamaker constant can be calculated using Lifshitz theory [33]; e.g., for silica colloids in water $A \approx k_B T$. We sketch the form of $U_{\text{vdW}}(r)$ in Fig. 3.1 (green line).

To prevent irreversible flocculation of the particles, it is necessary to introduce a repulsive stabilising force, which is typically achieved in one of two ways: charge repulsion, or steric stabilisation due to a polymer layer bound to the particle surface, Fig. 3.2.

3.1.2 Charge stabilisation

Many colloidal particles (e.g., silica and titania) become charged when immersed in a fluid, Fig. 3.2(a). The mechanism of charging depends on the specific surface

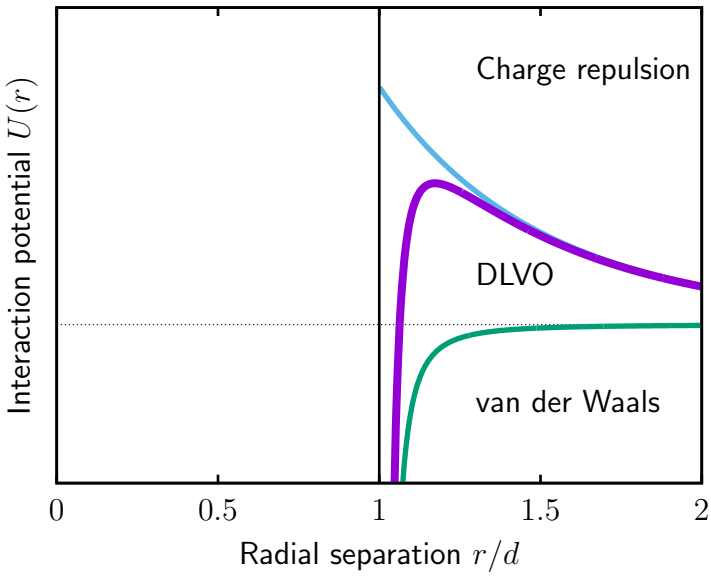

Figure 3.1: Sketch of the total pair interaction potential $U(r)$ (bold, purple line) for a charge-stabilised colloid decomposed into contributions from van der Waals attractions (green), Eq. (3.1), and repulsion due to the electric double-layer (blue line), Eq. (3.2).

chemistry of the particles (see chapter 14 in Israelachvili [33]), but occurs most commonly via dissociation of surface groups (e.g., Si–OH $\rightarrow$ Si–O^- + H^+ for silica in water), or the adsorption of ions in the fluid to a previously uncharged surface (e.g., the charging of PHSA-stabilised PMMA in cyclohexyl bromide has been attributed to the association of H^+ ions with the polymer brush [38]). Some of the counterions are bound to the surface in the so-called *Stern* layer, while further away from the surface they form a more diffuse layer. The two regions are collectively known as the *electric double layer*.

When two charged particles are brought close together, they experience a repulsive force whose origin is in the osmotic pressure exerted by the ions in the gap (and *not* directly due to Coulomb repulsion between the two charged surfaces). The potential energy of interaction $U_\mathrm{r}(r)$ is given by

$$U_\mathrm{r}(r) = Z(\varphi_0) R \exp[-\kappa(r - 2R)] \tag{3.2}$$

where $Z(\varphi_0) = 64\pi\epsilon_r\epsilon_0 \left(\frac{k_B T}{e}\right)^2 \tanh^2\left(\frac{ze\varphi_0}{4k_B T}\right)$ is a constant that depends on the

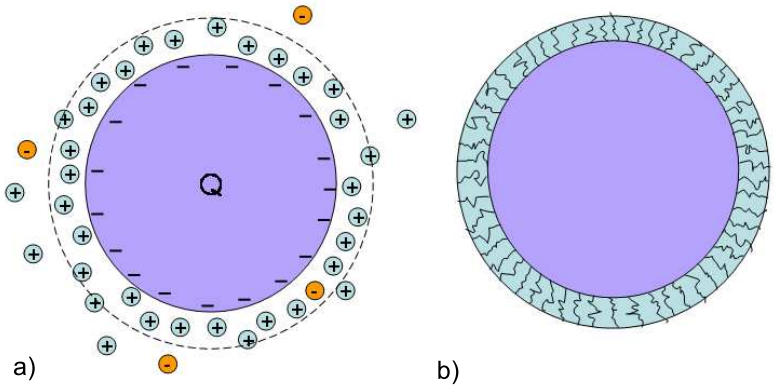

Figure 3.2: Schematic of a colloidal sphere with (a) charge stabilisation and (b) steric stabilisation. Taken from [37].

surface potential φ_0 of the particles and κ is defined as

$$\kappa = \left(\frac{2n_0 e^2}{\epsilon_0 \epsilon_r k_B T} \right)^{\frac{1}{2}}, \tag{3.3}$$

where n_0 is the concentration of ions in the fluid far away from the surface and ϵ_0 is the permittivity of free space. The constant κ^{-1} is known as the Debye length and is the length scale over which electrostatic interactions are screened in the fluid. The force between the particles is obtained by taking the derivative of Eq. (3.2) with respect to r:

$$F_{\text{rep}}(h) = Z(\varphi_0)(\kappa R) \exp(-\kappa h). \tag{3.4}$$

We sketch the form of the potential energy due to the charge stabilisation in Fig. 3.1 (blue line). It has a finite value at contact $U_r(2R) = ZR$ that depends on the surface potential (which in turn depends on the surface charge) and decays exponentially with r.

The total potential energy $U = U_{\text{vdW}} + U_{\text{r}}$, given by the sum of the charge, Eq. (3.2), and van der Waals, Eq. (3.1), contributions is denoted by the bold, purple

line [1].

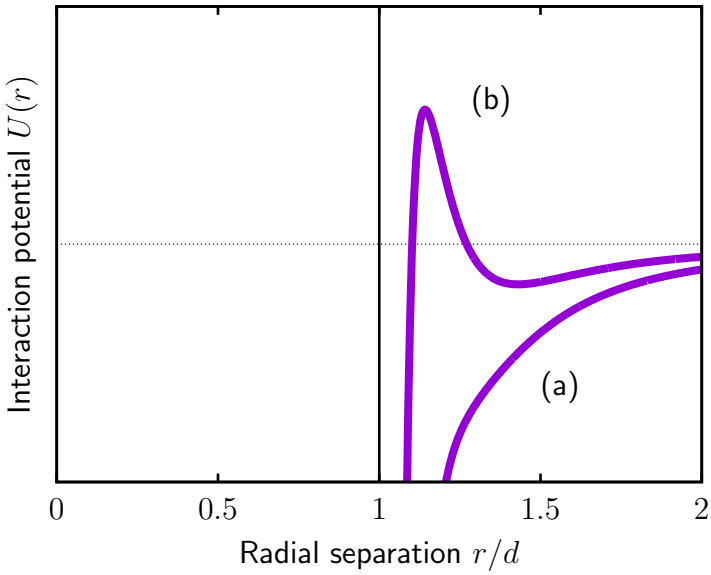

Figure 3.3: Same as Fig. 3.1, but for values of A, φ_0 and κ such that $U(r)$ is, (a) purely attractive, and (b) has a secondary minimum at $r \neq 0$.

For this particular choice of A, Z and κ, $U(r)$ is strongly attractive at small r, has a maximum at $r_{\max}$ and is repulsive for $r > r_{\max}$. Particles will be stable unless the normal compressive force exerted on a pair of particles is such that the barrier height is exceeded – if this happens, then they fall into the infinite minimum in their mutual interaction potential at $r = 0$. Of course, the depth of the minimum is only infinite for strictly smooth spheres and is cut off at some finite value set by the surface roughness of the particles in practice. Different combinations of the above parameters, Fig. 3.3, can lead to (a) pure attraction, or (b) a secondary minimum.

3.1.3 Steric stabilisation

The second form of stabilisation we consider is that due to a polymer brush, which is either physically bonded or adsorbed to the surface of the particles. (See the book by Rubinstein and Colby [40] for an introductory account of the topic.) In a good solvent, the grafted polymer molecules extend out into the fluid. When two brushes are compressed or interdigitated, there is a reduction in the configurational degrees of freedom of the polymers, resulting in an entropic penalty and a repulsive force $F_{\text{poly}}(r)$.

[1] The assumption that U_{vdW} and U_{r} are additive forms the basis of DLVO theory; see [32, 39].

Various models exist that predict $F_{\text{poly}}(r)$ based on the radial density profile of the brush and the grafting density on the surface, which we do not consider here [33, 41]. Instead, we can estimate the typical force required to interdigitate the two brushes as $F^* \approx k_B T/b$, where b is the size of a correlation blob in the chain, or, for oligomeric chains such as the PHSA used in this thesis, the size of a monomer. In the latter case b is typically $\sim$ 1 nm, from which we estimate $F^* \sim 10^{-12}$ N ~ 1 pN.

If the suspending fluid is not a good solvent for the brush, then energetic interactions between the monomers can lead to an attractive potential [41]. Osmotic repulsion invariably leads to a strongly repulsive potential for highly interdigitated brushes (but see [41] for certain caveats).

Derjaguin approximation

If the work done per unit area to bring two *planar* surfaces together from infinity to a surface separation D is $W_{||}(D)$, then the interaction force between two *spheres* is given by the Derjaguin approximation [33]:

$$F(D) = 2\pi R W_{||}(D). \tag{3.5}$$

In general, it is more convenient to measure the interaction potential between two curved cylinders rather than two planar surfaces. For polymer-coated surfaces, this is achieved using surface-force apparatus (SFA) (see [41, 42] and references therein), from which one can calculate $W_{||}(D)$ [43].

If the properties of the brush are independent of particle size (which is ostensibly the case for the PHSA-coated PMMA spheres used in this thesis; see Ch. 4), then Eq. (3.5) predicts that the force required to interdigitate two polymer brushes should scale as R.

3.1.4 Brownian motion

In addition to affecting each other via potential interactions, colloidal particles are sufficiently small that they are influenced by collisions with fluid molecules, leading to Brownian motion. An isolated spherical colloid will undergo Brownian diffusion with short-time self-diffusion constant D_s, which is related to the Stokes

drag coefficient $\tilde{\xi} = 6\pi\eta_f R$ by the fluctuation-dissipation theorem [36],

$$D_s = \frac{k_B T}{\tilde{\xi}} = \frac{k_B T}{6\pi\eta_f R}. \tag{3.6}$$

A useful quantity we will refer to frequently throughout the thesis is the (Brownian) time for a free particle to diffuse its own radius,

$$\tau_B = \frac{R^2}{6D_s} = \frac{\pi\eta_f R^3}{k_B T},$$

which sets the timescale for a colloidal system to reach equilibrium in response to an external perturbation. For a $R = 1$ μm colloid in water $\tau_B \sim 1$ s – colloidal systems equilibrate on timescales that are easily accessible in the laboratory.

3.1.5 Phase behaviour of hard sphere suspensions

Having introduced the colloidal interactions relevant to this thesis, we now discuss the phase behaviour of colloids at rest. For brevity, we consider the case of hard spheres only, that is, neglecting the effect of finite-range potential interactions such as van der Waals attraction and double-layer repulsion. For a neutrally-buoyant system of N spheres in a domain of volume V, the phase behaviour is determined by the *volume fraction*

$$\phi = \frac{4}{3}\pi R^3 \frac{N}{V}, \tag{3.7}$$

which is the fraction of V occupied by the particles. The assumption of hard-sphere-like interactions holds even for long-ranged ($\sim R$) repulsive potentials at the concentrations of interest in this thesis $\phi \gtrsim 0.5$. At these ϕ, the contributions from the $\mathcal{O}(10)$ nearest neighbours average out to a locally flat $U(r)$ [44]. For shorter-range ($\ll R$) repulsive potentials, nearly-hard-sphere interactions can also be achieved by adding salt to screen charges, decreasing κ^{-1} [45]. It is common to define an effective hard sphere radius (e.g., via the potential of mean force [12]) and an effective ϕ. We do not do so in this thesis and define ϕ in terms of the nominal volume occupied by the hard cores (see [12, 46] for caveats of this approach).

At $\phi < 0.494$, colloidal hard spheres are in a fluid phase [11]. For $0.494 \leq \phi < 0.545$ there is coexistence between fluid and an entropically-driven crystal phase, while for $\phi \geq 0.545$ the equilibrium phase is entirely crystalline. One finds, however, that above the glass transition volume fraction $\phi_g \approx 0.58$, homogeneous crystal nucleation is suppressed and the system dynamically arrests into a disordered phase. In contrast to the fluid phase at $\phi < 0.494$, in the glassy regime colloids are constrained to move within the cage made by their nearest neighbours and out-of-cage diffusion is arrested on experimental timescales. The mechanism of the colloidal glass transition is still an active area of research and a good starting point for the interested reader is the review article by Cipelletti and Weeks [8].

The crystallisation process is altered if the particles have a distribution of sizes. Specifically, if the polydispersity s, defined as the standard deviation of R divided by the mean,

$$s \equiv \frac{\sqrt{\langle R^2 \rangle - \langle R \rangle^2}}{\langle R \rangle}, \tag{3.8}$$

is larger than ≈ 0.07 then crystallisation is inhibited altogether [47]. Since $s > 0.1$ for all the systems studied in this thesis, we can safely ignore homogeneous crystallisation.

3.1.6 Colloids under shear

When a colloidal suspension is sheared at rate $\dot{\gamma}$ the particles interact via hydrodynamic forces mediated by the fluid, generating a stress $\propto \eta_f \dot{\gamma}$. Shearing the system also distorts the microstructure from its isotropic equilibrium state, reducing the available free volume and thereby generating an entropic stress that resisting the imposed shear $\propto k_B T/R^3$. The relative viscosity $\eta = (\sigma/\dot{\gamma})/\eta_f$ is determined by ϕ and the relative magnitude of hydrodynamic and entropic stresses, which is quantified by the Peclet number Pe, defined as

$$\mathrm{Pe} = \frac{\pi \eta_f \dot{\gamma}}{k_B T/R^3} = \tau_B \dot{\gamma}. \tag{3.9}$$

Pe can also be interpreted as the ratio of the time taken for a free particle to diffuse its own radius to the time taken to be advected its own radius by the

imposed flow field.

The form of $\eta(\mathrm{Pe}, \phi)$ is well known [48]; Fig. 3.4 shows representative flow curves (η, Pe) for different ϕ. At $\mathrm{Pe} \ll 1$, Brownian motion is able to randomise the microstructure on the timescale of the shear and the flow is Newtonian. The viscosity, $\eta_0(\phi)$, increases with ϕ and becomes immeasurably large at $\phi_g \approx 0.58$ [49]. Above ϕ_g, the system has a yield stress $\sigma_Y = \sigma(\mathrm{Pe} \to 0) \sim k_B T/R^3$ that increases with ϕ, Fig. 3.5. Below ϕ_g, the system shear thins at $\mathrm{Pe} \lesssim 1$, reaching a second Newtonian regime at $\mathrm{Pe} \gg 1$ with a viscosity $\eta_1(\phi)$ that diverges at $\phi_{\mathrm{RCP}} \approx 0.64$, the densest amorphous packing for lubricated (frictionless) hard spheres. In this regime, Brownian motion can no longer randomise the microstructure, which becomes highly anisotropic [35], and the viscosity is dominated by hydrodynamic interactions between the colloids.

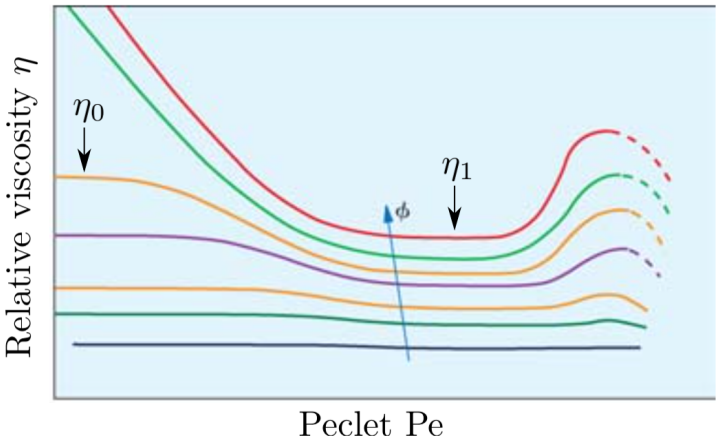

Figure 3.4: Schematic of relative viscosity η as function of Pe for colloidal hard spheres at different ϕ; η_0 and η_1 denote the limiting low- and high-shear viscosities, respectively. Adapted from figure 4 in [48].

The above scenario has been observed in a wide range of model HS systems [35, 50, 51]. Fig. 3.6 plots $\eta_1(\phi)$ for a mixture of charge- and sterically-stabilised colloids [49]. The data can be collapsed onto a single master curve by an $\sim 5\%$ shift in ϕ, which accounts for differences in polydispersity and discrepancies in ϕ due to different preparation methods [46].

In some cases, e.g., in [52], samples exhibit shear thickening at very large Pe (typically $\gtrsim 10^3$); although, this regime is typically avoided [50, 51].

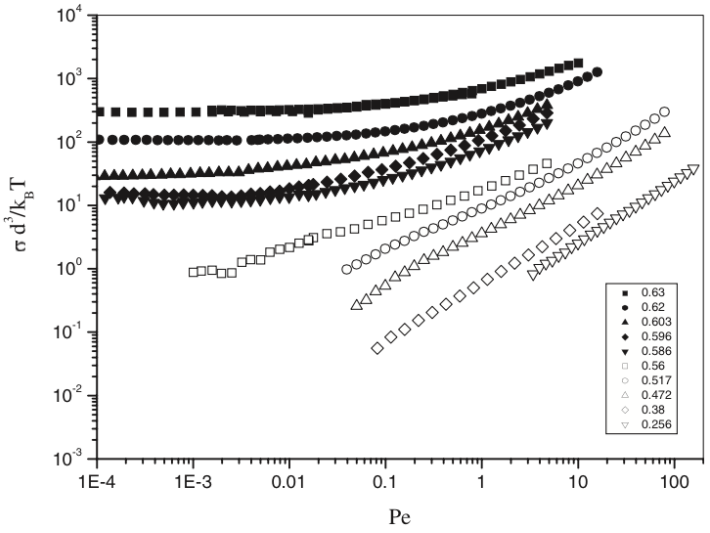

Figure 3.5: Shear stress in units of $k_BT/d^3 = k_BT/(8R^3)$ versus Pe for $R =$ 183 nm PMMA spheres in dodecane. Taken from [50].

3.1.7 When is a colloid no longer a colloid?

It is natural to ask when the above phenomenology ceases to hold – that is, the R at which a colloid ceases to be a colloid. This point is usually defined arbitrarily and the interpretation varies between researchers.

For a quiescent neutrally-buoyant suspension of spheres,the phase behaviour is independent of particle size, but the equilibration time is set by τ_B and therefore increases with R^3. In that case, the terminus of the colloidal regime is the size at which τ_B exceeds the timescale characterising the patience of the experimenter; e.g., for macroscopic objects, $R = 100$ μm, $\tau_B \sim 10^6$ s $\sim$ 2 weeks, which is impractically long. In practice, however, even small differences between the particle ρ_p and fluid densities ρ_f lead to sedimentation even for nominally density-matched colloids. The sedimentation velocity of aspherical free particle v_{sed} is given by balancing the Stokes drag force $6\pi\eta_f R v_{\text{sed}}$ and the buoyancy force $(\rho_p - \rho_f)(4/3)\pi R^3 g$,

$$v_{\text{sed}} = \frac{2}{9}\frac{(\rho_p - \rho_f)gR^2}{\eta_f}. \tag{3.10}$$

A useful measure of the extent to which sedimentation effects the equilibrium microstructure is given by the so-called gravitational Peclet $\text{Pe}_g = \tau_B/\tau_{\text{sed}}$, where $\tau_{\text{sed}} = R/v_{\text{sed}}$ is the time taken for a free particle to sediment a distance equal to its own radius. The colloidal regime can also be thought of as ending when

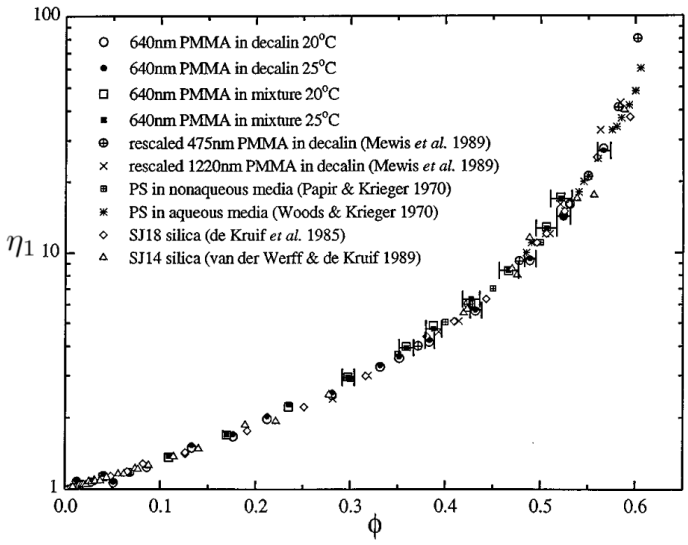

Figure 3.6: Limiting high-shear viscosity η_1 as a function of ϕ for diverse model colloidal HS dispersions. Taken from [49].

$\mathrm{Pe}_g = 1$. For silica spheres in water, $\mathrm{Pe}_g = 1$ corresponds to $R \approx 1$ μm; at larger R, one expects an inhomogeneous ϕ, whose exact profile $\phi(\underline{x})$ is determined by the balance between gravitational and osmotic forces.

Rheologically, the critical size at which a suspension is no longer colloidal is less well defined and we address this issue in Ch. 6.

3.2 Granular suspensions

We now review the relevant physics of granular suspensions, which comprise particles with $R \gtrsim 50$ μm fully immersed in a fluid. We do *not* consider the case in which the particles are particles are partially wet and connected by capillary bridges. We also assume that the suspending fluid is sufficiently viscous to render fluid and particle inertia effects unimportant [2] and that the particles are spherical and neutrally buoyant. Given the R^2 scaling of v_{sed} in Eq. (3.10), the need for a viscous suspending medium and careful matching of ρ_p and ρ_f is obvious – for a $R = 100$ μm silica sphere in water, $v_{\mathrm{sed}} \sim 1$ m.s^{-1} – and reliable measurements are accordingly sparse [27, 53]. It transpires that, owing to difficulties in preparing and handling concentrated granular suspensions at fixed ϕ, it is more convenient to measure the shear stress σ under imposed particle pressure P^p conditions

[2] A complete discussion of the distinction between inertial and non-inertial granular systems in relation to shear thickening is given in Ch. 7.

(where $P^p = p - p_f$ is the total mechanical pressure less the solvent pressure p_f) with a ϕ that is allowed to vary with P^p and $\dot{\gamma}$ [54]. From this, it is possible to deduce the relative shear viscosity as a function of ϕ that would be measured in a fixed-volume experiment.

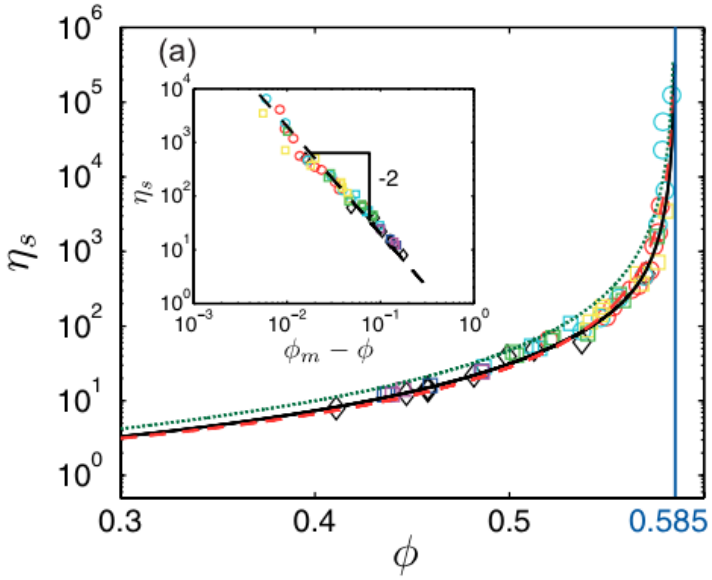

Figure 3.7: Volume fraction dependence of the viscosity of several wet granular systems with $0.1 \lesssim R \lesssim 1$ mm. Taken from [54].

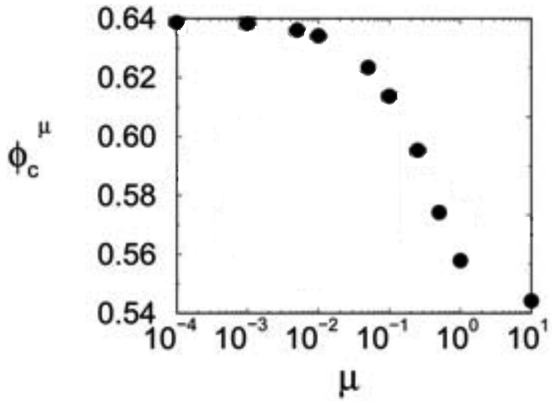

Figure 3.8: Frictional jamming volume fraction ϕ_m as a function of static friction coefficient μ_S from 3-d isotropic compression simulations. Taken from [55].

Since τ_B scales as R^3, granular HS inhabit the Pe$\gg 1$ regime at all practical shear rates. Extrapolating naïvely from the above description of colloidal flow, one expects Newtonian behaviour with a viscosity, $\eta_1(\phi)$, that diverges at $\phi_{\rm RCP}$. The imposed-P^p measurements do find a Newtonian viscosity, but it diverges at a volume fraction, $\phi_m = 0.585$ that is lower than $\phi_{\rm RCP}$, Fig. 3.7. This phenomenology is due to the presence of *static friction*. Simulations [55] show that

the exact value of ϕ_m depends on the value of the friction coefficient μ_S, Fig. 3.8, varying from random loose packing $\phi_{\mathrm{RLP}} \approx 0.55$ for $\mu_S = \infty$ to $\phi_{\mathrm{RCP}} = 0.64$ for $\mu = 0$ [55, 56].

Other works [27, 53, 57] find weak shear thinning rather than Newtonian behaviour, although no concrete explanation has been proposed for this yet. What it does reflect is the sensitivity of wet granular rheology to details of particle interactions, contrasting the system-independent phenomenology observed in the colloidal regime, which is dominated by entropic interactions.

3.3 Stress generation in suspension flow

We conclude the chapter with a discussion of how macroscopic stresses are related to particle-level forces in concentrated colloidal and granular suspensions. Most of the understanding presented in the following section came from simulations, as accessing particle-level forces experimentally has yet to be achieved for immersed particles (however, see future work, Ch. 10).

3.3.1 Contact forces

The contact force $\underline{f}^{\alpha\beta}$ between two particles α and β has a normal component f_N and a frictional tangential component f_T, which are related by a friction law. For Coulombic friction, there is no sliding if

$$F_T < \mu_S F_N \tag{3.11}$$

where μ_S is the *static friction coefficient*, and the particles are required to roll around one another. When the Coulomb criterion, $F_T = \mu_S F_N$, is met, contacts are mobilised and relative tangential motion between the surfaces occurs. The tangential and normal forces are then related by the dynamic (or sliding) friction coefficient μ_K,

$$F_T = \mu_K F_N. \tag{3.12}$$

If the forces are pairwise additive then the contact contribution to the stress

tensor σ_{ij}^{c} is given by [23]

$$\sigma_{ij}^{\mathrm{c}} = \frac{1}{V} \sum_{c} f_i^c b_j^c, \tag{3.13}$$

where the sum is over contacting particle pairs c in the averaging volume V (defined at the beginning of Ch. 2). f_i^c and b_i^c are the i-th components of the force between the two particles $\underline{f}$ and the branch vector $\underline{b}$ (the vector connecting their centres), respectively. Pairwise-additive potential interactions generate stress σ_{ij}^{U} in a similar manner to Eq. (3.13).

3.3.2 Hydrodynamic interactions

For simple shear, the shear stress σ_{12}^{h} generated by hydrodynamic interactions between colloids has the following form,

$$\sigma_{12}^{\mathrm{h}} = \eta_f \dot{\gamma} + n\langle S_{12} \rangle. \tag{3.14}$$

The first term on the left hand side is the Newtonian contribution resulting from affine shear of the solvent and this contribution is present even in the absence of particles. The second term is a quantity called the *stresslet* and is related to the average traction force exerted by the particles on the fluid (n is the number density of particles in the volume V). Evaluating $\langle S_{12} \rangle$ requires knowledge of the fluid flow field around each particle in the suspension and it embodies all hydrodynamic interactions, including short-range lubrication, long-range and many-body interactions. In concentrated suspensions, $n\langle S_{12} \rangle$ is dominated by the short-range lubrication forces between particles [58], which are pairwise additive, and the hydrodynamic stress is often approximated using an expression analogous to Eq. (3.13). The lubrication force between the surfaces has a normal ("squeeze") component $f_{\mathrm{sq}} \sim \eta_f R^2 W_N h^{-1}$, where h is the surface separation and W_N is the relative normal velocity of the surfaces; for tangential motion, $F_{\mathrm{sh}} \sim \eta_f R^2 W_T \ln h$, where W_T is the relative tangential velocity [25].

3.3.3 Brownian forces

Forces arising from Brownian motion are purely entropic in origin and depend only on excluded volume interactions. As mentioned earlier, shearing a colloidal suspension generates a Brownian stress σ^{B} because distorting the isotropic equilibrium microstructure causes a reduction in free volume, defined as the volume in which a specific particle can translate given that all the other particles in the system are held fixed [59]. We do not go into further detail here, but chapter 3 in the book by Wagner and Mewis [35] contains a good introduction to the topic.

Chapter 4

Materials and methods

In this chapter, we introduce the materials and rheological techniques employed in this thesis. In the first part of the materials section, we describe how samples were prepared for steady-state rheology measurements in the intermediate (Ch. 5), and colloidal and granular (Ch. 6) size regimes, focussing on PHSA-stabilised PMMA, with which we performed the most careful set of experiments. Details are also given for suspensions of cornstarch and zeolite. In the second part, we describe the protocols used for silica and DPDM-stabilised PMMA for the flow reversal experiments in Ch. 8. As voiced in the introduction to the previous chapter, this thesis is primarily concerned with the shear thickening phenomenology of suspensions and not with developing novel colloids or sample preparation methods. Most of the protocols we describe for PHSA-stabilised PMMA are based on previous work carried out within the group, so we provide only a skeleton overview and direct the interested reader to those works for full details.

In the methods section, we discuss some of the complications that arise during imposed-shear-rate start up, cessation and reversal measurements, and use this to judge the reliability of the data reported in Ch. 8.

Materials

4.1 Steady-state rheology: PHSA-stabilised PMMA

4.1.1 Particle synthesis, washing and drying

Poly(methyl methacrylate) (PMMA) spheres stabilised by covalently-grafted poly(12-hydroxystearic acid) (PHSA) were synthesised in house by Andrew Schofield following the procedure of Antl *et. al.* [60]. When dispersed in a good solvent (e.g., decalin), the chains extend to provide a repulsive steric layer with thickness $\delta \approx 5 - 15$ nm [43, 61]. The mechanical properties of the brush have been characterised by Bryant *et. al.* [43].

The particles produced during the synthesis are initially dispersed in dodecane, whose density 0.75 g.cm^{-3} is significantly lower than that of PMMA, $\rho_p \approx$ 1.18 g.cm^{-3} [62]. In order to transfer the particles into a density-matching solvent and to remove excess stabiliser, the particles were first transferred into decalin (a mixture of *cis* and *trans*) by repeatedly centrifuging and redispersing a suspension at $\phi \sim 0.3$. By monitoring the density of the removed supernatant, we determined then ten washes were sufficient to reduce the relative concentration of the original solvent to $\sim 10^{-3}$ and used this number for all samples (see [61] for a simple calculation justifying this number). The decalin was then removed by drying the sample under vacuum at 40 °C for at least 12 hours, a protocol that was found to lead to reproducible results in previous work [63]. We did not notice any systematic dependence of rheology on drying time or drying protocol.

4.1.2 Redispersal in a density-matching solvent

The dried powder was redispersed in a density-matching combination of cyclohexyl bromide (CXB, Sigma Aldrich; density 1.337 g.cm^{-3} at 19 °C) or cycloheptyl bromide (CHB, Sigma Aldrich density 1.309 g.cm^{-3} at 19 °C) and decalin (Sigma Aldrich; density 0.881 g.cm^{-3} at 19 °C). CXB photo-dissociates if left exposed to light, resulting in the creation of bromide Br^- ions . To remove these ions, the CXB was filtered through activated alumina. Decalin was filtered in the same way. The filtered solvents were subsequently stored in vials wrapped in tin foil to prevent exposure.

To density match the particles, we initially dispersed the dry powder in a solvent combination that approximately matched the dry density of the PMMA at 19 °C, the temperature at which rheology measurements were performed. We then centrifuged the sample at 19 °C until there was a visible change in concentration profile with height. If the sample sedimented, implying $\rho_p > \rho_f$, we added more CXB; if the sample creamed, implying $\rho_p < \rho_f$, we added more decalin. This process was iterated until equal portions by volume of the suspension creamed and sedimented, at which point the average density of the particles and solvent are matched (the bipartite sedimentation behaviour presumably reflects polydisperstiy in ρ_p).

4.1.3 Preparing samples at different volume fractions

We prepared samples at different reduced volume fractions $\Phi \equiv \phi/\phi_{\text{sed}}$ using the protocol described in [64], where ϕ_{sed} is the volume fraction of the sediment. The density of the solvent decreases with increasing temperature, which we exploit to obtain a close-packed sediment by centrifuging at 24 °C; the density of the supernatant at 19 °C ρ_f^{matched} yields an estimate of the particle density. We dilute this sediment by a factor of $f \approx 5$ with a CXB-decalin mixture with density ρ_f^{matched} and measure the density ρ^* of the diluted suspension. The density of the sediment is then given by

$$\rho_{\text{sed}} = \frac{\rho^* \rho_f^{\text{matched}}}{(1+f)\rho_f^{\text{matched}} - \rho^* f}. \tag{4.1}$$

Thus, when diluting a sediment of mass M_{sed} with a mass M_f of solvent, the

reduced volume fraction is given by

$$\Phi = \frac{\phi}{\phi_{\mathrm{RCP}}} = \left[1 + \frac{M_f}{M_{\mathrm{sed}}} \frac{\rho_{\mathrm{sed}}}{\rho_f^{\mathrm{matched}}}\right]^{-1}. \tag{4.2}$$

Samples were prepared at different Φ by subsequent dilutions of the same sediment. To convert Φ to an absolute volume fraction ϕ, we assumed that ϕ_{sed} was equivalent to random close packing, ϕ_{RCP}, and used simulations [65] to estimate ϕ_{RCP} based on the polydispersity of the particles.

How the sediment was redispersed depended on the particle size, of which we give details in Ch. 5 and Ch. 6.

Centrifugation protocol

The rheology of samples at $\phi \gtrsim 0.55$ was found to be sensitive to the maximum centrifugal force exerted on the suspension: samples centrifuged at high angular speeds Ω were difficult to redisperse and the resulting flow curves were very noisy at all stresses. We speculate that this is due to the steric barrier separating particle surfaces being overcome at large Ω, resulting in flocculation. Redispersing the particles requires that sufficient time has elapsed for particles to exit the van der Waals minimum of their mutual interaction potential. If the suspension has not fully de-aggregated before beginning rheological measurements, then the rheology is gel-like and time-dependent.

Working at low centrifugation speeds avoided these issues and lead to nearly-hard sphere behaviour. We operated at $\Omega = 2000$ rpm and the distance from this axis of rotation to the end of the sample vial in our swinging-bucket centrifuge was approximately $r \approx 10$ cm, corresponding to an angular acceleration of $\Omega^2 r \approx 4000$ m.s$^{-1} \approx 400$ g. We give a rationalisation of this choice below.

We will argue in Ch. 5 and 10 that the stress required to interdigitate the polymer brushes of two particles is related to the onset stress for shear thickening σ^*, which provides a lower bound on the local stress to push particles into the primary van der Waals minimum. We estimate the centrifugal force F_g on the largest particles studied, with radius $R = 1.89$ μm, using a typical density mismatch

$\rho_p - \rho_f \sim 10$ kg.m^{-3} to be

$$F_g = \frac{4}{3}\pi R^3(\rho_p - \rho_f)r\Omega^2 \approx 2 \times 10^{-12} \text{ N}. \tag{4.3}$$

The particle-level stress is approximately $F_g/R^2 \approx 0.3$ Pa, which is an order of magnitude less than the onset stress $\sigma^* \approx 2$ Pa measured for the same particles in Ch. 5. Accordingly, the rheology reported for that batch in Ch. 5 is free from attractions. Centrifuging the same batch at $\Omega = 6000$ rpm, corresponding to $F_g/R^2 \approx 5$ Pa $> \sigma^*$, resulted in attractive rheology.

4.1.4 Additional considerations

Swelling

CXB imbibes the cores of the PMMA particles, leading to a change in the particle radius R and density ρ_p, as well as changing the composition of the solvent and hence ρ_f. We characterised the swelling extensively by monitoring the form factor $P(Q)$ measured with static light scattering (see [61] for details) and found evidence of changes in the optical structure of the particles due to the imbibition on the timescale of months. While the effect of swelling is a separately interesting topic, we will argue in Ch. 5 that is is unimportant rheologically in the context of this thesis and we do not go into detail here.

Charge interactions and salt

It is well known that the PHSA stabiliser acquires a positive charge when the particles are dispersed in CXB and decalin [45]. The exact mechanism of charging is unclear; although, [38] purports that it is due to association of H^+ ions that arise from the association of HBr with carboxyl groups on the polymer. This charging has been observed to drastically distort the hard-sphere phase diagram, leading to the formation of a Wigner crystal at $\phi \sim 0.1$. In previous rheological studies, a small amount of salt (tetrabutyl ammonium chloride, TBAC) was added to screen the charges [66]. We found that adding an excess of salt did not alter the rheology of our samples in the shear thickening regime, $\phi \gtrsim 0.4$, and therefore present salt-free data.

4.1.5 Particle sizing

We conclude the section on PHSA-stabilised PMMA by briefly describing how the particle radii and particle size distributions $f_{\mathrm{PSD}}(R)$ were measured. A detailed account of the procedures used can be found in [67] and we present only the salient results here.

Particles were dried and $f_{\mathrm{PSD}}(R_{\mathrm{dry}})$ measured by transmission electron microscopy (TEM); f_{PSD} is the size distribution for the unswollen particles, which is not necessarily the same as the solvated distribution. From this, we obtained an estimate of the polydispersity s, defined in Eq. (3.8). We measured the volume-weighted swollen radius of the particles R with static light scattering using standard methods [61, 67, 68] [1] with a typical uncertainty of $\approx 2\%$.

We report R and s for different batches in the results chapters, Ch. 5 and Ch. 6. The uncertainty in R was typically $\approx 2\%$.

4.2 Steady-state rheology: other systems in the intermediate size regime

In addition to PHSA-stabilised PMMA, we also studied suspensions of cornstarch and zeolite with particle sizes in the intermediate regime, $1\ \mu\mathrm{m} \lesssim d \lesssim 50\ \mu\mathrm{m}$. The primary purpose of doing so was to demonstrate that they exhibited qualitatively similar behaviour to PHSA-stabilised PMMA and we did not fully characterise the particles. The zeolite particles were provided by Johnson Matthey.

4.2.1 Cornstarch

We dispersed cornstarch (Sigma Aldrich) in a mixture of 2/3 glycerol (Fisher Scientific) and 1/3 distilled water by mass. Fig. 4.1 shows a bright-field microscopy image of cornstarch particles in water. The particles are approximately spheroidal, but are faceted and are faceted with considerable shape polydispersity. The volume-weighted particle size (the effective sphere radius) and polydispersity measured by a Beckman-Coulter Mastersizer are $R \approx 7\ \mu$m and $s \approx 40\ \mu$m,

[1] For some batches we were unable to perform TEM and instead used SLS to estimate s.

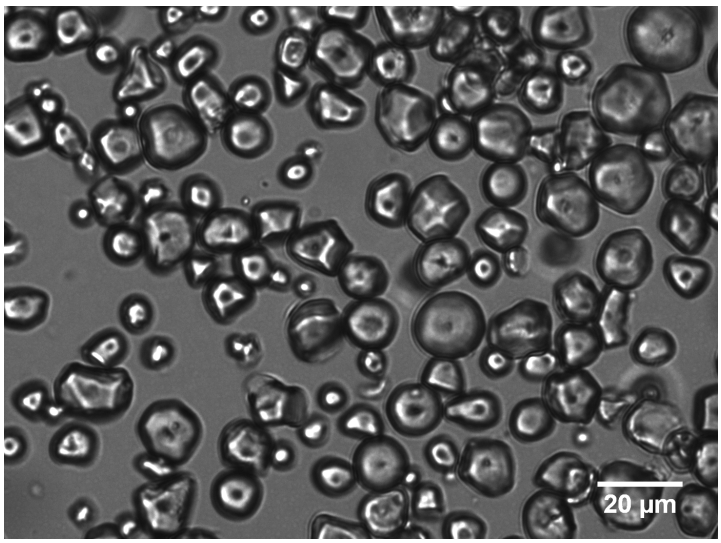

Figure 4.1: Bright-field microscope image of cornstarch particles in water. The scale bar is 20 μm.

respectively.

The reason for the use of a glycerol/water mixture was threefold. Firstly, dispersing the cornstarch in water only lead to evaporation issues, which were eliminated on the timescale of experiments ($\sim 10^3$ s) by the addition of glycerol. Secondly, the higher solvent viscosity, $\eta_f = 0.02$ Pa.s at 20 °C, limited the effects of sedimentation; with glycerol and water, sedimentation became noticeable as the development of a visible concentration gradient in unsheared samples only after ≈ 30 min. Thirdly, inertial edge fracture [30, 31] precluded proper study of the shear thickening regime in pure water, which was shifted into the accessible shear rate range by the larger η_f in the glycerol-water mixture.

Samples were prepared at different ϕ using the dry density of cornstarch $\rho_p = 1.45$ g.cm^{-3} (obtained by measuring the density of a dilute dispersion in water at different mass fractions; from [69]) and were mixed by hand with a spatula until visibly homogeneous.

4.2.2 Zeolite

We used zeolite (aluminosilicate, cubic particles) provided by Johnson Matthey with an equivalent sphere radius of $R = 2.5$ μm (measured by light scattering). Samples were dispersed in the same glycerol/water mixture as cornstarch and were also mixed by hand with a spatula. The volume fractions reported in Ch. 5

are based on the dry density of zeolite $\rho_p = 2.2$ g.cm^{-3} (provided by Johnson Matthey).

4.3 Flow-reversal rheology: PMMA and silica

4.3.1 DPDM-stabilised PMMA

As a model sterically-stabilised colloid for flow reversal we used PMMA particles with radius $R = 0.7$ μm stabilised by a poly-dimethyl-diphenyl siloxane (PDV-2335, Gelest) polymer covalently bonded to the core. The particles were synthesised in house following the procedure in Kogan *et. al.* [70]. In the original paper, the particles were dispersed in the same polymer used for the stabilisation, in which length of the polymer brush was found to be $\delta \approx 50$ μm using particle tracking methods. We dispersed the particles in a solvent of the same polymer but with a lower molecular weight, PDV-2331 (Gelest), as the lower viscosity of this solvent, $\eta_f = 1.78$ Pa.s, allowed us to observe the entire shear-thickening regime within the range of shear rates accessible with our rheometer. Since the high- and low-molecular-weight polymers are chemically identical, we assume that the solvency conditions for the polymer brush is the same in both cases, so that their measured value of δ is valid in the lower-molecular-weight solvent.

The particles are refractive index matched in this solvent, making the samples suitable for microscopy. We measured R using an analysis of the radial distribution function from 3-d confocal microscopy stacks; details of the method are given in [37].

Dispersing the samples

The PMMA particles were initially dispersed in hexane after synthesis and washed ten times in hexane to remove excess stabiliser. Drying and redispersing the particles directly in PDV-2331 was impractical owing to the high viscosity of the solvent. Instead, we added PDV-2331 to the hexane suspension and evaporated off the hexane to leave the particles in PDV-2331. We describe the process in detail below.

Suspensions of known volume fraction ϕ_H in hexane were prepared by allowing

the particles to settle under gravity into a close-packed sediment then diluting this sediment assuming $\phi_{\mathrm{RCP}} = 0.64$. The density of hexane $\rho_f = 0.789$ g.cm^{-3} and the dry density of PMMA $\rho_p = 1.18$ g.cm^{-3} were used to calculate the mass of colloids in a given mass of the hexane suspension and this was added to a known mass of PDV-2331. The volume fraction ϕ in PDV-2331 was calculated using the density of PDV-2331 and assuming that all of the hexane had evaporated.

In the evaporation step, the sample vials were left open in a fume hood – expediting the evaporation process by placing the samples under vacuum often resulted in rapid escape of the solvent that blew the particles out of the vial, so we left the samples exposed to atmospheric pressure. During the first 10 hours of the drying process the particles readily sedimented, so we redispersed the samples by vortex mixing at hourly intervals. They were mixed on a daily basis thereafter by slowly rotating the vials by hand until there were no visible inhomogeneities in ϕ. Measurements were begun when the rate of change in mass due to evaporation relative to the initial mass of hexane was $< 0.1\%$ per day (smaller changes in mass were not resolvable with the balance used).

4.3.2 Whitehouse Scientific silica

As a model charge-stabilised colloid, we used amorphous silica microspheres supplied by Whitehouse Scientific with $R = 1.5$ μm (from the supplier). We prepared suspensions at different ϕ in glycerol (Fisher Scientific, $\rho_f = 1.262$ g.cm^{-3} at 19 °C) using the dry density of the particles, $\rho_p = 1.97$ g.cm^{-3} at 19 °C, obtained by measuring the density of a dilute suspension at several known mass fractions.

Suspensions were mixed by first adding the solvent then dragging the denser particles through by centrifugation. They were then vibrated gently with a vortex mixer to wet any undispersed dry powder, sonicated for 30 mins and finally placed on a roller bank for three days before beginning experiments; this was the minimum time at which no aggregates were visible by eye. The rheology of the samples was sensitive to the sonication time, so we adhered strictly to the above protocol to ensure consistency between samples. Sonicating for longer lead to a systematically lower viscosity, which we attribute to the break up of aggregates. This point is discussed further in Ch. 5.

Methods

In this part of the chapter, we characterise the response of the rheometers used in this thesis for flow start-up, cessation and reversal. All three techniques are utilised in Ch. 8; however, we use flow reversal most extensively. The purpose of this section is to identify the minimum time after reversal $t_{\min}$ at which the measured stress or strain reflects the constitutive properties of the sample and is not influenced by artefacts caused by, e.g., the inertia of the rheometer shaft or the compliance of the torque transducer. As we will see in Ch. 8, this quantity is important for correctly extracting the hydrodynamic contribution to the viscosity.

Three rheometers were employed in this thesis: a TA DHR-2 stress-controlled rheometer operated in strain-rate-controlled mode, an Anton Paar MCR301 stress-controlled rheometer and a modified ARES shear-rate-controlled rheometer. Details of the measuring geometries (cone-plate, or parallel plate) used can be found in the results chapters. Measurements on the ARES rheometer were performed by Neil Lin of Cornell University and full details can be found in the Supplementary Material of [4]; we focus on the TA DHR-2 and MCR301 here.

4.4 Experimental transient rheology

We begin by describing the three basic types of transient shear experiment used in imposed-$\dot{\gamma}$ rheometry. These are shown schematically in Fig. 4.2:-

(a) *Flow cessation.* A non-zero shear rate $\dot{\gamma}_a = \dot{\gamma}_0$ is applied for $t < 0$, then zero shear rate $\dot{\gamma}_a = 0$ applied at $t = 0$.

(b) *Start-up flow.* $\dot{\gamma}_a = 0$ is imposed for $t < 0$, followed by $\dot{\gamma}_a > 0$ at $t = 0$.

(c) *Flow reversal.* $\dot{\gamma}_a = +\dot{\gamma}_0$ is imposed for $t < 0$, then the direction of shear

is immediately reversed at $t = 0$ and the shear rate applied in the opposite direction, $\dot{\gamma}_a = -\dot{\gamma}_0$, at $t \geq 0$.

In each case, one typically measures the evolution of the shear stress $\sigma(t)$ and normal force $F_N(t)$ as a function of time $t > 0$. It is common to combine steps (a), (b) and (c) in sequence, e.g., as in Fig. 2.5. In Ch. 8, we combine reversal and cessation to investigate the effect of stress relaxation on the hydrodynamic contribution to the viscosity. Analogous procedures exist in imposed-σ mode, in which one measures $\dot{\gamma}(t)$ and $F_N(t)$.

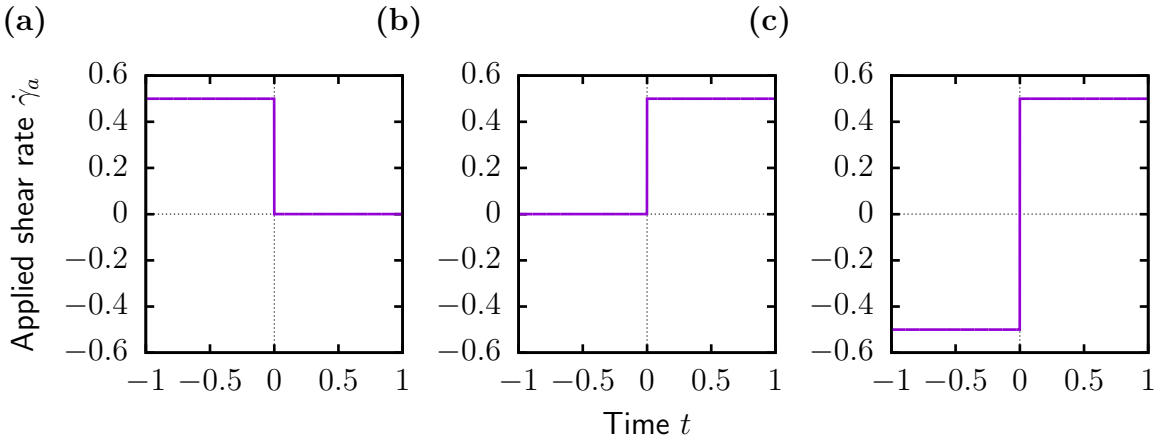

Figure 4.2: Imposed-$\dot{\gamma}$ transient rheology. (a) Flow cessation, (b) start-up flow and (c) flow reversal at $t = 0$.

Pushing the limits of conventional rheometers

Obtaining reliable transient measurements pushes the limits of most current commercial rheometers. The most significant issue is that for the first $\sim 10^{-2} - 10^{-1}$ s after cessation, start up or reversal, the measured torque and the actual strain γ are both influenced by the interplay of the mechanical compliance of the torque transducer, the inertia of the shaft and measuring tool and the mechanical properties of the sample. The exact behaviour in this period depends on the exact specifications of the rheometer, which are, in general, unavailable for modern instruments. We therefore do not attempt to deconvolve these effects to obtain the true material properties, and instead perform measurements on viscous oils with similar viscosities to those encountered in the suspensions. A detailed discussion of instrument response in transient rheometry is given in [71, 72].

4.4.1 TA DHR-2

For the imposed-$\dot{\gamma}_a$ tests performed in Edinburgh, we used the TA DHR-2 rheometer. In stress-controlled mode, an electrically-commutated motor applies a fixed torque to the shaft, itself levitated inside an air bearing to minimise friction, and the angular deflection of the shaft measured via an optical encoder. In $\dot{\gamma}_a$-controlled mode, the torque is adjusted to maintain the desired $\dot{\gamma}_a$ via a feedback loop with frequency $\approx 10^3$ Hz. The normal force exerted on the shaft is measured by a transducer in the rheometer head, but the torque is calculated from the current applied to the motor and is not measured directly in either mode of operation.

The data reported in this section are for a Newtonian oil (PDMS 200, Sigma Aldrich) and were obtained with a 20 mm roughened aluminium plate and larger roughened aluminium base plate with a gap height of 600 μm, the setup used in Ch. 8. In Fig. 4.3(a), we plot flow curves $\eta(\sigma)$ for consecutive upward and downward sweeps. The data are very noisy below $\sigma \approx 2$ Pa, which corresponds to the lower torque limit of the instrument.

Response to flow reversal

We begin by testing the instantaneity of the reversal response, that is, how quickly after reversal the actual shear rate $\dot{\gamma}(t)$ reaches the imposed shear rate $\dot{\gamma}_a$. In Fig. 4.3(b), we plot the evolution of $\dot{\gamma}(t)$ measured after reversal at $t = 0$ for different imposed shear rates $\dot{\gamma}_a$ for a Newtonian oil ($\dot{\gamma}_a$ is changed from negative to positive). At all $\dot{\gamma}_a$, $\dot{\gamma}(t)$ remains negative for 1 ms then undergoes oscillations until $\sim$ 10 ms, whence it reaches a steady value. The response for a shear-thickening silica suspension is similar (dot-dashed line), but the oscillations are damped out.

To assess the reliability of the stress signal $\sigma(t)$, we plot the instantaneous viscosity $\eta(t) = \sigma(t)/\dot{\gamma}(t)$ versus t in Fig. 4.3(c). For a Newtonian oil, one expects a flat response for an artefact-free system. Although $\dot{\gamma}(t) = \dot{\gamma}_a$ after 10 ms, the viscosity does not reach a plateau until $t_{\min} = 50$ ms, independent of $\dot{\gamma}_a$. The fact that $t_{\min}$ is independent of $\dot{\gamma}_a$ rules out geometry inertia as a possible origin, which leads us to suppose that $t_{\min}$ is instead determined by the speed of the feedback loop of the rheometer. It is possible to adjust $t_{\min}$ via the rheometer software by changing the effective "stiffness" of the motor. The data we present

are for the stiffest setting – using the softest setting resulted in a more gradual rise in $\dot{\gamma}(t)$ and $t_{\min} \sim 1$ s.

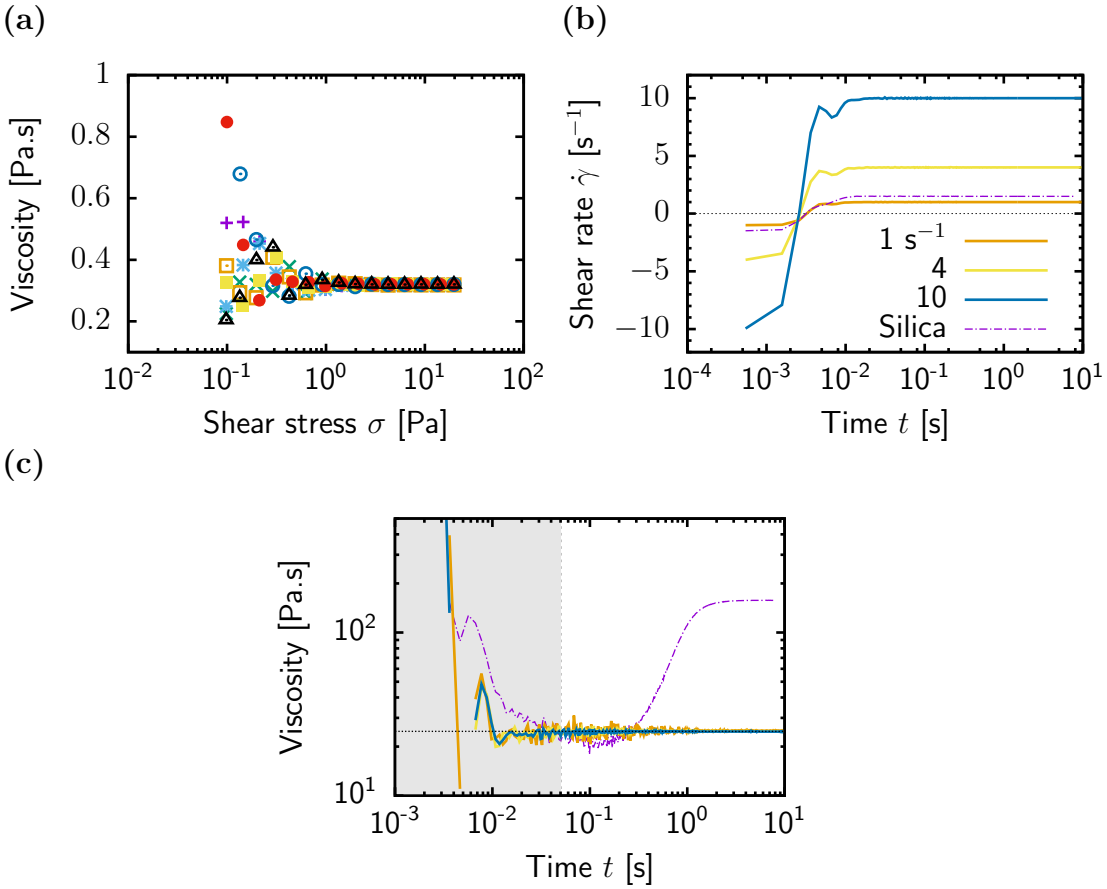

Figure 4.3: Flow reversal response for the DHR-2 rheometer operating in $\dot{\gamma}$-controlled mode. Measurements were made with a roughened aluminium plate (diameter 20 mm, gap height 600 μm). (a) Flow curves $\eta(\sigma)$ for a Newtonian oil (PDMS 200) with viscosity $\eta_f = 0.32$ Pa.s measured by consecutive upward and downward σ sweeps (denoted by different symbols). (b) Actual shear rate response $\dot{\gamma}(t)$ after reversal at $t = 0$ for a Newtonian oil (solid lines) at different applied shear rates $\dot{\gamma}_a$, as labelled, and for WHS silica in glycerol with $\phi = 0.516$ at $|\dot{\gamma}| = 1.46$ s^{-1} (dot-dashed line). (c) Viscosity response $\sigma(t)/\dot{\gamma}(t)$ after reversal. We identify $t_{\min} = 50$ ms as the time when $\eta(t)$ reaches a plateau for the Newtonian oil.

Response to flow cessation

Similar artefacts arise during shear cessation when operating a σ-controlled rheometer in simulated $\dot{\gamma}$-controlled mode. To test the limitations of the instrument, we applied a fixed shear rate $\dot{\gamma}_a > 0$ to the Newtonian oil in the positive direction, before imposing $\dot{\gamma}_a = 0$ at $t = 0$. Fig. 4.4(a) plots the evolution

of the actual shear rate $\dot{\gamma}(t)$ after cessation for $\dot{\gamma}_a = 0.1$, 1 and 10 s^{-1}. At all $\dot{\gamma}_a$, $\dot{\gamma}(t)$ is initially positive and undergoes an exponential decrease until at ≈ 50 ms it reaches the noise level of the machine and fluctuates between positive and negative (not shown on a log plot) values with $\langle\dot{\gamma}\rangle \approx 0$. The shear stress, $\sigma(t)$, Fig. 4.4(b), drops below the lower stress limit of ≈ 2 Pa, but oscillates between positive and negative values at earlier times.

Fig. 4.4(c) and (d) plot $\dot{\gamma}(t)$ and $\sigma(t)$ for flow reversal following a period of cessation with t_w. The system is first sheared at $\dot{\gamma}_a = -1$ s^{-1}, then $\dot{\gamma}_a = 0$ is imposed for a time t_w, followed by $\dot{\gamma}_a = 1$ s^{-1} at $t = 0$. The applied rate, Fig. 4.4(c), is attained after ≈ 10 ms for all t_w. There is a small discrepancy in $\sigma(t)$, Fig. 4.4(d), between $t_w = 0$ and 10 s after ≈ 50 ms. This time is comparable to $t_{\min}$ in flow reversal.

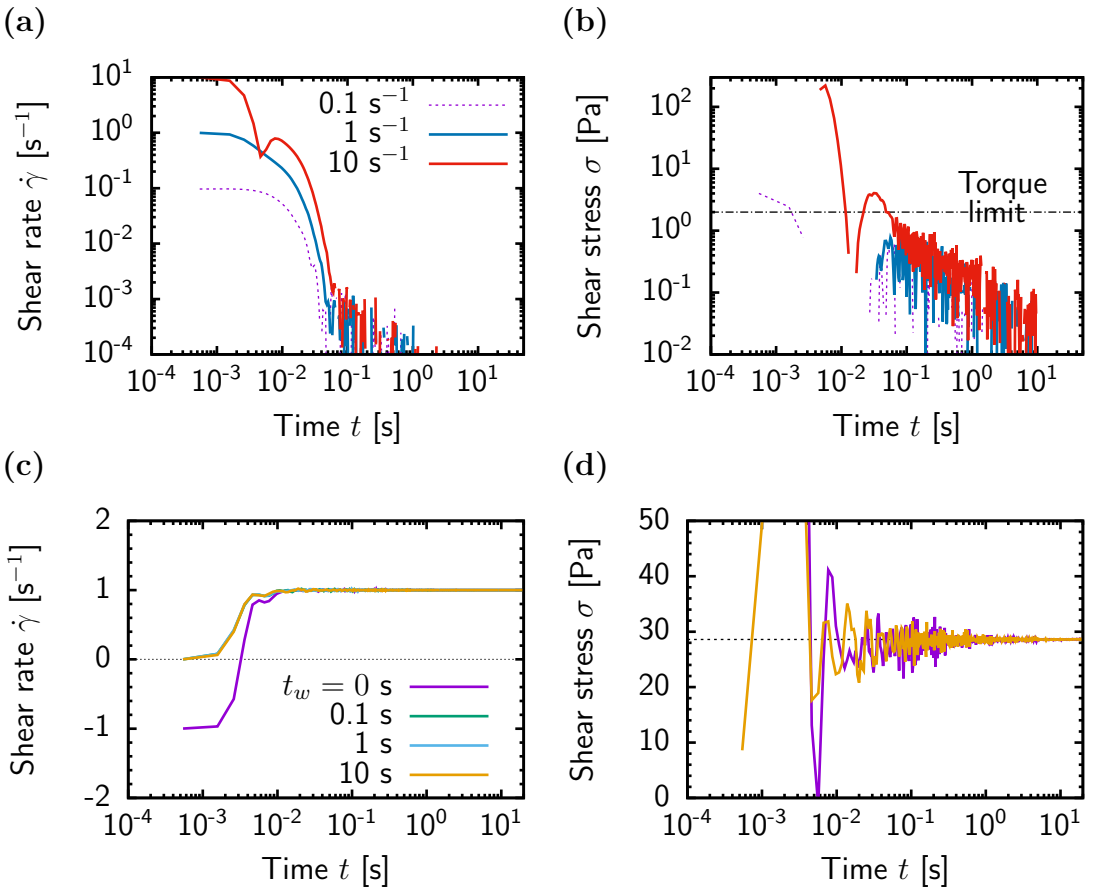

Figure 4.4: Response of DHR-2 rheometer to flow cessation, (a) and (b), and to flow reversal after a period of cessation, (c) and (d). (a) Actual shear rate $\dot{\gamma}(t)$ versus time t for shear cessation ($\dot{\gamma}_a = 0$) at $t = 0$ following different applied shear rates $\dot{\gamma}_a$, as labelled. (b) Shear stress $\sigma(t)$ after cessation [the legend is the same as in (a)]. The dot-dashed line corresponds to the practical lower torque limit of the instrument. (c) $\dot{\gamma}(t)$ for flow reversal at $t = 0$ following cessation for periods of different duration t_w, as labelled; the applied shear rate before cessation was $\dot{\gamma}_a = 1$ s^{-1}. The corresponding evolution of $\sigma(t)$ for $t_w = 0$ and 10 s is shown in (d).

4.4.2 Anton Paar MCR 301

The characteristics of the Anton Paar MCR 301 rheometer are similar under imposed-$\dot{\gamma}$ mode, with $t_{\min} \approx 60$ ms. To characterise the response under imposed-σ, we studied a Newtonian oil with $\eta_f = 30$ Pa.s for $\sigma < 500$ Pa, conditions typically encountered in experiments. The viscosity $\eta(t)$ reaches steady state after ≈ 60 ms in both start-up and reversal experiments over the full range of σ. In cessation experiments, where flow at $|\sigma(t)| > 0$ is followed by $\sigma(t) = 0$, $\dot{\gamma}(t)$ reaches zero after ≈ 0.01 s, independent of σ. For the largest σ probed in experiments, $\sigma = 100$ Pa, the additional strain accumulated during the deceleration of the rheometer shaft and cone to $\dot{\gamma} = 0$ is $\approx 0.5\%$, which is smaller than the minimum strains $\sim 10\%$ of interest in suspension flow reversal in Ch. 8 .

Modified ARES rheometer

The response time of the ARES rheometer is $\approx$ 30 ms, comparable to the inherently stress-controlled instruments (see Supplementary Material of [4] for details).

Chapter 5

Rheology in the intermediate size regime

Most of our current understanding of suspension rheology is confined to the colloidal (particle size $d \lesssim 1$ μm) and granular ($d \gtrsim 50$ μm) size regimes, for which the underlying physics is well understood. In contrast, our knowledge of the flow behaviour of intermediate-sized particles, 1 μm $\lesssim d \lesssim 50$ μm, is extremely limited, even for hard-sphere-like particles. This is surprising, since industrial systems as diverse and chocolate [73], ceramics [74] and cement [75], feature size distributions with a peak in precisely this regime, Fig. 5.1. In all of the above cases, flow plays an integral role in the processing of the material: ceramic green bodies are formed by extruding a concentrated paste through a narrow aperture, or die [76]; cement is required to flow down chutes, but have a yield stress when at rest; and the rheology of chocolate during mixing determines the texture of the final product. It is well known, however, that such systems are prone to erratic and inhomogeneous flow, which can lead, for example, to regular distortions on the surface of a ceramic extrudate [77], Fig. 5.2. A predictive understanding of intermediate-sized particles would be invaluable, but is currently lacking.

Besides being of industrial relevance, the intermediate regime poses an interesting academic challenge: one expects both the excluded-volume-dominated physics of colloidal particles and the particle-surface-dominated physics of granular particles each to play a role. Indeed, as we show in Ch. 6, understanding the intermediate regime is central to understanding how hard-particle rheology transitions from colloidal to granular behaviour with increasing d.

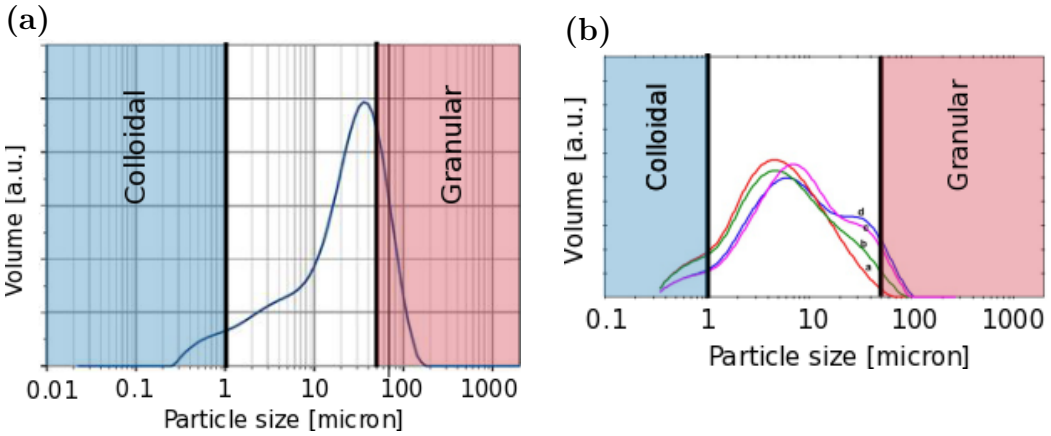

Figure 5.1: (a) Typical volume-weighted particle size distribution (PSD) for a ceramic green body (taken from [74]). The peak of the PSD lies in the intermediate size regime, 1 μm $\lesssim d \lesssim$ 50 μm. (b) PSD for dark chocolate (taken from [73]; different lines represent different batches).

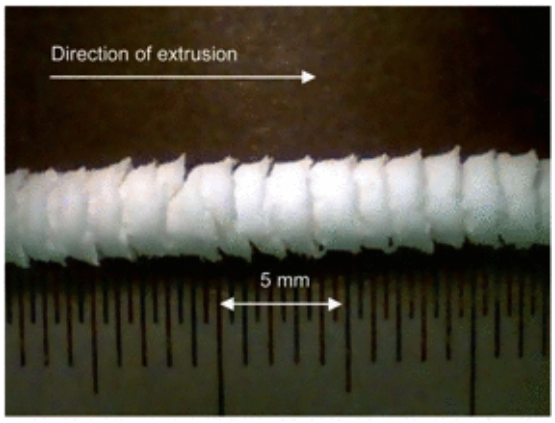

Figure 5.2: Regular surface defects for a micro-crystalline cellulose paste undergoing ram extrusion through a circular die (from [77]).

In this chapter, we elucidate the basic physics of suspensions of intermediate-sized particles under flow by performing rheology measurements on a range of model systems. We restrict our attention to particles with *repulsive* interactions, which already show a rich phenomenology, and postpone discussion of more complicated interactions (e.g., attractions) to Ch. 7. We find a phenomenology that is completely generic: in each system it is possible to identify a stress-dependent transition between two viscosity "branches" diverging at different concentrations. This transition manifests rheologically as shear thickening. Importantly, the existence of two viscosity branches implies a ϕ regime in which flow is inherently unstable beyond a threshold stress – interestingly, this is where many industrial dispersions are formulated.

We show that our shear-thickening data are well fit by the theory of Wyart and Cates [1], in which thickening is driven by the formation of frictional contacts. We discuss some of the assumptions of the theory in light of recent simulations [2, 56, 78], before concluding the chapter with a discussion of the generality of our findings.

5.1 Two-branch phenomenology

To establish the basic phenomenology, we study density-matched PHSA-stabilised PMMA spheres in the intermediate regime at different volume fractions ϕ using standard stress-controlled rheometry. We begin by describing the protocol used to prepare the suspensions and outline the protocols we use for loading the samples and obtaining reproducible flow curves.

5.1.1 Sample preparation and rheology protocol

Sample preparation

Full details of the sample preparation method are given in Ch. 4. We used PHSA-stabilised PMMA spheres with $d = 3770$ nm (measured by microscopy) and polydispersity $\approx 10\%$ (from electron microscopy) dispersed in a density-matching mixture of cyclohexyl bromide (CXB) and decalin (viscosity $\eta_f = 2.83 \times 10^{-3}$ Pa.s, density $\rho_f = 1.18$ g.cm^{-3}). The particles were left in the solvent for 7 days to swell, then prepared at different ϕ by diluting a close-packed sediment, using simulations [65] to estimate the sediment packing fraction ϕ_{sed} based on the polydispersity ($\approx 10\%$). The data we present are for subsequent dilutions of the same sediment, taking $\phi_{\text{sed}} = 0.64$.

At $\phi < 0.6$, samples were mixed on a roller bank for > 12 hours after each dilution; samples were visibly well mixed after this time. At $\phi \gtrsim 0.6$, samples were redispersed by gently vibrating and rotating the vial on a vortex mixer until the suspension was visibly homogeneous. Applying strong shear during mixing (for example, from vortex mixing too vigorously) was found to jam the sample, preventing mixing. Prolonged strong shear lead to destabilisation of the particles and evidence of strong attractions in the rheology. We present data for a stable batch.

Dispersing dried particles directly at the desired ϕ using the dry density of the powder ($\rho_p = 1.18$ g.cm^{-3}) gave similar results to the above method at $\phi \lesssim 0.55$, but there were differences in the flow at low σ at $\phi > 0.55$, which we attribute to the particles not being dispersed properly. Measurements on dried and weighed samples were begun two days after preparing the samples and took one day to complete, while measurements on samples prepared by dilution were begun after one week and took approximately one week to complete. One might expect to see systematic differences in rheology due to changes in ϕ caused by swelling over the course of the experiment; however, we find that the high shear relative viscosity – a sensitive measure of ϕ [49] – measured with both protocols can be collapsed onto the same curve by a $\lesssim 3\%$ shift in ϕ. The small shift in ϕ presumably accounts for a difference between the dry and swollen particle densities [1], and we conclude that any solvent imbibition that takes place after ≈ 2 days does not affect the rheology

Loading protocol

Rheological measurements were performed in an Anton Paar 301 rheometer in truncated cone and plate geometry (cone angle 1°; radius 25 mm; truncation gap 100 μm) in stress-controlled mode. A sandblasted steel cone and aluminium base plate roughened with silicon carbide powder were used to limit wall slip. The surface roughness of the base plate was estimated to be 5 μm from microscopy; the surface roughness of the cone is ~ 10 μm, from the manufacturer. A wall slip analysis performed with steel parallel plates with nominally the same surface roughness found a slip length ~ 100 μm [79]. Correcting the flow curves for slip has no bearing on any of the conclusions we draw; we present uncorrected data. We used a solvent trap containing a rag saturated with CXB and decalin to limit solvent evaporation, with which we could obtain reproducible results for up to $\sim 10^3$ s.

To load the rheometer, a slight excess of sample was poured onto the lower plate. The cone was lowered to the truncation height and the sample trimmed with a

[1] The direction of the shift is batch dependent, but in most of the cases the apparent dry volume fraction $\phi_{\rm dry}$ is systematically lower than the wet one $\phi_{\rm wet}$ by $\approx 3\%$. We obtained an estimate for the swollen particle density by determining the solvent composition that resulted in half of the particles sedimenting and half creaming during centrifugation and found $\rho_p^{\rm wet} = 1.16$ g.cm^{-3}. Taking a literature value for the dry density of PMMA, $\rho_p^{\rm dry} \approx 1.18$ g.cm^{-3}, we expect $\phi_{\rm wet}$ and $\phi_{\rm dry}$ to differ by a factor of $\sim \rho_p^{\rm dry}/\rho_p^{\rm wet} \approx 2\%$, approximately consistent with viscosity measurements.

spatula. Since the lower plate is larger than the cone, the air-sample meniscus invariably extended outside the geometry, even after trimming. We did not systematically study different air-sample boundary conditions with PMMA, but results for other systems were found to be unaffected by using, e.g., equal-sized plates or a Couette geometry (data not shown, but see [5]).

At $\phi \gg \phi_m$, lowering the cone rapidly drives the sample into a jammed state; the meniscus becomes matte and there is a concomitant rise in the normal stress N exerted on the cone, which becomes large and positive. Using the automatic gap setting, the rheometer applies a normal stress up to a maximum of 2×10^4 Pa. Doing so induces irreversible attractions between particles, resulting in noisy and massively irreproducible flow curves across the entire range of accessible shear stresses. In extreme cases, the suspension fractured into permanent millimetre-sized granules [80]. We avoid these issues by lowering the cone incrementally at a rate of < 5 μm.s^{-1} while imposing a maximum normal stress $N_{\max} = 10^3$ Pa. We stop the cone when $N \approx N_{\max}$, which typically occurs after reaching a compressive strain of $\mathcal{O}(1)$, and wait until N drops to ≈ 0 before lowering it further. For the most concentrated samples, we facilitated relaxation of N by tapping the lower metal plate and performing small-amplitude oscillations of the cone by hand. We waited until $N \approx 0$ before starting measurements; starting measurements when $N > 0$ lead to a systematic decrease in the viscosity with time as N decayed to ≈ 0, presumably due to the relaxation of shear-induced structure created during loading.

At $\phi \lesssim \phi_m \approx 0.55$, the rheology is insensitive to loading protocol; we loaded samples imposing $N_{\max} = 10^3$ for consistency with higher ϕ.

Rheological protocol

Steady state flow curves were obtained by either increasing or decreasing the imposed shear stress σ incrementally. The suspension viscosity is sufficiently low (at most $\sim$ 1 Pa.s) that it takes the cone $\approx$ 5 s to reach the steady-state $\dot{\gamma}$ after a step change in shear stress – this is an artefact of the combined inertia of the cone and rheometer shaft, rather than reflecting time dependence of the material properties of the sample. We therefore remain at each σ for 10 s. Before measuring $\eta(\sigma)$, all samples were pre-sheared at 0.5 Pa until the viscosity stopped changing with time (typically taking $\approx$ 60 s) to remove loading history.

At $\phi = 0.54$ and 0.51, reproducible results were obtained for multiple upward and downward stress sweeps; whereas, at $\phi < 0.51$ the viscosity was $\lesssim 1.5$ times lower in subsequent sweeps. We attribute this discrepancy to the finite inertia of the cone, which leads to a greater effective shear stress on the downward sweep as the cone is still decelerating at each point. One possible solution to this problem is to increase the equilibration time per point; however, we found that increasing the total experiment time further lead to drying artefacts. We report the first upward sweep in each case, apart from $\phi = 0.58$, which is a downward sweep.

5.1.2 Results

Fig. 5.3 shows the relative viscosity η as a function of shear stress σ for $d = 3770$ nm PMMA at different volume fractions ϕ. For $0.41 \leq \phi \leq 0.54$, there is a transition from a low-viscosity Newtonian plateau towards a higher, shear-thickened Newtonian plateau as σ is increased. The transition to the shear-thickened state begins above a ϕ-independent onset stress $\sigma \approx 2$ Pa, which we identify by eye to be the point at which the gradient of $\eta(\sigma)$ becomes greater than zero on a log-log plot. The air-sample interface fractures at a higher, ϕ-independent stress $\sigma^\dagger \approx 500$ Pa, above which the data show poor reproducibility and strong history dependence.

Approximately the same onset stress applies at $\phi \geq 0.56$, but now the data are noisy above σ^* and the high-shear Newtonian plateau vanishes. Taking a temporal average of the viscosity yields a curve with a gradient approximately equal to unity on a log-log plot, $d\log(\eta)/d\log(\sigma) \approx 1$. In a plot of $\sigma(\dot{\gamma})$, this corresponds to a discontinuous jump in σ and is commonly referred to as *discontinuous shear thickening* (DST) in the literature [81].

The two plateau viscosities fall on separate diverging branches, Fig. 5.4. The lower plateau viscosity, $\eta_1(\phi)$ (filled blue squares), diverges at $\phi \approx 0.63 = \phi_{\mathrm{RCP}}$, which is close to random close packing (RCP), the maximum amorphous packing fraction for frictionless spheres. The high-viscosity branch, $\eta_2(\phi)$ (open red squares), diverges at a lower volume fraction $\phi_m \approx 0.55 < \phi_{\mathrm{RCP}}$. Thus, shear thickening at $\phi < \phi_m$ can be viewed as a smooth transition from the lower to the upper branch as σ is increased above a threshold σ^*. Given this interpretation, it is natural to ask what happens in the window between ϕ_m and ϕ_{RCP}: here, there is no finite-viscosity branch to which the system may jump. For $\sigma < \sigma^*$ the system undergoes Newtonian flow on the lower branch, but becomes solid-like and jams

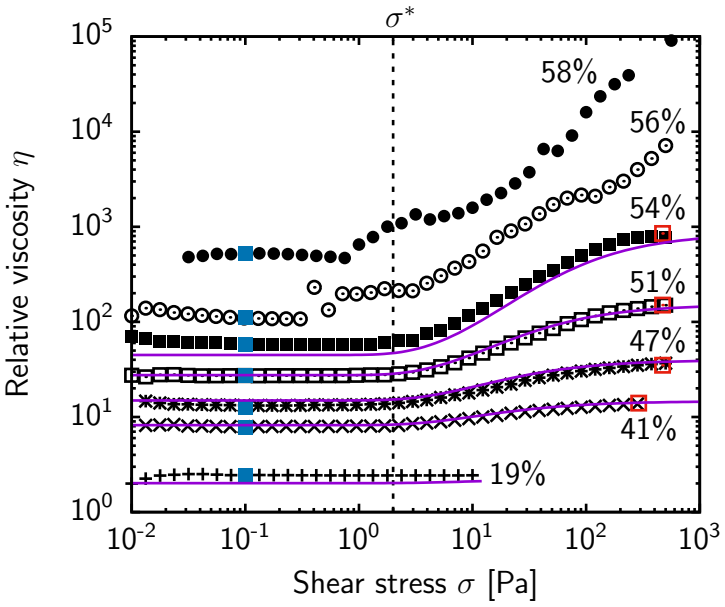

Figure 5.3: Relative viscosity η versus shear stress σ for 3770 nm diameter PMMA spheres at different volume fractions ϕ, as labelled. Symbols, experimental data; solid lines, fits to Wyart and Cates theory [1]. At $\phi \leq 0.54$, samples shear thicken above a ϕ-independent onset stress σ^* (vertical dashed line) from a low-viscosity Newtonian regime with viscosity $\eta_1(\phi)$ (filled blue squares) towards a high-viscosity Newtonian regime with viscosity $\eta_2(\phi)$ (open red squares). At $\phi \geq 0.56$, the flow is unsteady above σ^*.

when σ^* is exceeded. Any flow that we observed was unsteady and highly erratic, and accompanied by significant wall slip and deformation of the free surface.

5.1.3 Other systems

We now show that the above phenomenology is generic for intermediate-sized particles. In the following section we present data for three more suspensions also in the intermediate regime: cornstarch ($d = 14$ μm), charge-stabilised "potato-shaped" particles; Spheriglass 5000 ($d \approx 7$ μm) [82], charge-stabilised glass particles with massive size and shape polydispersity; and zeolites ($d \approx 5$ μm), industrial-grade aluminosilicate cubes. In each case we can identify two viscosity branches diverging at different concentrations, ϕ_m and ϕ_{RCP}, and an onset stress, σ^*, which controls the transition between the branches.

We begin with cornstarch dispersed in a glycerol and water mixture, Fig. 5.5. Details of the rheological protocol are described in the caption. For $0.37 \leq \phi \leq 0.41$, $\eta(\sigma)$ undergoes continuous shear thickening from a low-viscosity Newtonian

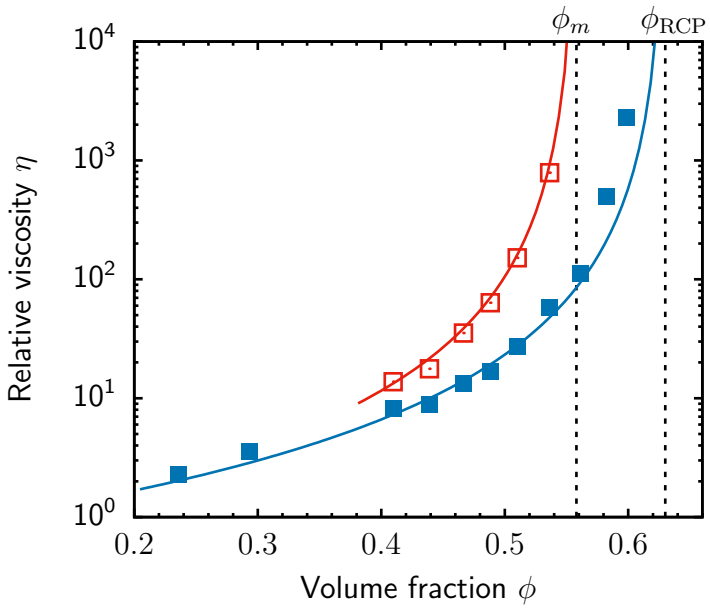

Figure 5.4: Relative viscosity η as a function of ϕ for the limiting low-shear viscosity, η_1, (filled blue squares) and high-shear viscosity, η_2, (open red squares) in Fig. 5.3. The values of η_1 and η_2 were read off by eye. Solid red line, least-squares fit to $\eta_2(\phi) = A(\phi_m - \phi)^{-n_2}$ with A=0.20(9), $\phi_m = 0.558(5)$ and $n_2 = 2.2(2)$. Solid blue line, fit by eye to the power law $\eta_1 = (1 - \phi/\phi_{\rm RCP})^{-2}$ with $\phi_{\rm RCP} \approx 0.63$; only points for $\phi < \phi_m$ were fitted, as this was found to give the best agreement with Wyart and Cates theory (§5.2).

regime to a high-viscosity regime which, unlike in PMMA, exhibits slight shear thinning at the lowest ϕ studied, Fig. 5.5(a). The viscosity starts to increase weakly above a critical stress $\sigma_1^* \sim 1$ Pa, then thickens more readily above a second stress, $\sigma_2^* = 5$ Pa, both of which are roughly independent of ϕ. Edge fracture occurs above $\sigma^\dagger \approx 600$ Pa.

We tentatively identify a low-viscosity Newtonian regime below σ_1^*, whose viscosity $\eta_1(\phi)$ we estimate by extrapolating the data at small σ. Similarly, we can read off a high-σ viscosity, $\eta_2(\phi)$, which we take to be the maximum value of $\eta(\sigma)$ for $\phi = 0.37$ and 0.39. Plotting $\eta_1(\phi)$ (open red squares) and $\eta_2(\phi)$ (filled blue squares) versus ϕ, Fig. 5.5(b), reveals divergences at $\phi_{\rm RCP} = 0.51$ and $\phi_m = 0.41$, respectively. Like PMMA, unsteady flow is observed at $\sigma > \sigma_2^*$ for $\phi_m \lesssim \phi < \phi_{\rm RCP}$, although the precise nature of the flow is qualitatively different.

Suspensions of Spheriglass in glycerol and water [82], Fig. 5.6, and zeolite in glycerol and water, Fig. 5.7, show a similar phenomenology.

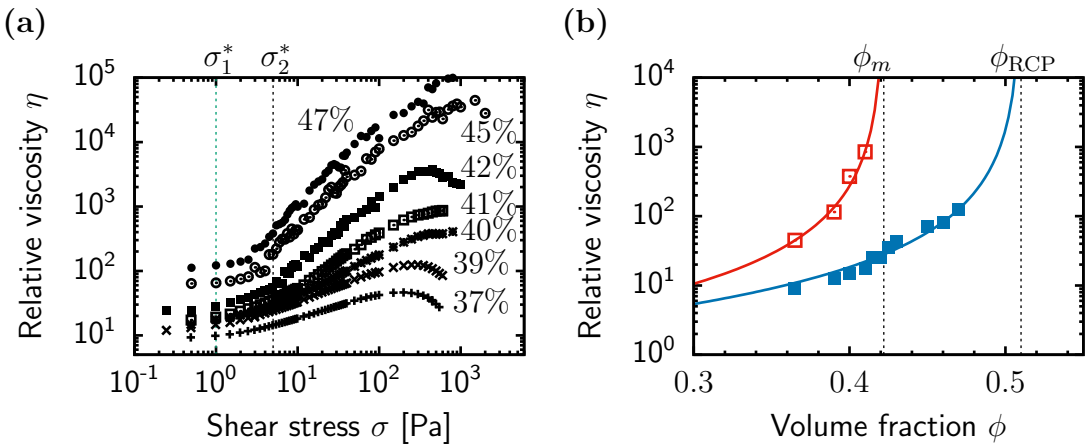

Figure 5.5: Rheology of cornstarch suspensions with $d \approx 14$ μm. (a) Flow curves $\eta(\sigma)$ at different volume fractions ϕ, as labelled. Gentle shear thickening begins above $\sigma_1^* \approx 1$ Pa, followed by a second, more marked change in viscosity above $\sigma_2^* \approx 5$ Pa. For $\phi \geq 0.42$, unsteady flow is observed above σ_2^*. Flow curves were measured using a TA AR2000 rheometer with a 40 mm steel cross-hatched plate at a gap height of 1 mm. We present upward stress sweeps with a waiting time of 8 s per point; symbols represent a temporal average of η over the last 2 s at each imposed σ. (b) Symbols, relative viscosity η versus volume fraction ϕ for the limiting low-viscosity (open red squares), η_1, and high-viscosity (filled blue squares), η_2, from (a). Solid lines, fits by eye of Eq. (5.13) to η_1 (blue) and η_2 (red) with ($A_1 = 1$, $\phi_{\mathrm{RCP}} = 0.50$,$n_1 = 1.9$) and ($A_2 = 1$, $\phi_m = 0.42$,$n_2 = 1.9$).

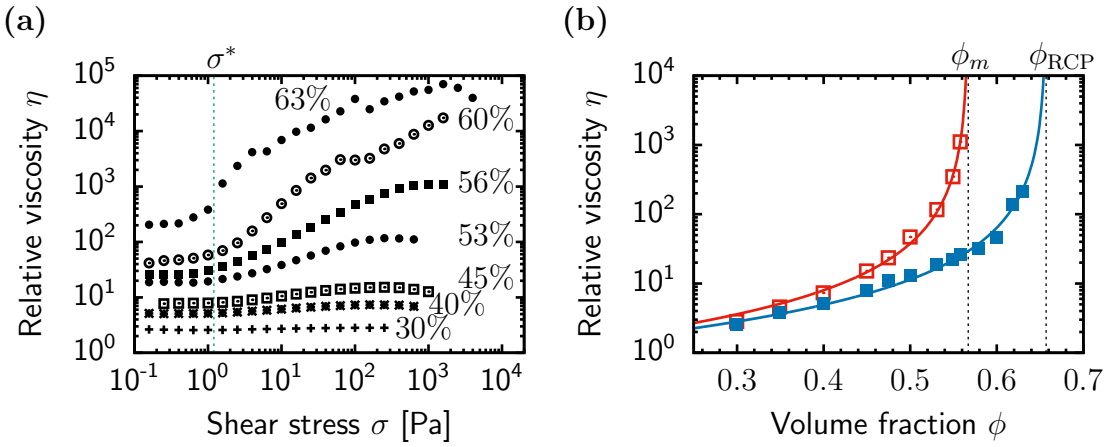

Figure 5.6: Rheology of Spheriglass suspensions with $d \approx 7$ μm (taken from [82]). (a) Flow curves $\eta(\sigma)$ at different ϕ, as labelled. The onset stress for shear thickening is $\sigma^* \approx 1$ Pa. (b) Symbols, limiting viscosities η_1 (filled blue squares) and η_2 (open red squares). Solid lines, fits of Eq. (5.13) to η_1 (blue) and η_2 (red) with ($A_1 = 1$, $\phi_{\mathrm{RCP}} = 0.66$, $n_1 = 1.7$) and ($A_2 = 1$, $\phi_m = 0.56$, $n_2 = 1.7$).

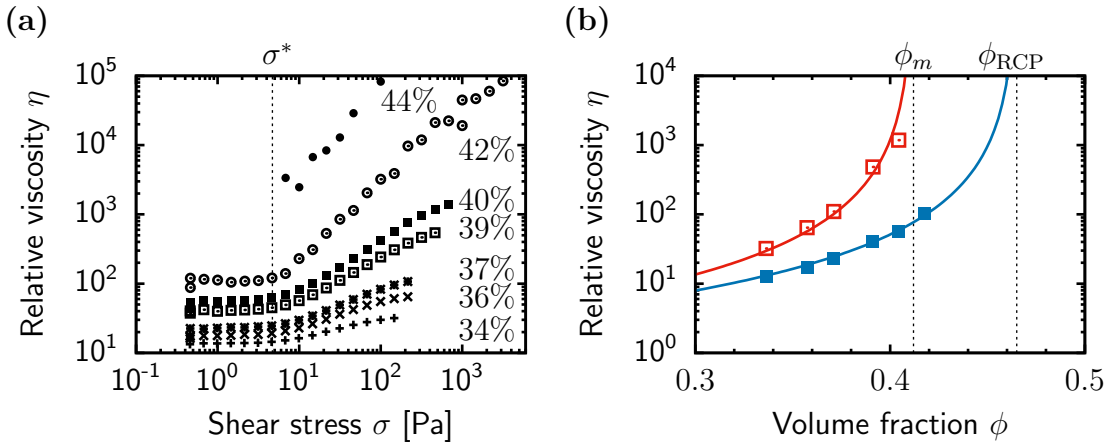

Figure 5.7: Rheology of zeolite suspensions with $d \approx 5$ μm. (a) Flow curves $\eta(\sigma)$ at different ϕ, as labelled. At $\phi < 0.40$, shear thickening occurs above an onset stress $\sigma^* \approx 5$ Pa. At $\phi = 0.42$, the flow becomes unsteady above σ, while the $\phi = 0.44$ sample has a yield stress $\sigma_Y \approx 10$ Pa and undergoes unsteady flow for $\sigma > \sigma_Y$. All flow curves were measured with upward stress sweeps with a waiting time of 15 s per point; points represent a temporal average of η over the last 5 s at each imposed σ. (b) Symbols, limiting low- and high-shear viscosities η_1 (filled blue squares) and η_2 (open red squares). Solid lines, fits of Eq. (5.13) to η_1 (blue) and η_2 (red) with ($A_1 = 1$, $\phi_{\mathrm{RCP}} = 0.465$, $n_1 = 2$) and ($A_2 = 1$, $\phi_m = 0.412$, $n_2 = 2$).

5.2 Wyart and Cates theory

For each of the four systems reported on, one can identify two viscosity branches diverging at different concentrations, ϕ_{RCP} and $\phi_m < \phi_{\mathrm{RCP}}$, and a ϕ-independent onset stress σ^* that controls a transition between them. One can also identify a fracture stress $\sigma^\dagger$ that is ϕ-dependent for some of the systems. We note that the values of σ^*, $\sigma^\dagger$, ϕ_m and ϕ_{RCP} are system dependent, and we explore this dependence in later chapters. Importantly, each system undergoes unstable flow in the ϕ-window between the viscosity divergences.

Given the ubiquity of the shear thickening phenomenology, it is natural to ask whether there is a microscopic theory that can account for our observations. To this end, we explored different theories of shear thickening. At present, there are two competing schools of thought: (a) that thickening is driven by hydrodynamic forces [83]; and (b), that it is caused by the formation of frictional contacts [1]. Currently, the only theory that provides testable predictions over the full range of ϕ and σ that we probe is for frictional shear thickening, so – upholding our primary role as experimentalists – we tested it. In the following section we describe how this was done and discuss its implications for the physical interpretation of the viscosity divergences in Fig. 5.4.

5.2.1 Qualitative description

It is now widely accepted that the finite surface roughness of real particles allows them to enter direct contact when immersed in a fluid [84]. This contrasts the traditional thinking, developed under the assumption that particles were perfectly smooth with no-slip boundary conditions, that such contacts would be prevented by a singularity in the lubrication force [25]. Building on this insight, Wyart and Cates (WC) have constructed a phenomenological theory for contact-driven shear thickening in non-Brownian suspensions [1]. WC argue that in all stable suspensions there is a finite-range repulsion between particles that keeps their surfaces apart: in sterically-stabilised systems this is due to the polymer brush; in charge-stabilised suspensions, it is Coulomb repulsion. This repulsion sets a stress scale p^*, such that when $p \ll p^*$, there is a lubrication film between particle surfaces and particles can slide past each other. For non-Brownian hard spheres, this means that the suspension undergoes Newtonian flow with a viscosity

that diverges at random close packing, $\phi_{\mathrm{RCP}} \approx 0.64$, the maximum amorphous packing fraction for an assembly of frictionless spheres (blue line in Fig. 5.8). However, when $p \gg p^*$, the lubrication films rupture and particles are pressed into contact. If the contact interactions include static friction, then the system undergoes quasi-Newtonian flow with a viscosity that diverges at a lower volume fraction $\phi_m < \phi_{\mathrm{RCP}}$, whose value depends on the static friction coefficient μ_S (red line in Fig. 5.8). Shear thickening is caused by a transition between these two regimes with increasing p.

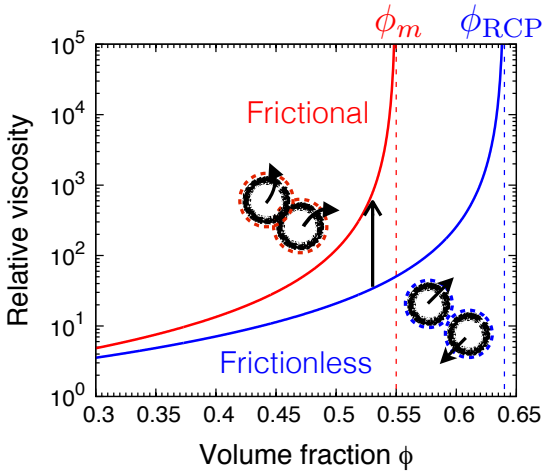

Figure 5.8: Schematic of the viscosity branches present in WC theory. Below a critical stress, σ^*, particles can slide past each other and the system undergoes Newtonian flow with a viscosity that divergences at random close packing ϕ_{RCP}. At $p \gg p^*$, particles are pressed into frictional contact, resulting in a viscosity that diverges at a lower concentration, $\phi_m < \phi_{\mathrm{RCP}}$.

Mathematical description

Mathematically, Wyart and Cates describe the rheology with a jamming volume fraction, $\phi_J(p)$, that depends on the particle pressure p (recall, §3.2, that this is equal to the total mechanical pressure minus the solvent pressure p_f; here, we use the symbol p to refer to the particle part for notational ease). This $\phi_J(p)$ intrapolates smoothly between ϕ_{RCP} and ϕ_m with increasing p,

$$\phi_J(p) = \phi_m f(p) + \phi_{\mathrm{RCP}}[1 - f(p)], \tag{5.1}$$

where $f(p)$ is the fraction of lubrication films in the system that have ruptured

to form frictional contacts. We take a stretched-exponential form for $f(p)$,

$$f(p) = \exp[-(p^*/p)^\beta]. \tag{5.2}$$

The precise form of $f(p)$ is inessential to the basic argument, but we can give a rationalisation of using Eq. (5.2) later based on what is known for dry granular materials. We plot $f(p)$ and $\phi_J(p)$ in Fig. 5.9(b) for $\beta = 1$, $\phi_{\rm RCP} = 0.64$ and $\phi_m = 0.56$.

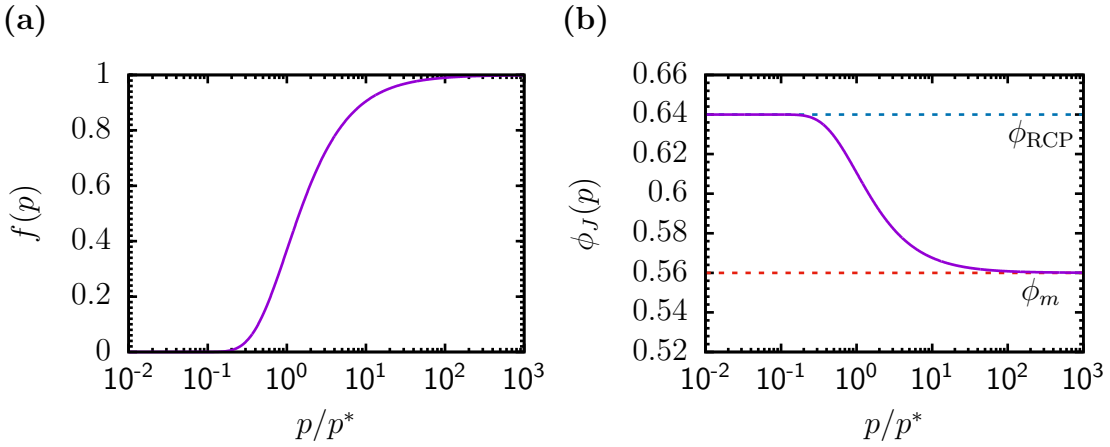

Figure 5.9: (a) Fraction of frictional contacts $f(p)$, Eq. (5.2), versus reduced stress p/p^* with $\beta = 1$. (b) Stress-dependent jamming volume fraction $\phi_J(p)$, Eq. (5.1), versus p/p^* computed using $f(p)$ in (a) and taking $\phi_{\rm RCP} = 0.64$ and $\phi_m = 0.56$.

WC generate flow curves by assuming that the bulk viscosity $p/\dot{\gamma}$ diverges algebraically at $\phi_J(p)$,

$$p(\dot{\gamma}, \phi) = A\eta_f\dot{\gamma}\left(1 - \frac{\phi}{\phi_J(p)}\right)^{-\alpha}. \tag{5.3}$$

The exponent α is assumed to be the same for both frictionless ($\phi_J = \phi_{\rm RCP}$) and fully-developed frictional flow ($\phi_J = \phi_m$) and A is a dimensionless constant. Previous experiments and simulations have reported exponents in the range $1.6 \lesssim \alpha \lesssim 2.4$ for both frictionless [35, 51, 86] and frictional flow [54, 87, 88]; thus, following WC, we take $\alpha = 2$ as a representative value.

In Fig. 5.10 we plot flow curves for the dimensionless pressure $p(\dot{\gamma}, \phi)/p^*$ versus the dimensionless shear rate $\dot{\gamma}\eta_f/p^*$ at different ϕ. Somewhat below ϕ_m, the viscosity shear thickens continuously from a low-stress to a high-stress quasi-Newtonian regime ($\phi = 0.45$). As ϕ is increased, the gradient of $p(\dot{\gamma})$ the slope

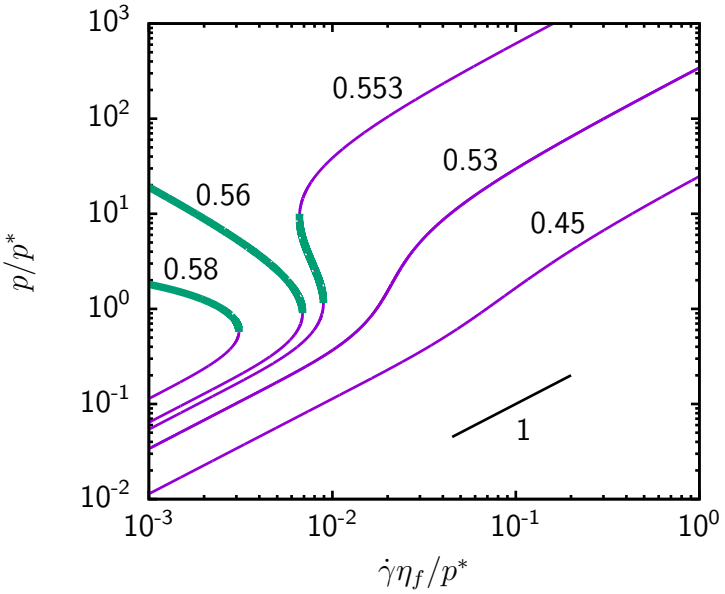

Figure 5.10: Flow curves $p(\dot{\gamma}, \phi)$ at different ϕ (as labelled) generated using Eq. (5.1-5.3) with $\beta = 1$, $\phi_{\rm RCP} = 0.64$, $\phi_m = 0.56$ and $A = 1$. Stresses p are reported in units of p^* and shear rates $\dot{\gamma}$ in units of p^*/η_f. Thick green lines indicate regions of $p(\dot{\gamma})$ with negative slope, $dp/d\dot{\gamma} < 0$, for which simple shear flow is mechanically unstable [85]. Volume fraction regimes: $\phi < \phi_C = 0.546$, continuous shear thickening; $\phi_c < \phi < \phi_m$, discontinuous shear thickening between flowing states; and $\phi \geq \phi_m$, shear-induced jamming.

$dp/d\dot{\gamma}$ increases ($\phi = 0.53$) until, at $\phi_C = 0.546$, $p(\dot{\gamma})$ becomes vertical. At $\phi_C < \phi < \phi_m$, $p(\dot{\gamma})$ has a sigmoidal shape and shear thickens between flowing low- and high-viscosity quasi-Newtonian states ($\phi = 0.553$). The flow curve has a region of negative slope (green line) for which steady homogeneous flow is mechanically unstable [85] [2]. At $\phi \gtrsim \phi_m$, the high-viscosity branch intersects the vertical axis and there is no longer a flowing state at large p.

For $\phi < \phi_C$, the theory predicts continuous thickening at $p > p^*$. For $\phi_C < \phi < \phi_m$, the theory predicts DST between flowing branches in a $\dot{\gamma}$-controlled experiment [89]. It makes no predictions for flow under imposed σ where $dp/d\dot{\gamma} < 0$, although it has been suggested that the system could separate into flowing shear bands [90, 91]. The width of the sigmoidal regime decreases with β [Eq. (5.2), i.e., the crossover from frictionless to frictional contacts becomes more gradual] and it disappears altogether for $\beta \leq 0.5$. Finally, at $\phi \gtrsim \phi_m$ the theory predicts DST from a flowing to a jammed state, which cannot flow without fracture or wall slip.

[2] This is analogous to the requirement for mechanical stability in equilibrium thermodynamics, $dV/dP < 0$, i.e., the bulk modulus must be positive.

5.2.2 Flow curve fitting

The particle pressure, or any of the individual particle normal stresses σ_{ii}, are inconvenient to measure at fixed ϕ. Measuring the thrust on the plates in a torsional geometry yields normal stress differences, rather than individual stress components, due to the curvilinear streamlines (see chapter 1 in [29]). Stress-dependent dyes [92] may eventually provide access to local contact stresses, but are still in development [93]. Rheology measurements with porous pressure sensors mounted flush to the plates purportedly measure individual σ_{ii}, but are only practical for granular particles with $d \sim 100$ μm. Thus, testing WC theory directly is beyond current experimental capabilities.

However, each of the normal stresses, σ_{11} (flow direction), σ_{22} (gradient) and σ_{33} (vorticity), is related to the shear stress $\sigma \equiv \sigma_{12}$ by a *stress ratio* μ_i:

$$\mu_i = \sigma/\sigma_{ii}, \tag{5.4}$$

where the subscript labels the direction of the normal stress (no summation implied). These μ_i will depend on p and ϕ in general, but, if known, would allow us to relate the $p(\dot{\gamma})$ to the experimentally-measurable $\sigma(\dot{\gamma})$ through the stress ratio for the pressure

$$\mu = \frac{\sigma}{p}. \tag{5.5}$$

Currently, there are no published predictions of $\mu_i(p, \phi)$ for shear thickening systems. To make progress, we assume for now that $\mu(p, \phi)$ has the simplest possible form, i.e., a constant. The relative shear viscosity $\eta = (\sigma/\dot{\gamma})/\eta_f$ is then given by

$$\eta = \mu A \left(1 - \frac{\phi}{\phi_J(\sigma)}\right)^{-2}, \tag{5.6}$$

where $\phi_J(\sigma) = \phi_m f(\sigma) + (1 - f(\sigma))\phi_{\mathrm{RCP}}$ and $f(\sigma) = \exp[-(\hat{\sigma}^*/\sigma)^\beta]$.

We fit Eq. (5.6) to the PMMA data, Fig. 5.3, in the following way. We first fit

$\eta_1(\phi)$ and $\eta_2(\phi)$ (Fig. 5.4) by eye to the power law

$$\eta(\phi) = \left(1 - \frac{\phi}{\phi_{\max}}\right)^{-2}, \tag{5.7}$$

and find $\phi_{\max} = \phi_{\rm RCP} = 0.63$ for η_1 and $\phi_{\max} = \phi_m = 0.555$ for η_2. Using these values for $\phi_{\rm RCP}$ and ϕ_m, and taking $A = \mu^{-1}$, we fit Eq. (5.6) to the (η,σ) curves in Fig. 5.3 by varying the stretch exponent β and onset stress $\hat{\sigma}^*$. The values $\beta = 0.85$ and $\hat{\sigma}^* = 8.5$ Pa were found to simultaneously fit the curves at $\phi = 0.41, 0.47, 0.51$ and 0.54; the lines of best fit (obtained by eye) are shown in Fig. 5.3. The difference between the experimentally-measured and theoretical onset stresses is due to a difference in definition. The experimental σ^* is taken as the stress at which the slope of the (η, σ) curve becomes > 1 on a log-log plot, while $\hat{\sigma}^*$ is the stress where $1/e \approx 0.37$ of the contacts are frictional.

Below ϕ_m, where samples continuously thicken, WC theory fits very well: there is quantitative agreement with the data over five orders of magnitude in σ and three orders of magnitude in η. The fits begin to deviate for $\phi > \phi_m$ (not shown), as the low-shear viscosity η_1 is no longer described by Eq. (5.7), although we do observe unsteady flow above σ^* in this regime, which is consistent with the theory. Our values for β and ϕ_m imply sigmoidal flow curves for $\phi_C = 0.548 < \phi < 0.555$, but we do not have data in this range.

5.3 Discussion

The quantitative agreement with WC theory is strong evidence that, in PMMA, thickening is caused by a transition from lubricated (frictionless) to frictional interactions. The flow curves for the three other systems – cornstarch (Fig. 5.5), Spheriglass (Fig. 5.6) [82] and zeolite (Fig. 5.7) – can also be fit by WC theory, albeit with different values of $\phi_{\rm RCP}$, ϕ_m, β and $\hat{\sigma}^*$. In Ch. 8 we explore the origin of thickening in greater depth, but for now take this as evidence that the frictional framework is generic for intermediate-sized particles.

While WC theory is completely phenomenological, the functional forms we chose for μ and f have interesting implications for the microscopic physics. We now show that some of our assumptions appear to be unphysical and mean that the close agreement between theory and experiment should be interpreted with

caution.

5.3.1 Crossover function $f(\sigma)$

We begin by discussing the crossover function $f(\sigma)$, the fraction of contacts in the system with $\sigma > \sigma^*$. The shape of $\sigma(\dot{\gamma})$ is sensitive to the choice of $f(\sigma)$ and we find we cannot simply fit our data with an arbitrary function that increases smoothly from 0 to 1. Our choice of a stretched exponential, Eq. (5.2), is motivated by simulations by Mari *et. al* [56], who also find a stretched exponential but with a larger exponent, $\beta \approx 1.1$. Like us, they find that $f(\sigma)$ is independent of ϕ for $0.40 \lesssim \phi \lesssim 0.55$.

This $f(\sigma)$ can be computed if the probability distribution $\mathrm{P}(\lambda, \sigma)$ of contact stresses λ for an applied mean stress σ is known. Then, $f(\sigma)$ is the integral of $\mathrm{P}(\lambda, \sigma)$ from σ^* to ∞,

$$f(\sigma, \sigma^*) = \frac{\int_{\sigma^*}^{\infty} \mathrm{P}(\lambda, \sigma) d\lambda}{\int_0^{\infty} \mathrm{P}(\lambda, \sigma) d\lambda}. \tag{5.8}$$

Experiments [94] and simulations [95] on dry granular media found that P follows an exponential distribution for large λ,

$$P(\lambda, \sigma) \propto \exp(-\lambda/\sigma),$$

which leads to $f(\sigma, \sigma^*) = \exp(-\sigma^*/\sigma)$. We have no microscopic explanation for why $f(\lambda, \sigma)$ has a stretched exponential form (this implies that P follows a Weibull distribution); although, it is possible that in our case it arises due to size polydispersity. Since $\sigma^* \propto d^{-2}$ (as we will show in Ch. 6), size polydispersity would give rise to a distribution of onset stresses, so that an exponential force distribution for monodisperse particles would turn into a stretched exponential.

5.3.2 Stress ratio μ

While our choice of $f(\sigma)$ can be rationalised with measurements on granular media, we have no reason to suppose that $\mu(p, \phi)$ is constant. The only direct measurements are for μ_{22}, for which this is not the case. Imposed-pressure

rheology on frictional non-Brownian spheres [54] and 2D simulations of circular discs [96] found $\mu_{22}(\phi)$ to be a monotonically decreasing function of ϕ, tending to a non-zero value μ_c at the jamming volume fraction ϕ_m, which itself is a function of the particle friction coefficient μ_S. Data for different μ_S, including $\mu_S = 0$, collapse onto the same master curve in the 2D simulations; since shear thickening is tantamount to varying μ_S at fixed ϕ in WC theory (see §7.4.2), this implies that μ is a function of ϕ only – that is, there is no dependence on σ. We sketch a likely form for $\mu_{22}(\phi)$ in Fig. 5.11(a).

Measurements of N_1 and N_2 in shear-thickening [97] and granular [98, 99] systems imply that μ_{11} and μ_{33} have similar functional forms to μ_{22}, so we infer that $\mu = \sigma/p$ also depends only on ϕ. If we take the form for $\mu(\phi)$ in Fig. 5.11(a), then the $\eta(\sigma)$ curves predicted by Eq. (5.3) have an onset *shear* stress σ^* that *decreases* with ϕ, Fig. 5.11(b). This is because, in WC theory, the onset *pressure* is independent of ϕ. Thus, using a physical form of $\mu(\phi)$ predicts flow curves that contradict all of our experimental data.

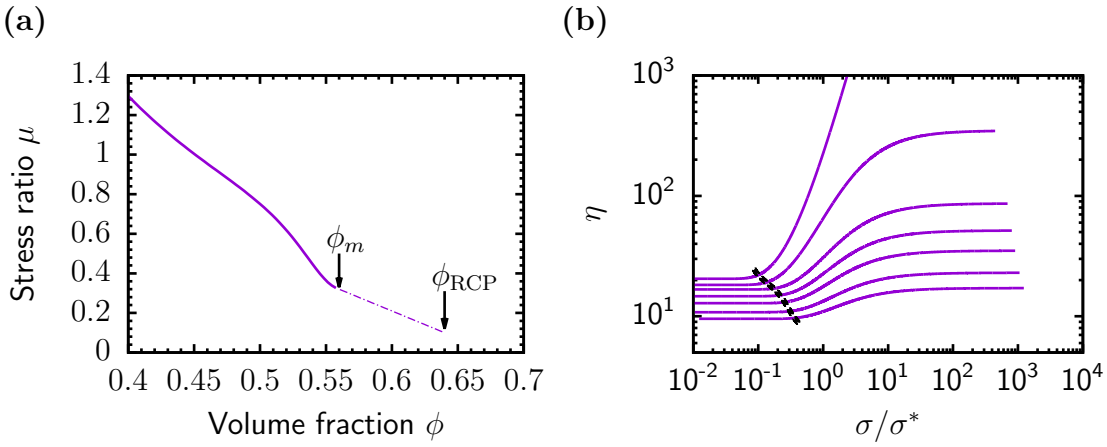

Figure 5.11: (a) Schematic of the stress ratio for the particle pressure $\mu = \sigma/p$ versus ϕ, based on [54, 96]. (b) Relative shear viscosity $\eta = (\sigma/\dot{\gamma})/\eta_f$ versus reduced shear stress generating assuming a ϕ-independent p^*.

Stress tensor at the onset of shear thickening

This discrepancy arises because the macroscopic particle pressure p is not straightforwardly related to the local pressure experienced by contacts, $p_{\mathrm{loc}} = f^c/d^2$. Wyart and Cates tacitly assume that p and p_{loc} are equivalent. To understand why this is not the case, we turn to molecular dynamics simulations of shear-thickening spheres by Seto *et. al.* [2, 56] and others [100]. In these

simulations, particles have a static friction coefficient μ_S that is zero until the normal load exceeds a fixed threshold f^*, whereupon μ_S assumes a positive value. The force f^* is regarded as an intrinsic property of the particle surface and is assumed to be independent of ϕ, but could be a function of d in real systems [101]. This assumption is reasonable for sterically-stabilised colloids, but may not be valid for charge-stabilised colloids where the surface charge is usually a function of ϕ [102].

Recall that, in the limit of pairwise interactions, the stress tensor σ_{ij} is given by:

$$\sigma_{ij} = \frac{1}{V} \sum_c f_i^c b_j^c,$$

where the sum is over interacting particle pairs c in the volume V, and f_i^c and b_i^c are the i-th components of the force between two particles $\underline{f}$ and the branch vector $\underline{b}$ (the vector connecting their centres), respectively. We can write the sum in terms of the volume average of the summand, $\langle f_i^c b_j^c \rangle_V$, to give

$$\sigma_{ij} = \frac{1}{V} N_c \langle f_i^c b_j^c \rangle_V \sim \frac{Z_c \phi}{d^3} \langle f_i^c b_j^c \rangle_V, \tag{5.9}$$

where N_c is the number of interacting particle pairs contained in V; we assume that interactions are short-ranged, so this N_c includes particles that are either in direct mechanical contact or whose surfaces are close together than the characteristic range of the interaction potential, e.g., the Debye length in charged systems. For the final term we have written N_c as a product of the number of particles in V, $V\phi/(\pi d^3/6)$, and the number of interacting neighbours per particle $Z_c/2$, where Z_c is the coordination number. This Z_c depends on ϕ, and $Z_c \sim \phi$ near ϕ_{RCP} [103].

Let us consider the shear stress σ_{12}. Just below the onset of shear thickening, $\mu_S = 0$ and $\underline{f}$ acts normal to the particle surfaces only. We can then write $f_1 = f \cos\theta_c$ and $b_2 = b \sin\theta_c$, where θ_c is the angle made by the line of centres relative to the flow (1) direction, Fig. 5.12 (f and b are the moduli of $\underline{f}$ and $\underline{b}$, respectively). The average in Eq. (5.9) can therefore be written $\langle f b \sin\theta_c \cos\theta_c \rangle_V$. We cannot evaluate this average as θ_c and f are correlated – contacts preferentially form along the compression axis [56]; however, we expect the interaction forces to scale as f^* and for a short-ranged interaction potential $b \approx d$, so the onset

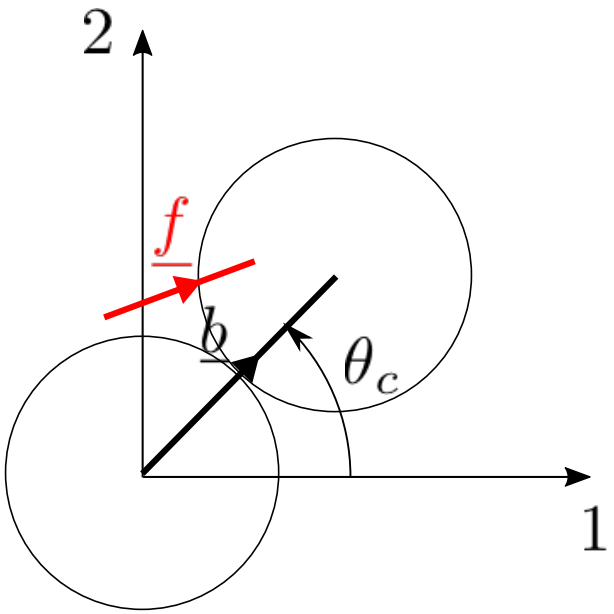

Figure 5.12: Schematic of two particles interacting in a shear field where 1 is the flow direction and 2 is the gradient direction. The branch vector $\underline{b}$ connecting the particle centres makes an angle θ_c with the flow direction. The vector $\underline{f}$ denotes the force exerted on the upper particle by the lower particle and is colinear with $\underline{b}$ when $\mu_S = 0$.

shear stress is given by

$$\sigma^*_{12} \sim \frac{f^*}{d^2}\phi Z_c(\phi) F_{12}(\phi). \tag{5.10}$$

where $F_{12}(\phi)$ is a dimensionless function.

Using the same argument, one can construct similar expressions for the other components of the stress tensor at the onset of thickening,

$$\sigma^*_{ij} = \frac{f^*}{d^2}\phi Z_c(\phi) F_{ij}(\phi), \tag{5.11}$$

so that the onset pressure p^* can be written:

$$p^* = \frac{f^*}{d^2}\phi Z_c(\phi)[F_{11}(\phi) + F_{22}(\phi) + F_{33}(\phi)] = \frac{f^*}{d^2}\phi Z_c(\phi) F(\phi). \tag{5.12}$$

Both p^* and σ^* are proportional to f^*/d^2, but also depend on the dimensionless function $F(\phi)$, which contains information about the average angle between contacts. This average angle varies with ϕ in non-Brownian suspensions [99],

so one expects $F(\phi)$ to depend on ϕ in general – Eq. (5.12) shows clearly that fixed f^* (and hence fixed $p^*_{\rm loc} = f^*/d^2$) does *not* imply fixed p^*.

Indeed, simulations by Ness and Sun [78] find that σ^*_{12} and p^* both depend on ϕ. This dependence is very weak, however, as σ_{12} decreases by less than a factor of two over the range $0.40 \lesssim \phi \lesssim 0.55$. Such a change would be difficult to discern in typical experimental data, and this is one reason why σ^* may appear to be fixed in practice. For p^* to be truly independent of ϕ would require $F(\phi) \sim [\phi Z_c(\phi)]^{-1} \sim \phi^{-2}$, or, if f^* was ϕ dependent, a fortuitous cancelation of $f^*(\phi)$ and $\phi Z_c(\phi) F(\phi)$. Thus, except in special circumstances, p^* and σ^* will both depend on ϕ.

Ness and Sun also measured μ in the unthickened state and found that it decreased linearly with ϕ, so that p and σ are essentially proportional to one another over the narrow ϕ window in which thickening is observed. Since we cannot measure p, we do not know if this is the case in experiments. The form of $\mu(\phi)$ in Fig. 5.11(a) implies that p^* increases strongly with ϕ.

Stress-dependence of μ

We conclude this section by briefly discussing the stress dependence of $\mu(\phi, p)$. Above f^*, particles experience tangential as well as normal forces and the stress contains a part $\propto \mu_S$. Simulations [100] have shown that the viscosity increase is due mainly to the contribution from normal particle forces, however, so we assume that the direct tangential contribution to p is negligible in the shear-thickened state. Mari *et. al.* [56] showed that the angular distribution function [related to $F(\phi)$ in Eq. (5.12)] becomes more isotropic, so we expect both F_{12} and F, and therefore $\mu = F_{12}/F$, to depend on σ. Preliminary results from Ness and Sun [78] indicate that μ decreases by a factor of two.

Preliminary work has found that the primary effect of σ dependence is to make the frictional plateau stress in $\eta(\sigma)$ vary with ϕ. This is one possible explanation for why for zeolite η reaches the upper branch at lower σ for lower ϕ Fig. 5.7(a). The fact that this stress is independent of ϕ for PMMA implies $\mu = \mu(\phi)$, which in turn implies that the microstructure does not change much during thickening.

5.3.3 Viscosity divergences

Estimating the static friction coefficient

In the last section, we saw that the $f(\sigma)$ and $\mu(\phi, \sigma)$ used to fit the flow curves allow us to make inferences about the microstructure and distribution of contact forces in the suspension during shear thickening. By the same token, experiments on polymer-coated glass beads [104] and simulations [55, 56] have shown that the value of the frictional jamming volume fraction ϕ_m is related to the static friction coefficient μ_S. Simulations by Silbert [55] found that, for monodisperse spheres, ϕ_m decreases from 0.64 at $\mu_S = 0$ to ≈ 0.56 at $\mu_S = \infty$ [55, 56]. We plot their data in Fig. 5.13 (inset). Since the frictionless jamming volume fraction $\phi_{\mathrm{RCP}} = 0.64$ is insensitive to μ_S, the ratio $\Lambda = \phi_m/\phi_{\mathrm{RCP}}$ is a measure of μ_S.

In polydisperse systems, $\eta_1(\phi)$ is controlled by the distance to jamming, $(\phi_{\mathrm{RCP}} - \phi)/\phi_{\mathrm{RCP}} = 1 - \phi/\phi_{\mathrm{RCP}}$, so that the viscosity for hard spheres with different polydispersities depends only on the reduced variable ϕ/ϕ_{RCP} [35]. This has been demonstrated experimentally by collapsing data for $\eta_1(\phi)$ from different systems onto a master curve by a small multiplicative shift in ϕ [49]. Similarly, frictional jamming is controlled by the distance to ϕ_m for a particular μ_S [54]; thus, it is reasonable to assume that the same shift in ϕ will simultaneously collapse η_1 and η_2. If this is true, then $\Lambda = \Lambda(\mu_S)$ can be used to measure μ_S in polydisperse systems. In the following section, we measure ϕ_m and ϕ_{RCP} for each of the systems and use this to estimate μ_S in each case.

We first fit the viscosity branches in Fig. 5.4, 5.5(b), 5.6(b) and 5.7(b) to a power law,

$$\eta_i(\phi) = A_i \left(1 - \frac{\phi}{\phi_{\max}}\right)^{-n_i}, \tag{5.13}$$

to obtain ϕ_m and ϕ_{RCP}. The best-fit parameters obtained by eye $(A_1, \phi_{\mathrm{RCP}}, n_1)$ and (A_2, ϕ_m, n_2) are reported in the figure captions. In Fig. 5.13, we plot η_1 and η_2 versus ϕ/ϕ_{RCP} for PMMA, zeolite, Spheriglass and zeolite using the ϕ_{RCP} so obtained. Vertical lines denote different Λ and are labelled with the corresponding friction coefficient taken from [55] (Fig. 3.8 and Fig. 5.13, inset).

The frictionless viscosities η_1 do not collapse onto a single curve. This is expected,

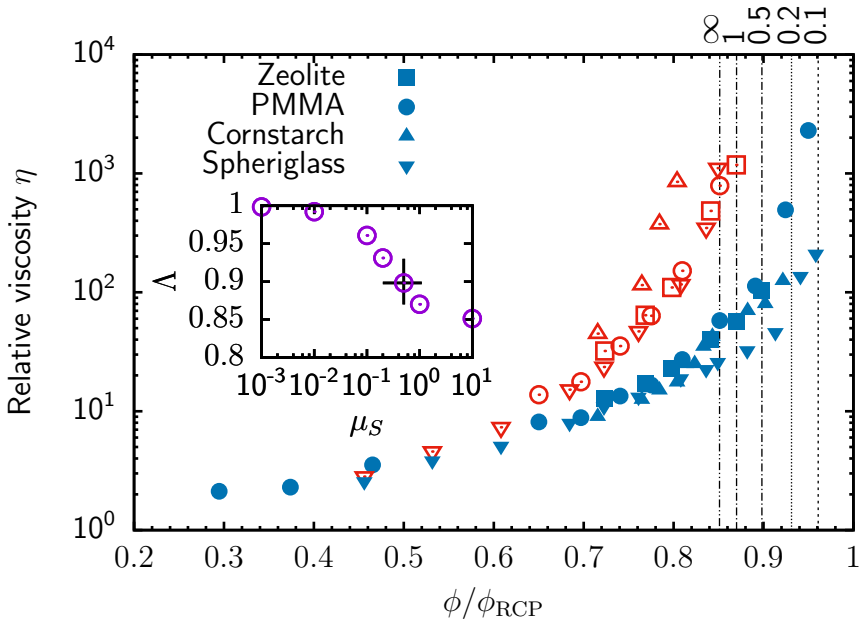

Figure 5.13: Viscosity divergences scaled by ϕ_{RCP}. Main, η_1 and η_2 versus ϕ/ϕ_{RCP}. Vertical lines denote values of μ_S (as labelled) for different Λ from [55], apart from $\mu = \infty$, which is from [56]. Inset, μ_S as a function of Λ from [55].

as η_1 is known to be sensitive to deviations from hard sphere behaviour [35] due to, for example, finite permeability of the polymer layer [49] (causing η_1 to be systematically higher for sterically-stabilised colloids) or weak residual attractions [35]. (If one considers particles of the same type, for example, PMMA, then the η_1 can indeed be collapsed onto a single curve, Ch. 6.) Nevertheless, one can read off $\mu_S \sim 1$ for PMMA, Spheriglass and zeolite and $\mu_S = \infty$ for cornstarch.

The main source of error in μ_S comes from locating ϕ_{RCP} accurately. The paucity of data for η_1 close to ϕ_{RCP} means that we have to fit a power law when the highest ϕ are far away from jamming (at best $1-\phi/\phi_{\mathrm{RCP}} \approx 2\%$, for PMMA, and at worst $\approx 10\%$, for zeolite). Physically, this means that n and ϕ_{RCP} do not necessarily reflect the true asymptotic behaviour of the divergence [103]. Mathematically, it incurs a large fit error in both n and ϕ_{RCP}. To illustrate this point, we consider η_1 for cornstarch in Fig. 5.5(b). Carrying out a least-squares fit allowing all three parameters in Eq. (5.13) to vary results in $\phi_{\mathrm{RCP}} \sim 0.6$ and an anomalously large exponent $n \sim 5$. If we constrain the exponent to the range $1.8 \leq n \leq 2.2$, closer to n reported in the literature [49], then, by eye, $\phi_{\mathrm{RCP}} \approx 0.50$ with an error of $\pm 3\%$. This leads to a $\pm 3\%$ error in Λ, which in turn corresponds to almost an order of magnitude error in μ_S owing to the steepness of $\Lambda(\mu_S)$ in the vicinity of $\mu_S \sim 1$. The error bars in Fig. 5.13 (inset) show the error in μ_S resulting from a 3% uncertainty in ϕ_{RCP} for $\Lambda = 0.9$, where $d\Lambda/d\mu_S$ is greatest – μ_S ranges from

$0.2 \lesssim \mu \lesssim 1$.

From Fig. 5.13, we estimate that μ_S could plausibly be anywhere in the range 0.5 to ∞ for all of the systems. This is, nevertheless, consistent with macroscopic measurements $\mu_S = 0.8$ for dry PMMA [105], 0.9 for glass [106], and 0.45 for zeolite [107].

The lack of data points close to ϕ_{RCP} is due to difficulties in dispersing samples above ϕ_m. The typical stresses encountered when combining dry powder and a viscous solvent ($\eta_f \gtrsim 10^{-2}$ Pa.s) exceed the onset stress for shear thickening $\sigma^* \sim 1$ Pa, which, for $\phi_m < \phi < \phi_{\mathrm{RCP}}$, results in the sample becoming rigid, inhibiting proper mixing. Higher ϕ can be accessed by dispersing the particles at a lower concentration then centrifuging the sample and diluting the sediment (the protocol used for PMMA); however, the same issue is encountered when trying to properly mix the sample at the highest ϕ, where the sample will readily jam.

Factors affecting the viscosity divergences

Before concluding, we note that it is incorrect to interpret η_1 and η_2 as *the* viscosity branches for a given system and using them as a probe of particle-level details should be done with caution, notwithstanding the difficulties in fitting the divergences described in the previous section. Although we do not demonstrate it explicitly here, ϕ_m and ϕ_{RCP} depend on the protocol used to prepare the samples. Samples of zeolite prepared by gently mixing dry powder and solvent at large ϕ would jam readily when probed with a spatula, but would flow easily after 30 s of sonication. This is because initial mixing of the dry powder and solvent results in irregular aggregates, which cause Λ to be smaller than if the particles were dispersed individually [108]. Sonication breaks up these aggregates, causing ϕ_m to increase and Λ to decrease. Since the overall volume fraction is unchanged, then a sample which was initially above ϕ_m moves below ϕ_m.

Zeolite and cornstarch were prepared at different ϕ by directly mixing solvent and powder, so it is likely that the measured flow curves are for a partially-aggregated system; however, since a consistent sonication protocol was used in each case the results are reproducible.

5.3.4 The generality of frictional shear thickening

The generality of frictional shear thickening

In this chapter, we have demonstrated that the rheology of repulsive particles in the intermediate size regime, $1 \lesssim d \lesssim 50$ μm, is governed by two viscosity "branches" diverging at different concentrations. Suspensions shear thicken from the lower branch, in which particle surfaces are separated by a lubrication film, to the upper branch, where they enter frictional contact, when a ϕ-independent onset stress σ^* is exceeded. Our data are quantitatively fit by the Wyart and Cates theory of shear thickening [1] below the frictional jamming volume fraction, ϕ_m, and exhibit unstable flow above ϕ_m, qualitatively consistent with the theory.

The data presented herein are selectively chosen to reveal the two-branch phenomenology. For some of the PMMA batches we studied in the intermediate regime, the shape of $\eta(\sigma)$ below ϕ_m was significantly different, implying that the form of the crossover function $f(\sigma)$ in Wyart and Cates theory is not generic. In many cases, for example in Fig. 5.14, there were two distinct shear thickening regimes with separate onset stresses and the sample fractured before the limited high σ behaviour could be probed, making it impossible to determine whether a second Newtonian plateau exists. Nevertheless, it is still possible to identify a critical volume fraction, $\phi_m < \phi_{\mathrm{RCP}}$, above which the rheology is unsteady in the shear-thickened state. It is this observation, rather than our ability to fit $\eta(\sigma)$ with WC theory, that lends greatest support to the frictional framework.

We conclude by emphasising that, in the frictional framework, it is the coefficient of *static* friction μ_S, not dynamic friction μ_K, that causes shear thickening. When $\mu_S = 0$, all the particles are free to slide over each other – there are no constraints on the rotational degrees of freedom – and the system becomes rigid when the average number of contacts per particle $Z_c = 6$, which occurs at $\phi_{\mathrm{RCP}} = 0.64$. When $\mu_S > 0$, some of the particles are required to roll over each other – rotational degrees of freedom are constrained – and must follow more tortuous [103] (and possibly collective [87, 100, 103]) paths through the suspending fluid for the suspension to flow. This leads to enhanced dissipation and an increase in η.

In our discussion so far, it is tacitly assumed that $\mu_K = 0$, that is, the frictional contacts which are mobilised do not dissipate any additional energy. This assumption is dubious, particularly for polymer-stabilised colloids in which

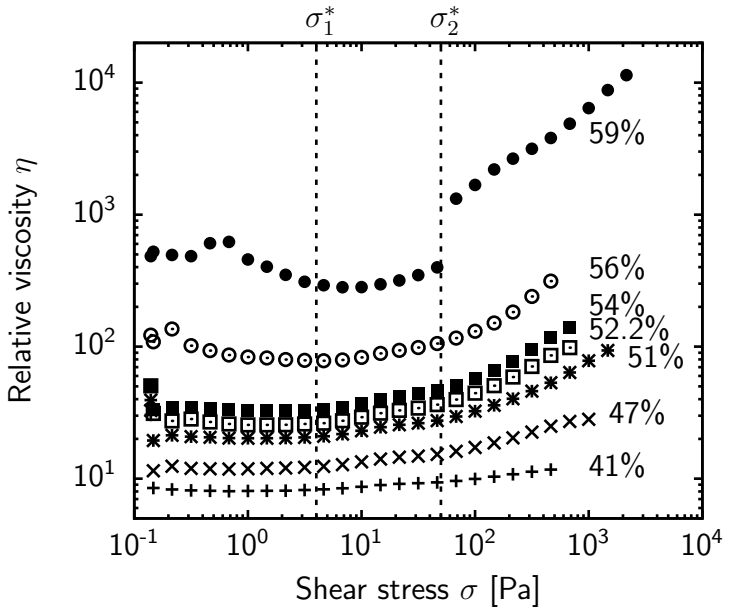

Figure 5.14: Relative viscosity η versus shear stress σ for 3580 nm diameter PMMA spheres at different volume fractions ϕ, as labelled. Flow curves were obtained by upward stress sweeps using a 25 mm sandblasted cone with a waiting time of 30 s per point; symbols denote an average of the viscosity over the last 5 s at each stress. Unlike the $d = 3770$ nm PMMA, there are two onset stresses, $\sigma_1^* = 4$ Pa and $\sigma_2^* \approx 50$ Pa, and the system fractures at a shear stress $\sigma^\dagger \sim 10^3$ Pa before reaching the frictional Newtonian plateau. The system shear jams at σ^* for $\phi_m \geq 0.59$.

thickening can occur purely through enhanced dissipation in sliding brushes [14]. We discuss this issue in Ch. 7 and 8, but note that we do not need to appeal to these ideas to explain any of our observations, and therefore assume that the static friction mechanism is dominant in the intermediate regime.

Chapter 6

Crossover from colloidal to granular rheology

In Ch. 5 we elucidated the important physics in the intermediate size regime, in which there is a stress-dependent transition between lubricated and frictional viscosity branches. In this chapter, we show how the frictional picture can be reconciled with the colloidal and granular size regimes, which are already separately well understood, but whose rheology is qualitatively different. We do so by studying the rheology of model PMMA spheres as the size is systematically increased from the colloidal regime to the cusp of the granular regime. Colloidal particles are found to shear thicken in a manner similar to intermediate-sized particles, but with an onset stress σ^* that scales with the inverse square of the particle size $\sigma \sim d^{-2}$. It is the competition between this size dependence and the scaling of the entropic stress $\sim d^{-3}$ that controls the onset of granular rheology – that is, the point at which the system is in a purely frictional state under typical experimental conditions. We conclude the chapter by proposing expressions, based on Wyart and Cates theory [1], that describe the rheology of hard-particle suspensions over the entire size spectrum.

6.1 Rheology in the colloidal, intermediate and granular regimes

We begin with a short overview of the distinction between colloidal and wet-granular flow of repulsive particles. The rheology of colloidal nearly-hard spheres (HS) is well known [50, 51, 109]: the viscosity is determined by the particle volume fraction ϕ and the dimensionless shear rate, or Peclet number, $\mathrm{Pe} = \tau_B\dot{\gamma}$ (where τ_B is the (Brownian) time needed for a free particle to diffusive its own radius). At $\mathrm{Pe} \ll 1$, flow is Newtonian with a viscosity η_0 that becomes immeasurably large near the glass transition $\phi_g \approx 0.58$ [49, 50]. Shear thinning starts at $\mathrm{Pe} \lesssim 1$, reaching a second Newtonian regime at $\mathrm{Pe} \gg 1$ with a viscosity that diverges at random close packing [35], ϕ_{RCP}, the densest amorphous packing for lubricated (frictionless) spheres. One can equivalently think of Brownian shear thinning as due to a competition between the applied shear stress σ and entropic stress scale, k_BT/d^3; $\mathrm{Pe} \gg 1$ then corresponds to $\sigma/(k_BT/d^3) \gg 1$.

Since τ_B (and k_BT/d^3) scales as d^3, granular HS inhabit the $\mathrm{Pe} \gg 1$ regime at all practical shear rates (stresses). Extrapolating naïvely from the above description of colloidal flow, one expects Newtonian behaviour with a viscosity diverging at ϕ_{RCP}. Careful experiments under imposed particle pressure [54] do find a Newtonian viscosity, but it diverges at a ϕ that is lower than ϕ_{RCP}, the precise value depending on the particle static friction coefficient μ_S. Previous studies of the size dependence of suspension rheology do exist, but are for systems entirely in the colloidal regime [51, 109, 110] or highly polydisperse systems near the granular limit [111].

Recent simulations have predicted that for soft, frictionless particles, e.g., emulsions, there should be a smooth crossover from entropy-dominated to deformation-dominated rheology as d is increased from colloidal to granular [112, 113] . Specifically, the stress on particles of a given size is well modelled by assuming that the two contributions are additive. There are currently no theoretical predictions for the regime transition in hard particles.

6.2 Sample preparation and rheology protocol

We explore the crossover with PHSA-stabilised PMMA spheres dispersed in a density-matching combination of cycloheptyl bromide (CHB) or cyclohexyl bromide (CXB) and decalin. In this chapter, we present data for $d = 404$ nm (from static light scattering) and 3770 nm (from microscopy) spheres both with polydispersity $\sim 10\%$ (from light scattering and electron microscopy, respectively). Data for $d \approx 280$ nm (in decalin), 268, 912, 1800 and 4500 nm (in CXB or CHB and decalin) gave a similar picture and we do not present full flow curves here. The particles were left in the solvent for at least 7 days to allow for swelling, then prepared at different ϕ by diluting a close-packed sediment, using simulations [65] to estimate the sediment packing fraction based on the polydispersity; details of the method have been given in Ch. 4. The data we present are for subsequent dilutions of this sediment. Samples were left on a roller bank for > 12 hours after each dilution so that the samples were visibly well mixed. As in the previous chapter, dispersing dry particles directly at the desired ϕ by using the density of the powder gave similar results below $\phi \approx 0.55$, but led to quantitative differences above. As in Ch. 5, data in this regime should be taken as representative and we postpone further discussion to Ch. 10. We also present data for $d = 45$ μm (from Beckman-Coulter Mastersizer), for which different ϕ were prepared by mixing dry powder and solvent, using a literature value for the particle density, 1.19 g.cm^{-3}. The solvent viscosity is $\eta_f = 2.83 \times 10^{-3}$ Pa.s for the 3770 nm particles and $\eta_f = 2.4 \times 10^{-3}$ Pa.s for the other particles.

Rheology was performed in an Anton Paar 301 rheometer in truncated cone and plate geometry (cone angle 1°, radius 25 mm, truncation gap 100 μm) in stress-controlled mode, unless otherwise stated. Rheology of the 45 μm particles was performed with a TA AR2000 rheometer using a parallel plate geometry (aluminium, radius 20 mm) with surface roughness ~ 20 μm (measured by microscopy). A gap height $H = 675$ μm was used, as it was not possible to form a stable meniscus at the edge of the plates at larger H.

Loading and experimental protocol

For $d = 404$ nm, the viscosity was measured in imposed-$\dot{\gamma}$ mode below $\sigma = 10$ Pa with a waiting time of at least $1/\dot{\gamma}$ per point. Working in imposed-σ mode did not properly capture the shear-thinning regime of $\eta(\dot{\gamma})$, as the gradient of the

flow curve $\sigma(\dot{\gamma})$ is approximately zero. Above 10 Pa, it was measured with an imposed-σ upward sweep with a waiting time of 10 s per point, the same protocol used for the intermediate-sized spheres in Ch. 5.

For $d = 45$ μm, samples were pre-sheared at 30 Pa for 40 s, before imposing $\sigma = 0$ for 30 s to allow the plate to come to rest. We then measured $\eta(\sigma)$ with an upward σ sweep with a waiting time of 20 s per point. This protocol was chosen to eliminate artefacts associated with the finite inertia of the cone.

6.3 Steady-state rheology in the colloidal, intermediate and granular size regimes

We first explore $d = 404$ nm colloids. Fig. 6.1(a) shows the relative viscosity $\eta = (\sigma/\dot{\gamma})/\eta_f$ as a function of shear stress σ, both in Pa and in units of k_BT/d^3, at different ϕ. The region *not* shaded dark grey is the "observable window" accessible by conventional rheometry. The left-hand slanted boundary corresponds to the minimum shear rate of the rheometer, $\dot{\gamma}_{\min} = 10^{-3}$ s^{-1}, below which the noise level in η is comparable to the signal. This limit is presumably set by the resolution of the encoder used to measure angular deflection of the rheometer shaft. The right-hand slanted boundary is due to an inertial instability expelling samples from the instrument at $\dot{\gamma}_{\max} \approx 8 \times 10^3$ s^{-1}. The left-hand vertical boundary at $\sigma_{\min} = 10^{-2}$ Pa is related to the torque resolution of the instrument. Additionally, the light grey region is accessible but typically not probed in previous work on colloidal systems [50, 51]. Lines are fits to the data of the theory in §6.4.

Our data for $\phi = 0.40$ and 0.47 show shear thinning to a Newtonian plateau $\eta_1(\phi)$ in the observable window, which we plot as a function of ϕ in Fig. 6.1(b). The $\phi = 0.53$ sample behaves similarly in this window, but shear thickens shortly after the viscosity reaches $\eta_1(\phi)$. At $\phi = 0.56$ and above the sample shear jams and flow becomes erratic; the time-averaged flow curves shows discontinuous shear thickening, characterised by a vertical flow curve, $d\dot{\gamma}/d\sigma$, with gradient $d\log\eta/d\log\sigma \approx 1$. Within experimental uncertainty, shear thickening begins at a ϕ-independent onset stress $\sigma^* \approx 200$ Pa. At a higher ϕ-independent stress $\sigma^\dagger \approx 5000$ Pa, samples fracture – this defines the high-σ boundary of the observable window.

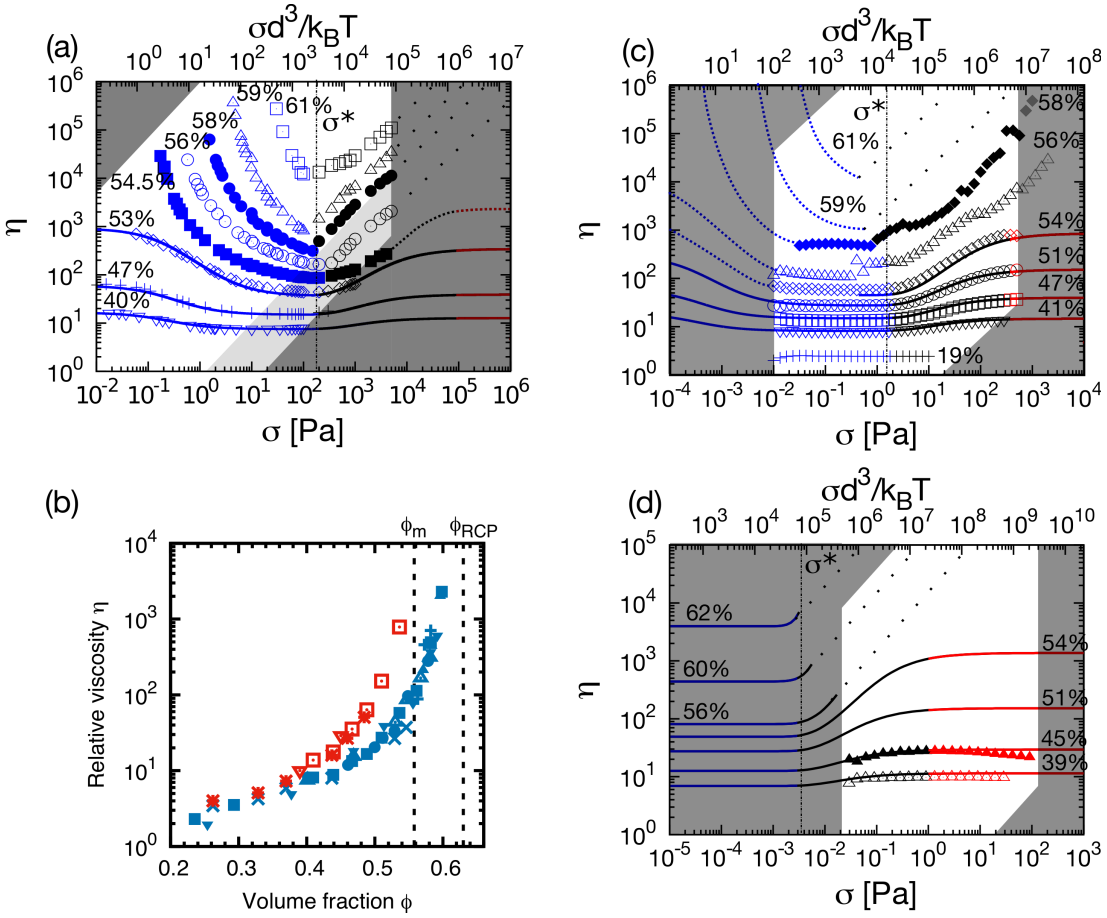

Figure 6.1: Rheology of PMMA spheres bridging the colloidal, intermediate and granular size regimes. (a) colloidal regime, $d = 404$ nm. (b) intermediate regime, $d = 3770$ nm. (c) viscosity branches for PMMA; different symbols correspond to different PMMA particle batches. (d) cusp of the granular regime, 45 μm.

Increasing d by an order of magnitude to 3770 nm has a dramatic effect on the rheology in the observable window, Fig. 6.1(c). Now, at $0.41 \leq \phi \leq 0.54$, there is a transition from a lower towards a higher, shear-thickened, Newtonian plateau as σ increases. Shear thickening again appears above a fixed onset stress, now at $\sigma^* \approx 2$ Pa. Approximately the same onset stress applies at $\phi \geq 0.56$, but flow is erratic for $\sigma > \sigma^*$ and the time-averaged $\eta(\sigma)$ exhibits discontinuous shear thickening. The onset of fracturing is now at $\sigma^\dagger \approx 500$ Pa.

The two viscosities for the $d = 3770$ nm particles fall on separate diverging branches, Fig. 6.1(b), as demonstrated in Ch. 5. The lower plateau viscosity here corresponds to $\eta_1(\phi)$ for the $d = 404$ nm particles: the branches for each size can be collapsed onto the same curve by a 2% shift in ϕ, which accounts for differences in polydispersity [35]. Both branches diverge at random close packing, $\phi \approx 0.63 = \phi_{\mathrm{RCP}}$, the maximum amorphous packing fraction for

lubricated (frictionless) spheres. Thus, we infer an experimentally-inaccessible shear thinning regime for these particles at lower $\sigma < \sigma_{\min}$, sketched schematically in Fig. 6.1(c). As discussed in Ch. 5, the upper branch, $\eta_2(\phi)$, likely corresponds to fully-developed frictional flow and diverges at $\phi_m \approx 0.55 < \phi_{\mathrm{RCP}}$. Since the flow becomes unsteady above $\phi \approx 0.56$, we infer the existence of a frictional branch in the 404 nm particles, and a regime of shear thickening beyond the observable window, Fig. 6.1(b).

6.3.1 Onset stress σ^* and the transition to granular rheology

We now show that the shift from colloidal to intermediate rheology is controlled by the d-dependence of the onset stress σ^*, and demonstrate that this leads to granular behaviour at large d. In Fig. 6.2 we plot σ^* versus d for all the particle sizes studied, alongside literature data for PHSA-stabilised PMMA spheres in other solvents. We find that σ^* decreases with d as $\sigma^* \approx Bd^{\alpha}$, with $B = 3 \times 10^{-11}$ J.m$^{-1.1}$ and $\alpha = -1.9(2)$. If we take our data as supporting $\sigma^* \sim d^{-2}$, then the constant $B = \tilde{f}^* = 3k_BT/\mathrm{nm}$ has units of force. Recall that in the frictional framework introduced in Ch. 5, this $\tilde{f}^*$ relates to a barrier separating particle surfaces, so that these data imply a d-independent normal load for pressing particles into frictional contact [1]. The nanoscopic origin of this $\tilde{f}^*$, which we discuss in Ch. 10, remains unclear [2].

The interplay between the d^{-2} scaling of σ^* and the d^{-3} of the entropic stress controls the onset of granular behaviour in our system. We illustrate this schematically in Fig. 6.3, which shows η versus reduced stress $\hat{\sigma} = \sigma d^3/(k_BT)$ for colloids in the observable window (here shaded grey). $\eta(\hat{\sigma})$ exhibits shear thinning, starting at $\hat{\sigma} = 1$, followed by shear thickening at a dimensionless onset stress $\hat{\sigma}^* = \sigma^* d^3/(k_BT) = \tilde{f}^* d/(k_BT)$ at the high end of accessible stresses. In most of the observable window colloids are in a lubricated (frictionless) state, which we denote with blue points in Fig. 6.1. As d increases, $\hat{\sigma}^*$ shifts right as d in reduced units and the high-Pe (frictionless) Newtonian regime is stretched out. However, the observable window, which is fixed in absolute units, shifts right faster, as d^3, in reduced units. As a consequence, shear thinning becomes

[1] We point out that this $\tilde{f}^*$ is related to but is not equal to the repulsive force f^* separating particle surfaces in the frictional framework introduced in Ch. 5. The two quantities are related by an approximately ϕ-independent factor, $[\phi Z_c(\phi) F_{12}(\phi)]$, which is not necessarily of order unity: $\tilde{f}^* = f^*[\phi Z_c(\phi) F_{12}(\phi)]$.

[2] We can rule out particle charging in CXB as the dominant repulsive mechanism, however, as σ^* is unchanged by adding an excess of salt; $\tilde{f}^*$ is ostensibly related to the polymer brush.

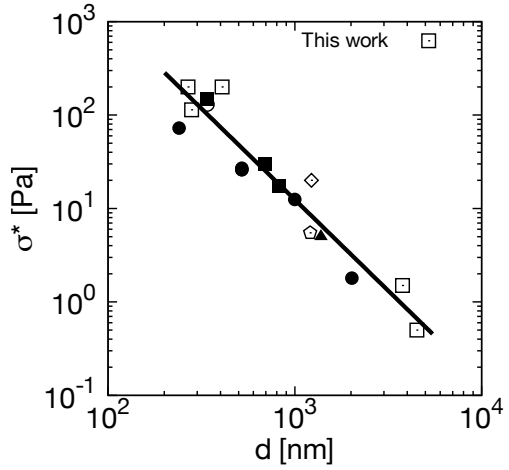

Figure 6.2: Onset stress versus particle diameter d for PHSA-stabilised PMMA spheres in this and previous work [101, 110, 114–116].

unobservable for intermediate particle sizes, while the frictional viscosity plateau becomes visible at the high-stress end of the observable window (red in Fig. 6.1). For granular particles, only the frictional, shear-thickened state is visible and both the shear thickening and Brownian shear thinning transitions lie to the left of the observable window.

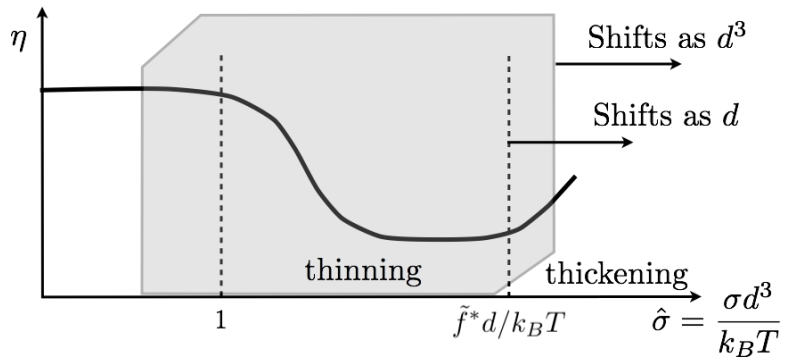

Figure 6.3: Relative viscosity, η, versus dimensionless stress, $\hat{\sigma}$. The observable window (shaded) for colloids shows shear thinning, which begins at $\hat{\sigma} \simeq 1$; shear thickening, beginning at a dimensionless onset stress of $\hat{\sigma}^* = \sigma^* d^3/k_B T = \tilde{f}^* d/k_B T$, occurs towards the high end of accessible stresses. As the particle diameter d increases, $\hat{\sigma}^*$ shifts right as d, and the second Newtonian regime in the $\eta(\hat{\sigma})$ curve is stretched out. However, the (shaded) observable window shifts right faster, as d^3. Thus, shear thinning becomes unobservable for intermediate particles sizes, and the shear-thickened state fills the observable window of the largest particles (grains). Figure 6.1(a), (c) and (d) show three snapshots of this scenario.

On the cusp of the granular regime, $d = 45$ μm, Fig. 6.1(d), the rheology in the observable window is dominated by the frictional state, with only a small amount

of shear thickening visible at the far left of the window.

6.3.2 Probing the repulsive granular regime

The existence of an onset stress σ^* means that residual van der Waals attraction sets a practical limit to the largest particle size, $d_{\rm crit}$, we could in principle study. When two PMMA particles just touch, the separation of their cores is $\sim 2\delta$, where $\delta \sim 5$ nm is the average length of the stabilising "hairs". Ignoring van der Waals interactions between the hairs, the van der Waals force between the cores at this point is $F_{\rm VW} = -Ad/(24\delta^2)$, where A is the appropriate Hamaker constant. If $F_{\rm WV}$ exceeds $\tilde{f}^* \approx 3k_BT/\text{nm}$ then attractions will mask shear thickening – there is no longer a barrier separating particle surfaces. Taking a literature value for the Hamaker constant $A \approx 0.066k_BT$ [49] yields $d_{\rm crit} \approx 22$ μm. When $d > d_{crit}$, we expect the system to have a yield stress σ_Y which exceeds σ^* above a critical volume fraction, $\phi_{\rm gel}$, so that the moment the system has yielded it flows on the frictional branch [117].

In Fig. 6.4(a), we plot $\eta(\sigma)$ over the full range of ϕ for 45 μm PMMA. Purple points denote the data already shown in Fig. 6.1(d) and green points are for higher ϕ. We did not observe a yield stress at the concentrations probed, so take $\phi_{\rm gel}$ to be the point at which $\eta(\sigma)$ exhibits significant shear thinning in the frictional state, $0.45 < \phi_{\rm gel} \leq 0.48$. The origin of the abrupt shear thickening at $\sigma < 0.1$ Pa is unclear and has also been observed in glass spheres dispersed in corn syrup and glycerin by Zarraga, Leighton and Hill [53]; we present their data in Fig. 6.4(b) for comparison. They attributed it to resuspension of an initially sedimented sample; however, there was no visual evidence of sedimentation in our sample, in which the particles are almost buoyancy matched. We did not explore this phenomenon systematically, so cannot comment further.

In some other model systems, e.g., [54], there is no evidence of attraction in the granular regime and the flow is Newtonian. This is presumably due to the particles having a large surface roughness r^* which cuts off the van der Waals force at a modest value $\sim Ad/r^{*2}$, so that σ_Y is no longer within the observable stress window.

Even if attractions are absent, sedimentation will usually inhibit proper study of the repulsive granular regime in real systems. For example, for 100 μm silica particles in water the stress required to displace a particle by its own diameter,

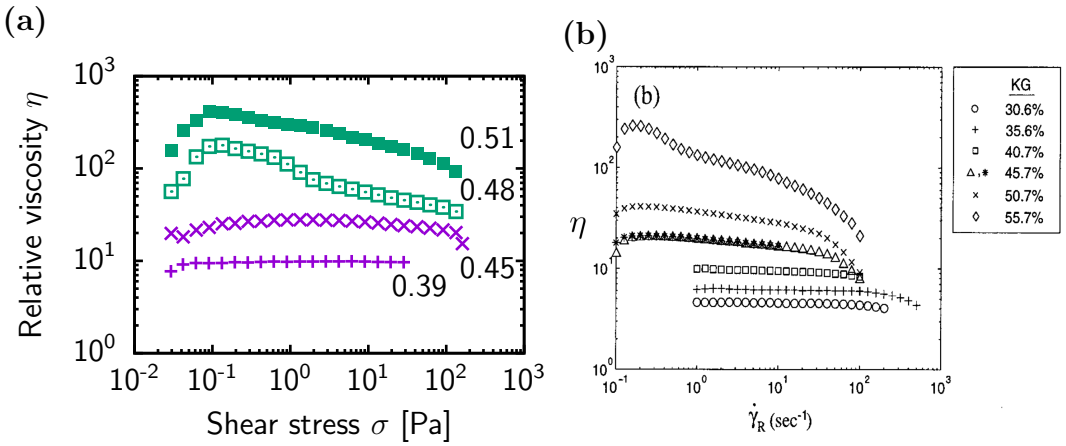

Figure 6.4: (a) Flow curves for 45 μm PMMA at different ϕ, as labelled. The labelled ϕ are shifted up from the nominal ϕ obtained using the dry density of PMMA by a factor of 1.065 so that the plateau viscosity at the lowest two ϕ agree with $\eta_2(\phi)$ in Fig. 6.1(b). (b) Relative viscosity as a function of shear rate for 43 μm glass spheres dispersed in a mixture of corn syrup and glycerin at different ϕ from [53].

$(\rho_P - \rho_F)gd \sim 10^3 \cdot 10 \cdot 10^{-4} \sim 1$ Pa (g is acceleration due to gravity and ρ_P and ρ_F are the particle and solvent densities, respectively), lies in the middle of the observable window. In that case shear thickening is observed, but with an onset stress that is related to the resuspension of the frictional sediment, $\sigma^* \sim \Delta\rho gd$ [81]. For macroscopic particles, $d \gtrsim 1$ mm, the effects of particle inertia are unavoidable even if sedimentation is circumvented, unless a highly viscous solvent is used, as in [54].

6.4 Flow curve fitting

In Ch. 5, we saw that expressions derived from Wyart and Cates (WC) theory can be used to accurately fit PMMA flow curves in the intermediate size regime. In this section, we extend the theory to colloidal spheres.

The Brownian shear thinning regime of the 404 nm particles in Fig. 6.1(a) in the main text can be described using an empirical expression for the viscosity $\eta(\sigma, \phi)$ as a function of stress σ and volume fraction ϕ proposed by Kobelev *et al.* [118]:

$$\eta_B(\sigma, \phi) = \eta_0(\phi)\left[1 + (\sigma/\sigma_{1/2})^\delta\right]^{-1} + \eta_1(\phi)\left\{1 - \left[1 - (\sigma/\sigma_{1/2})^\delta\right]^{-1}\right\}, \qquad (6.1)$$

where $\eta_0(\phi)$ is the Pe $\to 0$ viscosity, $\eta_1(\phi)$ is the high Pe (frictionless) viscosity

and δ and $\sigma_{1/2}$ are parameters obtained from experiments. The data for η_1, Fig. 6.1(b), are well fitted by the empirical form

$$\eta_1(\phi) = (1 - \phi/\phi_{\mathrm{RCP}})^{-2} \tag{6.2}$$

up to $\phi \approx 0.56$, with $\phi_{\mathrm{RCP}} = 0.63$. For the divergence of $\eta_0(\phi)$ we find that

$$\eta_0(\phi) = (1 - \phi/\phi_0)^{-n_0}, \tag{6.3}$$

with $n_0 = 2.15$ and $\phi_0 = 0.549$ fitting our data. We fitted equation (6.1) to the data by eye and found $\delta = 1$ and $\sigma_{1/2} = 0.17$ Pa $= 2.78\ k_BT/d^3$. This equation fails to capture the shape of the flow curves for $\phi \geq 0.54$, for which we sketch representative curves by hand. Curves in the inaccessible Brownian regime for the intermediate-sized particles Fig. 6.1(c) were also generated using Eq. (6.1) with $\sigma_{1/2} = 2.78\ k_BT/d^3$.

We describe the shear thickening part of the flow curves with WC theory, for which see Ch. 5. There was insufficient data in this regime to perform reliable fits, so we generate theoretical curves using the same values of $\phi_m, \phi_{\mathrm{RCP}}, \beta$ as for the 3770 nm particles with $\hat{\sigma}^* = 800$ Pa. It is reasonable to assume that, since the same batch of PHSA stabiliser was used to coat both particles, μ_S and hence ϕ_m are the same for both sizes.

6.4.1 Deviation of empirical form for shear thinning at $\phi \gtrsim 0.54$

Our expression for the Brownian shear thinning part of the flow curve, Eq. (6.1), fits the data very well below $\phi = 0.54$; however, the data deviate from this form at higher ϕ. The volume fraction at which the low shear viscosity diverges, ϕ_0, is somewhat lower than the glass transition volume fraction 0.58 measured in [50]. We discuss possible reasons for this below.

Firstly, evaporation of the solvent means that we cannot allow the sample to equilibrate fully at low shear rates, so the data we plot are not necessarily steady state. Secondly, the onset of shear thickening is associated with overcoming a barrier separating the particle surfaces, which for our system and most others corresponds to overcoming the particle stabilisation. Accordingly, we observed that persistent shear thickening inevitably lead to some attraction between

the particles, particularly close to and above the jamming volume fraction for frictional spheres, $\phi_m \approx 0.55$. This leads to a weak attractive yield stress which obfuscates the glass physics at low shear rates and could partially account for the observed deviation of $\eta(\sigma)$ from the form in Eq. (6.1). This is presumably also responsible for the sensitivity of data at $\phi > \phi_m$ to sample preparation protocol.

6.5 Summary

To summarise, our data, Fig. 6.1, show that the transition from colloidal to granular rheology is driven by shear thickening. They are consistent with recent suggestions that shear thickening is associated with the development of frictional particle contacts at an onset stress σ^*, which we find to decrease with particle size as d^{-2}. Consequently, for colloids σ^* is sufficiently large that they behave as frictionless, Brownian hard spheres at most accessible stresses. For intermediate-sized particles, frictionless and frictional states are observed at low and high stress, respectively. Finally, a particulate suspension is granular when σ^* is much smaller than commonly-encountered stresses; such a suspension is "always shear thickened". The size at which this happens depends on the "stabilising force" f^*, and is therefore expected to depend on the surface chemistry.

This scenario should be valid for any system in which $\sigma^* \propto d^{-\lambda}$ with $\lambda > 0$, with the exact value of λ controlling the sharpness of the crossover. Except for $\lambda = 3$, the different scaling of σ^* and the entropic stress $\propto d^{-3}$ means that a single set of master curves cannot be found to describe the suspension rheology for all d. Instead, there is a unique graph for each d, of which Fig. 6.1(a), (c) and (d) are three examples. This should be contrasted with the rheology of concentrated polymer solutions, for which a single scaling description exists for the viscosity over four orders of magnitude in molecular weight [40].

Finally, we emphasise that the observable window is unique to the specific rheometer and measuring geometry we use: in principle, one could extend the window by using a more sensitive torque transducer, effectively shifting the intermediate to granular crossover to larger d. In practical applications, the boundaries of the window would be set by processing limits such as flow rate and maximum pumping pressure.

A final note

We conclude this section with a note about Brownian motion. Heretofore, we have discussed only $\eta_1(\phi)$ and $\eta_2(\phi)$ and neglected the zero shear viscosity, $\eta_0(\phi)$, which appears to diverge at $\phi_g \approx 0.55$ for our 404 nm spheres. Above ϕ_g, the system has a yield stress within the observable window. We emphasise, however, that the divergence of η_0 is not obviously related to the divergence of η_1: the latter occurs at $\mathrm{Pe} \ll 1$ where interactions are frictionless, while the former pertains to $\mathrm{Pe} \gg 1$ where particles are in frictional contact. In the same way, η_1 and η_2 correspond to distinct phenomena, even though their scaling close to the relevant critical volume fraction, ϕ_{RCP} or ϕ_m, is similar.

The stress-induced friction theory of Wyart and Cates [1], developed for strictly non-Brownian suspensions, apparently holds for systems in which Brownian motion is not negligible, a finding which is in alignment with recent simulations of Brownian spheres with static friction [119]; they find that that primary effect of Brownian motion is to serve as an additional short-ranged repulsion keeping particle surfaces apart. The precise role of Brownian motion during shear thickening is still not well understood [3], however, and it plays fundamentally different roles at low and high Pe, as we will discuss in Ch. 7.

[3] How shear thickening is modified when the Brownian stress is comparable to the onset stress, $\sigma^* \sim k_B T/d^3$, is an intriguing case that has yet to be addressed in the literature. One can envision a situation in which the glassy yield stress is $> \sigma^*$, in which case the system would jam itself into a frictional solid at rest.

Chapter 7

What kinds of system shear thicken?

Hitherto, we have been rather one-track minded in our interpretation of shear thickening. Although the frictional contact theory of Wyart and Cates (WC) [1] quantitatively fits our data, it applies strictly to non-Brownian, inertialess particles undergoing Stokes flow and does not explicitly take into account finite-range potential interactions, Brownian motion, particle inertia and lubrication interactions, all of which are present to some extent in real particulate systems [25, 35, 120]. It is instructive to ask, therefore, what role these additional interactions play and specifically whether they can also give rise to the shear thickening we observed in experiments. In fact, there is a sizeable body of literature claiming that contacts are not necessary at all for shear thickening and that it is driven purely by hydrodynamic forces [83].

This chapter has two purposes. The first is to determine which of the above interactions can lead to a rate-dependent rheology and if so, whether this rheology can include shear thickening. The second is to ask which of the predicted types of thickening can account for the two-branch phenomenology observed experimentally in Ch. 5 and 6.

We start by considering the simplest possible system, a suspension of inertialess hard spheres in Stokes flow, and show by dimensional analysis that no rate-dependent rheology is possible, even if contacts are allowed. We then systematically add in non-hard-sphere interactions and use dimensional analysis and existing literature to determine whether shear thickening is possible in each case.

For systems where the inertia of the particles is negligible, we will see that thickening, or indeed any $\dot{\gamma}$-dependent rheology, is prohibited in steady state if there is only one stress scale (e.g., the viscous stress $\eta_f\dot{\gamma}$) in the system. The addition of other stress scales leads to two generic but fundamentally different mechanisms of thickening: one in which particles enter direct mechanical contact, and another in which particle surfaces remain separated by a lubrication film. Systems in which particle inertia is negligible do exhibit shear thickening without multiple stress scales, but dimensionless analysis predicts a specific scaling of the suspension viscosity with shear rate. We conclude the chapter by discussing which of the above mechanisms could lead to a two-branch phenomenology.

For simplicity, we restrict our attention to flows in which confinement effects are irrelevant, i.e., in which the system size is significantly larger than the particle radius. We also consider only steady-state rheology, ignoring transient effects such as strain thickening.

Although we do not present any new experimental data in this chapter, we believe that it is an original contribution to the field, as it approaches the issue of thickening from a purely dimensional standpoint. There are many instances in the literature, particularly for hydrodynamic thickening, in which the physical mechanism for thickening is speculative and itself not properly understood – we show that many of these can be ruled out on dimensional grounds alone. We acknowledge that our treatment may not turn out to be exhaustive. Other, unforeseen, physical effects could be important. To our knowledge, however, we have included all types of interaction that have been cited previously as possible causes for thickening.

A reminder of experimental observations

As a reminder, and for use as a reference, we present a brief review of the pertinent experimental observations. The data presented in Ch. 5 and 6 are representative of the phenomenology of most colloidal- and intermediate-sized particles, so, to avoid repetition, we present only a schematic overview; for a more comprehensive review, see [35, 121] and the introduction to [81].

For most shear-thickening systems, one can distinguish two qualitatively distinct kinds of thickening, Fig. 7.1: continuous (CST), where the shear viscosity η increases smoothly with shear rate $\dot{\gamma}$, and discontinuous (DST), where η jumps

abruptly – and often in an unsteady manner – at a particular $\dot{\gamma}$. As we saw in Ch. 5 and 6, CST is typically observed at low volume fractions $\phi \lesssim 0.55$ while DST occurs at $\phi \gtrsim 0.55$. A third form of thickening involves a discontinuous jump between two flowing states that depends on whether the flow curve is measured by an upward or downward $\dot{\gamma}$-sweep [89]. This form of thickening, which we refer to as *hysteretic DST* (h-DST), is often attributed to an underlying sigmoidal flow curve such as that predicted by WC theory, Fig. 5.10. Under imposed σ, it has been suggested that such a system will split into shear bands [91].

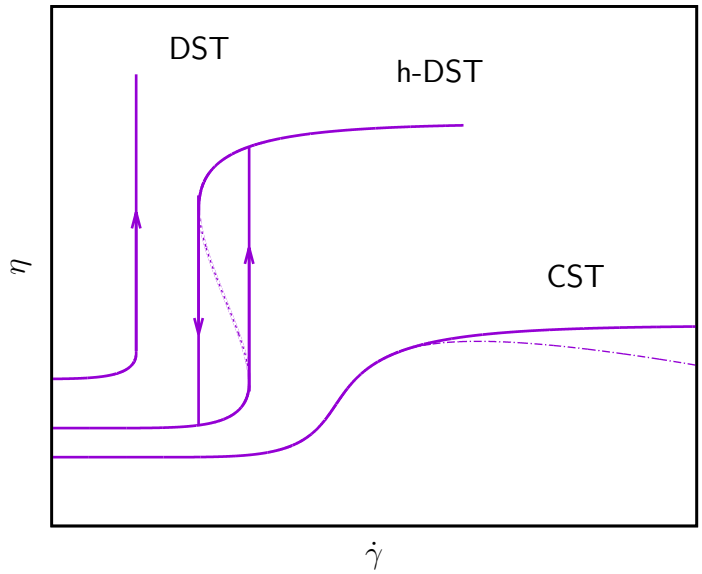

Figure 7.1: Schematic of the types of shear thickening observed in experiments: CST, in which $\eta(\dot{\gamma})$ increases continuously between a low-viscosity Newtonian (or shear thinning, dot-dashed line) regime to a high-viscosity Newtonian (or shear thinning) regime; h-DST, in which $\eta(\dot{\gamma})$ jumps discontinuously and hysteretically between low- and high-viscosity states under imposed-$\dot{\gamma}$ mode; and DST, in which $\eta(\dot{\gamma})$ jumps discontinuously at a critical $\dot{\gamma}$, but does not reach a second steady Newtonian or shear thinning state.

7.1 Smooth hard spheres in Stokes flow

We begin the chapter by considering the simplest possible suspension: an inertialess assembly of hard spheres with radius R immersed in an incompressible Newtonian fluid with viscosity η_f flowing at zero Reynolds number. This suspension is subjected to steady shear with shear rate $\dot{\gamma}$ between infinite parallel plates whose separation H is much larger than R, Fig. 7.2. We also make the assumption that there is no slip between the fluid and the surface of the particles [25].

In this section, and in the remainder of the chapter, we will first determine whether the relative shear viscosity of the suspension $\eta = \sigma/(\eta_f\dot{\gamma})$ (where σ is the macroscopic shear stress measured by the plates) is allowed to be rate dependent, and then, if so, whether this rate dependence could include shear thickening.

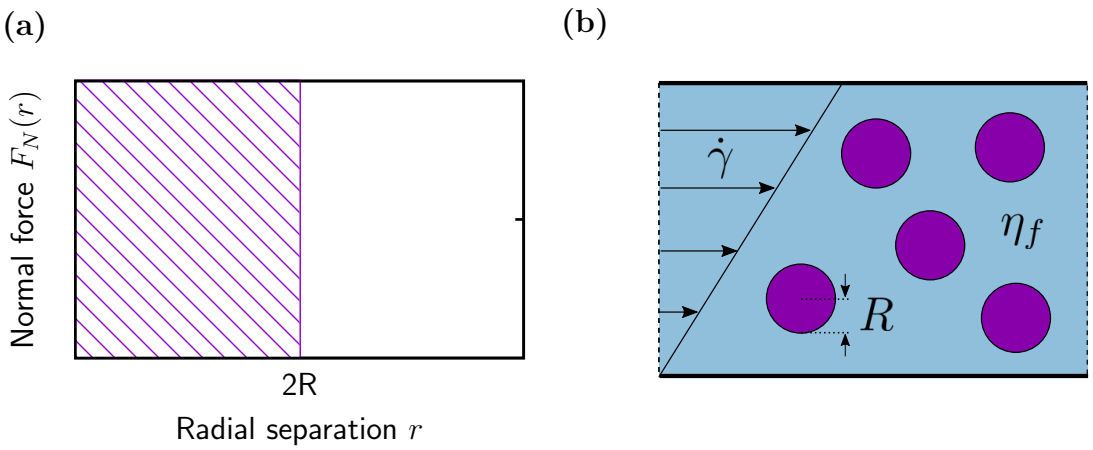

Figure 7.2: Smooth hard spheres in Stokes flow. (a) Normal force F_N as a function of centre-to-centre separation r for a pair of hard spheres with radius R. The tangential force $F_T = 0$. (b) Schematic of smooth hard spheres undergoing simple shear in the Stokes flow limit.

7.1.1 Dimensional analysis

We first use dimensional analysis to determine whether $\dot{\gamma}$-dependent rheology is possible. For simplicity, we will consider only the shear stress $\sigma \equiv \sigma_{12}$; there are three additional, non-zero components of the stress tensor, σ_{11}, σ_{22}, σ_{33}, which we consider later, but which can be ignored in the present analysis. We will work through the procedure in some detail in this first instance, but provide only a skeleton outline in future sections.

In our dimensional analyses, we make use of the *Buckingham Pi theorem* [122], which states that if we have a relation between a set of physical quantities $\{Q_i\}$ of m different kinds,

$$F(Q_1, Q_2, \cdots Q_m) = 0, \tag{7.1}$$

and there are k fundamental units (mass, length and time), there exists a relation in terms of $m - k$ dimensionless groups $\{\Pi_i\}$,

$$f(\Pi_1, \Pi_2, \cdots \Pi_{m-k}) = 0, \tag{7.2}$$

that does not depend on our choice of units. Eq. (7.2) can be solved for any one of the arguments, allowing any one of the dimensionless groups to be expressed in terms of the others, e.g.,

$$\Pi_1 = C(\Pi_2, \Pi_2, \cdots \Pi_{m-k}). \tag{7.3}$$

In our problem, Fig. 7.2 there are $m = 5$ relevant physical quantities: the shear stress σ, shear rate $\dot{\gamma}$, fluid viscosity η_f, particle radius R and particle number density n. We assume that there exists a relationship between these quantities that characterises the steady-state rheological behaviour:

$$F(\sigma, \dot{\gamma}, \eta_f, R, n) = 0. \tag{7.4}$$

There are $k = 3$ fundamental units; so, according the Π-theorem we can express Eq. (7.4) in terms of $m-k = 2$ independent dimensionless groups, Π_1 and Π_2. We choose $\Pi_1 = \sigma/(\eta_f\dot{\gamma})$ and $\Pi_2 = (4/3)\pi R^3 n = \phi$, where ϕ is the volume fraction, yielding

$$f(\Pi_1, \Pi_2) = f\left(\frac{\sigma}{\eta_f\dot{\gamma}}, \phi\right) = 0. \tag{7.5}$$

Our choice of Π_1 and Π_2 is not unique and other dimensionless groups, including the above groups raised to an arbitrary power, can be constructed. Our choice is intended to maximise physical insight.

Eq. (7.5) can be solved for $\sigma/(\eta_f\dot{\gamma})$ to yield an expression for the shear stress:

$$\sigma = \eta_f \dot{\gamma} C(\phi) \tag{7.6}$$

Thus, σ scales linearly with $\dot{\gamma}$ at fixed ϕ: the relative shear viscosity $\eta = \sigma/(\eta_f\dot{\gamma}) = C(\phi)$ is independent of $\dot{\gamma}$. The function $C(\phi)$ has been determined analytically up to $\mathcal{O}(\phi^2)$ [123], but is typically described by empirical expressions for $\phi \gtrsim 0.3$ [35].

Physically, the Newtonian behaviour arises because there is only a single stress scale in the system, the viscous stress $\eta_f\dot{\gamma}$, and a single timescale, the inverse shear rate $\dot{\gamma}^{-1}$: there is no additional stress or time scale against which they may compete, and hence no possibility of a $\dot{\gamma}$-dependent rheology. Although dimensional arguments lead very quickly to the result in Eq. (7.6), it is, at first sight, neither obvious nor intuitive. For this reason, we also address the problem from a traditional fluid mechanics perspective [1], which provides insight into the assumptions that lead to the $\dot{\gamma}$-independent rheology. The fluid-dynamical approach also serves to establish the implications of low Re for suspension flow, which we will make use of in future sections.

7.1.2 From Navier-Stokes to Stokes

We start by relaxing our assumption of Stokes flow and consider the general case of particles suspended in a fluid at finite Reynolds number. The velocity $u(\underline{x}, t)$ and pressure $p_f(\underline{x}, t)$ fields in the fluid surrounding the particles obey the Navier-Stokes equation:

$$\rho_f \left[\frac{\partial \underline{u}}{\partial t} + (\underline{u}\cdot\underline{\nabla})\underline{u}\right] = \underline{\nabla}\cdot\underline{\underline{\hat{\sigma}}} = \eta_f\nabla^2\underline{u} - \underline{\nabla}p_f, \tag{7.7}$$

where ρ_f is the fluid density and $\underline{\underline{\hat{\sigma}}}$ is the local stress tensor in the fluid. The second equality follows by assuming that $\underline{\underline{\hat{\sigma}}}$ and the local strain-rate tensor $\underline{\underline{\hat{e}}} = (1/2)(\partial u_i/\partial x_j + \partial u_j/\partial x_i)$ are related by a Newtonian constitutive equation,

$$\hat{\sigma}_{ij} = -p_f\delta_{ij} + 2\eta_f\hat{e}_{ij}. \tag{7.8}$$

[1] The problem was first studied in this way by Batchelor and Green [123, 124], which the interested reader should consult for a complete account.

For Stokes flow problems, one neglects the inertial term $\propto \rho_f$ on the left hand size of Eq. (7.7). This requires, firstly, that the fluid Reynolds number, defined as

$$\mathrm{Re} = \frac{\rho_f |(\underline{u} \cdot \underline{\nabla})\underline{u}|}{\eta_f |\nabla^2 \underline{u}|}, \tag{7.9}$$

is $\ll 1$ [2]. Physically, Re measures the relative magnitude of inertial forces that result from gradients in the velocity field, $\rho_f(\underline{u}\cdot\underline{\nabla})\underline{u} \propto \rho_f$, and viscous forces $\propto \eta_f$. We want velocity gradients to be small on the lengthscale of typical particle separations, which are $\lesssim R$ for concentrated suspensions ($\phi \gtrsim 0.4$). Relative velocities of particles are $\sim \dot{\gamma}R$, so we require

$$\mathrm{Re} = \frac{\rho_f(\dot{\gamma}R)R^{-1}(\dot{\gamma}R)}{\eta_f R^{-2}(\dot{\gamma}R)} = \frac{\rho_f \dot{\gamma} R^2}{\eta_f} \ll 1. \tag{7.10}$$

For micron-sized colloidal particles in a low viscosity solvent, e.g., water, $\mathrm{Re} \sim 10^{-6}\dot{\gamma}$, so even at the highest shear rates achievable with conventional rheometry, $\dot{\gamma} \sim 10^4$ s^{-1}, $\mathrm{Re} \ll 1$. Only for $R \sim 100$ μm is Re readily exceedable at typical $\dot{\gamma}$.

Neglect of the inertial term in Eq. (7.7) also requires that the Stokes number

$$\mathrm{St} = \frac{\rho_f |\partial \underline{u}/\partial t|}{\eta_f |\nabla^2 \underline{u}|} \sim \frac{R^2}{T\nu}, \tag{7.11}$$

is small [25], where T is an intrinsic timescale over which the velocity varies. The only timescale relevant to the imposed motion is $\dot{\gamma}^{-1}$; so, $T \sim \dot{\gamma}^{-1}$ and $\mathrm{St} \approx \mathrm{Re} \ll 1$.

7.1.3 Particles in Stokes flow

Under these assumptions, Eq. (7.7) reduces to the Stokes equation

$$\underline{\nabla} \cdot \underline{\underline{\hat{\sigma}}} = \eta_f \nabla^2 \underline{u} - \underline{\nabla} p_f = 0, \tag{7.12}$$

[2] One can also define a Reynolds number Re_p associated with the particle density ρ_p, which is strictly zero for massless particles. Eq. 7.9 refers to the inertia of the fluid flowing between the particles.

where $\underline{u}(\underline{x})$ and $p_f(\underline{x})$ are the velocity and pressure fields at position $\underline{x}$ in the fluid. The applicability of Eq. (7.12) has several crucial implications for suspension flow.

The suspension stress is purely hydrodynamic

The first concerns that nature of forces transmitted between the particles. Consider two spheres approaching each other normally with a speed W in a fluid at Re $\ll 1$, Fig. 7.3 (a). One can solve Eq. (7.12) in this geometry to find an expression for the normal ("squeeze") lubrication force F_{sq} experienced by the spheres in terms of the surface separation h:

$$F_{\text{sq}} \sim \eta_f R^2 W h^{-1},$$

which is valid for $h \ll R$. F_{sq} diverges as $1/h$: an infinite force is required to push the surfaces of the particles together at finite W. This ensures that a narrow lubrication film is always maintained between particles [25]. (A similar expression exists for tangential motion, Fig. 7.3(b), $F_{\text{sh}} \sim \eta_f R^2 W \ln h$ which diverges more weakly with h than F_{sq}.) Consequently, all forces in the system are transferred via the fluid and direct contact forces are forbidden. The particles generate stress by distorting the local velocity field of the solvent. The macroscopic stress exerted by the suspension on the plate is, therefore, purely viscous in origin, reflected by the fact that $\sigma \propto \eta_f \dot{\gamma}$ in Eq. (7.6).

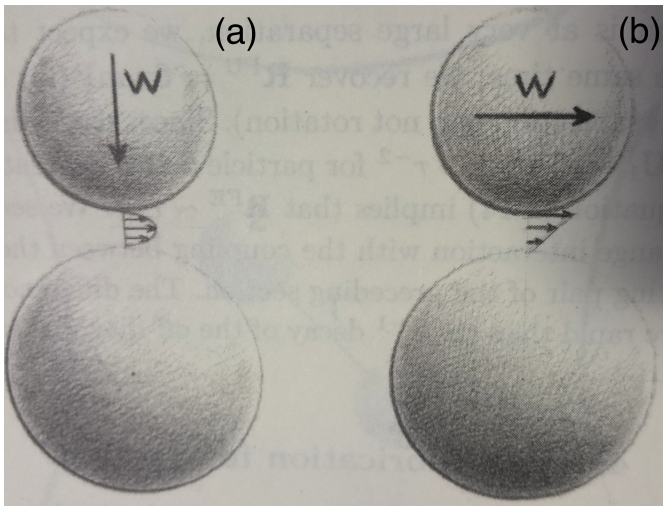

Figure 7.3: (a) Squeeze and (b) shear lubrication flow between two spheres with velocity W (taken from [25]).

Instantaneity: there is no t in Stokes equation

Stokes' equation does not contain time t by virtue of $\mathrm{St} \ll 1$: any time-dependent motion of the fluid, and hence the particles, enters only through the imposed macroscopic flow. Since we apply a shear rate that is constant in time, the only timescale in the problem is $\dot{\gamma}^{-1}$.

To better understand the physical meaning of $\mathrm{St} \ll 1$, consider the dynamic viscosity ν in Eq. (7.11). It has units of length^2/time and plays the role of diffusion coefficient for momentum transport in the fluid [125]: a disturbance created in the fluid by a colloid propagates a distance $l \sim \sqrt{\nu t}$ in a time t. The only relevant timescale in our system is $\dot{\gamma}^{-1}$, which sets a diffusive length scale $l_{\max} \sim \sqrt{\nu \dot{\gamma}^{-1}}$, that is, the distance the disturbance propagates during one strain unit. The hydrodynamic interactions between two particles can be considered instantaneous if their relative separation is $\ll l_{\max}$; for separations $\gtrsim l_{\max}$, the timescale for momentum transport, $\propto l$, is much shorter than that for diffusion, $\propto l^2$, and transient fluid inertia effects cannot be neglected. [25].

For example, for a suspension in water sheared at the maximum macroscopic shear rate accessible with conventional rheometry, $\dot{\gamma} \sim 10^3$ s^{-1}, $\nu = 10^6$ μm^2.s^{-1} and $l_{\max} \approx 30$ μm. For a dispersion of 1 μm colloids at $\phi \sim 0.5$, typical surface separations between nearest neighbours in an isotropic dispersion are $\sim 0.1R \sim 0.1$ μm $\sim 10^{-2} l_{\max}$, for which transient inertia effects are negligible. For particles that are further apart, at $l \sim 30R$, such effects are potentially important; however, it has been shown that in concentrated dispersions the hydrodynamic stress is dominated by nearest-neighbour lubrication interactions [58], so long-range interactions can be neglected. In contrast, for a suspension of 100 μm spheres at $\phi \approx 0.1$ is $l_{\max}$, $l_{\max}$ is comparable to the nearest-neighbour distance and inertial effects would have to be taken into account.

The Stokes number is ratio of the time taken for a disturbance to propagate a distance equal to its own diameter, R^2/ν, to a timescale of interest T. Since typical separations are $\ll R$ for concentrated dispersions ($\phi \gtrsim 0.4$), the condition $\mathrm{St} \ll 1$ guarantees that hydrodynamic forces are communicated instantaneously and we can neglect the time derivative in Eq. (7.7).

Linearity

The absence of the non-linear term in Eq. (7.12), owing to $\mathrm{Re} \ll 1$, means that Stokes equation is linear in $\underline{u}$. As a result, a change in the force exerted on the fluid is reflected linearly in the flow rate without changing the streamlines [25]. For example, in pressure-driven flow, a doubling of $\underline{\nabla} p_f$ leads to a doubling of $\underline{u}$ globally. For a sheared HS suspension, Fig. 7.2, doubling the shear rate imposed by the boundaries causes the fluid to follow the same streamlines around the particles: the particles follow the same path through the fluid, but do so at twice the rate. Since the suspending fluid is non-Newtonian and does not exhibit a $\dot{\gamma}$-dependent viscosity itself, it follows that the local viscous stress generated by the particles, and hence the macroscopic shear stress measured by the plates, also doubles – this is the origin of the Newtonian scaling in Eq. (7.6).

Reversibility

Linearity also implies that if $\underline{u}(\underline{x})$ is a solution of Stokes equation, then $-\underline{u}(\underline{x})$ is also a solution if we reverse the boundary conditions. This reversibility means that the trajectories of interacting pairs of particles possess *fore-aft symmetry*. Fig. 7.4 shows trajectories followed by a test sphere that has travelled from $x = \infty$ under the influence of an imposed shear field towards a second, fixed test sphere whose centre is at $x = 0$ [25]; both particles lie in the plane of shear. One can define two kinds of trajectory, which depend on the initial separation of the particles in the y-direction: open trajectories, which go to infinity, and closed trajectories, in which particles oscillate around each other in a "bonded" state. The presence of closed orbits is problematic for calculating the stress, as the probability distribution of particle positions is indeterminate in this region [25, 123, 124]. See [123] for a discussion of how this is obviated.

Importantly, however, the trajectories possess mirror symmetry about the y-axis; this symmetry is a direct consequence of the linearity and reversibility of Stokes flow [25]. As a consequence, if the pair of spheres are sheared at a shear rate $+\dot{\gamma}$ for a time t_0 then subsequently subjected to the same shear rate in the opposite direction for the same time they will return to their initial positions. Flow reversibility also applies in a concentrated suspension: applying a positive shear rate for t_0 will cause the particles to flow around each other and become displaced laterally. Subsequently reversing the direction of shear will cause the

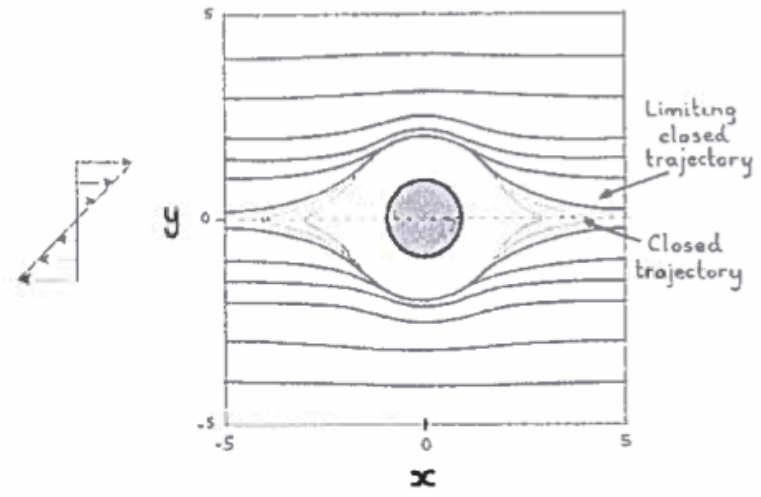

Figure 7.4: Relative pair trajectories of two smooth hard spheres under shear flow (taken from [25]).

particles to retrace the same path and return to their original positions – the trajectories will be more tortuous than in the two-particle case due to many-body effects [25].

7.1.4 Scaling of the full stress tensor

Before continuing, we return to the assumption we made in §7.1.1 of ignoring the components of the stress tensor σ_{ij} other than σ_{12} in dimensional analysis. We give this issue some attention, as it is relevant to subsequent sections.

We consider the deviatoric part of $\sigma_{ij} = -p\delta_{ij} + \tau_{ij}$, for reasons which will become apparent later. Aside from the shear stress $\tau_{12} = \sigma_{12}$, there are only two other independent stress components that can be non-zero, e.g., τ_{11} and τ_{22}, the third, τ_{33}, being determined by the condition that the trace of τ_{ij} vanishes. This is a physical argument, rather than a dimensional one, and arises from the assumption that the suspension is incompressible. For convenience, we choose the two independent stresses to be the first and second normal stress differences $N_1 = \tau_{11} = \tau_{22}$ and $N_2 = \tau_{22} - \tau_{33}$.

There are still only $m = 5$ kinds of physical quantity in the problem, as N_1 and N_2 also have units of stress. To proceed, we choose only one of these, e.g., σ_{12}, to construct dimensionless groups and express the other two quantities as ratios of this one [122]. In general, when there is more than one quantity of a particular

kind the dimensional equation may be written:

$$F(Q_1, Q_2, \cdots Q_m, r', r'', \cdots) = 0, \tag{7.13}$$

where $r', r'' \cdots$ denote ratios of dimensional quantities. The dimensionless equation can be written in terms of $m - k$ groups and the ratios as:

$$f(\Pi_1, \Pi_2, \cdots \Pi_{m-k}, r', r'', \cdots) = 0. \tag{7.14}$$

Following the above procedure and choosing the same $m - k = 2$ dimensionless groups as before, the shear stress can be written:

$$\tau_{12} = \eta_f \dot{\gamma} C \left(\phi, \frac{N_1}{\tau_{12}}, \frac{N_2}{\tau_{12}} \right); \tag{7.15}$$

Recall from Ch. 2 that $\tau_{12}(\dot{\gamma})$, $N_1(\dot{\gamma})$ and $N_2(\dot{\gamma})$ are *independent* rheological functions, which implies that τ_{12} cannot depend neither or N_1 nor N_2. Thus, Eq. (7.15) reduces to our original expression for the shear stress in Eq. (7.6),

$$\tau_{12} = \eta_f \dot{\gamma} C(\phi),$$

and the relative shear viscosity depends only on ϕ.

One can follow a similar line of reasoning to derive expressions for N_1 and N_2 in terms of the other stresses:

$$N_1 = \eta_f \dot{\gamma} C_{N_1} \left(\phi, \frac{\tau_{12}}{N_1}, \frac{N_2}{N_1} \right) = \eta_f \dot{\gamma} C_{N_1}(\phi) \tag{7.16}$$

and

$$N_2 = \eta_f \dot{\gamma} C_{N_2} \left(\phi, \frac{\tau_{12}}{N_2}, \frac{N_1}{N_2} \right) = \eta_f \dot{\gamma} C_{N_2}(\phi). \tag{7.17}$$

Like τ_{12}, both N_1 and N_2 scale linearly with $\dot{\gamma}$ with a coefficient that depends only on ϕ.

By taking suitable combinations of Eq. (7.16) and (7.17), and using the incompressibility constraint $\tau_{11} + \tau_{22} + \tau_{33} = 0$, one can easily show that the individual deviatoric normal stresses also scale linearly with $\dot{\gamma}$. The deviatoric stress tensor can therefore be written [126]:

$$\tau_{ij} = \eta_f \dot{\gamma} C_{ij}(\phi), \tag{7.18}$$

where $C_{ij}(\phi)$ is a constant tensor. Such an expression does not exist for the *total* stress tensor σ_{ij}, as in that case the normal stresses are also functions of an arbitrary (isotropic) pressure p that does not necessarily scale with $\dot{\gamma}$.

Importantly, this analysis implies that we can always investigate the $\dot{\gamma}$-dependence of the shear stress without worrying about the other components of the stress tensor, provided that the suspension is incompressible. From now on we consider only σ_{12}, but bear in mind that similar analyses could be performed for N_1 and N_2. The analysis also illustrates how to construct a non-dimensionalised equation when there are several physical quantities with the same dimensions; we make use of the procedure in future sections when there are multiple length scales present.

7.2 Rough hard spheres in Stokes flow

The next simplest case is a system of hard spheres that are allowed to come into direct mechanical contact due to finite surface roughness with characteristic length scale ξ [84], Fig. 7.5(a). As discussed in the previous section, for perfectly smooth spheres with no-slip boundary conditions, an infinite force is required to push their surfaces into contact. Physically, the force arises from the need to evacuate fluid from the gap. Surface roughness leads to a finite amount of slip, which facilitates drainage of the fluid and can lead to direct mechanical contact [84].

When particle surfaces are separated, the standard expressions for lubrication forces remain correct for realistic values of surface roughness [127]. When they contact, the hydrodynamic lubrication force is cut off at a value $F_{\mathrm{sq}} \sim \eta_f R^2 W \xi^{-1}$ set by ξ [120, 128, 129], Fig. 7.5(b).

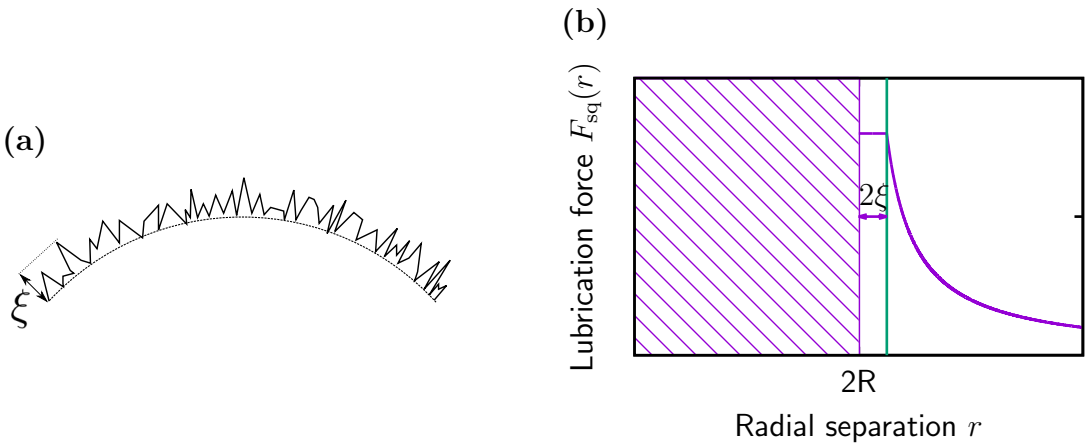

Figure 7.5: Rough hard spheres in Stokes flow. (a) Normal contact force $F_N(r)$ versus centre-to-centre separation r. (b) Squeeze lubrication force F_{sq}, which is cut off at $r = 2\xi$.

7.2.1 Dimensional analysis

For rough hard spheres, there are contributions to the total suspension stress from both hydrodynamics σ_h and contact forces σ_c. These contributions are typically assumed to be additive [25, 120, 130]:

$$\sigma = \sigma_h + \sigma_c. \tag{7.19}$$

The hydrodynamic stress is generated in the same manner as for smooth spheres and $\propto \eta_f \dot{\gamma}$. For the contact part, we assume that the particles experience Coulomb friction with static friction coefficient μ_S and dynamic friction coefficient μ_K; this assumption has been shown to hold in diverse dry [23, 131] and wet [23, 54] systems. There are now two length scales, the radius R and the surface roughness ξ. From dimensional analysis, we obtain:

$$\sigma = \eta_f \dot{\gamma} C \left(\phi, \mu_S, \mu_K, \frac{\xi}{R} \right). \tag{7.20}$$

We assume that ξ/R is fixed, i.e., that the roughness height does not vary with $\dot{\gamma}$. If both μ_S and μ_K are independent of $\dot{\gamma}$ then $\Sigma_{ij} \propto \dot{\gamma}$: the shear viscosity is independent of $\dot{\gamma}$ and hence there is no shear thickening.

Since μ_K can depend on the sliding velocity for many materials [132, 133] one might expect a $\dot{\gamma}$-dependent rheology in general; shear thickening can in principle

occur if $d\mu_K/d\dot{\gamma} > 0$. Existing measurements on granular suspensions (which permanently occupy the shear-thickened state, Ch. 6) find $\eta \approx$ constant [54, 134], or weakly shear thinning [53], implying that, in practice, $\mu_K \approx$ constant. A $\dot{\gamma}$-dependent μ_S is in principle also possible [1]; although, we postpone a discussion of this possibility to §7.4. For the remainder of this section, we assume that both friction coefficients are independent of $\dot{\gamma}$.

7.2.2 Viscous scaling of contact forces

The viscosity at fixed ϕ is constant because there is still only one stress scale $\eta_f\dot{\gamma}$ and one single time scale $\dot{\gamma}^{-1}$ in the system. Both μ_S and μ_K are dimensionless, so there is no characteristic stress scale associated with contacts: the contact stress also scales as $\eta_f\dot{\gamma}$. This fact can be rationalised as follows.

For perfect hard particles the normal force can take on any negative (compressive) value required to prevent particle overlaps [120]. In reality, this force arises because the particles are elastic and the force is generated by a small deformation δ. It has been shown, however, that the rheology of granular media does not depend on contact elasticity if the ratio δ/R is below 10^{-4} [120]. The elastic moduli of the particles we study in the next chapter, PMMA and silica, are $E \sim 10^9$ Pa and $E \sim 10^{10}$ Pa, respectively, and the highest accessible shear stress in our rheometers is $\sim 10^4$ Pa, corresponding to dimensionless overlaps of $\delta/R \sim 10^{-5}$ and 10^{-6}. Thus, for the purposes of this thesis, our particles can be regarded as being perfectly hard and σ_c is expected to scale as $\eta_f\dot{\gamma}$. For soft particles, one would have to explicitly include E (or δ) in the dimensional analysis, introducing a second stress scale and hence permitting a rate-dependent rheology. Simulations find a shear-thinning, rather than thickening, rheology when δ is not negligible [112].

7.2.3 Surface roughness ξ

The primary effect of decreasing the surface roughness ξ/R is to systematically increase both the hydrodynamic and contact contributions to the viscosity, which occurs because the typical gap size h is smaller and therefore the typical scale of hydrodynamic forces ($\propto h^{-1}$) is larger [88]. Surface roughness also prevents particles from entering the closed orbits depicted in Fig. 7.4, provided $\xi \gtrsim 10^{-4}$

[135, 136], which is the case in most practical situations.

In simulations, it is common to truncate the divergence of the lubrication force at $b/R \gtrsim 10^{-4}$ to mimic surface roughness. In the Stokesian dynamics simulations of Brady *et. al.* (e.g., [129, 137, 138]), which have been used extensively to study shear thickening, contact forces are not considered and this cut off simply acts as a "sieve" for particle centres. The effect of decreasing b is, again, to increase the viscosity, which in that case is purely hydrodynamic.

7.2.4 Microstructure and normal stress differences

Although the shear viscosity is constant in both cases, there are fundamental differences between hard sphere flow with and without contacts. Particle contacts break the reversal symmetry of Stokes flow [135, 136], so that particles no longer return to their original locations after reversing the direction of flow [27]. This leads to an anisotropic microstructure in steady state [139] and to non-zero normal stress differences [88]. Both N_1 and N_2 are found to be linearly proportional to $\dot{\gamma}$ (which is expected on dimensional ground given that $\sigma_{12} \propto \dot{\gamma}$) N_1 and negative, with $|N_2| > |N_1|$ [53].

The breaking of Stokes reversal symmetry means that the instantaneous microstructure, and hence the instantaneous viscosity, $\hat{\eta}(\gamma)$, depend on the shear history for transient flows. In that case one can observe *strain* thickening, $d\hat{\eta}/d\gamma > 0$, e.g., after flow reversal (see Ch. 8), but in a manner that is independent of $\dot{\gamma}$ – that is, $\hat{\eta}$ is a function of γ only [3] Whatever the transient behaviour, the steady state viscosity η must be independent of $\dot{\gamma}$ on dimensional grounds.

[3] This is nicely illustrated by figure 6 in Gadala-Maria and Acrivos [27].

7.3 Smooth hard spheres with Brownian motion

We now consider the effect of adding non-hard-sphere interactions, which introduce additional time and length scales. We begin with the most extensively studied case: smooth hard spheres (no contacts) with Brownian motion. There are two contributions to the stress in such a system: a hydrodynamic contribution $\sigma_h \propto \eta_f \dot{\gamma}$ and an entropic contribution σ_b, which is $\propto k_B T$:

$$\sigma = \sigma_h + \sigma_b. \tag{7.21}$$

7.3.1 Dimensional analysis

There are now $m = 6$ physical quantities: σ, $\dot{\gamma}$, η_f, R, n and the thermal energy $k_B T$, set by the temperature T. Accordingly, there are three independent dimensionless groups. For comparative purposes, we construct two of the groups as before, $\Pi_1 = \sigma/(\eta_f \dot{\gamma})$ and $\Pi_2 = \phi$. The third group is commonly chosen to have one of two forms in the literature [109]. The first is as the ratio of σ and the entropic stress scale $k_B T/R^3$, $\Pi_3 = \sigma/(k_B T/R^3)$, which leads to

$$\sigma = \eta_f \dot{\gamma} C\left(\phi, \sigma \frac{R^3}{k_B T}\right). \tag{7.22}$$

Eq. (7.22) implies that a σ-dependent rheology is possible at fixed ϕ, controlled by the relative magnitude of the viscous and entropic stresses. The second choice is in the form of a reduced shear rate, $\Pi_3' = \eta_f \dot{\gamma}/(k_B T/R^3)$, which is just the bare Peclet number Pe defined in Eq. (3.9) (up to a factor of π). In that case, one may write

$$\sigma = \eta_f \dot{\gamma} C'(\phi, \mathrm{Pe}), \tag{7.23}$$

which implies that a $\dot{\gamma}$-dependent rheology is possible, controlled by a competition between the timescale associated with the imposed shear $\dot{\gamma}^{-1}$ and the Brownian time $\tau_B \propto \eta_f R^3/(k_B T)$.

It is incorrect to conclude upon inspection of Eq. (7.22) that the rheology is an inherently σ-controlled phenomenon, just as it is incorrect to view it as an

inherently $\dot{\gamma}$-controlled phenomenon based on Eq. (7.23): the phenomenology described by both equations must be the same, as the underlying physics cannot depend on which dimensionless numbers we choose to describe it. Bearing this point in mind, we now investigate whether the $\dot{\gamma}$- (equivalently, σ-) dependent rheology can include shear thickening. Historically, most work on Brownian systems has been done by way of $\dot{\gamma}$-controlled simulations [128–130] where Pe is the natural variable, so we take this as our starting point.

7.3.2 Low ϕ: two-particle hydrodynamic thickening

With regards to shear thickening, the existing literature addresses two distinct regimes: moderate concentrations $0.3 \lesssim \phi \lesssim 0.5$, where two-particle interactions are regarded as begin dominant, and high concentrations, $\phi > 0.5$, where many-body effects are dominant. At $0.3 \lesssim \phi \lesssim 0.5$, Stokesian dynamics simulations found the relative viscosity $C'(\phi, \mathrm{Pe})$ to have the form shown in Fig. 7.6 [130, 140] (bold line). At $\mathrm{Pe} \ll 1$, the system exhibits shear thinning before shear thickening at $\mathrm{Pe} \sim \mathcal{O}(10)$. The rate of increase is greater at higher ϕ, but C' maintains approximately the same functional form and increases approximately logarithmically with Pe [140]. Bossis and Brady [130] and later Foss and Brady [140] separated the viscosity into a (conservative) Brownian contribution $\eta_B = \sigma_b/(\eta_f \dot{\gamma})$ and a (dissipative) hydrodynamic contribution $\eta_h = \sigma_h/(\eta_f \dot{\gamma})$, and found that the thickening was driven entirely by an increase in η_h (triangles in Fig. 7.6), while η_b (squares) exhibited shear thinning.

The microscopic origin of the increasing hydrodynamic contribution $\eta_h(\dot{\gamma})$ at high Pe was explored by Brady and Morris [129]. If the surfaces of two particles in the suspension are separated by a distance $h \gg R$, then their relative motion is dominated by the advection provided by the imposed shear field and unaffected by Brownian motion – the pair trajectories are symmetric upon flow reversal, as in Fig. 7.4. Below some critical separation $h_{\min}$, Brownian motion is able to influence their trajectories and break the symmetry of Stokes flow in a manner similar to direct mechanical contact [120]. They find that there is an $\mathcal{O}(R\mathrm{Pe}^{-1})$ boundary layer in which the non-Newtonian shear thickening high-Pe rheology is determined; this boundary layer also leads to a highly asymmetric $g(\underline{r})$, which shows an enhanced pair probability along the compression axis [140]. As Pe is increased, the boundary layer thickness decreases as Pe^{-1} and hence the typical lubrication force between particles pairs along the compression axis, $f_h \propto 1/h$,

increases. At the same time, the number of particles involved in the chains of particles along the compression axis scales as Pe, together giving rise to an $\mathcal{O}(1)$ increase in C'.

The onset of thickening was found to occur at a Pe that decreases with ϕ [140]. Brady and Morris argued that the onset of thickening is associated with a modified Peclet number $\bar{\text{Pe}}$ which takes into account the fact that the short-time self-diffusion coefficient $D_s(\phi)$ is an increasing function of ϕ,

$$\bar{\text{Pe}} = \frac{\dot{\gamma} R^2}{2D_s(\phi)} = \text{Pe}\frac{\eta'_\infty(\phi)}{\eta_f} \tag{7.24}$$

This $\bar{Pe}$ is related to the bare Peclet number by a factor of $\eta'_\infty(\phi)/\eta_f$, where $\eta'_\infty(\phi)$ is the so-called high-frequency hydrodynamic viscosity, defined as the hydrodynamic contribution to the viscosity for an equilibrium microstructure, i.e., in the limit of $\text{Pe} \to 0$, Fig. 7.6; $\eta - \eta'_\infty$ is then the contribution to η from particle interactions.

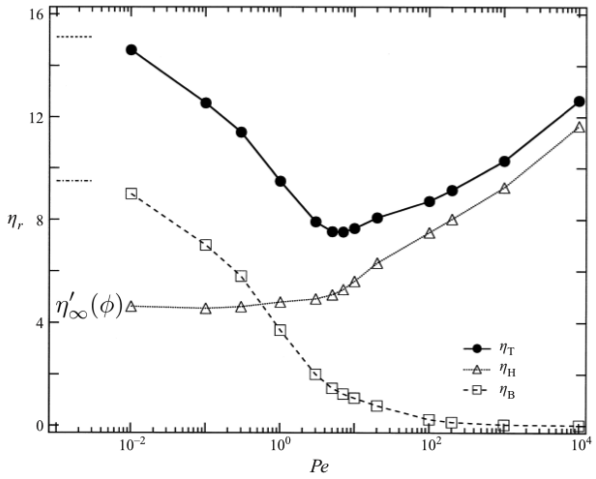

Figure 7.6: Relative viscosity versus Pe for Stokesian dynamics simulations of a $\phi = 0.45$ suspension of hard spheres with Brownian motion. The bold line corresponds to the total viscosity, triangles to the component due to hydrodynamics, and squares to the direct contribution from Brownian motion. Adapted from [140].

It is more intuitive to view the phenomenon from an imposed-stress standpoint, Eq. (7.22). At high Pe ($\sigma \gg k_B T/R^3$), Brownian motion plays the role of a short-ranged repulsive force $f_b \sim k_B T/h$, Fig. 7.7 [4]. As σ is increased, the entropic

[4]This can be seen by considering two Brownian hard spheres confined to move one dimension,

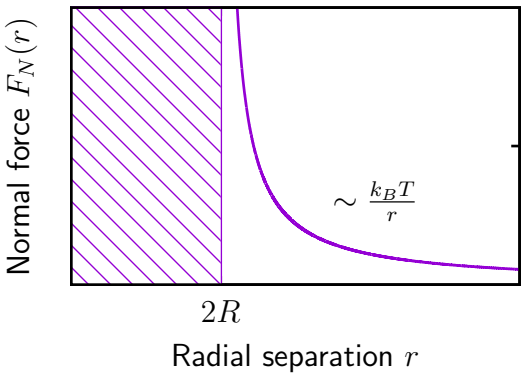

Figure 7.7: Repulsive force between a pair of smooth spheres due to Brownian motion.

"springs" between particles are compressed and the average separation between their surfaces decreases, resulting in an increase in hydrodynamic dissipation. The edge of the boundary layer is the surface separation, $h_{\min}$, at which the local Brownian stress $f_b(h_{\min})/R^2 = k_B T/(h_{\min} R^2)$ acting to separate the surfaces balances the viscous stress $\sim \eta_f \dot{\gamma}$ driving them together:

$$h_{\min} = \frac{k_B T}{\eta_f \dot{\gamma} R^2} = R\mathrm{Pe}^{-1}, \tag{7.25}$$

i.e., we recover the $R\mathrm{Pe}^{-1}$ scaling predicted by Morris and Brady [129].

However we choose to view it, this type of thickening is a two-particle phenomenon and is purely hydrodynamic in origin: it results from a decrease in the average separation between particle surfaces with increasing $\dot{\gamma}$.

7.3.3 Low ϕ: repulsive potential

A similar form of shear thickening occurs when, instead of Brownian motion, there is a finite-range repulsive potential $U(r)$ between particles, e.g., due to repulsion via an electric double layer. The shear stress in such a system has the

which mimics two neighbouring spheres in chain of lubricated particles aligned along the compressive axis. The first sphere is fixed at the origin and the second sphere is free to move along the x axis such that the surface separation can vary from zero (when the spheres are touching) to some maximum value h. The free energy of such a system is $\mathcal{F}(h,T) = -k_B T \ln(h/\lambda_T)$, where λ_T is a constant length scale (set by, e.g., the de Broglie wavelength of the solvent molecules), and the entropic repulsive force that arises when h is decreased is $f_b = -\partial\mathcal{F}/\partial h \sim k_B T/h$.

usual viscous contribution σ_h and a (conservative) potential contribution σ_r:

$$\sigma = \sigma_h + \sigma_r. \tag{7.26}$$

If the interaction potential is characterised by a length scale ϵ and repulsive force f^* (e.g., set by the Debye length κ^{-1} in a charged system), then we can write the shear stress as

$$\sigma = \eta_f \dot{\gamma} C \left(\phi, \sigma \frac{R^2}{f^*}, \frac{\epsilon}{R} \right). \tag{7.27}$$

Eq. (7.27) is similar to Eq. (7.22), but with f^*/R^2 playing the role of the entropic stress $k_B T/R^3$ [the absence of a dimensionless length scale in Eq. (7.22) is because the Brownian force is described by a power law]. Simulations again find that thickening is caused by a decrease in the average inter-particle spacing [14]. Specifically, it is found that $\eta \sim \ln[h/(2R)]$, with the exact form of $\eta(\sigma)$ depending on the pair potential $U(r)$ [14, 141].

The direct contribution to the suspension viscosity from finite-range repulsion $\eta_r = \sigma_r/(\eta_f \dot{\gamma})$, like Brownian motion, is found to exhibit shear thinning [130], which occurs because the effective volume fraction is reduced as σ is increased [142]. Brady and Bossis [130] showed that, in such a system, the shear thickening is also driven entirely by the hydrodynamic contribution η_h.

One can equivalently view this form of thickening as a competition between $\dot{\gamma}^{-1}$ and the time scale $\eta_f R^2/f^*$, and the stress can be written as

$$\sigma = \eta_f \dot{\gamma} C \left(\phi, \frac{\eta_f \dot{\gamma} R^2}{f^*}, \frac{\epsilon}{R} \right), \tag{7.28}$$

Experimentally, the onset of thickening in systems with finite-range repulsion is almost always associated with a ϕ-independent *stress* σ^* [81] whose particle size dependence is governed by the R-dependence of $f^*(R)$, so it is more convenient to consider Eq. (7.27).

7.3.4 The small gap problem

It is important to emphasise that the foregoing discussion concerns *steady-state* rheology. Simulations of smooth hard spheres with no-slip boundary conditions are susceptible to the so-called "small gap problem": if shear is applied to an assembly of hard spheres at $\phi \gtrsim 0.40$ interacting only hydrodynamically (no Brownian motion) it is found that the gaps between the particles shrink rapidly from $\sim 10^{-1}R$ to $\sim 10^{-8}R$ over a strain of $\mathcal{O}(1)$, resulting in a viscosity that diverges with increasing strain [58, 143]. The simulations eventually crash when a system-spanning cluster is formed and the system never reaches steady state.

The effect of adding Brownian motion or finite-range repulsion is to delay the formation of a system-spanning cluster to some finite Pe value [143]. Thus, for every flow curve, e.g., Fig. 7.6, there is a critical Peclet above which the viscosity of the system rapidly becomes infinite, the exact value being sensitive to the choice of integration scheme used in the simulation [58].

Even before this point, typical gap sizes can become unphysically small; e.g., at $\phi = 0.55$, thickening begins at Pe ≈ 10 and by Pe $= 10^3$ typical gap sizes are in the range $h/R \sim 10^{-4} - 10^{-7}$. For a $R \sim 1$ μm colloid, this corresponds to separations that are comparable to the dimensions of the solvent molecules and molecules on the surface of the particles – the suspension can no longer be viewed as smooth particles in a liquid continuum. Despite the orders of magnitude change in $h/(2R)$ during thickening, the viscosity increases by only a factor of ≈ 1.5.

In simulations, the pathological collapse of particle gaps is artificially cut off by truncating the divergence of the hydrodynamic force at a finite length scale b; then, $\eta(\dot{\gamma})$ ostensibly tends to a plateau [119], although it is unclear from the literature if this is generic. In the shear-thickening regime, η is still a logarithmically increasing function of $\dot{\gamma}$; but, the magnitude of the viscosity increases as b/R is made smaller [138] owing to the smaller typical particle surface separations.

In real systems, this pathological collapse is presumably cut off by finite surface roughness: particles instead enter direct mechanical contact.

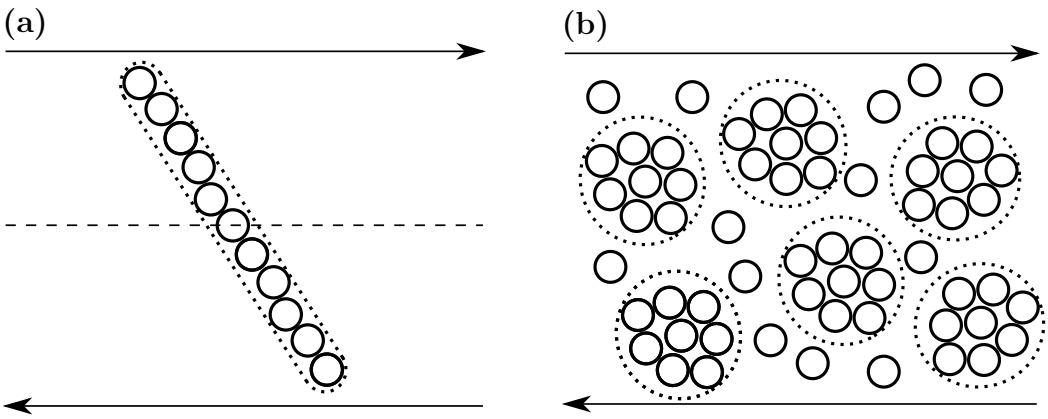

Figure 7.8: Schematics of the different kinds of hydrodynamic clustering proposed in the literature: (a) elongated clusters of particles aligned with the compression axis that behave as a rigid slender body and (b) temporary aggregates that increase the effective volume fraction of the suspension by shielding pockets of the suspending fluid.

7.3.5 High ϕ: "hydroclustering"

It is now widely accepted [35, 81], for the above reasons, that the order-of-magnitude or more increases in $\eta(\dot{\gamma})$ observed for $\phi > 0.50$ experimentally are not related to this two-particle mechanism, which is always weak and continuous in steady state. This realisation prompted researchers to propose theories that involve many-body effects. The search for an alternative theory was also motivated by scattering dichroism measurements on model hard-sphere colloids [144], which revealed the presence of transient density fluctuations during shear thickening that relaxed on time scales of $\mathcal{O}(10\text{ s})$ after flow cessation. The central idea in these theories is that clusters of particles bonded to each other by strong lubrication forces ("hydroclusters") disrupt the flow field differently to homogeneously dispersed particles, resulting in a more pronounced increase in η. To the author's knowledge, there is no predictive theory for hydrocluster thickening and the details of how hydroclusters form, the morphology of the clusters and how they affect η all remain unclear. In spite of these shortcomings, the notion of a hydrocluster is used frequently in the literature, so we present a short review of the main ideas.

The term "hydrocluster" was first used three decades ago by Brady and Bossis to refer to a chain of particles separated by narrow lubrication films aligned with the compression axis [128], Fig. 7.8(a). They showed that the hydrodynamic stress obtained in the usual way by computing the average stresslet over the particles

within the chain (see §3.3.2) was the same as the stress that the chain would exert if it was a rigid slender body [137]. Thus, the two-particle thickening described in the last section can be thought of as being caused by rigid clusters of particles that grow in size with Pe. In steady state, it is unclear to us how this clustering gives rise to an increase in $\eta(\dot{\gamma})$ above the two-particle prediction, §7.3.2 [129].

Melrose *et. al.* suggested that such clustering might lead to an infinite viscosity if the inter-particle gaps collapsed and a percolating cluster was formed, providing a potential mechanism for shear jamming; however, since the shear stress is purely hydrodynamic in origin, it would drop to zero immediately after $\dot{\gamma}$ dropped to zero as there would be no relative motion between the colloids. (It cannot, therefore, account for the existence of static granules formed by hard-sphere-like particles [80, 126].)

An alternative idea, due to Wagner [97], supposes that roughly spherical, rather than elongated, clusters are formed, Fig. 7.8(b). The solvent on the interior of the clusters is shielded from the rest of the suspension, so the effective volume fraction of the suspension comprising these temporary aggregates is increased [130], resulting in closer proximity to random close packing and a higher viscosity. The viscosity in the shear-thickened state could in principle diverge at $\phi < \phi_{\mathrm{RCP}}$; although, such a system could never be jammed at $\dot{\gamma} = 0$ for the reason described above.

7.4 Frictional hard spheres with finite-range repulsion

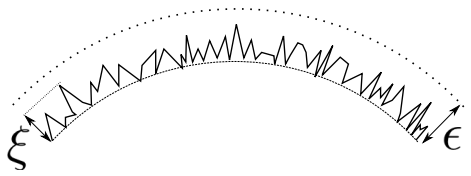

Figure 7.9: (a) Schematic of a hard particle with surface roughness ξ and repulsive potential with range ϵ.

We now consider hard spheres interacting with a finite-range potential, but which are allowed to enter direct mechanical contact, Fig. 7.9. As before, the interaction potential has a characteristic force f^* and range ϵ and the surface roughness is ξ. The total stress has contributions from hydrodynamics $\sigma_h \propto \eta_f \dot{\gamma}$, contacts σ_c

and potential interactions σ_r:

$$\sigma = \sigma_h + \sigma_c + \sigma_r. \tag{7.29}$$

There are still only two stress scales, $\eta_f\dot{\gamma}$ and f^*/R^2, but now three length scales: R, ϵ and ξ.

7.4.1 Dimensional analysis

As in §7.2, we restrict our attention to Coulombic friction and can write, by dimensional analysis:

$$\sigma = \eta_f\dot{\gamma}C\left(\mu_S, \mu_K, \sigma\frac{R^2}{f^*}, \frac{\xi}{R}, \frac{\epsilon}{R}, \phi\right); \tag{7.30}$$

or, equivalently:

$$\sigma = \eta_f\dot{\gamma}C\left(\mu_S, \mu_K, \sigma\frac{\eta_f\dot{\gamma}R^2}{f^*}, \frac{\xi}{R}, \frac{\epsilon}{R}, \phi\right). \tag{7.31}$$

As before, we assume that f^*, ϵ and ξ are rate independent. Any $\dot{\gamma}$ dependence therefore enters via μ_S, μ_K and $\eta_f\dot{\gamma}R^2/f^*$ (or $\sigma R^2/f^*$).

The effect of varying the six arguments in Eq. (7.30) and (7.31) has yet to be explored systematically and we do not attempt to do so here. The only case to be given serious attention so far in the literature is for $\epsilon \approx \xi$ [2, 56], i.e., when the range of the interaction potential is just sufficient to keep the surfaces of the particles apart. We focus on this special case, but speculate later on possible mechanisms for thickening when $\epsilon > \xi$.

7.4.2 Short-ranged repulsion: $\epsilon \approx \xi$

We assume that ϵ remains equal to ξ when changing R (this could be achieved by suitably tuning the Debye length in a real system), so that σ depends on

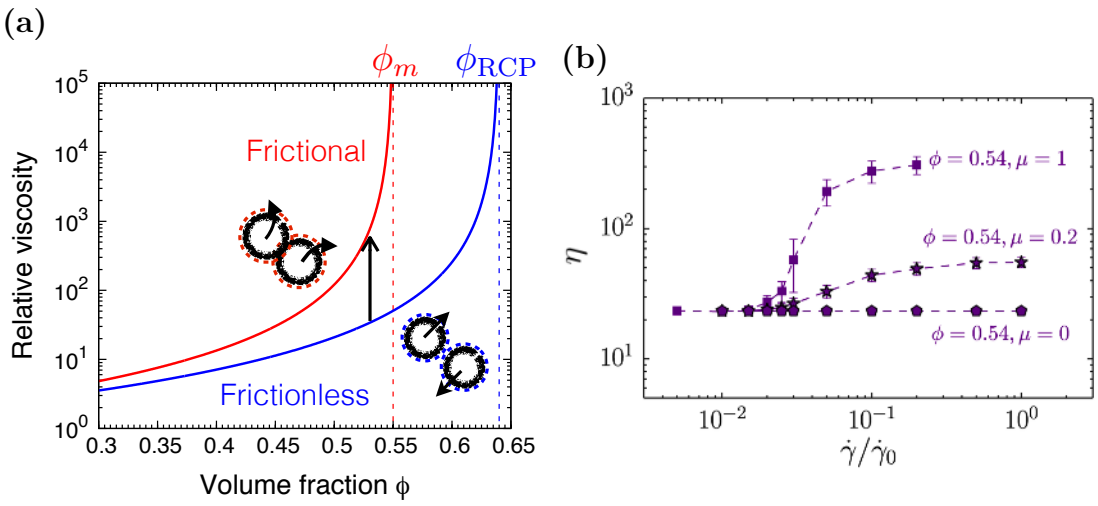

Figure 7.10: (a) Schematic of the viscosity branches present in WC theory. At $\sigma R^2/f^* \ll 1$, particles can slide past each other and the system undergoes Newtonian flow with a viscosity that divergences at random close packing $\phi_{\rm RCP}$. At $\sigma R^2/f^* \gg 1$, particles are pressed into frictional contact, resulting in a viscosity that diverges at a lower concentration, $\phi_m < \phi_{\rm RCP}$. Shear thickening corresponds to a transition from the lower to the upper branch at fixed ϕ (vertical arrow). (b) Relative as a function of reduced shear rate $\dot\gamma/\dot\gamma_0$ from simulations with a normal-load-dependent static friction coefficient at $\phi = 0.54 < \phi_m$; $\dot\gamma_0 = \hat f/(6\pi\eta_f R^2)$, where $\hat f$ is the normal load at which the static friction coefficient switches from zero to $\mu > 0$. Different curves correspond to different values of μ_S, as labelled. Shear thickening is eliminated altogether by setting $\mu_S = 0$. Taken from [56].

$\xi/R = \epsilon/R$ only; then, Eq. (7.30) reduces to

$$\sigma = f\left(\mu_S, \mu_K, \sigma\frac{R^2}{f^*}, \frac{\xi}{R}, \phi\right)\eta_f\dot\gamma. \tag{7.32}$$

Wyart and Cates (WC) theory, first introduced in Ch. 5, makes predictions for just such a system for the special case of constant $\mu_S > 0$ and $\mu_K = 0$. They argue that at $\sigma R^2/f^* \ll 1$ particle surfaces are separated by a thin lubrication film with thickness $\sim \mathcal{O}(\epsilon - \xi)$ and the stress in the system is mainly hydrodynamic. (At this point, the value of μ_S is irrelevant, as there are no contacts in the system.) At $\sigma^2/f^* \approx 1$, lubrication films begin to rupture as particles are pushed over the repulsive barrier and into contact. For $\sigma R^2/f^* \gg 1$, all particles are in contact and the rheology is equivalent to non-Brownian, frictional flow at fixed μ_S, described by Eq. (7.20). The transition between these two limiting regimes as a function of $\dot\gamma$, or σ, manifests as shear thickening.

The reader is referred to Ch. 5 for a complete discussion of WC theory. Here, we comment on the physical origin of frictional thickening, which is fundamentally different to the hydrodynamic thickening in §7.3. On the frictionless branch [blue line in Fig. 7.10(a)] particles can slide past one another and there are no constraints on the rotational degrees of freedom: the viscosity diverges at random close packing $\phi_{\mathrm{RCP}} \approx 0.64$, where the number of contacts per particle $Z_c = 6$ (in 3-d; $Z_c = 4$ in 2-d) [23]. The microscopic origin of the divergence is still unclear; however, a popular explanation is that it is caused by a divergence in the non-affine displacement particles must execute to avoid particle overlaps [86] as jamming is approached. Since the particles have to move through the fluid and are subjected to viscous drag this leads to a divergence in dissipation. Simulations [145] found these non-affine displacements to be spatially heterogeneous, where the heterogeneity is characterised by a length scale ζ that grows approaching ϕ_{RCP}; although, it has yet to be established if ζ also diverges at ϕ_{RCP} [5].

On the thickened branch [red line in Fig. 7.10(b)], where all the particles are in direct mechanical contact, static friction places constraints on their rotational degrees of freedom: some of the contacting particles are required to roll around, rather than slide past, each other. The fraction of frictional contacts that are rolling is determined by the value of μ_S; at $\mu_S = 0$, all contacts are mobilised, while at $\mu_S = \infty$ all contacts are rolling. The presence of rollers reduces the number of contacts per particle Z_c required for the system to become rigid, which ranges from $Z_c = 4$ for $\mu_S = \infty$ to $Z_c = 6$ for $\mu_S = 0$, corresponding to a range of jamming volume fractions $0.55 \lesssim \phi_m \leq \phi_{\mathrm{RCP}}$. Thus, at fixed ϕ, the onset of static friction results in a closer proximity to jamming and hence a higher viscosity, Fig. 7.10(a).

In WC theory, shear thickening is a continuous transition between these limiting frictionless and frictional states as the fraction of frictional contacts in the system, $f(\sigma)$, increases from zero to one with increasing σ [Fig. 5.9(a)]. For the case of $\mu_S = \infty$, $f(\sigma)$ also corresponds to the fraction of rolling contacts in the system; hence, increasing $f(\sigma)$ amounts to interpolating the jamming volume fraction $\phi_J(\sigma)$ between ϕ_{RCP} and ≈ 0.55. For finite μ_S, where there are some mobilised contacts at any σ, $f(\sigma)$ does not correspond to the fraction of rollers, but instead interpolates ϕ_J between ϕ_{RCP} and some $\phi_m > 0.55$. Since there is a one-to-one relationship between Z_c and μ_S, this situation is ostensibly equivalent to one in

[5] Whether or not ζ diverges is important for systems of finite size, because if $\zeta \sim H$ then confinement effects will become relevant and the rheology can no longer be described by a local constitutive equation.

which there is no repulsive barrier [i.e., $f^* = 0$ in Eq. (7.32)] but μ_S itself is directly dependent on σ [126].

Simulations of hard spheres with a normal-load-dependent static friction coefficient support the above scenario [56], Fig. 7.10(b). The friction coefficient between a pair of particles is zero below a critical normal load [related to f^* in Eq. (7.32))] and $\mu_S > 0$ otherwise. They find continuous shear thickening between quasi-Newtonian states below $\phi_m < \phi_{\mathrm{RCP}}$, whose magnitude depends on the value of μ_S (top two curves). Thickening is eliminated entirely by setting $\mu_S = 0$ (bottom curve) – the system occupies the lower, frictionless branch at all $\dot{\gamma}$. A similar phenomenology was observed for frictional Brownian spheres, in which Brownian motion acts as an effective short-range repulsion [119].

To the author's knowledge, there has been no relevant microscopic study of the mechanism behind frictional jamming and hence there is little understanding of the microstructural and dynamical changes that accompany frictional shear thickening. Mills and Snabre [87] proposed that the viscosity divergence is caused by a divergence in the size of locally-jammed regions with concentration ϕ_m higher than the suspension average ϕ; although, their prediction is for an isotropic system and simulations predict a microstructure that is markedly anisotropic, at least during continuous shear thickening [56]. Ness and Sun [100] observed a growth in velocity fluctuations near ϕ_m reminiscent of the non-affine fluctuations in frictionless systems; however, they simulate using soft particles and it is unclear whether the fluctuations diverge at ϕ_m.

7.4.3 Long-ranged repulsion

We now briefly address the case of $\epsilon > \xi$, where the range of the repulsive potential extends beyond the surface roughness. There has yet to be a systematic investigation of such a system; however, we speculate that one would observe two-particle hydrodynamic thickening of the kind described in §7.3.3 until the average surface separation became comparable to ξ, whereupon the hydrodynamic contribution to the viscosity would saturate. At higher σ, we expect to see frictional shear thickening as lubrication films start to rupture. The relative role of frictional contacts and lubrication forces are not clear when repulsion is finite ranged and we address the problem experimentally in the next chapter.

7.5 Hard spheres with inertia

In §7.1 and 7.2 we considered the case of inertialess hard spheres in Stokes flow, for which the rheology is independent of $\dot{\gamma}$. In this section, we consider the case where particle inertia is not negligible but the fluid flow around the particles is still described by Stokes' equation. There are now two time scales: the inverse shear rate, $\dot{\gamma}^{-1}$, and the inertial time $\tau_I = m/\xi$, where m is the particle mass and ξ is the Stokes drag. We will restrict our attention to spherical particles, for which $\xi = 6\pi\eta_f R$ and $m = (4/3)\pi R^3 \rho_p$, where ρ_p is the particle density. One can then define the *particle* Reynolds number as the ratio of these two time scales [6]:

$$\mathrm{Re}_p = \tau_I \dot{\gamma} = \frac{\rho_p R^2 \dot{\gamma}}{\eta_f}. \tag{7.33}$$

This is not to be confused with the *fluid* Reynolds number, Eq. (7.9), which we assume to be $\ll 1$

There are two stress scales, the viscous stress $\eta_f \dot{\gamma}$ and the inertial stress scale, which is set by the kinetic energy of the particles per unit volume $mv^2/R^3 \sim (m\dot{\gamma}^2 R^2)/R^3 = \rho_p \dot{\gamma}^2 R^2$ [120]. Re_p can also be interpreted as the ratio of these two stresses.

Experiments [23, 35] have observed two distinct flow regimes depending on the value of Re_p, Fig. 7.11. At $\mathrm{Re}_p \ll 1$, one recovers viscous flow with $\sigma \propto \eta_f \dot{\gamma}$ and the phenomenology is as described in §7.2. At $\mathrm{Re}_p \gg 1$, viscous effects are negligible and the flow is dominated by particle inertia. One can estimate the size of particle required to access the inertial thickening regime experimentally. For silica in water, $\rho_p \sim 2 \times 10^3$ kg.m^{-3} and $\eta_f = 10^{-3}$ Pa.s, and taking the maximum achievable shear rate in conventional rheometry $\dot{\gamma} \sim 10^3$ s^{-1}, $\mathrm{Re}_p = 1$ corresponds to $R \approx 20$ μm. We focus on this regime in the following analysis.

[6] The physical meaning of Eq. (7.33) can been seen by considering the motion of an isolated sphere of mass m that is initially at rest in a fluid and is subjected to a constant force F at time $t = 0$. The equation of motion of the particle is $m\dot{v} = -\xi v + F$, which can be solved to yield $v(t) = v_\infty[1 - \exp(-\xi t/m)]$, where $v_\infty = F/\xi$ is the terminal velocity of the particle. The timescale $\tau_I = m/\xi$ is therefore the characteristic time for the particle to accelerate to v_∞: if the characteristic timescale of the flow $\dot{\gamma}^{-1}$ is shorter than τ_I, then the acceleration of the particles in the suspension cannot be neglected. So far, we have only considered the case of $m = 0$, for which $\tau_I = 0$ and the particles instantaneously attain their steady velocity.

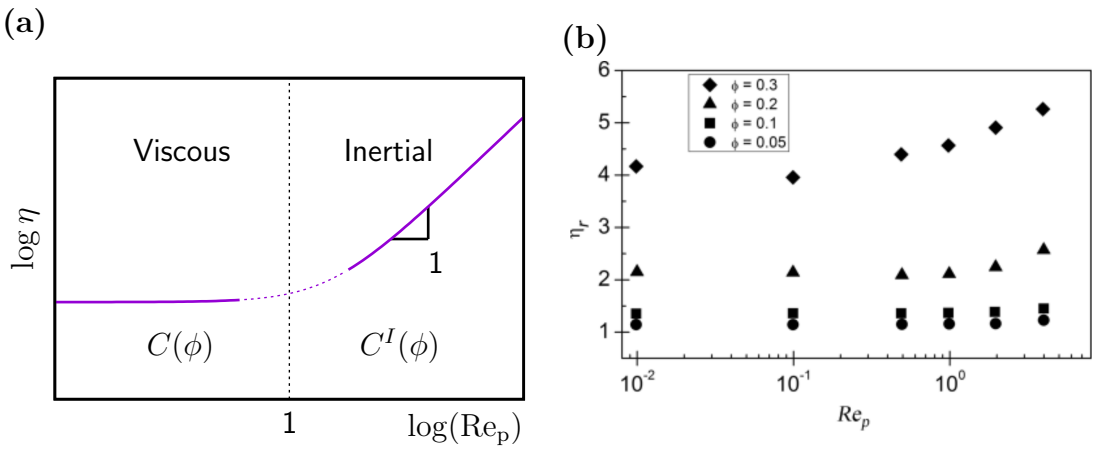

Figure 7.11: (a) Schematic of continuous inertial thickening of hard particles. (b) Simulation data from [35] (figure 8.28, therein) for the viscous-to-inertial crossover.

7.5.1 Dimensional analysis

For simplicity, we ignore potential interactions and the finite length of surface roughness, but assume that particles are allowed to come into contact. There are $m = 6$ physical variables, σ, $\dot{\gamma}$, η_f, n, R and ρ_p, and $6 - 3 = 3$ independent dimensionless groups, which we choose for convenience to be $\Pi_1 = \sigma/(\rho_p \dot{\gamma}^2 R^2)$, $\Pi_2 = \phi$ and $\Pi_3 = \mathrm{Re}_p$. The resulting non-dimensionalised equation is

$$\sigma = \rho_p \dot{\gamma}^2 R^2 C^I(\phi, \mathrm{Re}_p). \tag{7.34}$$

Experimentally, it is found that the rheology becomes independent of Re_p at $\mathrm{Re}_p \gg 1$ [23] – the viscous stress scale $\eta_f \dot{\gamma}$ is no longer relevant. In that limit, one obtains

$$\sigma = \rho_p \dot{\gamma}^2 R^2 C^I(\phi). \tag{7.35}$$

where C^I is a function of ϕ only. Thus, at fixed ϕ the shear stress scales quadratically with $\dot{\gamma}$: inertial hard spheres shear thicken with a viscosity that increases linearly with $\dot{\gamma}$, $\eta \propto \dot{\gamma}$ (this is referred to as Bagnold scaling in the literature).

Furthermore, if Re_p is increased from a value $\ll 1$ to a value $\gg 1$ then one expects $\eta(\dot{\gamma})$ to transition from viscous Newtonian rheology [governed by Eq. (7.20)] to

continuous inertial thickening with a slope of one on a log-log plot, Fig. 7.11(a). Simulations [35] find this transition to occur at a critical $\mathrm{Re_p} \sim \mathcal{O}(1)$ that is a decreasing function of ϕ up to $\phi = 0.30$, Fig. 7.11(b); the ϕ dependence at higher concentrations has not been reported.

7.5.2 Inertial thickening with changing friction

Contact dynamics simulations in the paper by Fernandez *et. al.* show that additional thickening (beyond linear in $\dot{\gamma}$) is possible within the fully inertial regime if the particle friction coefficient changes with $\dot{\gamma}$. This form of thickening is analogous to the friction-driven thickening predicted by WC theory for inertialess particles. In this section, we outline the salient findings of their work.

They begin by considering the state of lubrication between two spheres of radius R, which is characterised by the Sommerfeld number s, defined as

$$s = \frac{\eta_f v R}{N}, \tag{7.36}$$

where v is the relative sliding velocity of the surfaces and N is the normal load. Physically, the Sommerfeld number can be related to the distance of closest approach between two spheres in a typical interaction [7]. At high s, the surfaces are separated by a lubrication film with a dynamic friction coefficient μ_K that increases with s, Fig. 7.12(a). At low s, the lubrication film ruptures and the particles are in mechanical contact. In that limit, commonly referred to as *boundary lubricated*, μ_K is approximately independent of s.

To make a connection with a sheared suspension, Fernandez *et. al.* estimate $v \sim R\dot{\gamma}$ and $N \sim \sigma R^2$, whence, using Eq. (7.35) [8]:

[7] This can be seen by considering two spheres in Stokes flow approaching each other under the influence of a normal force N. The particles are force free, so N is balanced by the hydrodynamic lubrication force $-\eta_f R^2 \dot{x}/x$, where $x(t)$ is the separation of the surfaces. For an initial surface separation of x_0, one finds $x(t) = x_0 \exp[-Nt/(\eta_f R^2)]$.

The typical timescale of interaction in suspension flow is given by R/v, with v the tangential velocity of the spheres. The relative change in normal separation in this time is therefore $x(R/v)/x_0 = \exp[-N/(\eta_f R v)]$, from which we find that the Sommerfeld number is related to the logarithm of the change in separation, $s = \eta_f R v/N = \{\ln[x_0/x(R/v)]\}^{-1}$.

[8] In the original analysis, the authors consider the particle pressure $p = m\dot{\gamma}^2 d^{-1} P^I(\phi)$ rather than σ. As in purely viscous systems, all the components of σ_{ij} scale similarly with $\dot{\gamma}$, so the expressions for σ and p have the same form and the basic argument is unchanged.

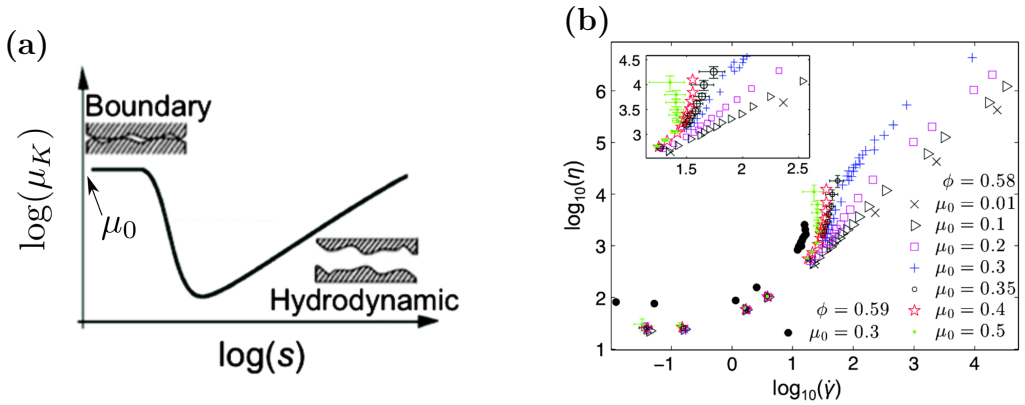

Figure 7.12: (a) Dynamic friction coefficient μ_K as a function of Sommerfeld number s for two surfaces separated by a fluid. (b) $\eta(\dot{\gamma})$ at different ϕ from contact dynamics simulations of frictional, inertial spheres at different ϕ and μ_0. Both figures were taken from [104].

$$s = \frac{\eta_f}{\rho_p R^2 \dot{\gamma} C^I(\phi)}.$$

This form of Eq. (7.36) implies that s is a decreasing function of $\dot{\gamma}$ in an inertial suspension, i.e., there is a transition from fully-lubricated to boundary-lubricated contacts with increasing $\dot{\gamma}$. This transition manifests rheologically as shear thickening with increasing $\dot{\gamma}$ Fig. 7.12(b): firstly, as a transition from Newtonian to Bagnoldian rheology; secondly, as a super-linear increase in $\eta(\dot{\gamma})$ which depends on the value of the friction coefficient at contact $\mu_0 = \mu_K(s \to 0)$; and thirdly, with a second Bagnoldian regime at high $\dot{\gamma}$. Recent molecular dynamics simulations of soft frictional spheres by Grob, Heussinger and Zippelius [146] paint a roughly consistent picture: they find that $\eta(\dot{\gamma})$ thickens from a Bagnoldian regime to an ultimately shear thinning regime, in which particle deformability is important. In their work, thickening occurs above a critical σ, rather than $\dot{\gamma}$.

At a critical concentration ϕ_c, whose value depends on μ_0, the thickening predicted by Fernandez *et. al.* becomes discontinuous and there is no high-$\dot{\gamma}$ flowing regime, Fig. 7.12(b). For example, at $\phi = 0.58$ thickening becomes discontinuous at $\mu_S = 0.4$, while at $\phi = 0.59$ it becomes discontinuous at $\mu_0 = 0.3$, Fig. 7.12(b). This phenomenology is reminiscent of WC theory, but it is not made clear whether μ_0 is equivalent to the static friction coefficient μ_S, and hence it is presumptuous to identify their ϕ_c with ϕ_m.

7.5.3 Viscous flow of rough hard spheres revisited

Before concluding the chapter, we compare the cases of fully-inertial and fully-viscous flow for hard spherical particles. For viscous flow, the particle pressure is linear in the shear rate, so that $N \sim \eta_f \dot{\gamma} C(\phi) R^2$ and hence

$$s = \frac{1}{C(\phi)},$$

which is independent of $\dot{\gamma}$. Physically, this means that the lubrication state (and hence the typical separation between particle surfaces) in a viscous suspension of hard spheres is a function of ϕ only, consistent with the $\dot{\gamma}$-independent viscosity. Finite inertia therefore plays a similar role to the repulsive force f^* in non-inertial systems: it allows the state of friction to depend on $\dot{\gamma}$, leading to shear thickening.

7.6 Summary: what kind of thickening is present in our model systems?

We conclude with a brief summary of the possible types of shear thickening identified in this chapter, before discussing which of these could be responsible for the two-branch phenomenology reported in Ch. 5 and 6.

Firstly, no $\dot{\gamma}$-dependence is possible for inertialess hard spheres in a fluid at $\mathrm{Re} = 0$, even if direct mechanical contacts are permitted: there is only a single stress scale $\eta_f \dot{\gamma}$ and a single time scale $\dot{\gamma}^{-1}$. To obtain a $\dot{\gamma}$-dependent rheology of any kind requires the existence of an additional stress (time) scale to compete with $\eta_f \dot{\gamma}$ ($\dot{\gamma}^{-1}$). For Brownian systems, this is provided by $k_B T/R^3$; for a finite-range repulsive potential with characteristic force f^*, by f^*/R^2. If particle inertia is dominant, then the relevant stress scale is $\rho_p \dot{\gamma}^2 R^2$ and the system naturally shear thickens as $\eta \propto \dot{\gamma}$; adding friction yields a viscosity that increases superlinearly with $\dot{\gamma}$. We can rule out the former kind of inertial thickening as a potential explanation for our experimental results, as we do not observe the predicted $\eta \propto \dot{\gamma}$ scaling at all ϕ. We also do not observe limiting low- or high-$\dot{\gamma}$ Bagnoldian regimes. We therefore concentrate on the case of inertialess particles.

We summarise the inertialess shear-thickening phenomenology in tables 7.1 and 7.2. Table 7.1 lists the possible kinds of thickening for the case in which direct

mechanical contacts are forbidden: any shear thickening is purely hydrodynamic in origin. At low concentrations, it is caused by enhanced viscous dissipation in lubrication films that narrow with increasing σ. This narrowing is caused by a competition between the viscous stress and a repulsive barrier separating particle surfaces, be it due to Brownian motion (B, solid line) or potential interactions (C, solid line). This two-particle thickening is continuous and cannot, therefore, be responsible for the discontinuous thickening and shear jamming observed at $\phi \gtrsim 0.55$ in experiments (B and C, dashed line). Moreover, unphysically small gaps are required to generate the orders of magnitude or more increases in η during CST close to ϕ_m.

If hydrodynamics alone is to account for thickening at $\phi \gtrsim 0.5$, it must be via the formation of hydroclusters. Of the two posited mechanisms, we believe that only the temporary-aggregate one of Wagner *et. al.*, Fig. 7.8(b) would lead to a two-branch phenomenology. In that case, the lower branch would correspond to unaggregated, lubricated flow of homogeneously-dispersed particles, while the upper branch would correspond to the lubricated flow of temporary aggregates at a larger effective ϕ. It is unclear to us what sets the values of the viscosity divergences, ϕ_m and ϕ_{RCP}, and whether a shear-jammed state could arise.

If contacts are allowed, table 7.2, frictional shear thickening is possible if $\mu_S > 0$, leading directly to the two-branch phenomenology described in Ch. 5. This phenomenology and the associated CST-DST transition with increasing ϕ, appear to be independent of whether Brownian motion (B) or potential interactions (C) provide the repulsive barrier, although the DST regime has not been explored extensively for the Brownian case. The case of attractive interactions is subtle and we avoid a detailed discussion in this thesis. We do note, however, that strong attractions typically lead to shear thinning (table 7.1 D), but that weak, short-range attractions in as suspension of rough particles could give rise to static friction (table 7.2 D) [33].

7.6.1 Looking forward

Having thought about existing experimental data in light of our dimensional approach to shear thickening, two main outstanding issues remain. The first is to determine whether the experimental two-branch phenomenology is attributable to static friction or to hydrodynamic clustering. The second is to determine the relative roles of hydrodynamic and contact forces when a finite-range potential is

present. We address both of the above issues experimentally in the next chapter.

A. HS (no contacts)	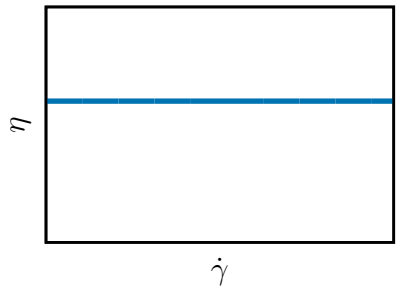
B. HS + Brownian motion	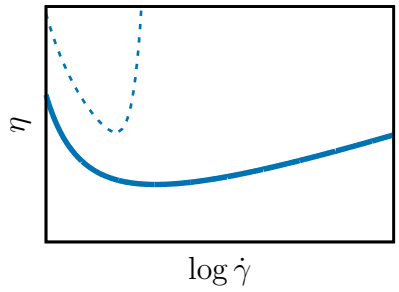
C. HS + finite-range repulsion	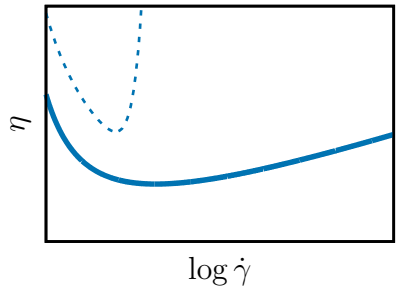
D. HS + attraction	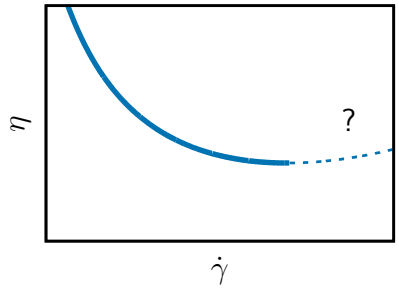

Table 7.1: Overview of possible types of shear thickening for hard spheres *without* contacts.

A. HS (with contacts)	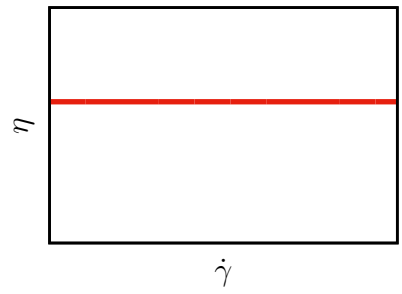
B. HS + Brownian motion	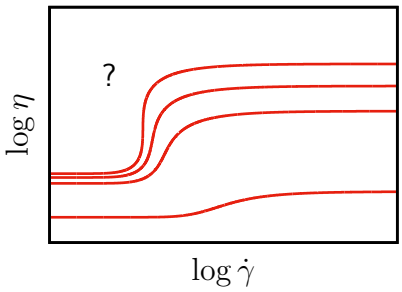
C. HS + finite-range repulsion	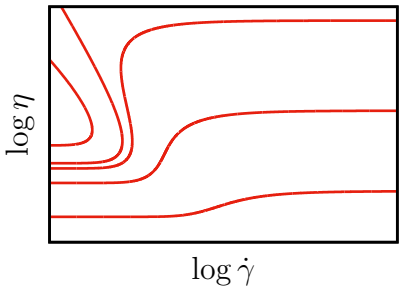
D. HS + attraction	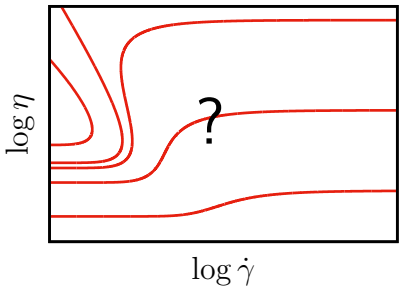

Table 7.2: Overview of possible types of shear thickening for hard spheres *with* contacts.

Chapter 8

Contact- and hydrodynamic-driven shear thickening

A flow reversal study

At the end of the previous chapter, we used the steady-state rheology presented in Ch. 5 and 6 and literature data to eliminate several potential mechanisms for shear thickening. Our analysis proved inconclusive, however, and we identified two important issues to be resolved in order to make progress: (A) whether continuous shear thickening (CST) is driven by contacts or lubrication hydrodynamics in real systems, and (B), whether the two-branch phenomenology and the onset of DST is caused by static friction or the formation of hydroclusters.

In this chapter, we address both issues experimentally using the technique of flow reversal, which allows the relative contributions of contact and hydrodynamic forces to the steady-state viscosity to be disentangled. The basic idea of flow reversal is simple, but powerful: immediately upon reversal, instantaneous contact stresses vanish, but hydrodynamic stresses remain unchanged because of Stokes flow reversibility. We study two charge-stabilised dispersions and one polymer-stabilised colloidal dispersion, all of which are canonical shear-thickening systems in the intermediate size regime.

We begin the chapter by introducing the technique of flow reversal and describe the model systems and rheology protocols used. The first set of results we report address issue (A) for charge- and sterically-stabilised systems at a single ϕ below

ϕ_m. To address issue (B), we work at a range of $\phi \lesssim \phi_m$ and determine the relative contributions of contacts and hydrodynamics in the shear-thickened state as a function of ϕ.

8.1 Flow reversal background

Flow reversal is a rheological technique originally introduced by Galada-Maria and Acrivos [27] to study wet granular suspensions interacting through hydrodynamic and contact forces only. In the basic experiment, Fig. 8.1(a), a shear rate $+\dot{\gamma}_a$ is applied in one direction for a time t_s, then the direction of shear immediately reversed and the same shear rate $-\dot{\gamma}_a$ applied in the opposite direction. At the reversal point, hydrodynamic forces between particles have the same magnitude but opposite sign owing to the reversal symmetry of Stokes flow, whereas the contact forces vanish, Fig. 8.2(a).

Fig. 8.2(b) shows the instantaneous relative viscosity $\eta(\gamma) = \sigma(\gamma)/(\eta_f\dot{\gamma})$ as a function of accumulated strain γ after reversal for $d = 40$ μm polystyrene spheres from [27]. Before reversal, $\eta(\gamma)$ has a value equal to its steady-state value η_∞. Microstructurally, contacting particles form a network of force-bearing chains oriented along the compression axis. Immediately after reversal, η drops to a lower value, η_h, that corresponds to the hydrodynamic contribution to the viscosity. The viscosity undergoes a transient with increasing γ as the contact network is built up in the new direction [147], reaching steady state at $\gamma \sim \mathcal{O}(1)$. The contribution to the viscosity from contacts is given by $\eta_c = \eta_\infty - \eta_h$. In this example, hydrodynamics and contacts each account for $\approx 50\%$ of the total viscosity.

In a similar experiment, Fig. 8.1(b), a shear rate of zero is applied for a waiting period of duration t_w before reversal. We also perform a procedure analogous to Fig. 8.1 (b) for imposed-σ reversal; for those experiments, we impose $\sigma = 0$ during the waiting period.

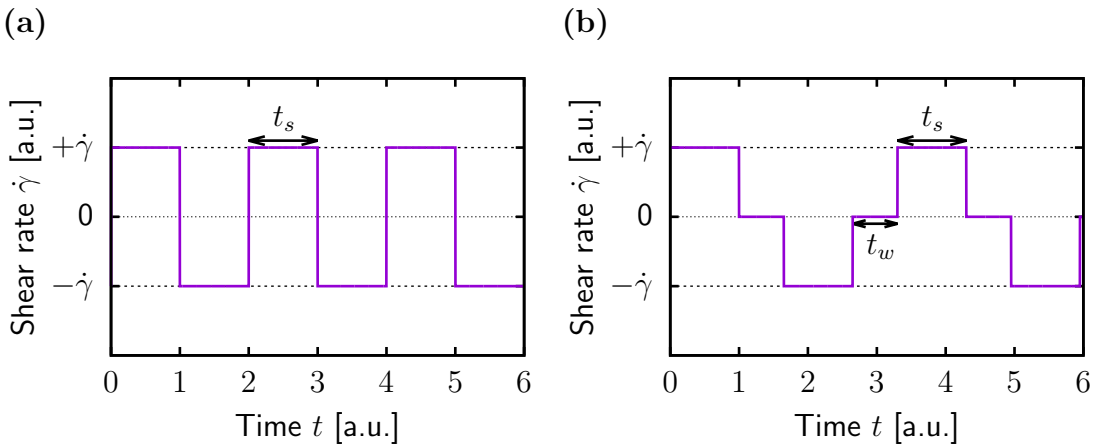

Figure 8.1: Schematics of the flow reversal protocol. (a) Instantaneous reversal from a positive shear rate $+\dot{\gamma}$ to a negative shear rate $-\dot{\gamma}$ after shearing for a time t_s. (b) Flow reversal with $\dot{\gamma} = 0$ imposed for a time t_w between reversal events.

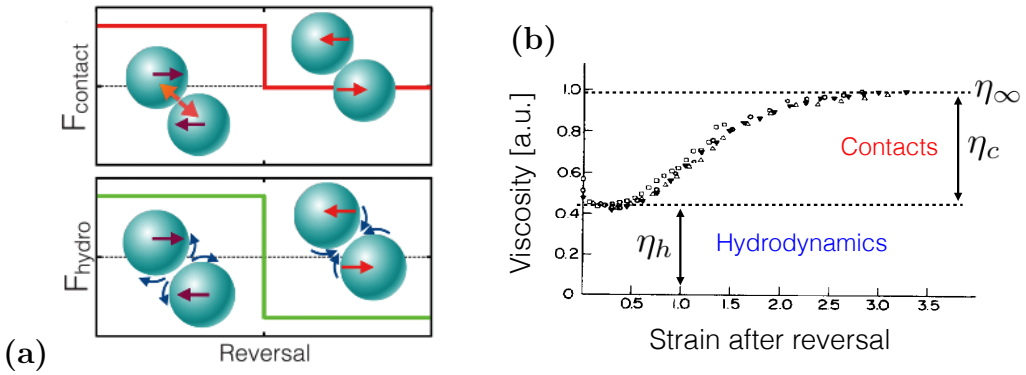

Figure 8.2: Flow reversal for hard particles. (a) Immediately after reversal, the contact forces between particle pairs vanish (top panel), while the hydrodynamic forces have the same magnitude but opposite sign (bottom panel). Taken from [4]. (b) Viscosity versus strain after reversal for 40 μm polystyrene spheres in silicone oil at $\phi = 0.50$. The viscosity immediately after reversal corresponds to the steady-state hydrodynamic viscosity, and the difference between the steady state and hydrodynamic viscosities is that due to particle contacts. Adapted from [27].

8.2 Model systems and experimental method

8.2.1 Model systems

As a model polymer-stabilised colloid, we used polymethylmethacrylate (PMMA) spheres with diameter $d = 1.4$ μm stabilised with poly(dimethyl-diphenyl siloxane) (PDV-2335, Gelest) with chain length $\delta \approx 50$ nm suspended in PDV-2331 (Gelest, viscosity $\eta_f = 1.78$ Pa.s at 20 °C). Experiments were performed at a volume fraction $\phi = 0.54$, made by diluting a close-packed sediment.

We also present results for two model charge-stabilised systems: Whitehouse Scientific (WHS) silica microspheres with $d = 3$ μm (from the manufacturer) dispersed in glycerol (Fisher Scientific, $\eta_f = 1.14$ Pa.s at 20 °C and 7.8 Pa.s at 4 °C at $\phi = 0.41, 0.44, 0.47, 0.49, 0.516, 0.53, 0.54$ (calculated using the density of the solvent $\rho_f = 1.26$ g.cm^{-3} and the dry density of the particles $\rho_p = 1.97$ g.cm^{-3} at 20 °C) and Sekisui Chemical (SC) silica microspheres with $d = 2.0$ μm suspended in a mixture of glycerol and water ($\eta_f = 0.98$ Pa.s at 20°C) at $\phi = 0.49$. Full details of the sample preparation can be found in Ch. 4 for the PMMA and WHS silica suspensions, and in the Supplementary Information of [4] for SC silica. The preparation of, and all rheological measurements on, SC silica were performed by Neil Lin of Cornell University; the data were interpreted and written up for publication by an Edinburgh-Cornell collaboration in which I participated.

8.2.2 Experimental method: imposed-$\dot{\gamma}$ flow reversal

Flow reversal for the Whitehouse Scientific silica was performed on a DHR-2 rheometer operating in controlled-$\dot{\gamma}$ mode with a roughened 20 mm diameter aluminium upper plate (home made; roughened with F-24 grade silicon carbide to give a surface roughness of ≈ 20 μm, measured by eye with fluorescence microscopy) and a larger roughened aluminium base plate, itself screwed onto a Peltier plate. We used a gap size of $H = 600$ μm, chosen because of the small volume of sample available. Experiments with equal-sized parallel plates with the same surface roughness produced the same results.

To shift the onset of shear thickening to a $\dot{\gamma}$ regime suitable for flow reversal, we performed measurements at a nominal temperature of $T = -5$ °C as reported by a thermometer in the Peltier plate. To prevent condensation of water

from the atmosphere, we circulated nitrogen gas through a metallic chamber enclosing the sample. The volumetric flow rate of nitrogen used was too low to be detectable by conventional flow rate meters, so to ensure reproducibility between experiments we measured the pressure exerted by a gauge pressure sensor (Honeywell TSC00IPDUCV) fixed to the end of a constant length of tubing before each run. The flow rate was liable to drop to zero after several hours, so we checked the pressure on an approximately hourly basis for experiments longer than one hour. In practice, the actual temperature of the sample is higher than -5 °C and we inferred that $T \approx 4$ °C by comparing our measured value for the viscosity of glycerol to the T-dependent data in [148].

In a typical experiment, we loaded and trimmed the sample, then lowered the nitrogen chamber into place and sealed the contact with the base plate with vacuum grease or vaseline. We then started the nitrogen flow and set the temperature to -5 °C. The thermometer in the Peltier plate reads -5 °C after ~ 2 mins, but it takes a further 10^3 s for the temperature to equilibrate, which we checked by measuring the viscosity of pure glycerol as a function of time under the same conditions. Experiments began after 1000 s.

Glycerol water absorption

Saturating the environment with nitrogen also limits the absorption of water by glycerol, which can result in profound systematic variations in the viscosity. We illustrate the effect of absorption in Fig. 8.3, which plots the viscosity of glycerol as a function of time, $\eta_f(t)$, both with and without nitrogen flow. Without nitrogen, there is an initial rise in $\eta_f(t)$ over the first $\sim 10^2$ s which we attribute to temperature equilibration, followed by a decrease by almost a factor of two over the next 10^4 s. After 10^5 s (≈ 30 hours), $\eta_f(t)$ has dropped by a factor of three. With nitrogen, there is a slight increase due to temperature equilibration, but no subsequent decrease in $\eta_f(t)$, which reaches a plateau after $\approx 10^3$ s.

Loading and trimming samples with the nitrogen chamber typically takes between 10 and 15 mins, during which time the water content of the glycerol has increased. Accordingly, the initial viscosity with the nitrogen chamber is comparable to that measured after 10 mins without, Fig. 8.3. Repeat measurements with nitrogen found that the final η_f varied by up to 20% between different loadings, both at $T = 20$ °C and ≈ 4 °C. In experiments on suspensions, this absorption also leads to a change in the volume of solvent and hence ϕ. From [148], we estimate that

a 20% decrease in η_f corresponds to an $\sim 1\%$ decrease in ϕ.

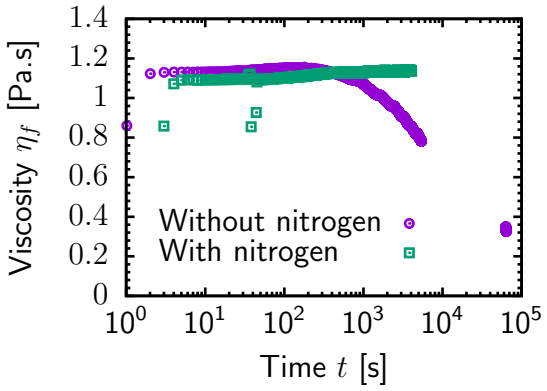

Figure 8.3: Evolution of glycerol viscosity η_f with time t at $T = 20°$C both exposed to the atmosphere and in a nitrogen-saturated environment.

Rheological protocol

After allowing the temperature to equilibrate, we adhere to a strict rheological protocol. We first impose a shear *stress* of $\sigma = 1$ Pa for 60 s to remove loading history and spread the sample evenly within the plates. During this time, the viscosity η reaches a steady state, but σ is sufficiently small that there is no slow decay in $\eta(t)$ indicative of particle migration [27]. We then perform flow reversal measurements at different $\dot{\gamma}_a$ using the following protocol:-

1. $\dot{\gamma} = +0.08$ s^{-1} for $t_s = 12/0.08$ s.
2. $\dot{\gamma} = -0.08$ s^{-1} for $t_s = 12/0.08$ s.
3. $\dot{\gamma} = +|\dot{\gamma}_a|$ for $t_s = 12/\dot{\gamma}_a$.
4. $\dot{\gamma} = -|\dot{\gamma}_a|$ for $t_s = 12/\dot{\gamma}_a$.
5. $\dot{\gamma} = +|\dot{\gamma}_a|$ for $t_s = 12/\dot{\gamma}_a$.
6. $\dot{\gamma} = -|\dot{\gamma}_a|$ for $t_s = 12/\dot{\gamma}_a$.

Before each different $\dot{\gamma}_a$, we perform a single flow reversal at 0.08 s^{-1} (steps 1 and 2). This step serves two purposes: firstly, it ensures that the system is in nominally the same state before each $\dot{\gamma}_a$; secondly, it serves as a check for systematic drift in the viscosity due to, for example, temperature variations

caused by fluctuations in the nitrogen flow rate. The choice of 0.08 s^{-1} is motivated by the fact that, at the lowest ϕ studied, the system is in an unthickened state at this shear rate. For consistency, we adopted the same rate at all ϕ. Using lower $\dot{\gamma}$ resulted in impractically long experiments, during which the nitrogen flow rate was prone to vary. For all $\dot{\gamma}_a$, we sheared for a time $t_s = 12/\dot{\gamma}_a$ (corresponding to $\gamma = 12$), which was the minimum time required for us to reliably extract a steady-state viscosity from $\eta(\gamma)$.

The results of step 3 are typically different to the others and depend on both the sign and magnitude of the preceding shear rate. The data we present for $\eta(\gamma)$ are averaged over steps 4, 5 and 6. The $\eta(\gamma)$ measured during steps 1 and 2 drifted by up to a factor of 1.5 over the course of the experiment, which we attribute to particle migration. We discuss the physical origin of this drift further in appendix A, where we also propose a correction scheme. Correcting the data does not affect any of the conclusions we draw, so we present uncorrected data.

8.2.3 Experimental method: imposed-σ flow reversal

Flow reversal for the DPDM-stabilised PMMA was performed on an Anton Paar MCR 301 rheometer in imposed-σ mode with a 50 mm diameter sandblasted steel cone (truncation 100 μm, surface roughness $\sim$ 10 μm) and a larger roughened aluminium base plate (surface roughness $\sim$ 5 μm). The lower plate was maintained at 19°C by a circulating water bath.

Samples were loaded by pouring the sample from a vial onto the lower plate. This process typically took several hours owing to the high viscosity of the samples ($\sim$ 100 Pa.s) and was achieved by holding the vial in a tilted position above the plate with a clamp. We did not systematically explore different loading protocols for PMMA; however, we found that decreasing the gap at a rate of 1 μm while limiting the normal force to 2 N (corresponding to a normal stress $\sim 10^3$ Pa) gave reproducible results between different loadings. We waited until $F_N \approx 0 \pm 0.2$ N before beginning any measurements.

Rheological protocol

We measured the response to stress reversal with the following protocol:-

1. $\sigma = +|\sigma_a|$ for $|\gamma| \approx 20$.
2. $\sigma = 0$ for t_w.
3. $\sigma = -|\sigma_a|$ for $|\gamma| \approx 20$.
4. $\sigma = 0$ for t_w.
5. $\sigma = +|\sigma_a|$ for $|\gamma| \approx 20$.
6. $\sigma = 0$ for t_w.
7. $\sigma = -|\sigma_a|$ for $|\gamma| \approx 20$.
8. $\sigma = 0$ for t_w.

As with WHS silica, the reversal curve in step 1 depends on the magnitude and direction of the preceding stress, while steps 3, 5 and 7 all produce similar results. In general half of a reversal cycle was sufficient to remove all memory of the prior shear history unless the fracture stress $\sigma^\dagger \approx 200$ Pa was exceeded, in which case $\eta(\gamma)$ was altered irreversibly. In contrast to WHS silica in parallel plates, there was no systematic drift in the reversal response over the duration of the longest experiments (≈ 2 days), from which we conclude that sedimentation and particle migration effects are negligible. Consequently, the measured $\eta(\gamma)$ did not depend on the order in which different stresses were visited or the strain accumulated at each σ; our choice of $\gamma \approx 20$ is arbitrary, but sufficiently large for a steady-state viscosity to be extracted at all σ studied. The shearing time t_s required to reach $\gamma \approx 20$ was determined *ad hoc* at the beginning of an experiment by measuring the steady state $\dot{\gamma}$ at each σ_a. The minimum waiting time before reversal was $t_w = 0.01$ s due to limitations of the software.

8.2.4 Instrument limitations

As discussed in Ch. 4, the viscosity after reversal is unreliable before a time $t_{\min}$ that depends on the specifications of the rheometer and the choice of measuring tool; we omit data before $t_{\min}$. For the DHR-2 and Anton Paar rheometers $t_{\min} = 50$ ms. For the modified ARES rheometer used for SC silica $t_{\min} = 30$ ms.

8.3 Mechanism of continuous shear thickening

8.3.1 Experimental reversal phenomenology

We begin by determining whether CST is driven by contacts or hydrodynamics for WHS silica at $\phi = 0.516$. In Fig. 8.4 we monitor the relative instantaneous viscosity $\hat{\eta} = (\sigma(\gamma)/\dot{\gamma}_a)/\eta_f$ as function of strain γ after reversal at six representative shear rates $\dot{\gamma}_a = 0.08,\ 0.15,\ 0.25,\ 0.60,\ 0.85$ and $1.50\ \mathrm{s}^{-1}$. Immediately before reversal, $\hat{\eta}$ has a value (not shown) equal to the steady-state viscosity η_∞, which we obtain by averaging $\hat{\eta}(\gamma)$ over the interval $8 \leq \gamma \leq 10$. The steady-state flow curve $\eta_\infty(\dot{\gamma})$ undergoes shear thickening in the accessible range of $\dot{\gamma}_a$, Fig. 8.5 (solid line), and reaches a high-viscosity Newtonian regime at $\dot{\gamma}_a^\dagger \approx 3\ \mathrm{s}^{-1}$ (corresponding to a steady-state stress $\sigma^\dagger = \eta_\infty(\dot{\gamma}_a^\dagger)\dot{\gamma}_a^\dagger \approx 500$ Pa). The unthickened regime lies below the torque resolution of our instrument, denoted by the black dashed line in Fig. 8.5; we conclude that the onset stress for shear thickening $\sigma^* < 2$ Pa.

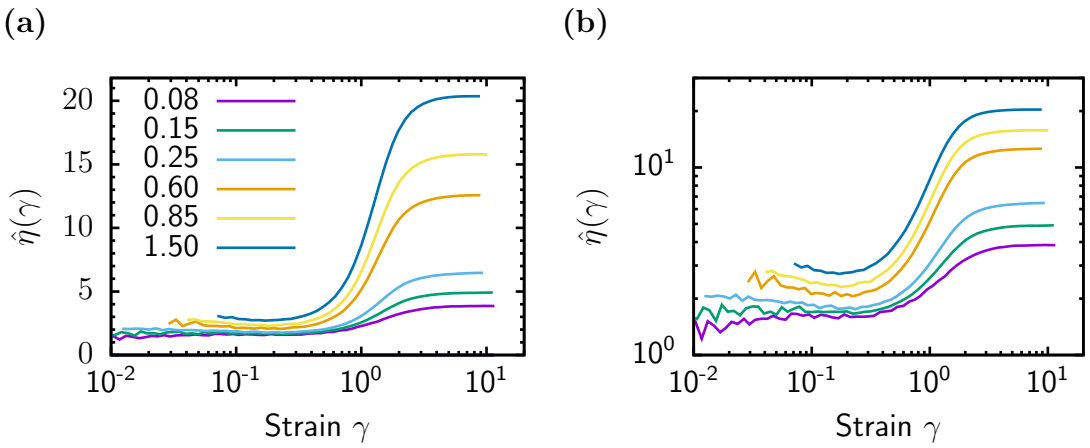

Figure 8.4: Instantaneous relative viscosity $\hat{\eta}$ versus strain after reversal γ for $d = 3\ \mu$m Whitehouse Scientific silica at different shear rates (in units of s^{-1}), as labelled for (a) linear-log and (b) log-log axes. The volume fraction is $\phi = 0.516$.

The instantaneous viscosity evolves similarly at all $\dot{\gamma}_a$: it immediately drops to a lower value after reversal, passes through a $\dot{\gamma}_a$-dependent minimum at $\gamma_{\mathrm{min}} \approx 0.2$, before reaching η_∞ after $\gamma \approx 5$. We cannot access the viscosity before $t_{\mathrm{min}} \approx 50$ ms, which imposes a $\dot{\gamma}_a$-dependent minimum strain. Consequently, we do not have access to the viscosity at the instant of reversal. We estimate the hydrodynamic contribution η_h by averaging $\hat{\eta}(\gamma)$ over the interval $0.1 \leq \gamma \leq 0.2$, as this range of γ is accessible for all of the shear thickening transition. The

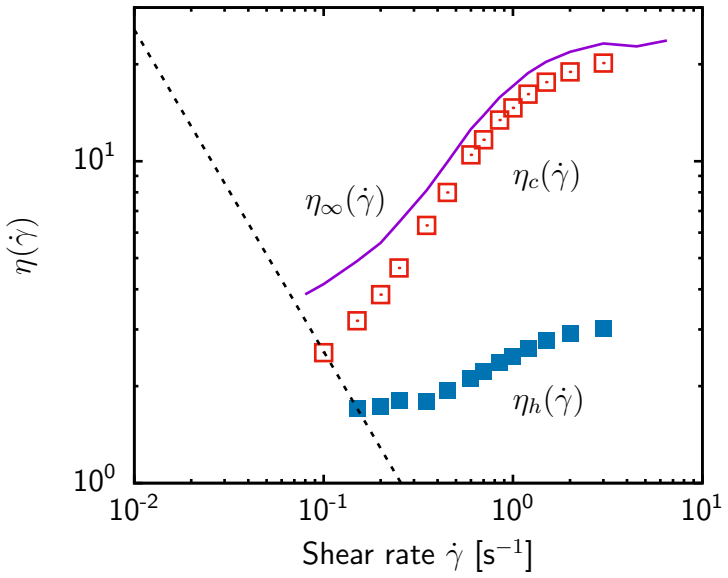

Figure 8.5: Relative viscosity η versus $\dot\gamma$ for $d = 3$ μm Whitehouse Scientific silica at $\phi = 0.516$. Purple line, steady state viscosity η_∞ from Fig. 8.4; filled blue squares, hydrodynamic viscosity η_h; and filled red squares, contact viscosity η_c. The slanted, dotted black line denotes the lower stress limit of the instrument, $\sigma = 2$ Pa.

implications of this choice are discussed in §8.3.3. The contact contribution is $\eta_c = \eta_\infty - \eta_h$.

In Fig. 8.5 we plot the hydrodynamic and contact contributions so obtained versus $\dot\gamma_a$. While $\eta_c(\dot\gamma_a)$ increases by an order of magnitude and dominates the viscosity in the shear-thickened state, $\eta_h(\dot\gamma_a)$ varies by less than a factor of two: this demonstrates the essential role played by contact forces in the shear thickening of WHS silica. The reversal phenomenology for SC silica at $\phi = 0.49$ is even more striking: $\hat\eta(\gamma)$ has a similar form to WHS silica, Fig. 8.6(a), but $\eta_h(\dot\gamma_a)$ remains constant as the suspension shear thickens, Fig. 8.6(b).

These results are consistent with the frictional framework in §7.4 and Ch. 5. The increase in $\eta_c(\dot\gamma)$ can be attributed to an increase in the fraction of lubrication films that have fractured to form frictional contacts, and saturates in the shear-thickened state where $\eta_c(\dot\gamma)$ is Newtonian and all contacts in the system are frictional.

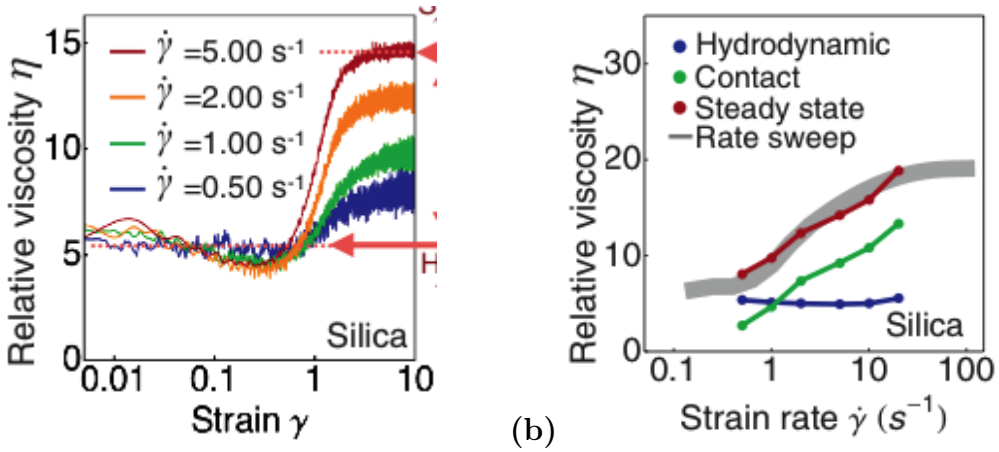

Figure 8.6: (a) $\hat{\eta}$ versus γ for $d = 2$ μm Sekisui Chemical silica at different $\dot{\gamma}$, as labelled. The volume fraction is $\phi = 0.49$. The data were collected by Neil Lin from Cornell University with a modified ARES rheometer. (b) Relative viscosity versus $\dot{\gamma}$ for a conventional upward $\dot{\gamma}$ sweep and η_∞, η_h and η_c (as labelled) obtained from flow reversal.

8.3.2 Flow reversal simulations

Support for this interpretation comes from simulations of repulsive spheres (radius R) implemented in a classical discrete element method code (see Supplementary Material of [4] for details; simulations were performed by Chris Ness of the School of Engineering at Edinburgh University). Particle interactions are modelled in the same way as [2, 56] and are outlined in §7.4: frictional interactions appear beyond a critical normal force between particles f^*, which also sets a shear rate scale $\dot{\gamma}_0 = f^*/6\pi\eta_f R^2$. We note that there are no finite-range non-hydrodynamic interactions, i.e., the simulations mimic the case where the range of $U(r)$ is comparable to the surface roughness of the particles (see §7.4). The steady-state flow curve exhibits CST above a critical shear rate $\dot{\gamma}^* \approx 0.05\dot{\gamma}_0$, Fig. 8.7(c).

The observed evolution of $\hat{\eta}(\gamma)$ after reversal, Fig. 8.7(a), is qualitatively similar to experiments. In simulations, we have the advantage of being able to directly access the hydrodynamic and contact contributions to the stress throughout the reversal cycle, which we show for $\dot{\gamma} = 0.74\dot{\gamma}_0$ in Fig. 8.7(b). Consistent with the interpretation we have offered for our experimental data, the contact contribution (green) drops to zero immediately after reversal and only increases back to its steady-state value after a strain of $\mathcal{O}(1)$. There is less variation in the hydrodynamic contribution, which passes through a minimum shortly before the total viscosity reaches steady state.

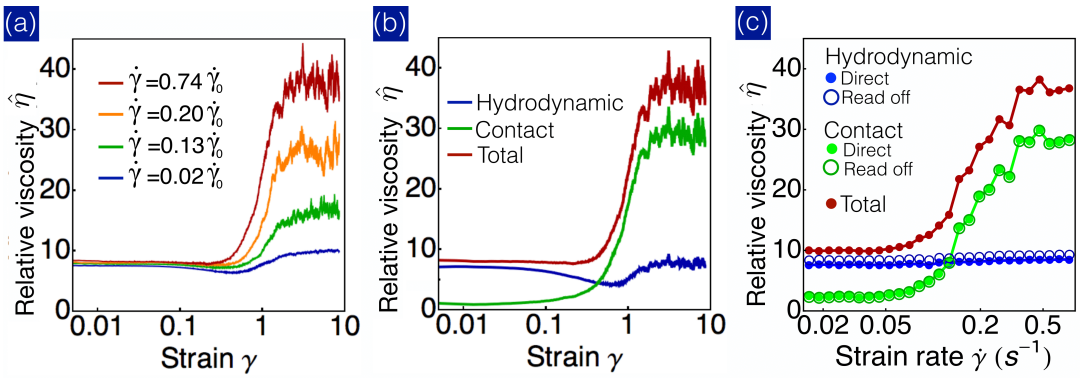

Figure 8.7: Flow reversal results from simulations [142] with a load-dependent particle static friction coefficient which is activated when the local force between a particle pair exceeds a critical force f^* (taken from [4]). This f^* sets a shear rate scale $\dot{\gamma}_0 = f^*/(6\pi\eta_f R^2)$. (a) $\hat{\eta}$ versus γ for different $\dot{\gamma}$ in units of $\dot{\gamma}_0$, as labelled. (b) $\hat{\eta}(\gamma)$ decomposed by direct evaluation into hydrodynamic and contact contributions. (c) Total steady state viscosity $\eta_\infty(\dot{\gamma})$ decomposed into hydrodynamic and contact contributions by direct evaluation (open symbols) and by averaging $\hat{\eta}(\gamma)$ over the interval $0 \leq \gamma \leq 0.2$.

In Fig. 8.7(c), we plot the steady-state hydrodynamic and contact viscosities obtained by direct evaluation as a function of $\dot{\gamma}$ (filled symbols). Thickening is driven almost entirely by contact forces, with only an $\sim$ 10% increase in the hydrodynamic contribution. For comparison, we plot the hydrodynamic η_h and contact η_c viscosities obtained from flow reversal by averaging over the interval $0 \leq \gamma \leq 0.2$, a protocol comparable to experiments (open symbols). The data obtained via flow reversal are indistinguishable from those obtained via direct evaluation, validating our interpretation of the experimental flow reversal data.

8.3.3 Hydrodynamic thickening and contact relaxation after reversal.

Although shear thickening in both WHS (Fig. 8.5) and SC [Fig. 8.6(b)] silica is dominated by an increase in η_c, there is also a two-fold increase in η_h for WHS silica. We speculate that this increase is a consequence of the finite range of the repulsive force separating particle surfaces ϵ, presumably set by the Debye length κ^{-1} in our system. This leads to the two-particle hydrodynamic thickening discussed in the previous chapter: higher stresses result in narrower lubrication films and enhanced dissipation.

To determine if this claim is viable, we note that the existence of a length scale

$\epsilon > 0$ implies a timescale associated with contact relaxation $\tau_{\rm rel} \propto \eta_f R\epsilon/f^*$, the time required for two particles that are initially in contact to separate under the influence of their mutual interaction potential. This expectation motivated us to perform flow reversal experiments in which we ceased shear for a time t_w before reversal, using the protocol schematised in Fig. 8.1(b).

In Fig. 8.8, we plot the instantaneous stress $\hat{\sigma}(\gamma)$ as a function of strain after reversal for WHS silica at $\phi = 0.51$ for $t_w = 0$, 1 and 10 s. We do not have data over the entire range of $\dot{\gamma}$ for this ϕ; but, see the data for $\phi = 0.516$ in Fig. 8.5. Below the onset of thickening, $\dot{\gamma} = 0.1$ s^{-1}, the evolution of the shear stress $\hat{\sigma}(\gamma)$ is, to a good approximation, independent of t_w. In each case, the hydrodynamic viscosity is ≈ 16 Pa.s, obtained by averaging over the flat region at $0 < \gamma \leq 0.2$. Above the onset of thickening, at $\dot{\gamma} = 0.5$ s^{-1}, the stress immediately after reversal is $\hat{\sigma}(t = t_{\rm min}) \approx 12$ Pa for $t_w = 0$ s, corresponding to a viscosity of 24 Pa; but, it falls by a factor of ≈ 1.5 to ≈ 8 Pa for $t_w = 10$ s, corresponding to a viscosity of ≈ 16 Pa, which is the constant value below the onset of shear thickening.

We propose that, just at the onset of thickening, $\dot{\gamma}_a = 0.1$ s^{-1}, the average surface separation is comparable to the range of the interaction potential $h(\dot{\gamma}_a = 0.1 \text{ s}^{-1}) = \epsilon$. At $\dot{\gamma}_a = 0.5$ s^{-1}, in the thickened state, this barrier is overcome and h has some smaller value $h(\dot{\gamma}_a = 0.5 \text{ s}^{-1}) = h_{\rm th}$ set by a balance of the local stress due to the imposed flow and the double-layer repulsion. If the flow is reversed immediately ($t_w = 0$) at $\dot{\gamma}_a = 0.5$ s^{-1}, one measures a relative viscosity $\eta(h_{\rm th})$; whereas, if the particles are allowed to separate under the influence of their mutual interaction potential before reversal ($t_w = 10$ s), one measures a lower viscosity $\eta(\epsilon)$.

Recall, §7.3.3, that for a system dominated by lubrication hydrodynamics $\eta \propto \ln(h/d)$, from which a relation can be deduced between ϵ, $h_{\rm th}$, $\eta(\epsilon)$ and $\eta(h_{\rm th})$:

$$\frac{\eta(h_{\rm th})}{\eta(\epsilon)} = \frac{\ln(h_{\rm th}/d)}{\ln(\epsilon/d)}. \tag{8.1}$$

To determine whether the above scenario is possible, we estimate $h_{\rm th}$ from Eq. (8.1). Assuming that ϵ is set by the Debye length κ^{-1} and that κ^{-1} is comparable to that in distilled water $\sim \mathcal{O}(10^2$ nm), and using $\eta(h_{\rm th}) = 24$ Pa.s$/\eta_f$ and $\eta(\epsilon) = 16$ Pa.s$/\eta_f$, we find $h_{\rm th} \sim 20$ nm. Physically, $h_{\rm min}$ must be greater than or equal to the length scale of the surface roughness ξ. We have not measured ξ for WHS silica; but, the surface roughness of SC silica measured by AFM is

$\xi = 2$ nm. Assuming a similar roughness for WHS silica, the above scenario is certainly plausible.

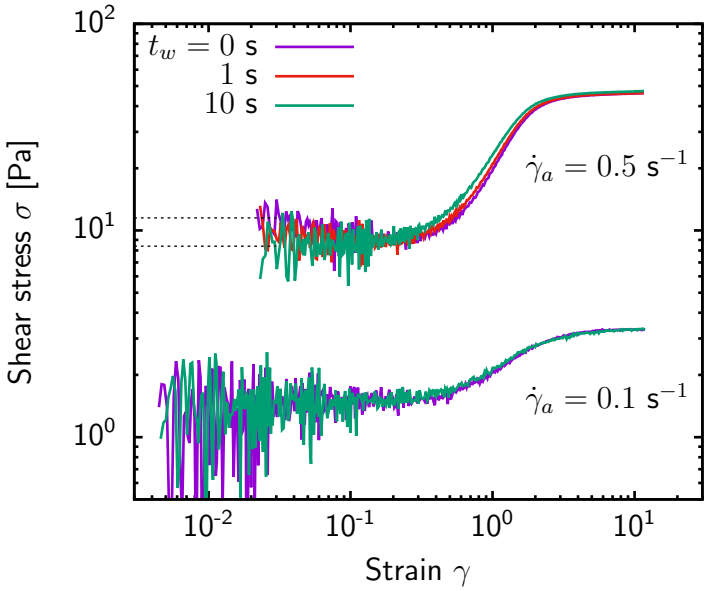

Figure 8.8: Flow reversal for WHS silica at $\phi = 0.51$ at different applied shear rates $\dot{\gamma}_a$ (as labelled) with waiting times of $t_w = 0$, 1 and 10 s (see legend).

Given the above argument, it is natural to ask why there is no increase in the hydrodynamic contribution for SC silica. One possibility is that the increase in $\eta_h(\dot{\gamma})$ is an artefact of using a σ-controlled rheometer in $\dot{\gamma}$-controlled mode and that the "true" hydrodynamic response measured with a inherently $\dot{\gamma}$-controlled rheometer would be flat. Although the $\dot{\gamma}$-independence of the reversal response measured with the Newtonian oil in Fig. 4.3 suggests that this is not the case, we have insufficient knowledge of the feedback system used to impose $\dot{\gamma}$ to predict the transient stress for an unknown non-Newtonian fluid. Taking the data as artefact free, another possibility is that the dynamic friction coefficient μ_K depends on $\dot{\gamma}$ in WHS silica but not in SC silica. This could be due to the presence of an adsorbed surfactant [14], whose presence we cannot rule out, as the WHS particles were used as received from the manufacturer without cleaning.

8.3.4 Accessing the "true" hydrodynamic contribution

So far, we have assumed that the viscosity calculated by averaging $\hat{\eta}$ over the interval $0.1 \leq \gamma \leq 0.2$ is a good approximation to the "true" steady state hydrodynamic viscosity, i.e., the viscosity at the instant of reversal. The fact that we can only access $\hat{\eta}(\gamma)$ after $t_{\min} \approx 50$ ms is problematic, as little is known

about the exact shape of $\hat{\eta}(\gamma)$ immediately after reversal for a shear-thickening system. In particular, we cannot immediately rule out the case schematised in Fig. 8.9 by the solid blue line, in which $\hat{\eta}(\gamma)$ is very close to η_∞ at $t = 0$, then drops rapidly before reaching the observable part of $\hat{\eta}(\gamma)$ (unshaded region). In such a situation, our η_h would grossly underestimate the true η_h and thickening driven by hydrodynamics could be mistaken for thickening driven by contacts.

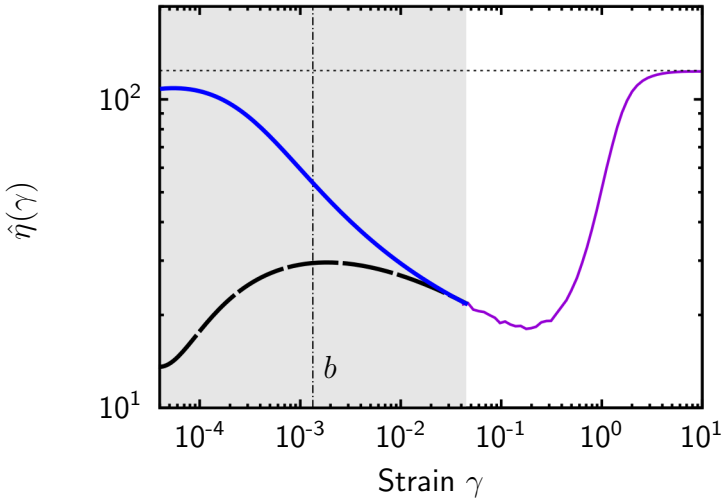

Figure 8.9: Relative instantaneous viscosity after flow reversal $\hat{\eta}(\gamma)$ for WHS silica at $\phi = 0.516$ and $\dot{\gamma} = 0.85$ s^{-1} from Fig. 8.4 (solid purple line). Light grey region, range of γ that corresponds to $t < t_{\text{min}}$; vertical dot-dashed line, strain corresponding to the dimensionless surface roughness of the particles ξ/R, assuming $\xi = 2$ nm; horizontal dotted line, η_∞. Below $\gamma(t_{\text{min}})$, we sketch possible evolutions of $\hat{\eta}(\gamma)$ for cases where the viscosity is predominantly hydrodynamic in origin (bold solid blue line) and dominated by contacts (bold dashed black line; based on [142]).

Recent simulations by Ness and Sun [142] of frictional granular spheres found $\hat{\eta}(\gamma)$ to have the generic form schematised by the bold dashed line in Fig. 8.9. The simulations are identical to Fig. 8.7, but with a friction coefficient $\mu_S = 1$ that is independent of the particle normal load, so that the system occupies the frictional viscosity branch at all $\dot{\gamma}$. Their $\hat{\eta}(\gamma)$ is, therefore, a prediction of the reversal response in the shear-thickened state.

Their $\hat{\eta}(\gamma)$ forms a broad peak centred at $\gamma \approx b/R$ (where b is the length scale used to cut off the lubrication divergence), before decreasing to a minimum η_{min} and increasing to the steady state value. The authors directly evaluate the hydrodynamic $\hat{\eta}_h(\gamma)$ and contact $\hat{\eta}_c(\gamma)$ contributions to $\hat{\eta}(\gamma)$ during reversal from the positions and velocities of the particles in the same manner as Fig. 8.7(b). In Fig. 8.10, we show typical data for the hydrodynamic and contact stresses

after reversal in units of $\eta_f\dot{\gamma}$ from [142]; since $\dot{\gamma}(\gamma)$ is constant, this is equivalent to plotting the instantaneous relative viscosity $\hat{\eta}(\gamma) = \sigma(\gamma)/(\eta_f\dot{\gamma})$. The peak in $\hat{\eta}(\gamma)$ is related by a peak in $\hat{\eta}_h(\gamma)$ (inset), whose physical origin is still under investigation [142, 149].

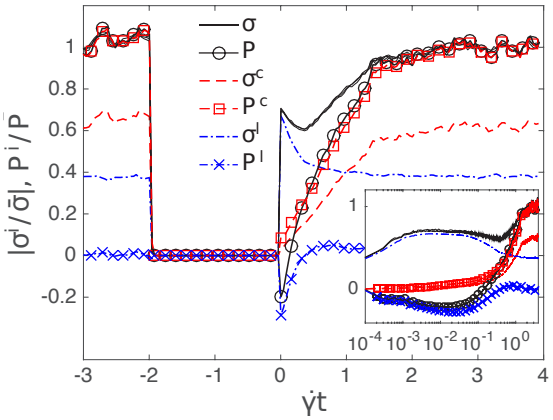

Figure 8.10: Shear stress σ normalised by the steady state stress $\bar{\sigma}$ as a function of strain after reversal for a sheared assembly of frictional Hookean spheres at $\phi = 0.54$ taken from [142]. Only short-range lubrication hydrodynamics are included. The flow is stopped at $\dot{\gamma}t = -2$ and resumed in the opposite direction at $\dot{\gamma}t = 0$. Shown are the contact shear stress σ^c, hydrodynamic shear stress σ^l and total shear stress σ, along with the mechanical pressure P [defined via Eq. (5.3)]. decomposed into its contact, P^c, and hydrodynamic, P^l, components, as labelled. Inset, response immediately after flow reversal with strain plotted on a log scale.

In the example shown, Fig. 8.10 the peak in $\hat{\eta}_h$, and correspondingly the minimum in $\hat{\eta}$, are $\approx 50\%$ greater than the true steady-state hydrodynamic contribution, so that in this scenario our definition of η_h would actually overestimate the steady-state contribution. Very recent simulations by Peters *et. al.* [149] predicted a similar $\hat{\eta}(\gamma)$; but, they further found that the ratio of $\hat{\gamma}$, η_{min} and the true steady-state hydrodynamic contribution is the same $\sim O(1)$ constant for a range of ϕ, ξ and μ_S, including $\mu_S = 0$. This finding implies that our definition of η_h is a good approximation to the true value across the entire shear thickening transition.

8.3.5 Flow reversal of sterically-stabilised colloids

As a canonical polymer-stabilised shear-thickening system, we investigate $d = 1.4$ μm PMMA spheres stabilised by a poly-dimethyl-diphenyl siloxane brush with length $\delta \approx 50$ nm. Reversal measurements were made by imposing the shear stress σ_a and measuring the shear rate $\dot{\gamma}(\gamma)$. We report the instantaneous viscosity $\hat{\eta}(\gamma) = (\sigma_a/\dot{\gamma}(\gamma))/\eta_f$. Working in imposed-$\dot{\gamma}$ mode did not lead to any qualitative differences.

In Fig. 8.11, we present data for $\phi \approx 0.54$; lower concentrations exhibited a similar phenomenology. In Fig. 8.11(a), we plot $\hat{\eta}(\gamma)$ after reversal for $t_w = 0.01$ s at a range of σ_a (see caption). For each σ_a, $\hat{\eta}$ reaches a steady state value η_∞ at $\gamma \approx 5$, which we plot as a function of σ_a in Fig. 8.11(b).

The steady-state rheology shows shear thickening with an onset stress $\sigma^* \approx 0.5$ Pa, below which $\eta_\infty(\sigma_a)$ is Newtonian. In the unthickened state, $\hat{\eta}(\gamma)$ is similar to the charge-stabilised systems, Fig. 8.4 and 8.6(a), and is approximately flat until $\gamma \approx 0.3$, whereupon it increases back to η_∞. The behaviour at $\sigma_a > \sigma^*$ shows marked differences, however: at 1.9 Pa $\leq \sigma_a \leq 6$ Pa, $\hat{\eta}(\gamma)$ first exhibits a peak centred at $\gamma_{\text{peak}} \approx 5\%$ before decreasing to a minimum $\hat{\eta}_{\text{min}}$ at $\gamma_{\text{min}} \approx 0.3$.. We infer the presence of a peak at $\sigma_a > 6$ Pa which we cannot fully resolve due to the finite response time of the rheometer.

The peak is reminiscent of that observed in simulations, Fig. 8.10, in which γ_{peak} is the strain corresponding to the cut off length scale for the lubrication force b/R. Interestingly, our γ_{peak} is comparable to the dimensionless length of the polymer brush, $\xi/R \approx 50$ nm/700 nm $= 7\%$, suggesting that the brush may play the role of surface roughness; although, a systematic variation of δ would be required to validate this claim. Following Peters *et. al.* [149], who also observe a peak, we take the hydrodynamic viscosity η_h to be the viscosity at the minimum of $\hat{\eta}(\gamma)$

We plot η_h and η_c as a function of σ_a in Fig. 8.11(b). Thickening is driven primarily by η_c, accompanied by a $\approx 30\%$ increase in η_h. Like the charge-stabilised systems, thickening in our model sterically-stabilised system is dominated by contact forces.

Imposed-$\dot{\gamma}$ reversal using the ARES rheometer on the same particles at a lower concentration, $\phi = 0.51$, paints a similar overall picture, Fig. 8.12; however, the peak in $\eta(\gamma)$ is absent, Fig. 8.12(a). It is possible, therefore, that the peak is

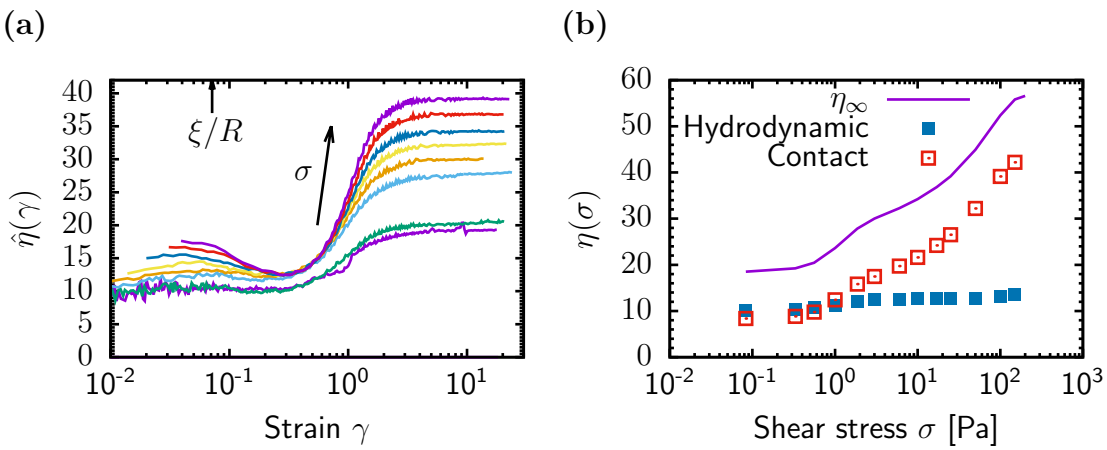

Figure 8.11: Flow reversal rheology of DPDM-stabilised PMMA in PDV-2331. (a) Instantaneous relative viscosity $\hat{\eta}(\gamma) = [\sigma/\dot{\gamma}(\gamma)]/\eta_f$ versus strain γ after reversal under imposed stresses of $\sigma_a = 0.33$, 0.56, 1.86, 3.00, 6.00, 10.0, 17.0 and 25.0, from bottom to top. Experiments were performed with a waiting time of 0.01 s between shear cessation and reversal. The arrow denotes the strain corresponding to the length scale of the polymer brush, ξ/R. (b) Symbols, as labelled: steady-state viscosity η_∞; hydrodynamic viscosity η_h, calculated by averaging $\hat{\eta}(\gamma)$ over the interval $0.25 \leq \gamma \leq 0.35$ and contact viscosity $\eta_c = \eta_\infty - \eta_\mathrm{h}$.

an instrument artefact that depends on whether the rheology is measured with a $\dot{\gamma}$-controlled or σ-controlled rheometer.

8.3.6 Hydrodynamic and contact contributions to continuous shear thickening

Experiments on one sterically-stabilised and two charge-stabilised colloidal systems indicate that CST is driven primarily by an increase in the contribution to the viscosity from contact forces. Although flow reversal provides no *a priori* information about the nature of the contacts, the qualitative similarity of the reversal response with simulations strongly suggests that the particles experience static friction. The thickening of the contact part is then consistent with Wyart and Cates theory [1], with the increase in η_c being related to an increase in the fraction of lubrication films that have fractured to form frictional contacts.

In WHS silica, there was also an increase in the hydrodynamic contribution, which we showed to be caused by a change in the average surface separation as particles are pushed into contact (blue squares in Fig. 8.5). Details of the interplay between contact formation and the hydrodynamic stress, e.g., why $\eta_h(\sigma)$ and $\eta_c(\sigma)$ both plateau at the same steady-state stress, Fig. 8.5, are still to be explored; we do

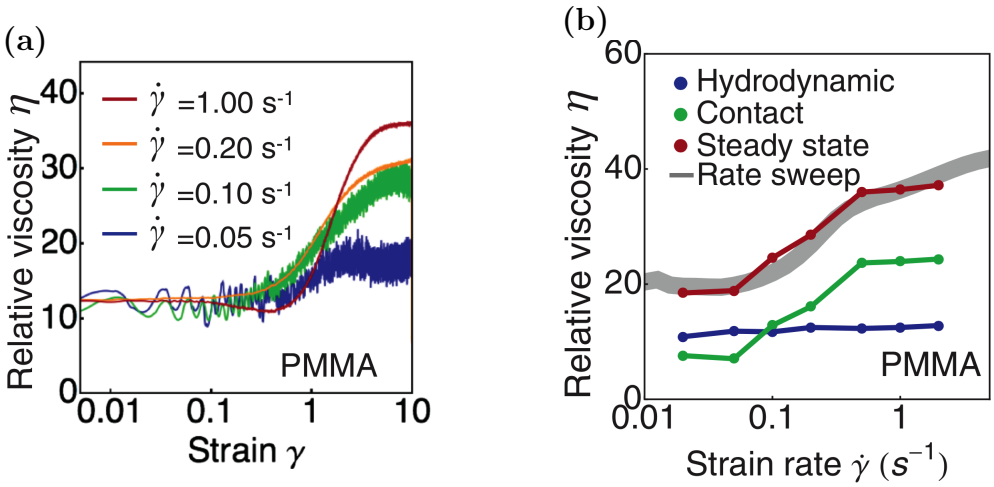

Figure 8.12: (a) $\hat{\eta}$ versus γ for $d = 1.4$ μm PMMA at different $\dot{\gamma}$, as labelled. The volume fraction is $\phi = 0.51$. The data were collected by Neil Lin from Cornell University on a modified ARES rheometer. (b) Relative viscosity versus $\dot{\gamma}$ for a conventional upward $\dot{\gamma}$ sweep and η_∞, η_h and η_c obtained from flow reversal, as labelled.

not speculate further in this thesis, as we cannot rule out instrument artefacts as a potential cause of the increase in $\eta_h(\dot{\gamma})$. Taking the data to be artefact free, however, they support the notion that frictional and hydrodynamic thickening can occur simultaneously in the same system.

8.4 Origin of the two-branch phenomenology

In the previous section, we showed that somewhat away from ϕ_m thickening was dominated by contact forces with a small amount of hydrodynamic thickening. In this section, we explore how the scenario changes with varying ϕ as ϕ_m is approached. In particular, we seek to understand whether $\eta_2(\phi)$ is dominated by the hydrodynamic contribution or the contact contribution close to jamming. As discussed in §7.4, one expects the contact forces between hard particles to diverge at $\phi_m < \phi_{\mathrm{RCP}}$ for a system dominated by frictional contacts. In contrast, the hydroclusters proposed by Wagner *et. al.* interact purely hydrodynamically with one another and so should lead to a divergence in the reversible part of the viscosity at $\phi < \phi_{\mathrm{RCP}}$. This distinction allows an unambiguous test of which mechanism is relevant: if friction dominates, then the divergence of the frictional branch is controlled by η_c; if hydroclusters are dominant, then it is controlled by η_h.

8.4.1 Flow reversal at different ϕ

We performed flow reversal on WHS silica at different concentrations $\phi = 0.41,\ 0.44,\ 0.47,\ 0.49,\ 0.516,\ 0.53\ , 0.54$ and extracted $\eta_h(\dot{\gamma})$ and $\eta_c(\dot{\gamma})$ in the same manner as before [we do not show data for $\hat{\eta}(\gamma)$ for brevity, but there are no qualitative differences with Fig. 8.4(a)]. Fig. 8.13 shows (a) η_∞, (b) η_h and (c) η_c as a function of the steady-state shear stress $\sigma \equiv \eta_\infty(\dot{\gamma})\dot{\gamma}$. The steady-state flow curves exhibit shear thickening towards a Newtonian plateau whose viscosity $\eta_\infty^{(2)}$ we plot as a function of ϕ in Fig. 8.13(d) (filled purple circles) [1]. The data are well fit by the power law

$$\eta = A\left(1 - \frac{\phi}{\phi_m}\right)^{-n} \tag{8.2}$$

[1]Before proceeding, we note that all of the relative viscosities in Fig. 8.13 are anomalously low; e.g., η_h at $\phi = 0.54$ in Fig. 8.13(b) is lower than the Einstein viscosity $1 + 2.5 \cdot 0.54 = 2.35$, which is unphysical. Our data for $\eta_\infty^{(2)}$ can be collapsed onto the frictional viscosity branch for Spheriglass silica in Fig. 5.6 by a single shift in viscosity (Fig. B.1). We believe that this is due to seepage of water from the pores of the particles into the glycerol after dispersal, thereby reducing η_f from the value for pure glycerol, 7.8 Pa.s, to $\eta_f \approx 1$ Pa.s. This process will likely incur a change in the true ϕ; however, since we do not need to stretch the data in the ϕ-direction to obtain good agreement close to ϕ_m we assume that any such change is unimportant rheologically. We therefore assume $\eta_f = 1$ Pa.s in the discussion that follows (see appendix B for a full discussion).

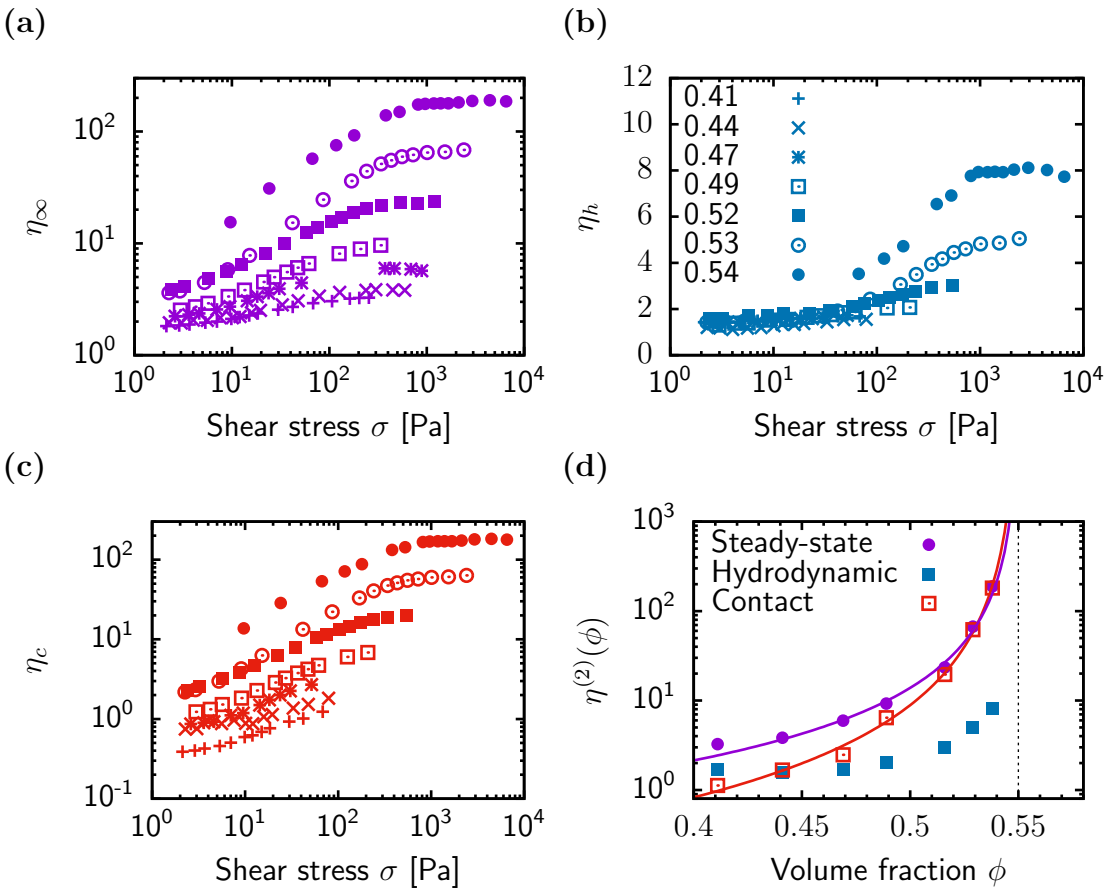

Figure 8.13: Shear-thickening rheology of Whitehouse Scientific silica decomposed at different ϕ. Relative viscosity η versus σ for the (a) steady-state, η_∞; (b) hydrodynamic, η_h, and (c) contact, η_c, viscosities at different ϕ, as labelled. (d) Steady-state shear-thickened, $\eta_\infty^{(2)}(\phi)$, hydrodynamic, $\eta_h^{(2)}$ and contact $\eta_c^{(2)}$ viscosities versus ϕ. The $\eta^{(2)}$ were calculated by averaging last two points on each curve in (a)-(c). Red line, fit by eye of $\eta_c(\phi)$ with Eq. (8.2) with $A = 0.05$, $\phi_m = 0.55$ and $n = 2.16$. Purple line, fit to $\eta_\infty(\phi)$ with $A = 0.235$, $\phi_m = 0.55$ and $n = 1.7$.

with $A = 0.235$, $\phi_m = 0.55$ and $n = 1.7$. We tentatively identify $\eta_\infty^{(2)}(\phi)$ as the upper, shear-thickened viscosity branch observed for similar systems in Ch. 5, $\eta_2(\phi)$. We expect, therefore, that there is an unthickened state that we cannot access with a viscosity $\eta_\infty^{(1)}(\phi) = \eta_1(\phi)$ that diverges at $\phi_{\mathrm{RCP}} > \phi_m$.

The hydrodynamic contribution $\eta_h(\sigma)$ is approximately independent of ϕ for $\sigma < 20$ Pa, where it increases only weakly with σ. At $\sigma \geq 20$ Pa, $\eta_h(\sigma)$ thickens logarithmically with a slope on a semi-log plot that increases with ϕ, and approaches a plateau at $\sigma^\dagger \approx 10^3$ Pa,the same stress as η_∞. We estimate the plateau viscosity $\eta_h^{(2)}(\phi)$ by averaging the last two points of each curve and plot this as a function of ϕ in Fig. 8.13(d) (filled squares). $\eta_h^{(2)}(\phi)$ increases more

slowly with ϕ than $\eta_\infty^{(2)}(\phi)$.

The flow curves for the contact contribution more closely resemble $\eta_\infty(\sigma)$ and approach a Newtonian regime at $\sigma^\dagger$ with viscosity $\eta_c^{(2)}(\phi) = \eta_\infty^{(2)} - \eta_h^{(2)}$, Fig. 8.13(d). Strikingly, while $\eta_c^{(2)}(\phi)$ is comparable to $\eta_h^{(2)}(\phi)$ for $\phi \lesssim 0.45$, it becomes almost indistinguishable from $\eta_\infty^{(2)}(\phi)$ close to ϕ_m: the divergence of the shear-thickened viscosity is clearly driven by a divergence in the contact contribution. If we constrain the jamming volume fraction for the contact part to $\phi_m = 0.55$, then the data are fit by the power law in Eq. (8.2) with $A = 0.05$ and a larger exponent $n_c = 2.2$ [solid red line in Fig 8.13(d)].

8.4.2 Evidence for static friction?

That $\eta_\infty^{(2)}(\phi) \approx \eta_c^{(2)}(\phi)$ close to ϕ_m is consistent with the particles experiencing static friction when pushed into contact, supporting the frictional interpretation of shear thickening. It is unclear from our data if the hydrodynamic part, $\eta_h^{(2)}(\phi)$, diverges, and, if it does, what the value of the jamming volume fraction ϕ_h is. A previous flow reversal study on wet granular materials (which we know, from Ch. 6, permanently occupy the shear-thickened state) found that both contributions diverged at the same concentration, $\phi_h = \phi_m$; whereas, in simulations of soft particles [100], $\eta_h^{(2)}$ is finite at ϕ_m [57]. If $\eta_h^{(2)}(\phi)$ does diverge algebraically at ϕ_m in experiments, then the exponent n_h is less than the one describing the divergence of the contact part $n_h < n_c = 2.2$; indeed, [57] find $n_h = 1$.

The physical origin of the increase in $\eta_h^{(2)}(\phi)$ close to ϕ_m is unclear. The two-particle mechanism responsible for the modest increase in $\eta_h(\dot{\gamma}_a)$ at $\phi = 0.516$, Fig. 8.5, cannot account for the eight-fold increase at $\phi = 0.54$, which would require a surface separation of $\sim 10^{-1}$ Å. It is possible that the divergence is driven by the formation of hydrocluster-like structures; although, theoretical predictions are too vague for us to comment on what ϕ_h or n_h should be in that case. Whatever the cause, in WHS silica shear thickening close to ϕ_m is dominated by the contribution from frictional contacts, rendering the exact details of hydrodynamic thickening irrelevant for the steady-state rheology. Although the results presented in this final section are preliminary, they could, if replicated, prove decisive in settling the controversy surrounding the mechanism of shear thickening.

Chapter 9

Conclusions

In this chapter we summarise the main conclusions of the thesis.

9.1 Rheology of suspensions of intermediate-sized particles

Understanding how the rheology of concentrated particulate suspensions depends on particle size is a long-standing and unresolved problem, even for the simplest case of hard-sphere-like particles in a Newtonian solvent. Most previous work has focussed either on colloidal particles, with diameter $d \lesssim 1$ μm, or suspensions of granular particles, with $d \gtrsim 50$ μm. Both regimes are separately well understood: colloidal rheology is dominated by excluded volume and hydrodynamic interactions between particles, while granular suspension rheology is non-Brownian and sensitive to details of particle surface properties, such as the static friction coefficient μ_S. In contrast, the relevant physics in the intermediate size regime, $1 \lesssim d \lesssim 50$ μm, is currently unclear; this is symptomatic, in part, of a deficiency in our understanding of how colloidal and granular rheology are related.

In Ch. 5, we elucidated the physics of suspension flow in the intermediate regime for a range of model and industrial systems. In each system, it was possible to identify two viscosity "branches", $\eta_1(\phi)$ and $\eta_2(\phi)$, diverging at two different concentrations, ϕ_{RCP} and $\phi_m < \phi_{\mathrm{RCP}}$, and a transition between them above a

critical onset stress σ^*. The rheological manifestation of this transition is shear thickening. Crucially, there exists a range of concentrations, $\phi_m \leq \phi < \phi_{\mathrm{RCP}}$, in which flow is unsteady and erratic when σ^* is exceeded – this is referred to as *discontinuous shear thickening* (DST) in the literature [81].

The Wyart and Cates theory of shear thickening [1] predicts just such a two-branch structure. In it, σ^* corresponds to a barrier separating particle surfaces, in most practical situations due to the stabilisation mechanism, i.e., an electric double layer, or polymer brush; $\eta_1(\phi)$ then corresponds to lubricated flow when surfaces are separated, and $\eta_2(\phi)$ to frictional flow, when surfaces are pushed into contact. We obtained quantitative fits to our data of their theory by making assumptions about the probability distribution of forces in the sheared suspension based on measurements on dry granular media. The theory is purely phenomenological, however, and we showed that the assumption of a ϕ-independent σ^* is unphysical given microstructural measurements on other systems: in general, σ^* cannot be straightforwardly related to local, particle-level stresses.

Taking the above fits as evidence that the frictional framework is applicable to the intermediate size regime, measuring the ratio of ϕ_m and ϕ_{RCP} in principle provides a measure of μ_S. We showed, however, that even modest uncertainties in fitting $\eta_1(\phi)$ and $\eta_2(\phi)$ to obtain the jamming volume fractions can lead to $\mathcal{O}(1)$ errors in μ_S

9.2 Unifying colloidal and granular rheology

By varying the particle size of a canonical nearly-hard-sphere system from colloidal to granular, we showed that the frictional framework developed for the intermediate regime applies across the entire size spectrum. The crossover between the two regimes is controlled by a competition between the size dependence of the onset stress $\sigma^* \propto d^{-2}$ and the scaling of the intrinsic (entropic) stress $k_BT/d^3 \propto d^{-3}$. For colloids, σ^* lies beyond the upper stress limit of the observable window accessible in our rheometer, so they behave as frictionless (lubricated) particles under typical conditions – they permanently occupy the low-viscosity, unthickened branch. In contrast, σ^* is readily exceeded for granular particles, which behave as frictional hard spheres in the observable window – they permanently occupy the high-viscosity, shear-thickened branch. The onset stress

for intermediate particles lies in the middle of the observable window, leading to a stress-dependent transition between frictionless and frictional states. In our model system, van der Waals attractions preclude the repulsive granular regime by overcoming the repulsive stress separating particle surfaces and the rheology is gel-like [53, 117].

In general we expect the details of the crossover to depend on the specific scaling of $\sigma^* = f^*(d)/d^2$ and the magnitude of the repulsive force f^*, which depends on the surface chemistry of the particles. We expect the observable window to be specific to the choice of rheometer and measuring geometry, or, in an industrial setting, processing parameters such as minimum and maximum pumping pressure and flow rate.

9.3 The mechanism of shear thickening

Although the findings of the first two results chapters are strong evidence for the frictional framework for suspension rheology, shear thickening – which plays a central role in the framework – remains a hotly-debated topic, and other fundamentally different mechanisms have been proposed for it in the literature. The frictional theory of Wyart and Cates [1] only makes predictions for non-Brownian hard spheres with a σ-dependent friction coefficient and ignores other interactions present in real suspensions, including finite-range potential interactions (repulsive and attractive), Brownian motion, particle inertia, and finite surface roughness. In Ch. 7, we adopted a dimensional approach to determine which of these interactions could lead to a $\dot{\gamma}$-dependent rheology and discussed whether this rheology would be consistent with the two-branch thickening phenomenology borne out by experiments.

The most pertinent outcome of the analysis was in identifying two fundamentally distinct categories of thickening: one in which particle surfaces remain separated by a lubrication film and another in which lubrication films rupture to allow direct mechanical contact. Lubricated thickening can be further subdivided into two-particle thickening, which leads to only a weak and continuous increase in viscosity, and many-particle "hydrocluster" thickening, in which shear-induced clusters ostensibly lead to a two-branch rheology. In the presence of static friction, contact formation leads to thickening á la Wyart and Cates, which directly predicts two branches. It was not possible to determine whether hydrocluster or

frictional thickening was responsible for the two-branches based on existing data, and the extent to which two-particle lubricated thickening applies at $\phi \ll \phi_m$.

To address these issues, we used the technique of *flow reversal* to disentangle the relative contributions to the viscosity from hydrodynamic and contact forces during the shear thickening of three canonical hard-sphere-like systems. Firstly, we showed that continuous shear thickening was driven predominantly by contact formation at ϕ somewhat lower than ϕ_{RCP}; the two-particle hydrodynamic mechanism was present even in the presence of contacts, but its relative contribution to the viscosity increase was small and system-dependent. Secondly, we showed that as ϕ_m is approached the divergence of the upper, shear-thickened branch is dominated by a divergence in the contact contribution to the viscosity, consistent with the presence of static friction [100]. Interestingly, the hydrodynamic contribution also grew approaching ϕ_m, although we had insufficient data to determine whether it diverged. The hydrodynamic viscosity increases were not explicable with the two-particle mechanism, indicating that another reversible contribution to the viscosity becomes important at higher ϕ, potentially due to the aforementioned hydroclusters. Nevertheless, even if both mechanisms are at play in real systems, our preliminary results indicate that the hydrodynamic one is subdominant.

Chapter 10

So what next?

The primary achievement of this thesis was to demonstrate that static friction, or the absence thereof, plays a central role in the rheology of concentrated dispersions. This finding is by no means trivial. The notion of particles entering direct mechanical contact is heretical in the realm of traditional microhydrodynamics, in which contact formation of any kind is precluded by a divergence in the lubrication force. Indeed, exactly how two particles come into contact in the presence of an intermediary fluid, and once in contact, experience static friction, remain unclear and are active areas of research [23]. It is clear that any framework that predicts the macroscopic response of a suspension to an applied deformation must take into account nanoscopic and microscopic details of the constituent particles, which play a decisive role in determining the qualitative behaviour. In this chapter, we outline a scheme for how such a predictive understanding could be achieved in future work, supported by preliminary measurements that have not been presented hitherto.

In the first section we consider the case that the suspension can flow at all stresses (or, if it has a yield stress, that it flows after yielding), i.e., $\phi < \phi_m$. In the second section, we consider $\phi_m \leq \phi \leq \phi_{\mathrm{RCP}}$, where the suspension jams into a solid at high stresses.

10.1 Predicting suspension flow below ϕ_m

In Fig. 10.1 we show a schematic plan for future work. The ultimate goal is to make predictions about the macroscopic rheology (IV) given information on particle surface properties (I), or, conversely, to use macroscopic rheology as a type of mechanical spectroscopy to infer surface details. To do so requires us to tackle the problem at several length scales.

I. Nanoscopic

At the nanoscopic scale ($\sim$nm, I), it is necessary to characterise the surface topology and mechanical properties of particle surfaces, as well as the properties of any adsorbed polymer layer. Atomic force microscopy (AFM) can already measure surface roughness to a precision of ~ 1 nm; however, more work is needed to synthesise colloids with tuneable surface chemistry and surface roughness, as most existing methods are still crude [150].

II. Microscopic

A considerable challenge exists in linking the above nanoscopic details to interactions between particles on the microscopic scale ($\sim R$, II) in terms of static μ_S and dynamic μ_K friction coefficients. Additionally, one must also have access to the mutual interaction potential between particles $U(r)$. For polymer-coated surfaces, surface-force apparatus (SFA) has been successfully used to measure both $U(r)$ and μ_K, and in some cases it was even possible to link the latter to relaxation processes in the brush [132]. For uncoated surfaces, the only option is currently colloid-probe AFM [151]; although, this method measures interactions between specific pairs of particles only, making obtaining statistically meaningful results tedious, and is difficult for particles with $R \lesssim 10\ \mu$m. A higher throughput technique is necessary.

III. Mesosopic

As we encountered in Ch. 5, knowledge of the interactions between individual particles (II) is not sufficient to predict the macroscopic stress: this requires

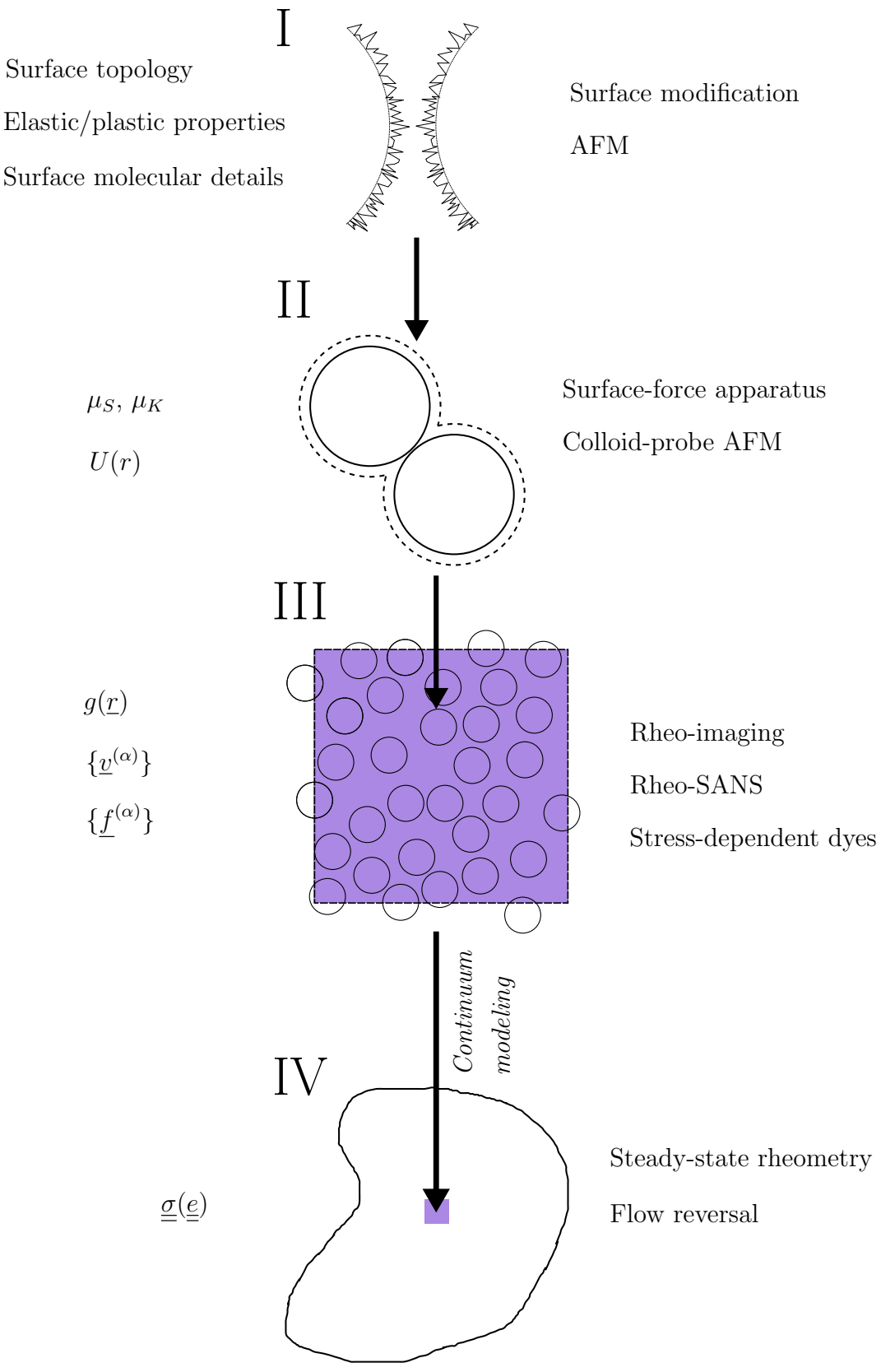

Figure 10.1: Schematic overview of future work in suspension rheology.

information on the microstructure (III) via, e.g., the pair distribution function $g(\underline{r})$, and the distribution of force vectors $\{\underline{f}\}$. Hydrodynamic forces and velocity-dependent friction forces require us to additionally know the velocities of all the particles $\{\underline{v}\}$.

The divergence of $\eta_1(\phi)$ has been shown to be related to a divergence in velocity fluctuations for hard particles, so measuring $\{\underline{v}\}$ in principle allows one to calculate the viscosity [86] [1]. With rheo-imaging on a fast confocal microscope [66], one can measure $\{\underline{v}\}$ for $\sim 10^3$ micron-sized particles at an acquisition rate of ~ 1 Hz in 3-d and ~ 100 Hz in 2-d. Preliminary measurements on the Whitehouse Scientific silica system in Ch. 8 found no change in the shear-induced dynamics for a ten-fold increase in viscosity, however, so that any increase in velocity fluctuations may occur at a length scale that is currently too small for us to resolve.

It is possible to measure $g(\underline{r})$ accurately under shear for $r \gtrsim R$ using light scattering [152] or neutron scattering [153]; however, lubrication and frictional interactions are sensitive to $\sim$ nm variations in surface separation, and it is not possible to resolve these differences with existing techniques. Local stresses are measurable in 2-d dry granular assemblies of photoelastic discs [154], although the technique has yet to be extended to 3-d colloids. Currently, stress-dependent dyes are the most promising avenue of pursuit to measure the distribution of forces [93], although the technique is relatively new.

IV. Macroscopic

Given a complete mesoscopic description of the sheared suspension (III), it remains to calculate the macroscopic stresses that are measured in a rheology experiment (IV) – this is the domain of continuum modelling. It has long been known how to calculate the hydrodynamic contribution to the stress: this was first done by Batchelor [123, 124] and involves calculating the average stresslet, which is related to the integral of the fluid traction over the surface of the particle. If contact forces are pairwise additive (a reasonable assumption unless there are overlaps involving three or more particles [155], which is possible only for soft particles) then the macroscopic stress due to contact forces can be calculated using the formula in Eq. (3.13). The contribution from potential interactions is calculated in the same manner [25].

[1] See equation (2) in [86]).

Given the paucity of data on local forces and dynamics (III), an important challenge is to be able to calculate the stress with only limited structural information, e.g., $g(r)$. Future models should also take into account the history dependence of the shear, for example, during flow reversal. A first step would therefore be to measure static quantities such as $g(r)$ during shear reversal with rheo-imaging, develop a model that describes the evolution of $g(r)$ and then link this microstructural information to the stress.

Throughout this thesis, we have assumed that the suspension behaves as a single, homogeneous phase. This assumption breaks down in reality, even in rheometric geometries, as particle migration leads to gradients in $\sigma(\underline{x})$ and $\phi(\underline{x})$. In order to capture these phenomena, which are unavoidable and ubiquitous in reality, a *two-phase* description is needed. In two-phase modelling, one considers separate mass and momentum balances for the fluid and particle phases with a coupling term to describe interactions between them. There is still much debate about the form of this coupling term [23] and even the correct way to apportion the hydrodynamic stress generated by particle-particle interactions [13]. A major experimental challenge is to be able to extract rheological information about a homogeneous mixture based on measurements of an inhomogeneous system. This last challenge will involve separately measuring fluid- and particle-phase stresses, and a number of groups [156, 157] have already begun to do some using permeable rheometer plates.

Next step?

There are still a number of open questions in the field of rheophysics; however, we believe that the most important next step is to experimentally characterise the effect of modifying surface properties, changing μ_S, μ_K and $U(r)$, on the shear rheology. The ultimate goal remains to bridge all four regimes in Fig. 10.1.

10.2 The onset stress for shear thickening σ^*

The scheme outlined in Fig. 10.1 may seem superfluous; however, it reflects the likely fact that suspension rheology is dominated by system-specific, particle-level details, so that elegant scaling descriptions and mean-field arguments that have enjoyed considerable success in polymer rheology no longer apply. To illustrate

the need for the scheme, and to establish a starting point for future investigations, we consider the size dependence of the onset stress for shear thickening σ^*.

Recall from Ch. 5 that the onset stress σ^* is the ϕ-independent stress above which the viscosity starts to increase as a function of shear stress σ (or shear rate $\dot{\gamma}$). For PMMA, σ^* was found to scale with the inverse square of the particle diameter d, Fig. 6.2. In his seminal review of shear thickening, Barnes [121] showed that the onset shear *rate* $\dot{\gamma}$ scaled approximately as d^{-2} for diverse systems, albeit with considerable data scatter. In Fig. 10.2, we replot the same data as a function of shear stress, including data from this thesis and the literature since the publication of the original review. We denote charge stabilised systems by open symbols and sterically-stabilised systems with closed symbols. With the exception of several points at $d > 10$ μm, for which sedimentation is important [81], both data sets are consistent with $\sigma \propto d^{-\alpha}$ with $\alpha \approx 2$. In this section, we attempt to account for this scaling microscopically using the limited nanoscopic information available to us. We will see that this is rendered difficult by our lack of knowledge about the connection between macroscopic stress (IV), microstructure (III) and local forces (II).

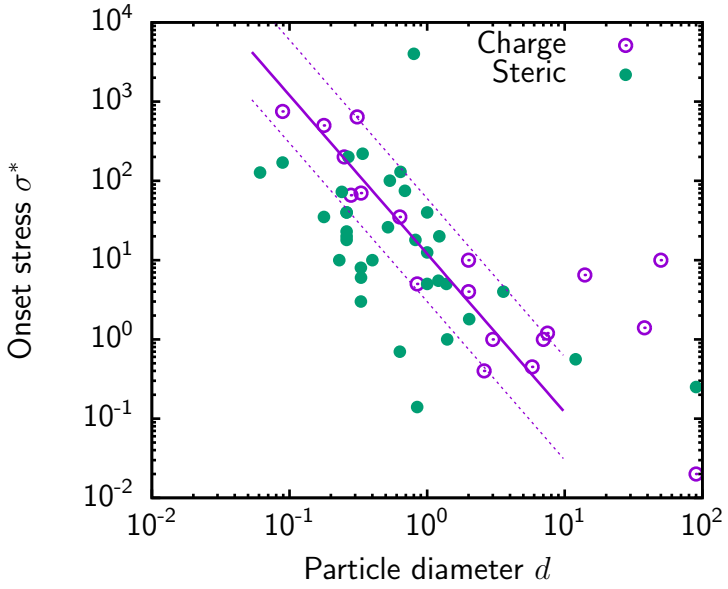

Figure 10.2: Onset shear stress for shear thickening σ^* as a function of particle diameter d for diverse systems (adapted from [121]). The solid line represents $\sigma^* \propto d^{-2}$.

10.2.1 The onset stress and static friction

In Ch. 8, we showed further that σ^* is the stress above which particles experience static friction. We assume that this is the case for all the systems in Fig. 10.2 with $d \leq 10$ μm.

In Wyart and Cates theory, which applies to strictly hard, non-Brownian spheres, σ^* is related to a barrier separating the surfaces of the particles, e.g., due to a polymer brush or electric double-layer repulsion. In practice, however, overcoming this repulsive barrier and pushing particles into mechanical contact does not guarantee $\mu_S > 0$, and is therefore a necessary but not sufficient condition for shear thickening: in real systems, μ_S depends on the local normal load f_N and contact time, both of which are sensitive to the exact surface topology and mechanical properties of the particles [33, 158]. Specifically, f_N should be large enough to plastically deform the contacting asperities [159].

10.2.2 Relating details of the barrier to macroscopic stress

For ease of discussion, we assume that the local contact stresses generated by overcoming the repulsive potential barrier are sufficiently large to ensure $\mu_S > 0$; although, this is not obviously the case for any of the systems we have studied. We extend the interpretation of Wyart and Cates and assume that particles are pushed into frictional contact when the separation between their surfaces is equal to the surface "roughness" ξ, given by the typical asperity size in charge-stabilised systems and the polymer brush length δ in sterically-stabilised systems.

Recall from Ch. 5 that the onset stress has the following form for hard particles:

$$\sigma^* = \frac{f^*(d,\xi)}{d^2}\mathcal{F}(\phi),$$

where $\mathcal{F}(\phi)$ is a weakly-varying function of ϕ, which we assume to be constant for the purposes of this discussion. The size dependence of σ^* is determined by the onset force f^*, which depends on d both directly and via the surface roughness $\xi(d)$. If ξ is independent of particle size, then $\sigma^*(d)$ is determined by the derivative of the interaction potential evaluated at ξ,

$$f^*(d,\xi) = -\left.\frac{\mathrm{d}U(h)}{\mathrm{d}h}\right|_{h=\xi}.$$

For an onset force that is independent of d, then $\sigma^* \propto d^0/d^2 = d^{-2}$ [2]; if $f^* \propto d$, as expected from the Derjaguin approximation [33], then $\sigma^* \propto d^{-1}$; and if $f \propto d^{-1}$, then $\sigma^* \propto d^{-3}$. The data in Fig. 10.2 are roughly consistent with the first case.

One scenario in which f^* is independent of d for charge-stabilised particles is when the repulsion is due to Brownian motion, $f^* \approx k_B T/\xi$. The data spread in Fig. 10.2 could then be attributed to a range of surface roughnesses in the different systems. In order to relate σ^* (IV in Fig. 10.1) and ξ (I), however, we need to know the value of $\mathcal{F}$ in Eq. (10.2.2), which encodes information about the distribution of angles and magnitudes of the force vectors between contacting particles. Thus, even though we know the characteristic force scale between particles, we cannot *a priori* deduce σ^* – to do so requires us to link stress to microstructure.

We nevertheless estimate $\mathcal{F}$ for Sekisui Chemical silica (see Ch. 8) using the measured value of the average surface roughness $\xi = 2$ nm and the onset stress $\sigma^* = 10$ Pa, yielding

$$\mathcal{F}(\phi) = \frac{\sigma^* d^2}{k_B T/\xi} \approx 20.$$

Taking this number to be generic for charge-stabilised systems, the region delimited by the dashed lines in Fig. 10.2 corresponds to ξ ranging from ≈ 1 nm (upper boundary) to 30 nm (lower boundary) and the solid line corresponds to $\xi = 7$ nm.

The fact that PMMA exhibits a d^{-2} scaling, Fig. 6.2, is puzzling, as we expect $f^* \propto d$ and hence $\sigma^* \propto d^{-1}$ based on the Derjaguin approximation [43]. It is possible that the onset of thickening is also related to the cut off of Brownian motion, with the polymer brush playing the role of surface roughness.

[2] If $\xi \propto d$, i.e., thickening occurs at a fixed dimensionless separation ξ/d, then $\sigma^* \propto d^{-3}$; this is the expected scaling for hydrodynamic thickening of Brownian spheres.

Final remarks

This example illustrates the need for a proper characterisation of the suspension at all length scales: one cannot infer the macroscopic onset stress from nanoscopic surface details alone and vice-versa. One also needs to know how the potential interactions providing the barrier to contact formation (Brownian motion, or otherwise) influence the microstructure (II $\rightarrow$ III) and how, in turn, this is related to the macroscopic stress (III $\rightarrow$ IV).

10.3 Understanding suspension flow at $\phi \gtrsim \phi_m$

In this section, we outline future work for concentrations above the frictional jamming volume fraction ϕ_m. In contrast to $\phi \ll \phi_m$, flow at $\phi \gtrsim \phi_m$ is unsteady and inhomogeneous above σ^* and profoundly sensitive to the flow geometry and differences in sample preparation protocol. There is currently no predictive understanding of flow in this regime. Wyart and Cates [1] do predict the existence of such a regime, but they do not make any predicts for the type of flow, other than that it cannot be steady and homogeneous.

The first step is to qualitatively predict the kind of flow, if any, that is expected. From our observations and those in the literature, several possible scenarios can unfold when the suspension jams into a solid: (a) wall slip; (b) fracture of the free surface; (c) (transient) shear banding [90]; or (d) particle migration. Typically, any one of these mechanisms results in unsteady flow, characterised by viscosity that evolves erratically with time, but where the precise mechanism is sensitive to details of the suspended particles and the flow geometry. In our experience, many industrial dispersions, including ceramic green bodies and chocolate, are almost certainly formulated in this regime; formulators aim to maximise particle loading to maximise mechanical strength and in doing so achieve a ϕ that is close to ϕ_{RCP}. It is crucial, therefore, to be able to predict which kind of flow will occur during processing of these materials.

10.3.1 An example: periodic jamming of cornstarch

As an example of flow above ϕ_m, and to highlight possible directions for future research, we present preliminary results obtained for a suspension of cornstarch

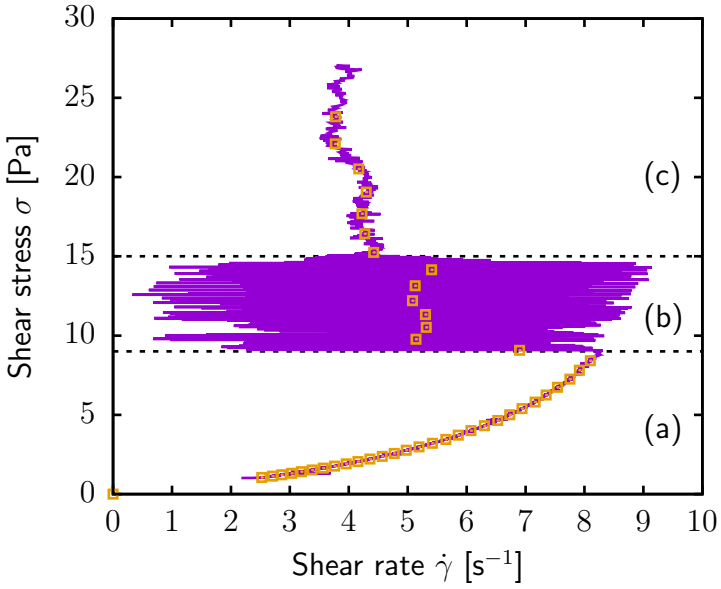

Figure 10.3: Continuous upward stress ramp for a cornstarch suspension at $\phi > \phi_m$.

in glycerol and water, Fig. 10.3 and 10.4. We measured the rheological response using 40 mm diameter cross-hatched plates in imposed-stress mode.

Fig. 10.3 plots σ versus $\dot{\gamma}$ for a continuous σ ramp from zero (solid purple line). One can identify three qualitatively distinct flow regimes. In regime (a), at $\sigma < \sigma^* = 8$ Pa, the sample is initially Newtonian, then undergoes slight CST. At $\sigma^* \leq \sigma \leq 15$ Pa, regime (b), $\dot{\gamma}$ oscillates from ≈ 0 to a well-defined non-zero value, then, at $\sigma \geq 15$ Pa, regime (c), the amplitude of the oscillations is greatly diminished but the flow remains unsteady.

In Fig. 10.4(a-c) we plot $\dot{\gamma}(t)$ measured at three representative values of σ obtained by increasing σ in a stepwise fashion. In (a), after a slight increase at $t < 1$ s due to the inertia of the measuring tool, $\dot{\gamma}(t)$ is steady in time. In (b), one observes periodic fluctuations, visible as macroscopic jerks of the rheometer tool, with a frequency ν that increases approximately linearly with σ (data not shown). In (c), there is an initial burst of periodic fluctuations followed by random (and possibly chaotic) fluctuations in $\dot{\gamma}(t)$. These observations prompt several questions. What determines ν? What sets the upper threshold stress for periodic oscillations? Is this behaviour generic?

The periodic regime does not occur in all systems, however. In silica, for example, the sample transitions immediately to the chaotic regime after thickening and changing the composition of the suspending medium for cornstarch has a similar

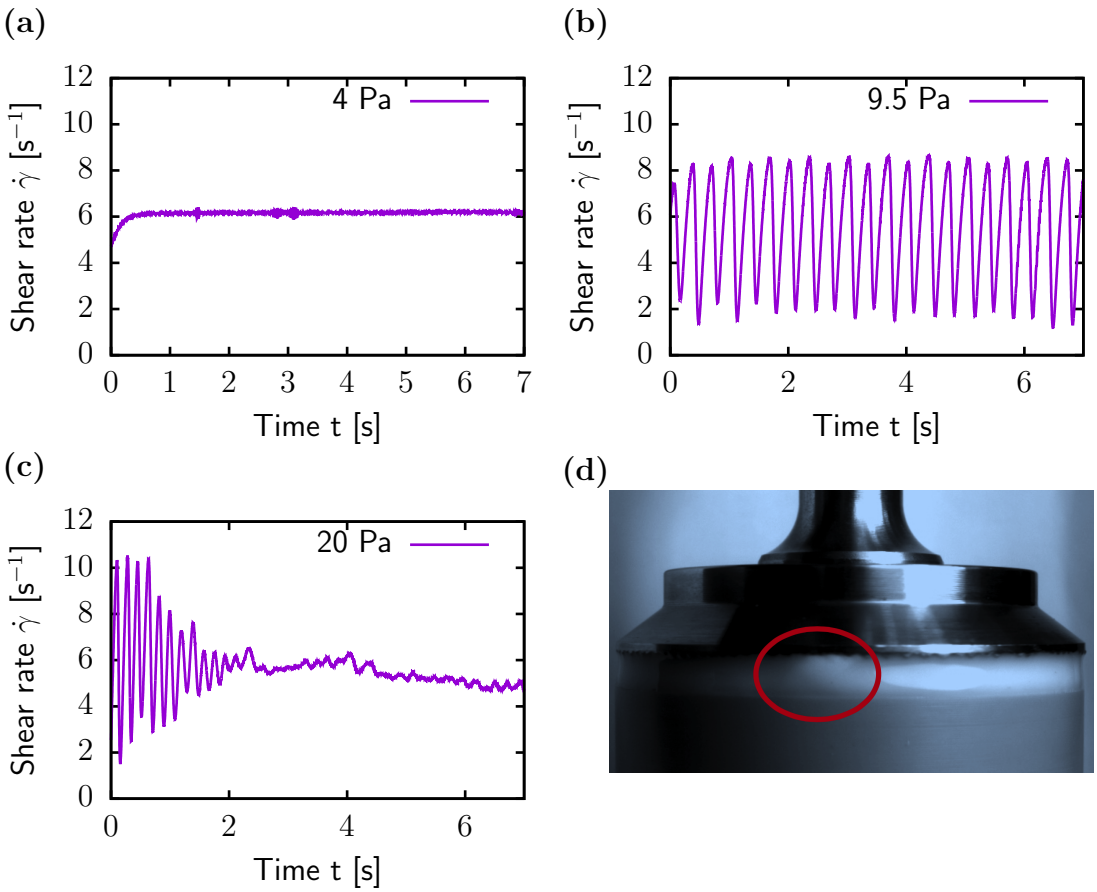

Figure 10.4: Breakdown of the flow regimes in Fig. 10.3. (a) Unthickened regime, (b) oscillatory regime and (c) chaotic regime. Transient edge distortions (d) were visible in regimes (b) and (c).

effect. It is also sensitive to system size: for cornstarch, increasing H changes ν and can eliminate the periodic regime altogether for small H. This is reminiscent of periodic velocity fluctuations observed in channel flows of concentrated PMMA dispersions, which disappear for large channel widths [37].

The progression of scenarios with increasing σ is reminiscent of the onset of "rheo-chaos" predicted in [160] (and references therein), which is generically linked to the competition between a "fast" timescale and a "slow" timescale. Identifying what sets these timescales in general would be an interesting topic for future work. For example, in [160] the slow timescale is set by particle migration; using a combination of rheology with microscopy [66] or NMR imaging [90] could test whether this is the case.

10.3.2 Final remarks

The above example illustrates an important difference between rheology above and below ϕ_m. Below ϕ_m, the stress (or shear rate) measured by a rheometer is governed by the constitutive properties of the suspension and is insensitive to the choice of measuring geometry. Particle migration [161] and edge fracture [31] are sensitive to the geometry, but are determined only by the geometry and not by intrinsic instabilities [3]. Above ϕ_m, σ (or $\dot{\gamma}$) is determined by the interplay between the sample and flow geometry – the rheology is non local, in the sense that the shear rate $\dot{\gamma}(\underline{x})$ at a particular position $\underline{x}$ is not completely determined by $\underline{\underline{\sigma}}(\underline{x})$, but also by the stress at the plates and free surface.

A major challenge is to develop a general understanding of flow above ϕ_m in terms of a few parameters characterising the suspension and the flow geometry. For channel flow, one of the parameters could be the effective friction coefficient between the solid plug of jammed suspension and the channel walls [37]. A systematic study of the effects of gap size and particle stability in cornstarch, and a revisiting of the problem of velocity oscillations in channel flow, would be a logical first step.

As shown in [108], discontinuous shear thickening is elegantly linked to the industrial process of granulation, in which an initially fluid suspension fractures into persistent lumps of jammed suspension under shear. The suspension is maintained in a jammed state by capillary stresses at the air-suspension interface when the shear is ceased, resulting in semi-permanent granules. Like the periodic jamming in Fig. 10.4, the existence of a granulation regime below ϕ_{RCP} is sensitive to particle-particle interactions; for example, the PMMA system in Ch. 5 granulates; whereas, cornstarch does not. Understanding the link between granulation and shear jamming, particularly while varying particle surface properties, is another interesting area.

[3] Such an instability arises above ϕ_m in shear-jammed non-Brownian suspensions when the system attempts to form shear bands which are unstable to particle migration [5].

Appendix A

Flow reversal data correction

In this appendix, we describe a correction scheme for the systematic drift in viscosity observed during shear reversal experiments on Whitehouse Scientific silica with the 10 mm parallel plate. We consider a volume fraction $\phi = 0.516$; the same procedure was used for other ϕ. Fig. A.1 shows the instantaneous viscosity $\sigma/(\eta_f\dot{\gamma})$ as a function of the absolute strain after reversal $|\gamma|$ for each of the -0.08 s^{-1} pre-shear runs. The thick black line denotes the first -0.08 s^{-1} run after loading, which we take as a benchmark. Subsequent runs show a non-monotonic shift in both η_∞ and η_h with $\dot{\gamma}$, which we plot relative to the benchmark values, $\eta_\infty^{\mathrm{ref}}$ and η_h^{ref}, in Fig. A.2.

We can rule out a drift in temperature as the cause of this variation, as in that case one would expect η_h^{pre} and $\eta_\infty^{\mathrm{pre}}$ to shift proportionately. Water absorption and sedimentation can also be ruled out, as both would lead to a monotonic decrease in both η_h^{pre} and $\eta_\infty^{\mathrm{pre}}$. We suspect that it is caused by local changes in concentration due to particle migration (either towards the centre of the plate, or out into the meniscus), which would affect $\eta_\infty^{\mathrm{pre}}$ but leave η_h^{pre} relatively unchanged, as the latter is only weakly dependent on ϕ [88]. Data transfer issues mean that the suspension continues to be sheared at $\dot{\gamma}$ for an arbitrary time (≈ 0.5 s) after the specified point time $12/\dot{\gamma}$, meaning that the absolute deflection angle about which the plate is reversed systematically drifts in time. Eccentricity in the plate can lead to a variation in η_∞ of up to a factor of two, which could account for the variation in Fig. A.2.

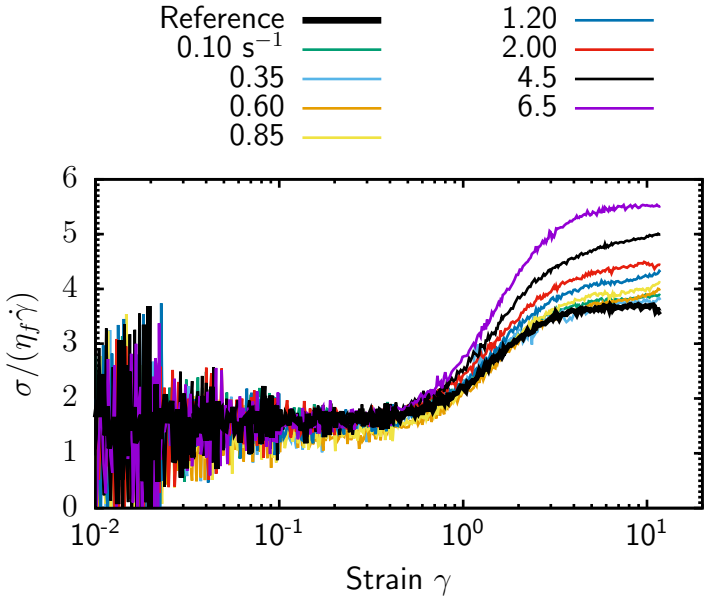

Figure A.1: Instantaneous relative viscosity $\sigma/(\eta_f\dot{\gamma})$ versus strain γ for the $\dot{\gamma} = -0.08$ s^{-1} pre-shear preceding different $\dot{\gamma}$, as labelled. The steady state viscosity η_∞ shifts upward as $\dot{\gamma}$, and hence the total duration of the experiment, increases.

Correcting for the systematic drift

We assume that whatever physical effect that causes $\eta^{\rm pre}$ to differ from $\eta^{\rm ref}$ will influence the subsequent reversal measurement at $\dot{\gamma} \neq 0.08$ s^{-1}. We correct data at different $\dot{\gamma}$ for this effect in two ways. Firstly, we shift all of $\eta(\gamma)$ such that the the steady state viscosity of the pre-shear $\eta_\infty^{\rm pre}$ is equal to $\eta_\infty^{\rm ref}$,

$$\eta(\gamma)^{\rm true} = \frac{\eta_\infty^{\rm ref}}{\eta_\infty^{\rm pre}}\eta(\gamma). \tag{A.1}$$

We refer to this henceforth as a "partial correction". Secondly, we squash $\eta(\gamma)$ vertically so that $\eta_\infty^{\rm pre} = \eta_\infty^{\rm ref}$ and $\eta_h^{\rm pre} = \eta_h^{\rm ref}$. We refer to this as a "full correction".

In Fig. A.3, we plot the steady state viscosity, (a), the hydrodynamic viscosity, (b), and the contact viscosity, (c), calculated in the usual way for uncorrected, partially-corrected and fully-corrected data. The steady state viscosity is unchanged up to $\dot{\gamma} \approx 1$ s^{-1}, above which the corrected $\eta_\infty(\dot{\gamma})$ is a factor of ≈ 2 lower than the uncorrected η_∞. The hydrodynamic part, $\eta_h(\dot{\gamma})$ varies by a factor of 1.5 for different correction methods; however, since $\eta_c(\dot{\gamma}) \gg \eta_h(\dot{\gamma})$, the choice of full or partial correction makes no visible difference to the contact component. For both correction methods, η_c is systematically lower than the

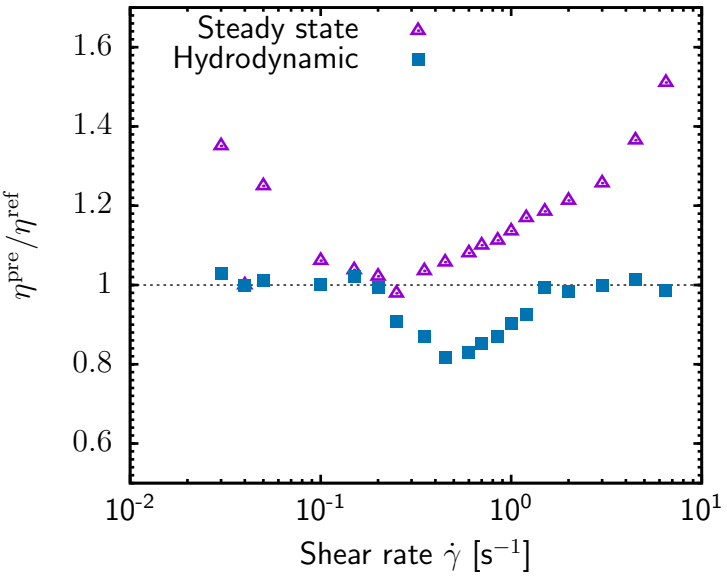

Figure A.2: Open purple triangles, steady-state viscosity for the 0.08 s^{-1} pre-shear at different $\dot{\gamma}$ relative to the reference run, $\eta_\infty^{\rm ref}/\eta_\infty^{\rm pre}$. Filled blue squares, ratio of the hydrodynamic viscosities, $\eta_h^{\rm ref}/\eta_h^{\rm pre}$.

uncorrected data. The choice of correction method is also unimportant at lower ϕ, where $\eta_h(\dot{\gamma})$ and $\eta_c(\dot{\gamma})$ are comparable.

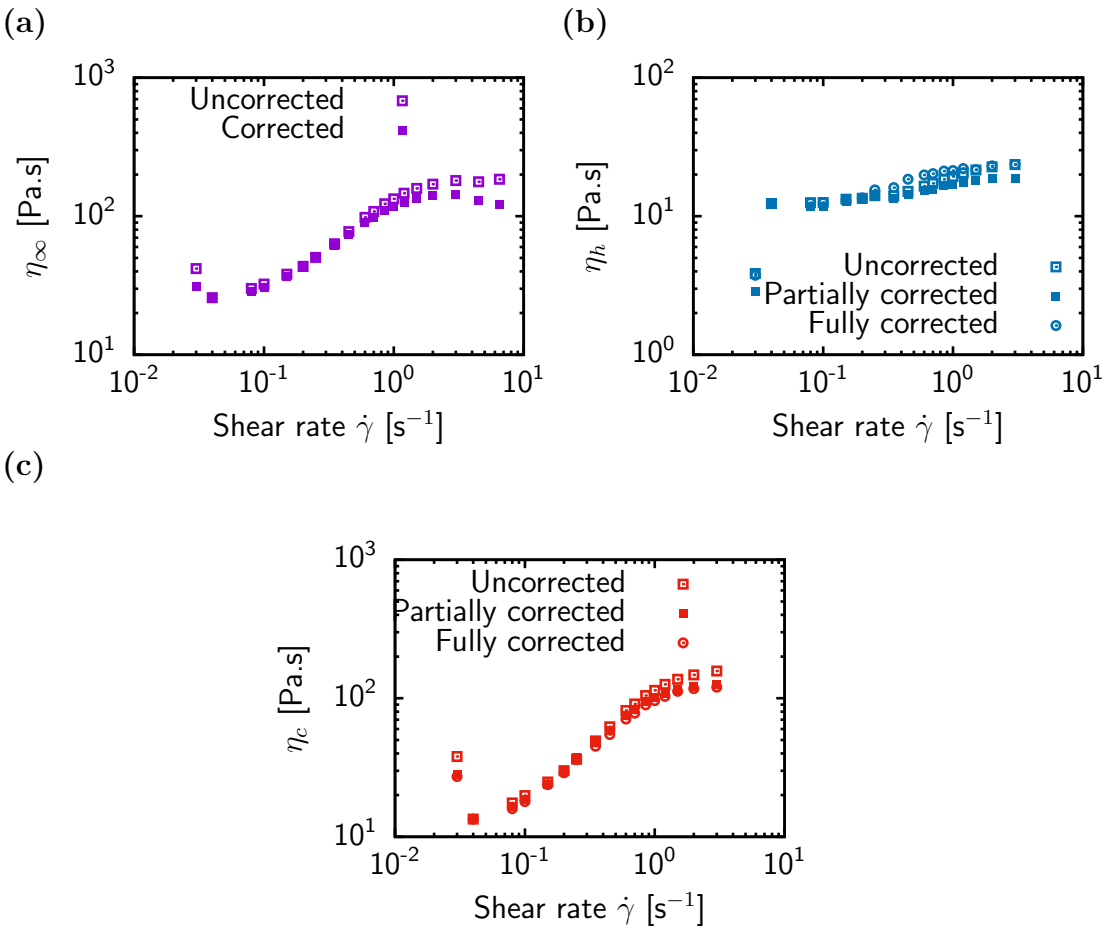

Figure A.3: Steady state η_∞, (a), hydrodynamic η_h, (b), and contact η_c, (c), viscosities versus $\dot{\gamma}$ for full, partial and no correction, as labelled. The data are shifted using the correction factors in Fig. A.2.

Appendix B

Whitehouse Scientific Silica viscosity correction

Both the frictionless (unthickened) $\eta^{(1)}(\phi)$ and frictional (shear thickened) $\eta^{(2)}(\phi)$ viscosities for Whitehouse Scientific (WHS) silica are systematically lower than the systems studied in Ch. 5. If we assume a reasonable value for random close packing, $\phi_{\mathrm{RCP}} = 0.63$, then $\eta^{(1)}$ and $\eta^{(2)}$ can be collapsed onto the existing data when plotted as a function of ϕ/ϕ_{RCP} by a single shift in the viscosity $\eta'(\phi) = \alpha\eta(\phi)$, with $\alpha \approx 7$, Fig. B.1. We attribute the discrepancy to a decrease in the viscosity of the solvent when the particles are added. We speculate that pores of particles received from the manufacturer contain water that was not removed during drying (the manufacturer does not specify how the particles are synthesised; however, we suppose that they were first dispersed in water before being dried into a powder). During sample preparation the trapped water seeps out into the surrounding glycerol, being replaced by glycerol, or, alternatively, resulting in shrinkage of the particles. The viscosity of glycerol is highly sensitive to water contact, so that the addition of water results in a sharp drop in η_f while changing ϕ by only a small amount. In this appendix, we estimate the fraction of the particle volume that must be occupied by water to cause to the seven-fold decrease in η and compare this to the porosity of the particles calculated from pycnometry. We also estimate the expected shift in ϕ.

Immediately after dispersal, the volume of glycerol V_{gly} present in a sample at nominal volume fraction ϕ is given by

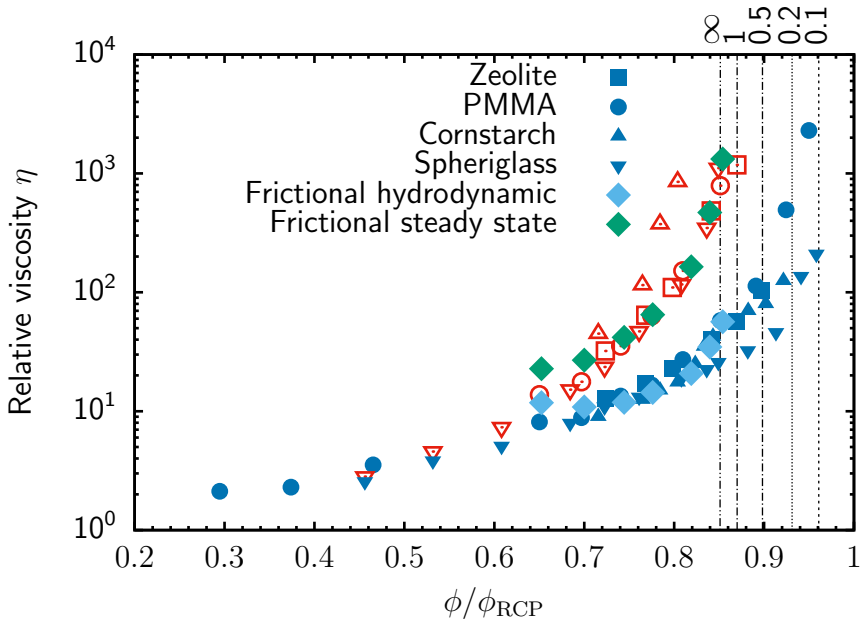

Figure B.1: Viscosity divergences for various systems in the intermediate size regime with the steady-state viscosity $\eta_\infty^{(2)}(\phi)$ and hydrodynamic $\eta_h^{(2)}(\phi)$ viscosity obtained by flow reversal on the shear-thickened branch for WHS silica superimposed. The WHS data were shifted up by a factor of $\alpha = 7$ to agree with the other $\eta_2(\phi)$ data.

$$V_{\mathrm{gly}} = (1-\phi)V,$$

where V is the total volume of the suspension. This ϕ assumes that the particles are composed of silica, water and potentially air, and do not contain glycerol. The total volume of water V_{water} is given by

$$V_{\mathrm{water}} = \phi V x,$$

where x is the fraction of the particles occupied by water by volume. For simplicity, we assume that all the trapped water leaves the particles and is not replaced by glycerol, so that the particles shrink by an amount $\sim (1 - V_{\mathrm{water}}/V)$. Then, volume ratio of water and glycerol in the solvent is given by

$$\frac{V_{\mathrm{water}}}{V_{\mathrm{gly}}} = \left(\frac{\phi}{1-\phi}\right) x. \tag{B.1}$$

Using the empirical expression for the viscosity a glycerol and water mixture from [148], we calculate that a seven-fold decrease in the viscosity of pure glycerol

corresponds to $V_{\text{water}}/V_{\text{glycerol}} = 0.14$, which, at $\phi = 0.50$, corresponds to $x = 0.28$.

Pycnometry

We now compare this x to an independent estimate of the pore volume obtained from helium pycnometry. In the pycnometry experiment [1] we assume that any fluid contained trapped in the pores of the particles is displaced by helium, so that the measured density is equal to the skeletal density of the silica $\rho_{\text{skel}} = 3.2$ g.cm^{-3}. We also measured measured the density of the particles when dispersed in water, $\rho = 1.97$ g.cm^{-3}, by measuring the density of the mixture at different mass fractions of silica with a density meter (Anton Paar DMA4500). The relative pore volume can be written as

$$x_{\text{pore}} = \frac{\rho - \rho_{\text{skel}}}{\rho_{\text{pore}} - \rho_{\text{skel}}}, \tag{B.2}$$

where $\rho_{\text{pore}} = 1$ g.cm^{-3} is the density of the fluid occupying the pores. Using the measured values of ρ and ρ_{skel} yields $x_{\text{pore}} \approx 0.5$, which is large enough to accommodate to the observed change in solvent viscosity.

Change in ϕ

It is not possible to properly estimate the change in ϕ induced by water seepage, as it is unclear what fraction of the water is replaced by glycerol and the extent to which the particles swell during this process. If the water is not replaced by glycerol and the particles shrink, then the true volume fraction ϕ' is (taking V_p to be the initial volume of the particles)

$$\phi' = \frac{V_p - V_{\text{water}}}{V_p + V_{\text{gly}}} = \frac{V_p(1-x)}{V_p + V_{\text{gly}}} = \phi(1-x), \tag{B.3}$$

where we have used $V_{\text{water}} = V_p x$. For $\phi = 0.5$ this predicts $\phi' = 0.86$ and $\phi = 0.43$, which is implausibly low given Fig. B.1. The fact that the WHS silica data can be collapsed onto the data for other systems with a vertical shift only implies that ϕ' is unchanged from its nominal value, so that the discrepancy

[1] We acknowledge Shreenath Krishnamurthy of the School of Engineering at Edinburgh for performing the helium pycnometry experiments.

between the data sets is due solely to a decrease in the solvent viscosity from $\eta_f = 7.8$ Pa.s to $\eta'_f \approx 1$ Pa.s. We note that the value of x required to effect the decrease in η_f could be lower than our estimate if glycerol imbibes the particles; our x should therefore be taken as an upper bound.

Bibliography

[1] M. Wyart and M. E. Cates, "Discontinuous shear thickening without inertia in dense non-brownian suspensions," *Physical Review Letters*, vol. 112, no. 9, p. 098302, 2014.

[2] R. Seto, R. Mari, J. F. Morris, and M. M. Denn, "Discontinuous shear thickening of frictional hard-sphere suspensions," *Physical Review Letters*, vol. 111, no. 21, p. 218301, 2013.

[3] B. Guy, M. Hermes, and W. Poon, "Towards a unified description of the rheology of hard-particle suspensions," *Physical Review Letters*, vol. 115, no. 8, p. 088304, 2015.

[4] N. Y. Lin, B. M. Guy, M. Hermes, C. Ness, J. Sun, W. C. Poon, and I. Cohen, "Hydrodynamic and contact contributions to continuous shear thickening in colloidal suspensions," *Physical Review Letters*, vol. 115, no. 22, p. 228304, 2015.

[5] M. Hermes, B. M. Guy, G. Poy, M. E. Cates, M. Wyart, and W. C. Poon, "Unsteady flow and particle migration in dense, non-brownian suspensions," *arXiv:1511.08011*, 2015.

[6] P. M. Chaikin and T. C. Lubensky, *Principles of condensed matter physics*, vol. 1. Cambridge Univ Press, 2000.

[7] R. K. Pathria, *Statistical Mechanics*. Butterworth-Heinemann, 1996.

[8] L. Cipelletti and E. R. Weeks, "Glassy dynamics and dynamical heterogeneity in colloids," in *Dynamical Heterogeneities in Glasses, Colloids, and Granular Media*, Oxford University Press, 2011.

[9] P. G. Debenedetti, *Metastable liquids: concepts and principles*. Princeton University Press, 1996.

[10] S. R. Elliott, *Physics of amorphous materials*. Longman Group, 1983.

[11] P. Pusey and W. Van Megen, "Phase behaviour of concentrated suspensions of nearly hard colloidal spheres," *Nature*, vol. 320, no. 6060, pp. 340–342, 1986.

[12] C. P. Royall, W. C. Poon, and E. R. Weeks, "In search of colloidal hard spheres," *Soft Matter*, vol. 9, no. 1, pp. 17–27, 2013.

[13] P. R. Nott, E. Guazzelli, and O. Pouliquen, "The suspension balance model revisited," *Physics of Fluids*, vol. 23, no. 4, p. 043304, 2011.

[14] J. Melrose, J. Van Vliet, and R. Ball, "Continuous shear thickening and colloid surfaces," *Physical Review Letters*, vol. 77, no. 22, p. 4660, 1996.

[15] S. R. Waitukaitis and H. M. Jaeger, "Impact-activated solidification of dense suspensions via dynamic jamming fronts," *Nature*, vol. 487, no. 7406, pp. 205–209, 2012.

[16] A. Lodge, *Elastic liquids*. Academic Press, 1964.

[17] R. B. Bird, R. Armstrong, and O. Hassager, *Dynamics of polymeric liquids. Vol. 1: Fluid mechanics*. John Wiley and Sons Inc., New York, NY, 1987.

[18] P. Oswald and D. Constantin, *Rheophysics: the deformation and flow of matter*. Cambridge University Press, 2009.

[19] R. Jackson, "Locally averaged equations of motion for a mixture of identical spherical particles and a newtonian fluid," *Chemical Engineering Science*, vol. 52, no. 15, pp. 2457–2469, 1997.

[20] G. Mase, *Schaum's outline of theory and problems of continuum mechanics*. McGraw-Hill, 1970.

[21] B. Lautrup, *Physics of continuous matter: exotic and everyday phenomena in the macroscopic world*. CRC Press, 2004.

[22] R. Aris, *Vectors, tensors and the basic equations of fluid mechanics*. Dover, 1962.

[23] B. Andreotti, Y. Forterre, and O. Pouliquen, *Granular media: between fluid and solid*. Cambridge University Press, 2013.

[24] D. Barthès-Biesel, *Microhydrodynamics and complex fluids*. CRC Press, 2012.

[25] E. Guazzelli and J. F. Morris, *A physical introduction to suspension dynamics*, vol. 45. Cambridge University Press, 2011.

[26] C. B. Holmes, *The jamming of dense suspensions under imposed stress*. PhD thesis, University of Edinburgh, 2004.

[27] F. Gadala-Maria and A. Acrivos, "Shear-induced structure in a concentrated suspension of solid spheres," *Journal of Rheology*, vol. 24, no. 6, pp. 799–814, 1980.

[28] C. W. Macosko, *Rheology principles, measurements and applications*. VCH, New York, 1994.

[29] S. E. Spagnolie, *Complex Fluids in Biological Systems*. Springer, 2015.

[30] R. Tanner and M. Keentok, "Shear fracture in cone-plate rheometry," *Journal of Rheology*, vol. 27, no. 1, pp. 47–57, 1983.

[31] M. Keentok and S.-C. Xue, "Edge fracture in cone-plate and parallel plate flows," *Rheologica acta*, vol. 38, no. 4, pp. 321–348, 1999.

[32] W. B. Russel, D. A. Saville, and W. R. Schowalter, *Colloidal dispersions*. Cambridge University Press, 1989.

[33] J. N. Israelachvili, *Intermolecular and surface forces: revised third edition*. Academic press, 2011.

[34] R. A. Jones, *Soft condensed matter*, vol. 6. Oxford University Press, 2002.

[35] J. Mewis and N. J. Wagner, *Colloidal suspension rheology*. Cambridge University Press, 2012.

[36] J. K. Dhont, *An introduction to dynamics of colloids*, vol. 2. Elsevier, 1996.

[37] L. Isa, *Capillary flow of dense colloidal suspensions*. PhD thesis, University of Edinburgh, 2007.

[38] M. Leunissen, "Manipulating colloids with charges and electric fields," 2007.

[39] J. T. G. Verwey, Evert Johannes Willem Overbeek, *Theory of the stability of lyophobic colloids*. Courier Corporation, 1999.

[40] M. Rubinstein and R. H. Colby, *Polymer physics*. 2003.

[41] J. Klein, "Shear, friction, and lubrication forces between polymer-bearing surfaces," *Annual review of materials science*, vol. 26, no. 1, pp. 581–612, 1996.

[42] B. d. L. Costello, P. Luckham, and T. F. Tadros, "Investigation of the interaction forces of polymer-coated surfaces using force balance, rheology, and osmotic pressure results," *Langmuir*, vol. 8, no. 2, pp. 464–468, 1992.

[43] G. Bryant, S. R. Williams, L. Qian, I. Snook, E. Perez, and F. Pincet, "How hard is a colloidal hard-sphere interaction?," *Physical Review E*, vol. 66, no. 6, p. 060501, 2002.

[44] B. Widom, "Intermolecular forces and the nature of the liquid state," *Science*, vol. 157, no. 3787, pp. 375–382, 1967.

[45] A. Yethiraj and A. van Blaaderen, "A colloidal model system with an interaction tunable from hard sphere to soft and dipolar," *Nature*, vol. 421, no. 6922, pp. 513–517, 2003.

[46] W. C. Poon, E. R. Weeks, and C. P. Royall, "On measuring colloidal volume fractions," *Soft Matter*, vol. 8, no. 1, pp. 21–30, 2012.

[47] P. Pusey, E. Zaccarelli, C. Valeriani, E. Sanz, W. C. Poon, and M. E. Cates, "Hard spheres: crystallization and glass formation," *Philosophical Transactions of the Royal Society of London A: Mathematical, Physical and Engineering Sciences*, vol. 367, no. 1909, pp. 4993–5011, 2009.

[48] J. J. Stickel and R. L. Powell, "Fluid mechanics and rheology of dense suspensions," *Annu. Rev. Fluid Mech.*, vol. 37, pp. 129–149, 2005.

[49] S.-E. Phan, W. B. Russel, Z. Cheng, J. Zhu, P. M. Chaikin, J. H. Dunsmuir, and R. H. Ottewill, "Phase transition, equation of state, and limiting shear viscosities of hard sphere dispersions," *Physical Review E*, vol. 54, no. 6, p. 6633, 1996.

[50] G. Petekidis, D. Vlassopoulos, and P. Pusey, "Yielding and flow of sheared colloidal glasses," *Journal of Physics: Condensed Matter*, vol. 16, no. 38, p. S3955, 2004.

[51] J. Van der Werff and C. De Kruif, "Hard-sphere colloidal dispersions: The scaling of rheological properties with particle size, volume fraction, and shear rate," *Journal of Rheology*, vol. 33, no. 3, pp. 421–454, 1989.

[52] H. M. Laun, "Rheological properties of aqueous polymer dispersions," *Die Angewandte Makromolekulare Chemie*, vol. 123, no. 1, pp. 335–359, 1984.

[53] I. E. Zarraga, D. A. Hill, and D. T. Leighton Jr, "The characterization of the total stress of concentrated suspensions of noncolloidal spheres in newtonian fluids," *Journal of Rheology*, vol. 44, no. 2, pp. 185–220, 2000.

[54] F. Boyer, É. Guazzelli, and O. Pouliquen, "Unifying suspension and granular rheology," *Physical Review Letters*, vol. 107, no. 18, p. 188301, 2011.

[55] L. E. Silbert, "Jamming of frictional spheres and random loose packing," *Soft Matter*, vol. 6, no. 13, pp. 2918–2924, 2010.

[56] R. Mari, R. Seto, J. F. Morris, and M. M. Denn, "Shear thickening, frictionless and frictional rheologies in non-brownian suspensions," *Journal of Rheology*, vol. 58, no. 6, pp. 1693–1724, 2014.

[57] F. Blanc, F. Peters, and E. Lemaire, "Local transient rheological behavior of concentrated suspensions," *Journal of Rheology*, vol. 55, no. 4, pp. 835–854, 2011.

[58] R. Ball and J. Melrose, "Lubrication breakdown in hydrodynamic simulations of concentrated colloids," *Advances in colloid and interface science*, vol. 59, pp. 19–30, 1995.

[59] S. Sastry, T. M. Truskett, P. G. Debenedetti, S. Torquato, and F. H. Stillinger, "Free volume in the hard sphere liquid," *Molecular Physics*, vol. 95, no. 2, pp. 289–297, 1998.

[60] L. Antl, J. Goodwin, R. Hill, R. H. Ottewill, S. Owens, S. Papworth, and J. Waters, "The preparation of poly (methyl methacrylate) latices in non-aqueous media," *Colloids and Surfaces*, vol. 17, no. 1, pp. 67–78, 1986.

[61] V. Martelozzo. PhD thesis, University of Edinburgh, 2001.

[62] D. R. Lide, *Handbook of Chemistry & Physics, 82nd edition*. CRC press, 2001.

[63] A. B. Schofield. private communication, 2016.

[64] P. Ballesta, G. Petekidis, L. Isa, W. Poon, and R. Besseling, "Wall slip and flow of concentrated hard-sphere colloidal suspensions," *Journal of Rheology*, vol. 56, no. 5, pp. 1005–1037, 2012.

[65] R. S. Farr and R. D. Groot, "Close packing density of polydisperse hard spheres," *The Journal of chemical physics*, vol. 131, no. 24, p. 244104, 2009.

[66] R. Besseling, E. R. Weeks, A. Schofield, and W. Poon, "Three-dimensional imaging of colloidal glasses under steady shear," *Physical Review Letters*, vol. 99, no. 2, p. 028301, 2007.

[67] S. M. Liddle, *Polydispersity effects on colloidal phase transitions and kinetic arrest*. PhD thesis, University of Edinburgh, 2014.

[68] D. J. Fairhurst, *Polydispersity in colloidal phase transitions*. PhD thesis, University of Edinburgh, 1999.

[69] G. Poy, *Shear Thickening in Dense Suspensions*. PhD thesis, University of Edinburgh, 2014.

[70] M. Kogan, C. J. Dibble, R. E. Rogers, and M. J. Solomon, "Viscous solvent colloidal system for direct visualization of suspension structure, dynamics and rheology," *Journal of colloid and interface science*, vol. 318, no. 2, pp. 252–263, 2008.

[71] M. Mackay, C. Liang, and P. Halley, "Instrument effects on stress jump measurements," *Rheologica acta*, vol. 31, no. 5, pp. 481–489, 1992.

[72] K. Dullaert and J. Mewis, "Stress jumps on weakly flocculated dispersions: Steady state and transient results," *Journal of colloid and interface science*, vol. 287, no. 2, pp. 542–551, 2005.

[73] "Dark chocolate particle size distribution." `http://www.azom.com/article.aspx?ArticleID=2794`. Accessed: 2016-01-15.

[74] "Ceramic casting slip particle size distribution." `http://www.azom.com/article.aspx?ArticleID=2794`. Accessed: 2016-01-15.

[75] "Cement particle size distribution." `http://www.horiba.com/uk/scientific/products/particle-characterization/applications/cement/`. Accessed: 2016-02-17.

[76] F. Händle, *Extrusion in ceramics*. Springer Science & Business Media, 2007.

[77] B. Russell, S. Blackburn, and D. Wilson, "A study of surface fracture in paste extrusion using signal processing," *Journal of materials science*, vol. 41, no. 10, pp. 2895–2906, 2006.

[78] C. Ness and J. Sun. private communication, 2016.

[79] A. Yoshimura and R. K. Prud'homme, "Wall slip corrections for couette and parallel disk viscometers," *Journal of Rheology*, vol. 32, no. 1, pp. 53–67, 1988.

[80] M. Cates, M. Haw, and C. Holmes, "Dilatancy, jamming, and the physics of granulation," *Journal of Physics: Condensed Matter*, vol. 17, no. 24, p. S2517, 2005.

[81] E. Brown and H. M. Jaeger, "Shear thickening in concentrated suspensions: phenomenology, mechanisms and relations to jamming," *Reports on Progress in Physics*, vol. 77, no. 4, p. 046602, 2014.

[82] D. J. Hodgson, M. Hermes, and W. C. Poon, "Jamming and the onset of granulation in a model particle system," *arXiv preprint arXiv:1507.08098*, 2015.

[83] N. J. Wagner and J. F. Brady, "Shear thickening in colloidal dispersions," *Physics Today*, vol. 62, no. 10, pp. 27–32, 2009.

[84] C. Neto, D. R. Evans, E. Bonaccurso, H.-J. Butt, and V. S. Craig, "Boundary slip in newtonian liquids: a review of experimental studies," *Reports on Progress in Physics*, vol. 68, no. 12, p. 2859, 2005.

[85] J. Yerushalmi, S. Katz, and R. Shinnar, "The stability of steady shear flows of some viscoelastic fluids," *Chemical Engineering Science*, vol. 25, no. 12, pp. 1891–1902, 1970.

[86] B. Andreotti, J.-L. Barrat, and C. Heussinger, "Shear flow of non-brownian suspensions close to jamming," *Physical Review Letters*, vol. 109, no. 10, p. 105901, 2012.

[87] P. Mills and P. Snabre, "Apparent viscosity and particle pressure of a concentrated suspension of non-brownian hard spheres near the jamming transition," *The European Physical Journal E*, vol. 30, no. 3, pp. 309–316, 2009.

[88] S. Gallier, E. Lemaire, F. Peters, and L. Lobry, "Rheology of sheared suspensions of rough frictional particles," *Journal of Fluid Mechanics*, vol. 757, pp. 514–549, 2014.

[89] J. Bender and N. J. Wagner, "Reversible shear thickening in monodisperse and bidisperse colloidal dispersions," *Journal of Rheology*, vol. 40, no. 5, pp. 899–916, 1996.

[90] A. Fall, F. Bertrand, D. Hautemayou, C. Mezière, P. Moucheront, A. Lemaitre, and G. Ovarlez, "Macroscopic discontinuous shear thickening versus local shear jamming in cornstarch," *Physical Review Letters*, vol. 114, no. 9, p. 098301, 2015.

[91] P. D. Olmsted, "Perspectives on shear banding in complex fluids," *Rheologica Acta*, vol. 47, no. 3, pp. 283–300, 2008.

[92] Z. Pan, H. de Cagny, B. Weber, and D. Bonn, "S-shaped flow curves of shear thickening suspensions: Direct observation of frictional rheology," *Physical Review E*, vol. 92, no. 3, p. 032202, 2015.

[93] T. Suhina, B. Weber, C. E. Carpentier, K. Lorincz, P. Schall, D. Bonn, and A. M. Brouwer, "Fluorescence microscopy visualization of contacts between objects," *Angewandte Chemie*, vol. 127, no. 12, pp. 3759–3762, 2015.

[94] D. Howell, R. Behringer, and C. Veje, "Stress fluctuations in a 2d granular couette experiment: a continuous transition," *Physical Review Letters*, vol. 82, no. 26, p. 5241, 1999.

[95] C. S. O'Hern, S. A. Langer, A. J. Liu, and S. R. Nagel, "Force distributions near jamming and glass transitions," *Physical Review Letters*, vol. 86, no. 1, p. 111, 2001.

[96] M. Trulsson, B. Andreotti, and P. Claudin, "Transition from the viscous to inertial regime in dense suspensions," *Physical Review Letters*, vol. 109, no. 11, p. 118305, 2012.

[97] C. D. Cwalina and N. J. Wagner, "Material properties of the shear-thickened state in concentrated near hard-sphere colloidal dispersions," *Journal of Rheology*, vol. 58, no. 4, pp. 949–967, 2014.

[98] A. Singh and P. R. Nott, "Experimental measurements of the normal stresses in sheared stokesian suspensions," *Journal of Fluid Mechanics*, vol. 490, pp. 293–320, 2003.

[99] A. Sierou and J. Brady, "Rheology and microstructure in concentrated noncolloidal suspensions," *Journal of Rheology*, vol. 46, no. 5, pp. 1031–1056, 2002.

[100] C. Ness and J. Sun, "Shear thickening regimes of dense non-brownian suspensions," *Soft matter*, vol. 12, no. 3, pp. 914–924, 2016.

[101] L.-N. Krishnamurthy, N. J. Wagner, and J. Mewis, "Shear thickening in polymer stabilized colloidal dispersions," *Journal of Rheology*, vol. 49, no. 6, pp. 1347–1360, 2005.

[102] C. P. Royall, M. E. Leunissen, A.-P. Hynninen, M. Dijkstra, and A. van Blaaderen, "Re-entrant melting and freezing in a model system of charged colloids," *The Journal of chemical physics*, vol. 124, no. 24, p. 244706, 2006.

[103] C. Heussinger and J.-L. Barrat, "Jamming transition as probed by quasistatic shear flow," *Physical Review Letters*, vol. 102, no. 21, p. 218303, 2009.

[104] N. Fernandez, R. Mani, D. Rinaldi, D. Kadau, M. Mosquet, H. Lombois-Burger, J. Cayer-Barrioz, H. J. Herrmann, N. D. Spencer, and L. Isa, "Microscopic mechanism for shear thickening of non-brownian suspensions," *Physical Review Letters*, vol. 111, no. 10, p. 108301, 2013.

[105] "Engineers handbook static friction coefficient of plexiglass." `http://www.engineershandbook.com/Tables/frictioncoefficients.htm`. Accessed: 2016-02-23.

[106] "The engineering toolbox friction and coefficients of friction." `http://www.engineeringtoolbox.com/friction-coefficients-d_778.html`. Accessed: 2016-02-23.

[107] M. Marigo, D. Cairns, J. Bowen, A. Ingram, and E. Stitt, "Relationship between single and bulk mechanical properties for zeolite zsm5 spray-dried particles," *Particuology*, vol. 14, pp. 130–138, 2014.

[108] D. Hodgson, M. Hermes, and W. C. K. Poon. private communication, 2016.

[109] I. M. Krieger, "Rheology of monodisperse latices," *Advances in Colloid and Interface Science*, vol. 3, no. 2, pp. 111–136, 1972.

[110] J. Mewis and J. Vermant, "Rheology of sterically stabilized dispersions and latices," *Progress in organic coatings*, vol. 40, no. 1, pp. 111–117, 2000.

[111] S. C. Tsai and K. Zammouri, "Role of interparticular van der waals force in rheology of concentrated suspensions," *Journal of Rheology*, vol. 32, no. 7, pp. 737–750, 1988.

[112] A. Ikeda, L. Berthier, and P. Sollich, "Unified study of glass and jamming rheology in soft particle systems," *Physical Review Letters*, vol. 109, no. 1, p. 018301, 2012.

[113] A. Ikeda, L. Berthier, and P. Sollich, "Disentangling glass and jamming physics in the rheology of soft materials," *Soft Matter*, vol. 9, no. 32, pp. 7669–7683, 2013.

[114] W. J. Frith, P. dHaene, R. Buscall, and J. Mewis, "Shear thickening in model suspensions of sterically stabilized particles," *Journal of Rheology*, vol. 40, no. 4, pp. 531–548, 1996.

[115] T. Strivens, "The shear thickening effect in concentrated dispersion systems," *Journal of Colloid and Interface Science*, vol. 57, no. 3, pp. 476–487, 1976.

[116] M. Smith, R. Besseling, M. Cates, and V. Bertola, "Dilatancy in the flow and fracture of stretched colloidal suspensions," *Nature communications*, vol. 1, p. 114, 2010.

[117] E. Brown, N. A. Forman, C. S. Orellana, H. Zhang, B. W. Maynor, D. E. Betts, J. M. DeSimone, and H. M. Jaeger, "Generality of shear thickening in dense suspensions," *Nature materials*, vol. 9, no. 3, pp. 220–224, 2010.

[118] V. Kobelev and K. S. Schweizer, "Strain softening, yielding, and shear thinning in glassy colloidal suspensions," *Physical Review E*, vol. 71, no. 2, p. 021401, 2005.

[119] R. Mari, R. Seto, J. F. Morris, and M. M. Denn, "Discontinuous shear thickening in brownian suspensions by dynamic simulation," *Proceedings of the National Academy of Sciences*, vol. 112, no. 50, pp. 15326–15330, 2015.

[120] A. Lemaître, J.-N. Roux, and F. Chevoir, "What do dry granular flows tell us about dense non-brownian suspension rheology?," *Rheologica acta*, vol. 48, no. 8, pp. 925–942, 2009.

[121] H. Barnes, "Shear-thickening (dilatancy) in suspensions of nonaggregating solid particles dispersed in newtonian liquids," *Journal of Rheology*, vol. 33, no. 2, pp. 329–366, 1989.

[122] E. Buckingham, "On physically similar systems; illustrations of the use of dimensional equations," *Physical Review*, vol. 4, no. 4, p. 345, 1914.

[123] G. Batchelor and J. Green, "The determination of the bulk stress in a suspension of spherical particles to order c 2," *Journal of Fluid Mechanics*, vol. 56, no. 03, pp. 401–427, 1972.

[124] G. Batchelor and J.-T. Green, "The hydrodynamic interaction of two small freely-moving spheres in a linear flow field," *Journal of Fluid Mechanics*, vol. 56, no. 02, pp. 375–400, 1972.

[125] E. Guyon, *Physical hydrodynamics*. Oxford University Press, 2001.

[126] M. E. Cates and M. Wyart, "Granulation and bistability in non-brownian suspensions," *Rheologica Acta*, vol. 53, no. 10-11, pp. 755–764, 2014.

[127] J. R. Smart and D. T. Leighton Jr, "Measurement of the hydrodynamic surface roughness of noncolloidal spheres," *Physics of Fluids A*, vol. 1, no. 1, pp. 52–60, 1989.

[128] J. F. Brady and G. Bossis, "The rheology of concentrated suspensions of spheres in simple shear flow by numerical simulation," *Journal of Fluid Mechanics*, vol. 155, pp. 105–129, 1985.

[129] J. F. Brady and J. F. Morris, "Microstructure of strongly sheared suspensions and its impact on rheology and diffusion," *Journal of Fluid Mechanics*, vol. 348, pp. 103–139, 1997.

[130] G. Bossis and J. F. Brady, "The rheology of brownian suspensions," *The Journal of chemical physics*, vol. 91, no. 3, pp. 1866–1874, 1989.

[131] G. MiDi, "On dense granular flows," *The European Physical Journal E*, vol. 14, no. 4, pp. 341–365, 2004.

[132] R. Tadmor, J. Janik, J. Klein, and L. J. Fetters, "Sliding friction with polymer brushes," *Physical Review Letters*, vol. 91, no. 11, p. 115503, 2003.

[133] N. S. Tambe and B. Bhushan, "Nanoscale friction and wear maps," *Philosophical Transactions of the Royal Society of London A: Mathematical, Physical and Engineering Sciences*, vol. 366, no. 1869, pp. 1405–1424, 2008.

[134] G. Ovarlez, F. Bertrand, and S. Rodts, "Local determination of the constitutive law of a dense suspension of noncolloidal particles through magnetic resonance imaging," *Journal of Rheology*, vol. 50, no. 3, pp. 259–292, 2006.

[135] H. J. Wilson and R. H. Davis, "The viscosity of a dilute suspension of rough spheres," *Journal of Fluid Mechanics*, vol. 421, pp. 339–367, 2000.

[136] H. J. Wilson and R. H. Davis, "Shear stress of a monolayer of rough spheres," *Journal of Fluid Mechanics*, vol. 452, pp. 425–441, 2002.

[137] J. F. Brady and G. Bossis, "Stokesian dynamics," *Annual review of fluid mechanics*, vol. 20, pp. 111–157, 1988.

[138] J. Bergenholtz, J. Brady, and M. Vicic, "The non-newtonian rheology of dilute colloidal suspensions," *Journal of Fluid Mechanics*, vol. 456, pp. 239–275, 2002.

[139] J. F. Morris, "A review of microstructure in concentrated suspensions and its implications for rheology and bulk flow," *Rheologica acta*, vol. 48, no. 8, pp. 909–923, 2009.

[140] D. R. Foss and J. F. Brady, "Structure, diffusion and rheology of brownian suspensions by stokesian dynamics simulation," *Journal of Fluid Mechanics*, vol. 407, pp. 167–200, 2000.

[141] J. R. Melrose and R. C. Ball, "Continuous shear thickening transitions in model concentrated colloidsthe role of interparticle forces," *Journal of Rheology*, vol. 48, no. 5, pp. 937–960, 2004.

[142] C. Ness and J. Sun, "Two-scale evolution during shear reversal in dense suspensions," *Physical Review E*, vol. 93, no. 1, p. 012604, 2016.

[143] J. Melrose and R. Ball, "The pathological behaviour of sheared hard spheres with hydrodynamic interactions," *Europhysics Letters*, vol. 32, no. 6, p. 535, 1995.

[144] P. d'Haene, J. Mewis, and G. Fuller, "Scattering dichroism measurements of flow-induced structure of a shear thickening suspension," *Journal of colloid and interface science*, vol. 156, no. 2, pp. 350–358, 1993.

[145] C. Heussinger, L. Berthier, and J.-L. Barrat, "Superdiffusive, heterogeneous, and collective particle motion near the fluid-solid transition in athermal disordered materials," *Europhysics Letters*, vol. 90, no. 2, p. 20005, 2010.

[146] M. Grob, C. Heussinger, and A. Zippelius, "Jamming of frictional particles: A nonequilibrium first-order phase transition," *Physical Review E*, vol. 89, no. 5, p. 050201, 2014.

[147] F. Parsi and F. Gadala-Maria, "Fore-and-aft asymmetry in a concentrated suspension of solid spheres," *Journal of Rheology*, vol. 31, no. 8, pp. 725–732, 1987.

[148] N.-S. Cheng, "Formula for the viscosity of a glycerol-water mixture," *Industrial & engineering chemistry research*, vol. 47, no. 9, pp. 3285–3288, 2008.

[149] F. Peters, G. Ghigliotti, S. Gallier, F. Blanc, E. Lemaire, and L. Lobry, "Rheology of non-brownian suspensions of rough frictional particles under shear reversal: A numerical study," *Journal of Rheology*, vol. 60, no. 4, pp. 715–732, 2016.

[150] M. Jerkins, M. Schröter, H. L. Swinney, T. J. Senden, M. Saadatfar, and T. Aste, "Onset of mechanical stability in random packings of frictional spheres," *Physical Review Letters*, vol. 101, no. 1, p. 018301, 2008.

[151] W. A. Ducker, T. J. Senden, and R. M. Pashley, "Direct measurement of colloidal forces using an atomic force microscope," *Nature*, vol. 353, pp. 239–241, 1991.

[152] D. Leighton and A. Acrivos, "The shear-induced migration of particles in concentrated suspensions," *Journal of Fluid Mechanics*, vol. 181, pp. 415–439, 1987.

[153] A. K. Gurnon and N. J. Wagner, "Microstructure and rheology relationships for shear thickening colloidal dispersions," *Journal of Fluid Mechanics*, vol. 769, pp. 242–276, 2015.

[154] T. S. Majmudar and R. P. Behringer, "Contact force measurements and stress-induced anisotropy in granular materials," *Nature*, vol. 435, no. 7045, pp. 1079–1082, 2005.

[155] B. Chakraborty. private communication, 2016.

[156] A. Deboeuf, G. Gauthier, J. Martin, Y. Yurkovetsky, and J. F. Morris, "Particle pressure in a sheared suspension: a bridge from osmosis to

granular dilatancy," *Physical Review Letters*, vol. 102, no. 10, p. 108301, 2009.

[157] T. Dbouk, L. Lobry, and E. Lemaire, "Normal stresses in concentrated non-brownian suspensions," *Journal of Fluid Mechanics*, vol. 715, pp. 239–272, 2013.

[158] B. Persson, *Sliding friction: physical principles and applications*. Springer Science & Business Media, 2013.

[159] F. P. Bowden and D. Tabor, *The friction and lubrication of solids*, vol. 1. Oxford university press, 1950.

[160] A. Aradian and M. Cates, "Minimal model for chaotic shear banding in shear thickening fluids," *Physical Review E*, vol. 73, no. 4, p. 041508, 2006.

[161] J. F. Morris and F. Boulay, "Curvilinear flows of noncolloidal suspensions: The role of normal stresses," *Journal of Rheology*, vol. 43, no. 5, pp. 1213–1237, 1999.